chapter 3

THEORETICAL PREDICTIONS

Coordinator

G. Brasseur (Belgium)

Principal Authors and Contributors

B. A. Boville (USA)
G. Brasseur (Belgium)
C. Bruhl (FRG)
M. Caldwell (USA)
P. Connell (USA)
A. De Rudder (Belgium)
A. Douglass (USA)
I. Dyominov (USSR)
D. Fisher (USA)
J. F. Frederick (USA)
R. Garcia (USA)
C. Granier (France)
R. Hennig (FRG)
M. Hitchman (USA)
I. Isaksen (Norway)
C. Jackman (USA)
M. Ko (USA)
S. Madronich (USA)
M. Prather (USA)
R. Rood (USA)
T. Sasaki (Japan)
S. Solomon (USA)
F. Stordal (Norway)
G. Visconti (Italy)
S. Walters (USA)
D. Wuebbles (USA)
A. Zadarozhny (USSR)
E. Zhadin (USSR)

CHAPTER 3

THEORETICAL PREDICTIONS

TABLE OF CONTENTS

3.1 MODEL FORMULATION AND RELIABILITY 283

3.1.1 Introduction 283
3.1.2 Formulation of Stratospheric Models 284
3.1.3 Model-Model Intercomparisons 291
3.1.4 Comparison Between Model Calculations and Observations 301

3.2 MODEL PREDICTIONS 317

3.2.1 Projected Scenarios for Halocarbons and Trace Gases 317
3.2.2 Predicted Response of the Atmosphere for Sample Scenarios 326
3.2.3 Predicted Changes in Surface UV Radiation 383
3.2.4 The Effects of Ozone Changes on Circulation 392

REFERENCES 395

3.1 MODEL FORMULATION AND RELIABILITY

3.1.1 Introduction

In order to understand the impact of man-made chemicals on the atmospheric ozone layer, it is essential to develop models that can perform long-term predictions of future ozone changes. Such models should make use of current knowledge about atmospheric chemistry, physics, and dynamics and specifically resolve one, two, or three dimensions of the atmosphere. Models that do not resolve all three dimensions must assume a suitable average (or uniformity) over the remaining dimensions. The one-dimensional (1-D) models are strongly limited by their simplified treatment of atmospheric dynamics, based on a crude empirical vertical eddy diffusion formulation. One-dimensional models are usually used to determine global average changes in total ozone column, and in the vertical distribution of ozone density. As the conditions encountered by trace gases are very different as a function of latitude, and because globally averaged models oversimplify the mean atmospheric transport, 1-D model results must be interpreted with caution, subject to verification by more elaborated multidimensional models. The advantages of 1-D models, however, are that a detailed chemistry and the coupling between chemistry and radiation can be treated accurately, and an almost unlimited number of scenarios for future ozone changes can be run on the computers. This has turned out to be useful in connection with abatement strategy for limiting future ozone layer changes.

The advantage of 2-D models is that they can be used to predict latitudinal and seasonal changes in ozone. Current models that are used for long-term predictions of ozone changes have a rather detailed chemistry, and to some extent include radiative and dynamic feedbacks. This has made 2-D models central in the study of future ozone changes. However there are clearly some limitations in their use. The handling of feedback among chemistry, radiation, and dynamics is not straightforward in a 2-D framework. This could be of particular importance in the lower stratosphere, where moderate changes in dynamics could be significant for the ozone distribution and for the exchange of gases between the stratosphere and the troposphere. For studies of the special phenomena connected to polar stratospheric ozone depletion, 2-D models have clear limitations and should be used with care. These phenomena are regional in character and are not latitudinally homogeneous. Furthermore, the chemical processes leading to disturbed chemistry in connection with polar stratospheric clouds contain large uncertainties and are highly non-linear. The treatment of heterogeneous polar chemical processes included in current 2-D models is more uncertain than the treatment of stratospheric gas-phase reactions.

Section 3.1.2 describes the formulation and recent improvements in two-dimensional models, which are used in the present assessment, and describes the three-dimensional models that are currently being developed to better simulate transport of chemically active trace gases, especially in the polar regions. The range in 2-D model calculations is described in Section 3.1.3, which highlights results from a recent intercomparison workshop. Selected fields calculated by these models are compared in Section 3.1.4 with observations. In Section 3.2.1, a number of scenarios have been defined, which encompass possible emission rates of different halocarbons in the future. Because of large uncertainties in the rates for heterogeneous processes, which play an important role in polar regions and possibly at other latitudes, the calculated responses of the models, reported in 3.2.2, include only the effects of homogeneous chemistry. One important distinction among the models is their ability to account for temperature feedbacks on the calculated ozone changes. Predicted changes in biologically damaging surface radiation (UV-B) for selected scenarios included in this assessment are discussed in Section 3.2.3. Finally, the possibility of changes in the atmospheric circulation resulting from substantial ozone depletions in the stratosphere is discussed in Section 3.2.4.

3.1.2 Formulation of Stratospheric Models

3.1.2.1 Introduction

Differential heating can give rise to a weak meridional circulation in the upper stratosphere and mesosphere, thereby setting up non-zero zonal flows relative to the ground via advection of angular momentum. This meridional circulation is characterized by rising motion in the summer hemisphere, sinking motion in the winter hemisphere, and meridional transport from the summer to the winter hemisphere. Processes generated in the troposphere affect this circulation considerably. These include the extension of the tropospheric meridional circulation into the lower stratosphere and the propagation of waves into the middle atmosphere. The tropospheric meridional circulation is driven partly by convection and by baroclinic waves and is almost always prescribed in current two-dimensional models. *In situ* absorption of planetary-scale and baroclinic Rossby waves accentuates the lower stratospheric meridional circulation, with increased poleward and downward motion. Absorption of gravity wave activity in the mesosphere increases the interhemispheric circulation due to differential heating alone by an order of magnitude. Kelvin, Rossby, and gravity wave absorption give rise to tropical meridional circulations associated with the semiannual and quasi-biennial oscillations. These wave-driven circulations ensure that temperatures are removed from radiative equilibrium, distinctly so in both the mesosphere and winter stratosphere.

Wave-driven circulations advect trace constituents and help control their distribution. In addition, "wave breaking" leads to tracer transport by mechanical turbulence. Wave absorption by radiative damping can also lead to irreversible mixing, provided the photochemical time constant of a tracer is similar to the eddy advective time scale. The propagation and absorption of waves depends on the background dynamical state, which in turn depends on the distribution of radiatively active trace gases. This interaction among wave and mean flow dynamics, photochemistry, and radiation makes the middle atmosphere particularly challenging to model. Middle atmosphere dynamics are thoroughly reviewed in Chapter 6 of WMO (1986). Recent discussions on regimes of dynamical and radiative control are given by Garcia (1987), Snieder and Fels (1988), and Ko et al. (1989).

Chemistry and transport models are the fundamental tool for assessing future ozone depletion. Extensive descriptions of 1-D, 2-D, and 3-D assessment models are given in Chapters 6 and 12 of WMO (1986). There have been significant improvements in most models since then. At present, 2-D models represent the best compromise among computational efficiency, ease of diagnosis, detailed radiation and chemistry, and realistic dynamics. Therefore, 2-D models are the primary assessment tool currently in use. The most useful 2-D model would be one that solves for the time evolution of zonal mean variables using the coupled set of equations governing the atmosphere, where the effects of disturbances on the mean flow and tracers are represented as accurately as possible. Such a model would have a high degree of interaction among wave and mean flow dynamics, photochemistry, and radiation. It would be self-consistent in the sense that the governing equations are mutually satisfied. Subsection 3.1.2.2 addresses self-consistency and degree of interaction in current 2-D models. The usefulness of mechanistic 3-D and general circulation models (GCMs) is discussed in subsection 3.1.2.3. The influence of coupling and feedback on 2-D model scenarios is described at the end of Section 3.2.2. Some recent work on feedbacks in 3-D models is described in Section 3.2.3.

3.1.2.2 2-D Models

Differential radiative heating and rotation account for the zonal flow being stronger and more homogeneous than the meridional or vertical flow. Therefore, it is reasonable to formulate a model in terms of

zonally averaged variables. However, the forced eddies which strongly influence the middle atmosphere are either small-scale or fundamentally three-dimensional. Recently, linear wave theory has been used by 2-D modelers to close the zonal mean dynamical equations for the eddy flux convergence terms. Efforts have focused on determining the meridional circulation and wave driving self-consistently and on capturing the interactive nature of the waves, mean flow, chemistry, and radiation. An international group of 2-D models currently engaged in carrying out scenario calculations is listed in Table 3.1.1. Following a discussion of theory common to 2-D models, the various capabilities of each model will be described.

The Eulerian and transformed Eulerian mean (TEM) equations are described by Andrews and McIntyre (1976), Boyd (1976), and Edmon et al. (1980). Zonal mean isentropic equations are given by Tung (1986, 1987). When all terms are retained, Eulerian, TEM, and isentropic formulations are equally correct. When Rossby waves predominate, both the meridional flux convergence and vertical advection terms are large in the Eulerian mean thermodynamic energy equation. This is true even when the waves are very weakly dissipating, are approximately steady, and the mean flow is only weakly accelerating. It is difficult to interpret the net effect of Rossby wave eddy fluxes on zonal mean dynamical variables in the Eulerian mean system (wave driving), since the meridional heat and momentum fluxes ($\overline{v'\theta'}$ and $\overline{u'v'}$) are large, and zonal mean potential temperature and zonal wind ($\bar{\theta}$ and $\bar{u}$) are joined through the continuity and thermal wind relations. Therefore, for interpreting the effects of Rossby waves it is useful to employ the TEM equations, with the residual mean meridional circulation defined by

$$\bar{v}^* = \bar{v} - \frac{1}{\rho_o}\frac{\delta}{\delta z}\left[\rho_o \frac{\overline{v'\theta'}}{\bar{\theta}_z}\right] \tag{1a}$$

$$\bar{w}^* = \bar{w} + \frac{1}{cos\phi}\frac{\delta}{\delta y}\left[cos\phi \frac{\overline{v'\theta'}}{\bar{\theta}_z}\right], \tag{1b}$$

Table 3.1-1. Capabilities of an international group of 2-D assessment models. The second column indicates whether tracer diffusion coefficients and the meridional circulation are determined simultaneously. The third column indicates how the circulation and diffusion coefficients are determined. The fourth column indicates whether heating rates (δQ), temperatures (δT), or the meridional circulation (δX) is allowed to change.

Model (Representatives)		X/Ks	Interaction	Code
AER1 (Ko, Sze)	No	Observations/Fixed	No	A
Aquila (Visconti, Pitari)	No	Observations/Fixed	No	I
CAO-LI (Jadin, Zvenigorodsky)	No	Observations/Fixed	No	R
DuPont (Fisher)	No	Observations/Fixed	No	
MPI (Brühl)	No	Observations/Fixed	No	M
MRI (Makino)	No	Observations/Fixed	No	J
NSI (Dyominov, Zadorozhny)	No	Observations/Fixed	No	U
Oslo (Isaksen, Stordal)	No	Observations/Fixed	No	O
CalTech (Yung, Zurek)	Yes	Diagnosed	δQ, δX	
GSFC2 (Jackman, Douglass)	Yes	Observations/Fixed	No	G
LLNL (Wuebbles, Connell)	No	Observations/Fixed	δQ, δT	L
Washington (Tung)	Yes	Diagnosed	δQ, δX	
AER2 (Schneider, Ko)	Yes	Raleigh drag	δQ, δT, δX	
Cambridge (Gray, Eckman)	No	Gravity		C
NOCAR (Garcia, Solomon)	Yes	Gravity/fixed K_{yy}	δQ, δT, δX	N
WisCAR (Brasseur, Hitchman)	Yes	Gravity and Rossby	δQ, δT, δX	W

where $(\overline{\ })$ and $(\ )'$ are the zonal mean and deviations therefrom, ρ_o is basic state density, θ is potential temperature, ϕ is latitude, and v and w are the meridional and vertical wind components. In the TEM framework, the eddy terms in the energy equation are small for Rossby waves, and the chief effect of Rossby waves is expressed as the Eliassen-Palm (EP) flux divergence acting on the zonal momentum equation. Although this aids interpretation of cause and effect for the dynamics, two extra eddy terms complicate the tracer equation (Hitchman and Brasseur, 1988). Moreover, where gravity waves dominate, such as in the mesosphere, meridional fluxes are small, but $\overline{w'\theta'}$ and $\overline{u'w'}$ can both be large. The TEM system then has the same form as the Eulerian equations, and there is again difficulty in interpreting net wave effects. Thus, Eulerian and TEM models are about equally useful.

In solving the zonal mean equations, one must specify the wave driving (flux terms in the dynamical equations) and tracer eddy fluxes. All models make use of the linear perturbation form for tracer μ

$$\mu' = -\eta' \frac{\partial \overline{\mu}}{\partial y} - \zeta' \frac{\partial \overline{\mu}}{\partial z} \tag{2}$$

to obtain

$$\overline{v'\mu'} = -K_{yy} \frac{\partial \overline{\mu}}{\partial y} - K_{yz} \frac{\partial \overline{\mu}}{\partial z} \tag{3a}$$

$$\overline{w'\mu'} = -K_{zy} \frac{\partial \overline{\mu}}{\partial y} - K_{zz} \frac{\partial \overline{\mu}}{\partial z}, \tag{3b}$$

where $K_{yy} = \overline{\eta' v'}$, $K_{yz} = \overline{v'\zeta'}$, $K_{zy} = \overline{w'\eta'}$, and $K_{zz} = \overline{w'\zeta'}$, and η' and ζ' are meridional and vertical parcel displacements.

Often, use is made of the quasi-geostrophic relationship between Rossby wave driving and the meridional flux of quasi-geostrophic potential vorticity, q

$$DF_R = \frac{1}{\rho_o \, \alpha \, cos\phi} \vec{\nabla} \cdot \vec{F}_R = \overline{v'q'}, \tag{4a}$$

where $\nabla \cdot \vec{F}_R$ is the Rossby wave EP flux divergence (Edmon et al., 1980). It is further assumed that relevant disturbances are small in amplitude, so that the flux-gradient relationship

$$\overline{v'q'} = -K_{yy} \, \overline{q}_y, \tag{4b}$$

holds. Newman et al. (1986) used (4) to determine K_{yy} from observational data. The meridional mixing coefficient obtained under this linearity assumption provides for a self-consistent effect of Rossby waves on tracers and on the mean flow. In isentropic coordinates, when Rossby waves dominate and the flow is nearly adiabatic, analogous relations to (4) apply even in the ageostrophic case (Tung, 1986).

Table 3.1.1 indicates the capabilities of each assessment model. It indicates whether the same information is used to determine tracer diffusion coefficients and the meridional circulation (self-consistency) or whether separate information is used. It lists how the circulation and tracer diffusion coefficients are determined, and the degree of interaction that can occur. Model complexity generally increases

downward. It is tempting to assume that more complex models represent the real atmosphere more faithfully. But feedback capabilities are a recent development. Much more work remains in understanding how they work in each model. All of the models employ a type of TEM formulation, except the classical Eulerian models of MPI and Cambridge. This is rather a small difference compared to the various approximations made in each model.

The strategy in most models in Table 3.1.1, including all of those in the first group, is to specify temperatures and heating rates from observations and to employ constant tracer mixing coefficients (AER1, Aquila, CAO-LI, DuPont, MPI, MRI, NSI, Oslo, GSFC2, LLNL). In this formulation there is usually no allowance for interaction among changing trace gas concentrations, temperatures, and transport. Since ozone concentrations depend on temperature in much of the atmosphere, it is extremely important that temperatures be allowed to change with changing trace gas distributions. In the Oslo model off-line temperature changes are specified from the results of Fels et al. (1980).

Specification of heating rates is tantamount to specifying the mean meridional circulation and, implicitly, the wavedriving, hence the mixing coefficients. For self-consistency, heating rates and mixing coefficients should not be specified independently. The models in the second group in Table 3.1.1 have either self-consistency or an interactive capability. In the GSFC2 model a simultaneous set of satellite observations is employed to determine temperatures, heating rates, the meridional circulation, and, using (4), mixing coefficients. In the LLNL model, perturbed constituent values are allowed to alter temperatures such that the net heating rates do not change. But the circulation and mixing coefficients are fixed and specified separately.

The Washington and California Institute of Technology models employ a different self-consistent approach, described by Tung (1987) and depicted in Figure 3.1.1. Only observed fixed temperatures are required as input. Since observed temperatures implicitly contain information about the effects of wave

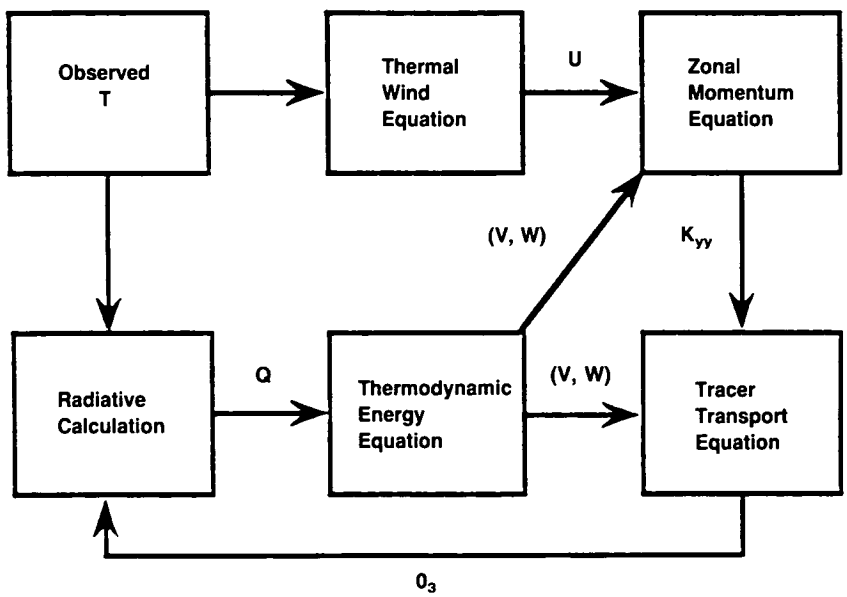

Figure 3.1-1. Schematic diagram showing an algorithm for determining the coupled set of transport parameters with prescribed T as input (adapted from Tung, 1987, Reidel, Inc.).

driving on the meridional circulation, the distribution of wave driving can be solved for. An ambiguity exists regarding the partitioning of $\vec{\nabla} \cdot \vec{F}$ into gravity, Rossby, and Kelvin wave effects. But in the extratropical winter stratosphere, Rossby waves dominate and (4) can be used. This is a powerful self-consistent technique for analyzing scenarios where temperatures are not expected to be perturbed very far. An interactive determination of simultaneous temperature and constituent changes (time integration) is not possible, although a new temperature field could be extrapolated and the process iterated.

In the last group of models in Table 3.1.1, the effects of one or several wave types are parameterized in an interactive manner. The AER2 model achieves a significant degree of interaction by parameterizing the wave-driving effects of gravity waves as a Rayleigh drag and those of Rossby waves as a diffusion of potential vorticity. Mixing coefficients are held fixed. The GSFC1 model is interactive for temperature, constituents, heating rate, and circulation, and includes a term that causes departures from a smooth annual cycle, but no information about wave physics is included.

The NOCAR, Cambridge, and WisCAR models each include the Lindzen (1981)/Holton (1982) parameterization of breaking gravity waves, which provides the body force, DF_g, due to those waves and the vertical eddy diffusion coefficient, K_{zz},

$$DF_g = B\,(c-\bar{u})^2 \left[(c-\bar{u}) + 3H\frac{\delta\bar{u}}{\delta z}\right] \tag{5a}$$

$$K_{zz} = DF_g \frac{(c-\bar{u})}{N^2} \tag{5b}$$

above the breaking height

$$z_b = 3\,H\,ln\left[\frac{|c-\bar{u}|}{\tilde{u}}\right] \tag{5c}$$

and below the critical level where c = $\bar{u}$. Wave driving and vertical diffusivity distributions co-evolve with model zonal winds. In (5) H is scale height, N is buoyancy frequency, B is proportional to the zonal wavenumber, k, and to the portion of a latitude circle occupied by waves, and $\tilde{u}$ is a measure of wave amplitude at the forcing level. Suitable values of B and ũ must be specified for discrete values of zonal trace speed c (Garcia and Solomon, 1985; Gray and Pyle, 1987; Brasseur and Hitchman, 1987).

In the Cambridge model constant eddy diffusivities are specified, while planetary Rossby wave momentum fluxes are determined from satellite observations. It has interactive parameterized Kelvin and mixed Rossby-gravity waves, which, together with the gravity wave parameterization, yield realistic semiannual and quasi-biennial oscillations (Gray and Pyle, 1987; 1989). The body force per unit mass due to the absorption of radiatively-damped equatorial waves is given by

$$DF_e = F_o\, e^{(z-z_o)/H}\; R(z)\; e^{-P(z)}\; e^{-(y/Y_L)} \tag{6a}$$

where F_o is the pseudomomentum flux at the forcing level z_o,

$$R(z) = \frac{\alpha(z)\,N}{k(\bar{u}-c)^2} \tag{6b}$$

is an inverse penetration scale given by the damping rate divided by the vertical group velocity,

$$P(z) = \int_{z_o}^{z} R(z')\, dz', \tag{6c}$$

α is a radiative damping profile, and Y_L is the meridional half-width about the Equator (Plumb 1977; Dunkerton 1979; Gray and Pyle, 1987). Suitable parameters are chosen for c and F_o for discrete Kelvin and mixed Rossby-gravity waves, where $Y_L = (2c/\beta)^{1/2}$ for Kelvin waves and $Y_L = (2 - 2ck^2/\beta)^{1/2}$ for mixed Rossby-gravity waves, and β is the northward gradient of planetary vorticity at the Equator.

The WisCAR model does not include equatorial planetary waves, but does include an interactive determination of wave driving and meridional diffusivity due to quasi-stationary planetary Rossby waves. This method, described in Hitchman and Brasseur (1988), makes use of the equation for conservation of Rossby wave activity, A,

$$\frac{\delta A}{\delta t} + \vec{\nabla} \cdot \vec{F}_R = -\alpha A \tag{7a}$$

$$\vec{\nabla} \cdot \vec{F}_R = \frac{1}{cos\phi} \frac{\delta}{\delta y} (cos\phi\, G_y\, A) + \frac{\delta}{\delta z} (G_z A), \tag{7b}$$

where $\vec{F}_R$ is the flux of Rossby wave activity. The WKBJ group velocity (G_y, G_z) depends only on model zonal winds. Solving this equation requires specification of the source of wave activity near the tropopause and the damping rate $\alpha(y, z)$. Once Rossby wave driving is obtained from (7) and applied to the meridional circulation, K_{yy} is determined from (4) and applied to all constituents.

Further details of the models may be found in the proceedings of the 2-D model intercomparison workshop held in Virginia Beach in 1988 (cf. Section 3.1.3). It should be emphasized that the strength and distribution of the meridional circulation and mixing coefficients vary a great deal among models. Efforts are being made to establish appropriate magnitudes by comparing model and observed tracer distributions. Schneider et al. (1989) and Jackman et al. (1989a) find that the distribution of total ozone is quite sensitive to the value of these parameters near the tropopause. Other uncertainties in the formulation of 2-D models lie in the applicability of mixing coefficients to individual tracers with differing sources and sinks (Smith et al., 1988) and nonlinearity associated with large amplitude waves.

3.1.2.3 3-D Models

Since the publication of the WMO report "Atmospheric Ozone 1985" (1986) there has been significant development in 3-D stratospheric chemistry models. This development has occurred both with mechanistic dynamical models and GCMs. As the models have evolved, it has become clear, from both theory and data, that some assessment problems are fundamentally three dimensional. It has also become clear that a synergism can exist between 2-D and 3-D models that will improve 2-D models and help to evaluate the impact of the fundamental assumptions of the 2-D formalism. This section describes the role of 3-D models in stratospheric assessment calculations.

Three-dimensional models have had only limited applications in assessment studies because of computational requirements. The computational aspects of stratospheric GCMs with chemistry has recently been discussed in Rood and Kaye (1989). The Goddard 3-D chemistry model, using a 4° latitude by 5° longitude grid with 19 vertical levels, would require approximately 5 hours of CYBER 205 CPU time per

model day. Therefore, assuming the model could be efficiently fit into core, it would require 76 days on a dedicated computer to model just 1 year. Given that the resolution of this model is known to be inadequate, it is obvious that 3-D assessment applications parallel to the 2-D efforts discussed in this chapter are impossible.

The most valuable assessment activity with 3-D models involves problems that are intrinsically three dimensional, and that can be investigated with time integrations of months. It is precisely such problems that 2-D models cannot properly simulate (e.g., stratospheric warmings). One such problem is the mixing of the Antarctic ozone hole with the rest of the atmosphere during the transition from winter to summer. To model this seasonal transition accurately, Rossby wave activity must be explicitly resolved. Calculations to compute the dilution of the Antarctic ozone hole into the global atmosphere are currently being performed at several laboratories (cf. Section 1.7). It will be required to use a 3-D model to account for the horizontal variation of column ozone change observed over the Northern Hemisphere during the last decade (Figure 2.2-9).

A similar problem exists for the Northern Hemisphere, where it is expected that heterogeneous processes taking place in the polar vortex might be producing enhanced levels of reactive chlorine compounds. In the Antarctic there is much longer isolation of the polar vortex from the rest of the hemisphere and, therefore, localized ozone destruction in the vortex. In the Northern Hemisphere the vortex mixes with the rest of the hemisphere in late winter or early spring, and the chlorine compounds produced within the vortex might deplete ozone more generally in the hemisphere. Once again it is necessary to represent Rossby wave activity accurately to evaluate this potential depletion mechanism.

Quantitatively accurate assessments for the two problems described above can be obtained by using a GCM as an analysis tool to generate wind fields that are representative of actual stratospheric conditions. The use of winds generated by data assimilation using a 3-D model to transport reactive constituents has been described in Rood et al. (1989). These studies suggest that accurate evolution of constituents in a Rossby wave dominated environment (wintertime stratosphere) can be modeled for 60 days or longer. Figure 3.1.2 shows the total ozone field on 28 February 1989 as measured by TOMS and as modeled from a January 1 initial condition. The model captures most of the important features of the Northern Hemisphere total ozone field, and suggests that mixing of high- and low-latitude air is properly represented.

The data assimilation studies also imply that the wintertime polar vortex in the Northern Hemisphere is largely isolated from the rest of the hemisphere, as suggested by Juckes and McIntyre (1987). This implies that studies of polar processes in general are best carried out within the 3-D model formulation. The 2-D model representation communicates nonpolar air with polar air on too short a time scale. Brasseur et al. (personal communication) have already shown the potential application of mechanistic 3-D models to the Antarctic ozone hole. Recent papers by Rose and Brasseur (1985), Grose et al. (1987), and Kaye and Rood (1989) present relatively complete chemical representations in 3-D model studies of the wintertime hemisphere.

The fact that 2-D models have difficulty representing the mixing of middle latitude air with polar air points out another role of 3-D models. Three-dimensional models can be used to quantitatively assess how well 2-D models represent intrinsically three-dimensional processes. Similarly, 3-D models can be used to guide the incorporation of 3-D processes (such as polar heterogeneous chemistry) into 2-D models in an accurate manner. Global or regional 3-D models are expected to contribute not only to polar chemistry processes, but to problems of stratosphere-troposphere exchange, gravity wave mixing, chemical eddy processes, dynamical changes due to ozone decrease and greenhouse gas increase, and any problem where wave propagation and dissipation is of fundamental importance.

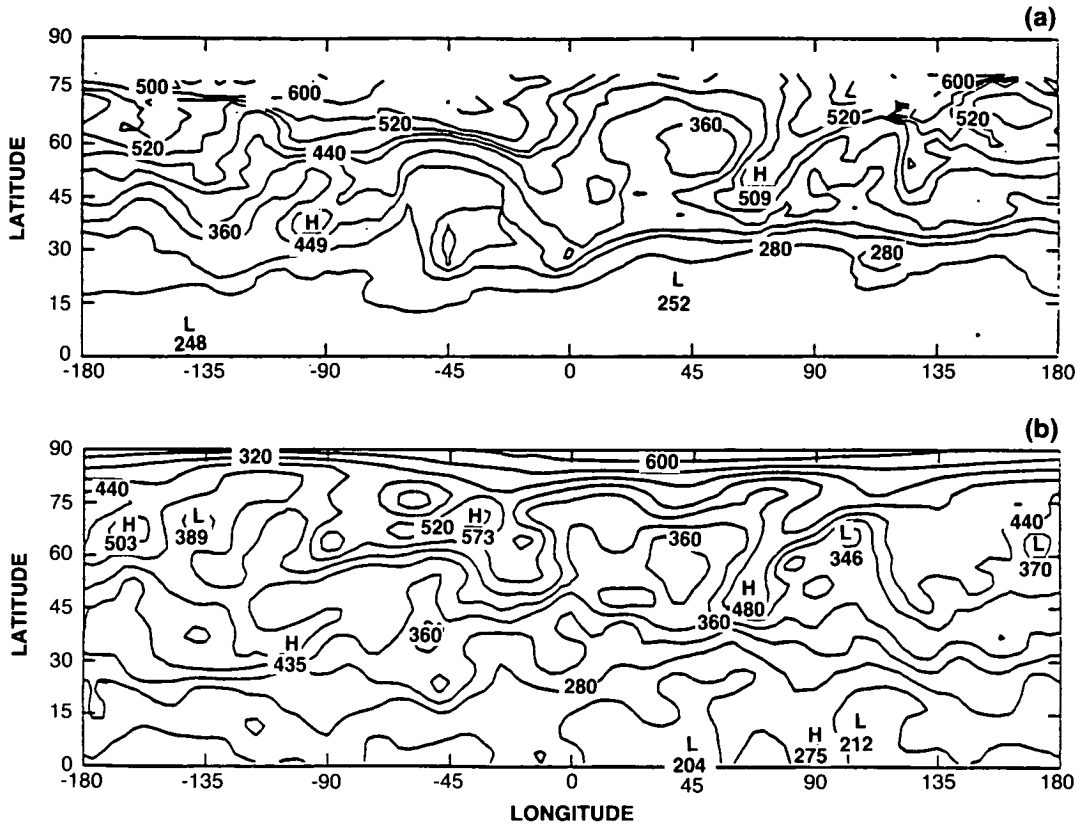

Figure 3.1-2. Total ozone field on 28 February 1989 (a) as measured by TOMS and (b) as modeled from a January 1 initial condition (after Rood et al., 1989).

Even with adequate computer resources, 3-D assessment experiments would not address and solve many of the problems inherent with 2-D assessments. Fundamental problems exist with 3-D simulations of dynamics (WMO, 1986, p. 307), and there is little indication that simply expanding to three dimensions will solve many of the classic problems of atmospheric chemistry (e.g., the 40-km ozone problem). Similar to the 2-D model experience, 3-D dynamics models are controlled to a large extent by the treatment of subscale processes (for instance, Rind et al., 1989). This treatment is necessarily parameterized, and leaves any long-term 3-D assessment with analogous uncertainties to 2-D assessments.

The current state of model development and computational resources limits the applications of 3-D models in assessment studies. Rood and Kaye (1989) estimate that computer speeds must be increased by a factor of 100–1000 (compared to a CYBER 205) for assessment applications similar to those performed by 2-D models. In the meantime, 3-D models will be valuable in limited assessment applications and as complements to 2-D models.

3.1.3 Model—Model Intercomparisons

3.1.3.1 Introduction

The responsibility of making predictions of future ozone levels, as well as the interest of the scientific community in testing and validating models, has led to a series of model intercomparisons. The primary

objective of these model intercomparisons is to understand the specific, fundamental differences among the stratospheric models and, in particular, their predictions of stratospheric ozone.

Another important objective of the intercomparisons is to promote basic improvements in the treatment of chemistry and transport in all models through the collective scientific effort of the community. The two-dimensional Intercomparison Workshop of September 1988 at Virginia Beach, Virginia was a major effort with international participation. Most of the groups involved in multi-dimensional modeling contributed to the planning and execution of the workshop.

Stratospheric models have become increasingly complex over the last decade, as they have strived to develop more accurate simulations of the radiative transfer in the atmosphere, of the chemical reactions coupling more than two dozen species, and of multi-dimensional transport. The end result of the assessments shown in this chapter, i.e., the perturbations to the ozone distribution at the end of a 100-year simulation, is the consequence of the interaction of the different numerical representations of the chemistry, radiation and atmospheric circulation in the models. In order to understand the difference in calculated ozone perturbations between two models, it is necessary to examine, in greater detail, the detailed components of radiation, chemistry, and transport in each model.

Therefore, the Virginia Beach Workshop (as did previous workshops) defined a set of detailed, but restricted, calculations for the intercomparison that were designed to allow for intercomparison of the individual components, as well as of the integrated model. The participating modeling groups agreed to perform series of specified calculations using the most recent set of photochemical rates (DeMore et al., 1987). The experiments were grouped in order to test several areas of the model simulation of the stratosphere:

(a) photodissociation and heating rates using the same O_3 and temperature fields in all models;

(b) transport of synthetic tracers with prescribed chemistry;

(c) distribution of stratospheric species in the current atmosphere; and

(d) predictions of perturbations to ozone and temperature for a specified future atmospheric composition.

The Virginia Beach Workshop was the most ambitious in the series of stratospheric model intercomparisons. The agenda was too extensive to be covered in the week-long meeting; and most effort was put into sections (a), (b), and parts of (c) above. A brief summary of the workshop is included here. The complete workshop report (Jackman et al., 1989b) includes over 1400 figures and tables from the participating models and is published as a NASA Conference Proceedings (available from Charles H. Jackman, Code 616, NASA/GSFC, Greenbelt, MD 20771, USA).

3.1.3.2 Photodissociation Rates

The comparison of photodissociation rates (J-values/sec) revealed substantial differences and similarities among the models. In the case of O_2 dissociation, the primary source of stratospheric O_3, the models fell into two groups. Within each group, agreement was very good over all latitudes and altitudes in the stratosphere, but the two groups disagreed systematically by a factor of 2. Similarly, systematic differences were found in the calculated J-values for CFC-11 and CFC-12. The largest disagreement among the models, up to a factor of 5, occurred for J(NO). Dissociation of NO leads to a sink for odd-nitrogen in the upper

stratosphere and mesosphere. Photolysis of NO occurs in the more opaque part of the Schumann-Runge bands, and the different methods of modeling this J-value have been noted in the previous assessment (WMO, 1986) but have not been resolved since then or in this intercomparison.

A comparison of J-values for species with significant photolysis at near-ultraviolet and visible wavelengths (O_3, NO_2, HNO_3, $ClONO_2$) points to substantial differences in the treatment of scattered light from the troposphere (Rayleigh, clouds, aerosols, and the surface). The importance of scattered light is greatest in the lower stratosphere where photodissociation is dominated by longer wavelengths, the shorter wavelengths being absorbed by ozone in the upper stratosphere. Among the models that included multiple scattering, there are differences in technique and in results; models that did not include scattered light had systematically lower J-values by about 30–50%.

The workshop participants viewed these differences in the modeled J-values as being too large to be explained by the different approaches in modeling (e.g., cross sections, spectral resolution, solar irradiance, diurnal cycles). Consequently, many of the modeling groups are continuing a specific intercomparison not only of J-values, but also of the monochromatic radiative transfer of solar radiation in the stratosphere and troposphere. Key issues involve diurnal averaging, scattering, and atmospheric transmission in the Schumann-Runge bands (175–205 nm).

Validation of the modeled photodissociation rates cannot rely on model intercomparisons alone; a further necessary component is the accurate measurement of the attenuation of sunlight in wavelength regions where O_2 is photodissociated (180–230 nm) and where much of the photolytically active ultraviolet occurs in the lower stratosphere and troposphere (280–340 nm). A limited number of atmospheric measurements and determinations of O_2 transmission are available (Anderson and Hall, 1986; Herman and Mentall, 1982) but have not been fully compared with these models.

3.1.3.3 Heating and Cooling Rates

Stratospheric heating by sunlight is provided almost entirely by absorption by ozone. Agreement between models varies, with some agreement in the lower stratosphere, but differences as large as 35% at the stratopause (about 45 km). Some of the differences in calculated heating rates point to errors in the diurnal averaging or to different treatments of scattered sunlight from the troposphere.

Stratospheric cooling (and on some occasions, heating) is controlled by the transfer of infrared radiation between the ground, clouds, different levels of the atmosphere, and space. The models include what are believed to be the most important species and wavelength intervals: CO_2 bands near 15 μm, O_3 bands near 9.6 μm, and water vapor bands. The calculated net cooling rates agree qualitatively in terms of latitudinal and vertical patterns, but quantitative differences may be large, for example 40% at the stratopause. The tropical lower stratosphere is very cold and presents difficulties in modeling: absorption of 9.6 μm radiation by ozone heats the stratosphere, and the overall effect of the infrared radiation may be a small net heating near the tropopause. As might be expected, the disagreement between models is greatest in this region, with differences even in the sign of the net cooling. The workshop participants are continuing the intercomparison of radiation schemes in a separate, more detailed study.

3.1.3.4 Circulation and Tracer Transport

The distribution of long-lived tracers in the stratosphere (e.g, CFCs, N_2O, CH_4, O_3 below 30 km) is a balance between photochemistry and transport. Transport in 2-D models is simulated by a combination of

advection by the mean meridional circulation (i.e., vertical and horizontal winds) and of diffusive mixing (often denoted by K, the diffusion coefficient). The diffusive mixing in 2-D models is intended to simulate tracer transport by those processes that are not explicitly resolved by the zonally and monthly averaged transport in these models (e.g., 3-D or transient eddies). One class of 2-D models specifies the meridional circulation; a more recent class of 2-D models calculates the circulation interactively along with the ozone and temperature fields. See Section 3.1.2 on model formulation for a more detailed discussion.

An intercomparison of the meridional circulation, in terms of residual winds, was made at the workshop. The overall pattern in all models was similar: upwelling in the tropical lower stratosphere and downward transport at mid- and high latitudes. At higher altitudes the pattern is more seasonal with upward motion over the summer pole, meridional transport through the mesosphere, and downward motion over the winter pole. The differences in the meridional wind field, however, cannot be assessed independently of the diffusion used in the models. Unfortunately, the diffusive mixing of the models was difficult to quantify, and thus to compare, because of the different formulations and combinations of vertical, horizontal, and quasi-horizontal mixing. Therefore we continued the intercomparison with a series of synthetic tracer experiments, which used the same specified chemistry in all models, in order to test the "effective" transport of the models.

One of the three synthetic tracers, X, was defined to have a source that would maintain a uniform tropospheric concentration of 1 ppbv below 850 mbar and a sink (similar in magnitude to N_2O) that was defined simply as a function of pressure. The model simulations were carried out to steady-state, and nine of the model results for December are shown here in Figure 3.1-3. Mixing ratios of X at 30 km are similar for all models (0.6–0.8 ppbv at the Equator and 0.1–0.2 ppbv at high latitudes), but by 40 km the values from different models diverge, indicating substantial differences in the strength of the equatorial upwelling in the mid- and upper stratosphere. The global, annually averaged lifetime of X varied from 97 to 127 years, consistent with the range for N_2O reported in Section 3.2.

Two other synthetic tracers were studied: tracer Y, with no atmospheric loss, in which a fixed amount was put initially into the lower troposphere and the rate of transport of a transient emission into the stratosphere was examined; and tracer Z with boundary conditions in the upper stratosphere and lower troposphere meant to resemble that of ozone. The steady-state distribution of the column of tracer Z resembled that of ozone in most models with equatorial minima of order 100 Dobson units (compared with 250 Dobson units for ozone) and a springtime maximum at high latitudes of order 500–600 Dobson units (compared with about 360–460 Dobson units for ozone). The Z experiment tested the seasonal changes in circulation that determine the month-by-month pattern in ozone column and, further, demonstrated the importance of ozone chemistry in the lower stratosphere: production in the tropics balanced by loss at mid- to high latitudes.

3.1.3.5. Current Atmosphere: 1980

The composition of the stratosphere is not uniquely defined by observations; indeed, some overlapping data sets provide conflicting results. Because of the focus and limited amount of time for the Virginia Beach intercomparison, we chose to limit our study to the model-model differences in predictions of the "present-day" atmosphere (defined as 1980 in terms of source gas concentrations). Detailed figures of the model predictions for many chemical species are presented in the conference proceedings and may be compared with available observations.

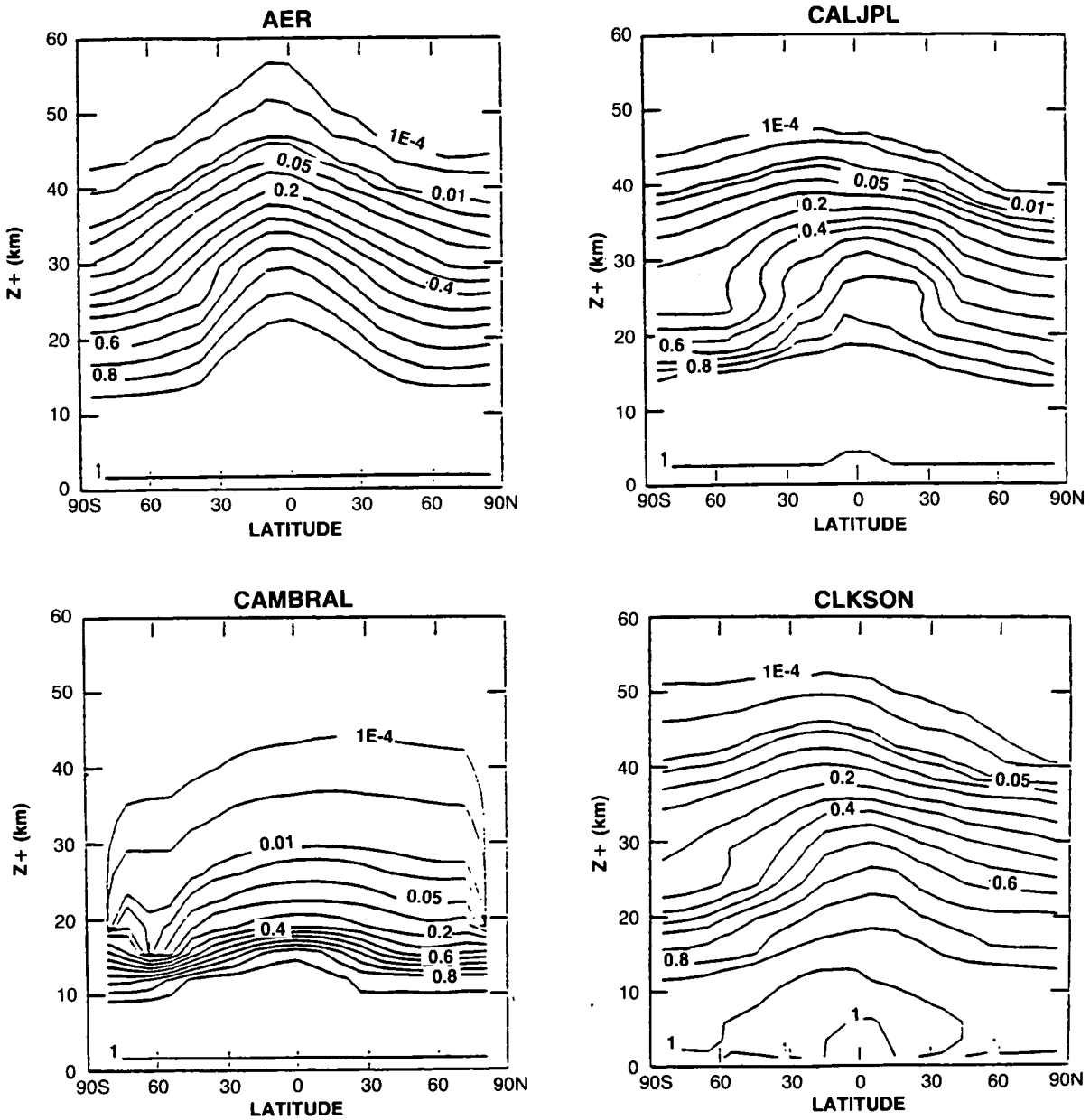

Figure 3.1-3. Two-dimensional distribution of tropospheric source gas X from nine models for the month of December.

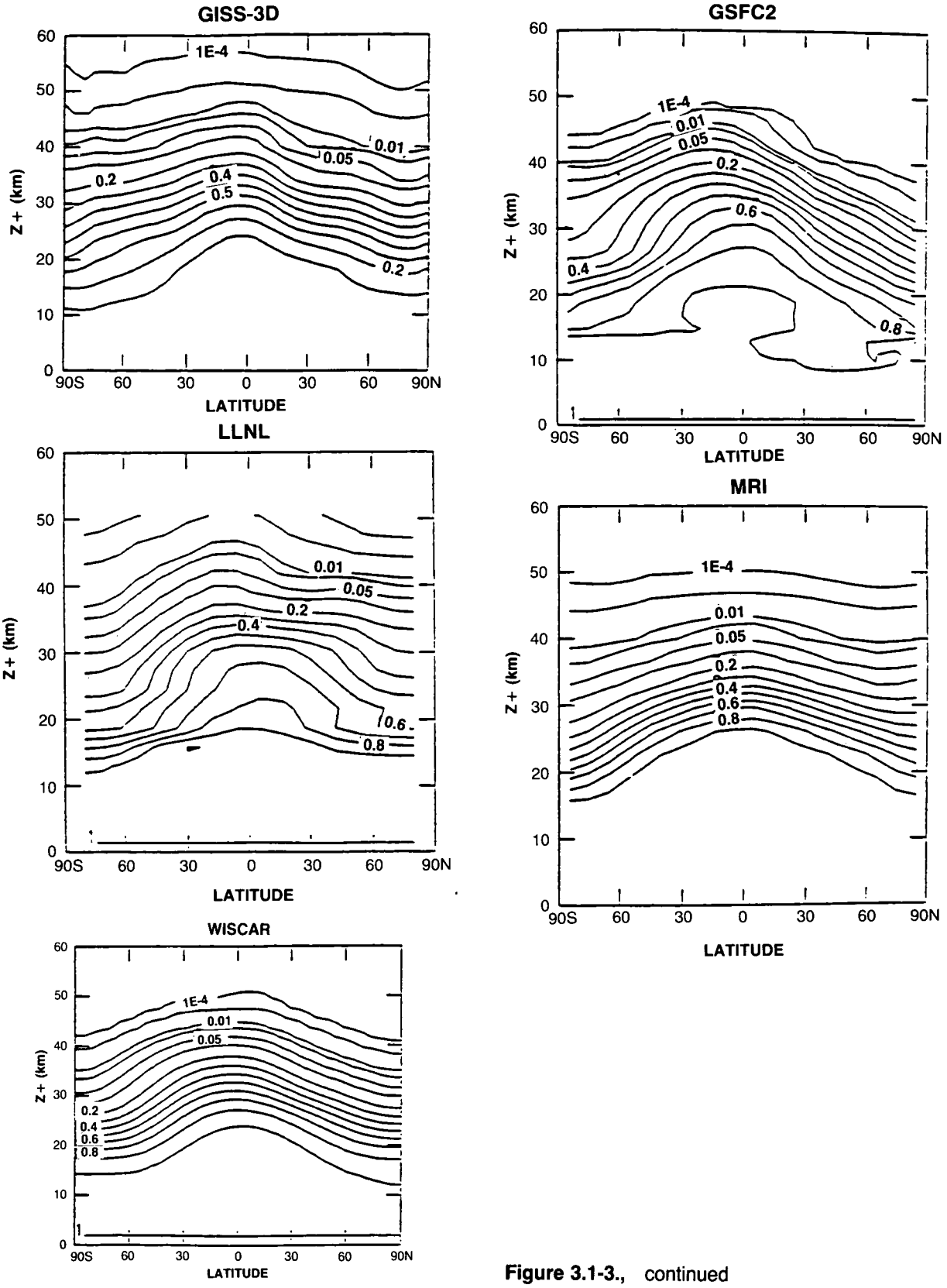

Figure 3.1-3., continued

The classic comparison of model with model and of model with observation is that of ozone column: a minimum in the tropics and a maximum at high latitudes in spring at the pole in the north and offset from the pole (60°S) in the south. In the 2-D models, that quantity is not always useful to intercompare because modelers often use the observed column ozone as a critical test and do not accept a new version of the model (e.g., new chemistry, circulation, diffusion) until it is able to simulate reasonably the observed seasonal and latitudinal patterns in ozone column.

In addition to ozone, the workshop examined the predicted stratospheric column abundances of HNO_3, HCl, and NO_2, for which observations of the latitudinal gradients are available. These columns are sensitive to transport and chemistry in the lower stratosphere. For the tropospheric source gases, N_2O, CH_4, CH_3Cl, CCl_4, $CFCl_3$, and CF_2Cl_2, we examined their patterns of decrease in the stratosphere which is sensitive to transport and chemistry in the upper and middle stratosphere.

Intercomparison of the faster photochemistry used latitude-by-altitude cross sections of some short-lived radicals (e.g., OH, HO_2, ClO) and of some ratios (e.g., NO/NO_2, ClO/HCl). The ratio ClO/HCl is a measure of the fraction of chlorine released from halocarbons that participates in catalytic ozone destruction. It is a result of the balance between several reactions: HCl with OH and subsequently Cl with O_3 to produce ClO, and the reverse sequence transforming ClO to Cl and subsequently Cl with CH_4 to form HCl. The ratio ClO/HCl (noontime or daytime averages for December) is shown in Figure 3.1-4. In the upper stratosphere (30–50 km) the models differ widely, and further examination of the other factors (e.g., OH, O_3, CH_4, NO) controlling this ratio is necessary.

The tropospheric simulations of the models were not specifically examined at the workshop. Differences in transport, chemistry, and heterogeneous removal processes within the troposphere are likely to affect some of the stratospheric results and are noted later in this section to introduce uncertainty into the assessment calculations.

A special topic of this intercomparison was the 40-km ozone "problem": models systematically underpredict the observed abundance by amounts varying from 10 to 50%. The concentration of ozone between 40 and 50 km is expected to be under photochemical control and to involve well-known catalytic loss cycles. As part of the intercomparison, participants contributed detailed tables of photochemical rates for the ozone budget at 3 mbar (Equator in March) from their simulation of the current atmosphere, see Table 3.1.2. The J-value for O_3 determines the ratio O/O_3 and hence the loss rate for odd-oxygen. Reported values varied by as much as 22%, resulting from inherent differences in the calculations of J-values (noted above) and from the different column abundances of ozone above 40 km in the model simulation of the current atmosphere. Production rates for odd-oxygen vary by only 3% across the five participating models; however, the loss rates attributed to individual families (HO_x, NO_x, Cl_x) vary by as much as 50%. Different factors are involved; due to the large variations in background gases (e.g., 50% in NO_y) and in family abundances, the cause of these differences could not be determined at the meeting. A re-examination of the 40-km problem will be part of the next intercomparison.

3.1.3.6 Predictions of Future Ozone

Only a limited number of ozone perturbations using hypothetical scenarios for future atmospheric composition were completed for this workshop. The comparisons focused on changes in ozone, temperature, and stratospheric circulation. A comparison of predicted ozone perturbations (not available for the workshop) is presented in Section 3.2.

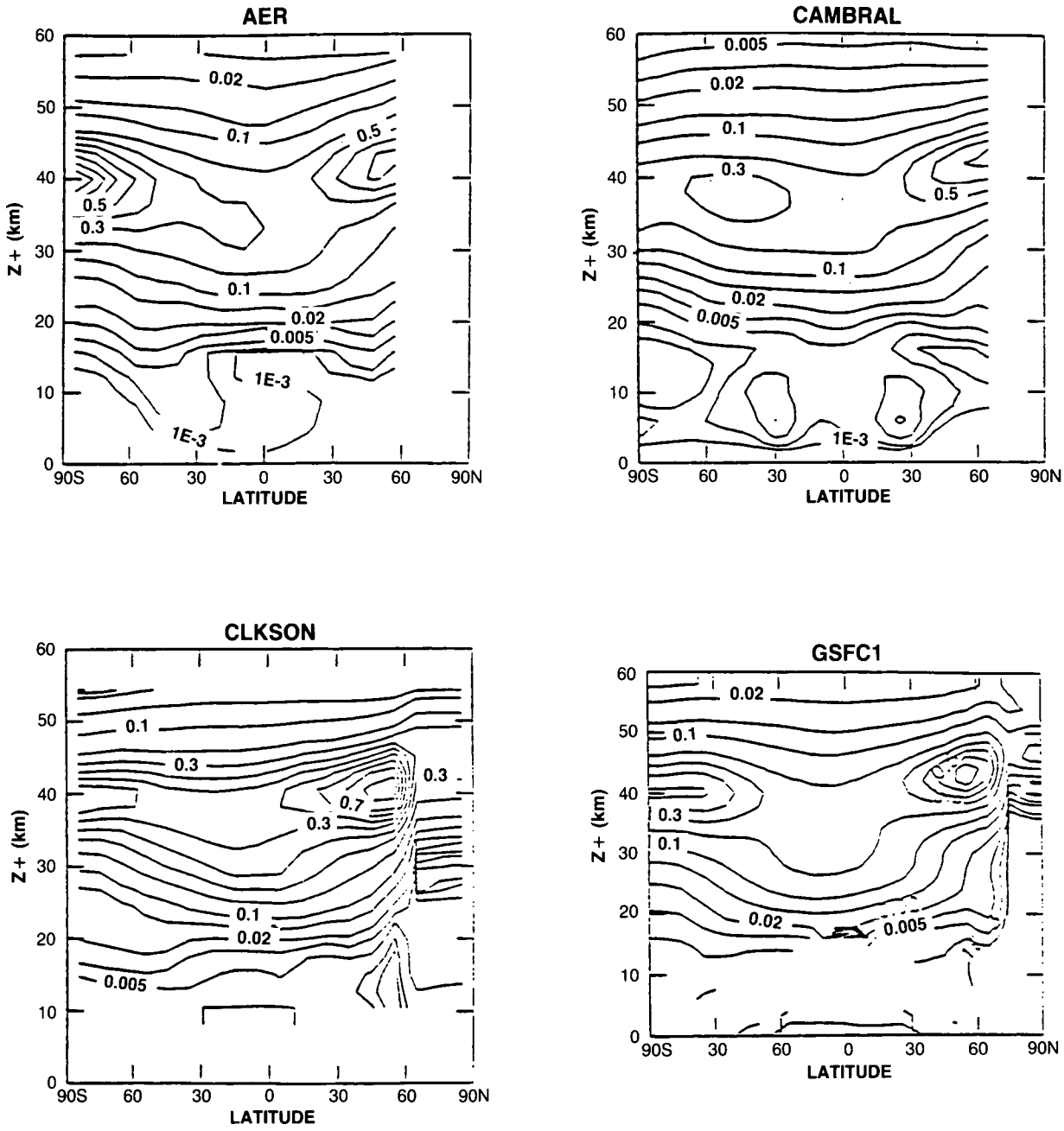

Figure 3.1-4. Two-dimensional distribution of the ClO/HCL ratio from nine models. Eight of the models (AER, CAMBRAL, CLKSON, GSFC2, LARC, MRI, NOCAR, and OSLO) show December values, while one model (GSFC1) shows January values.

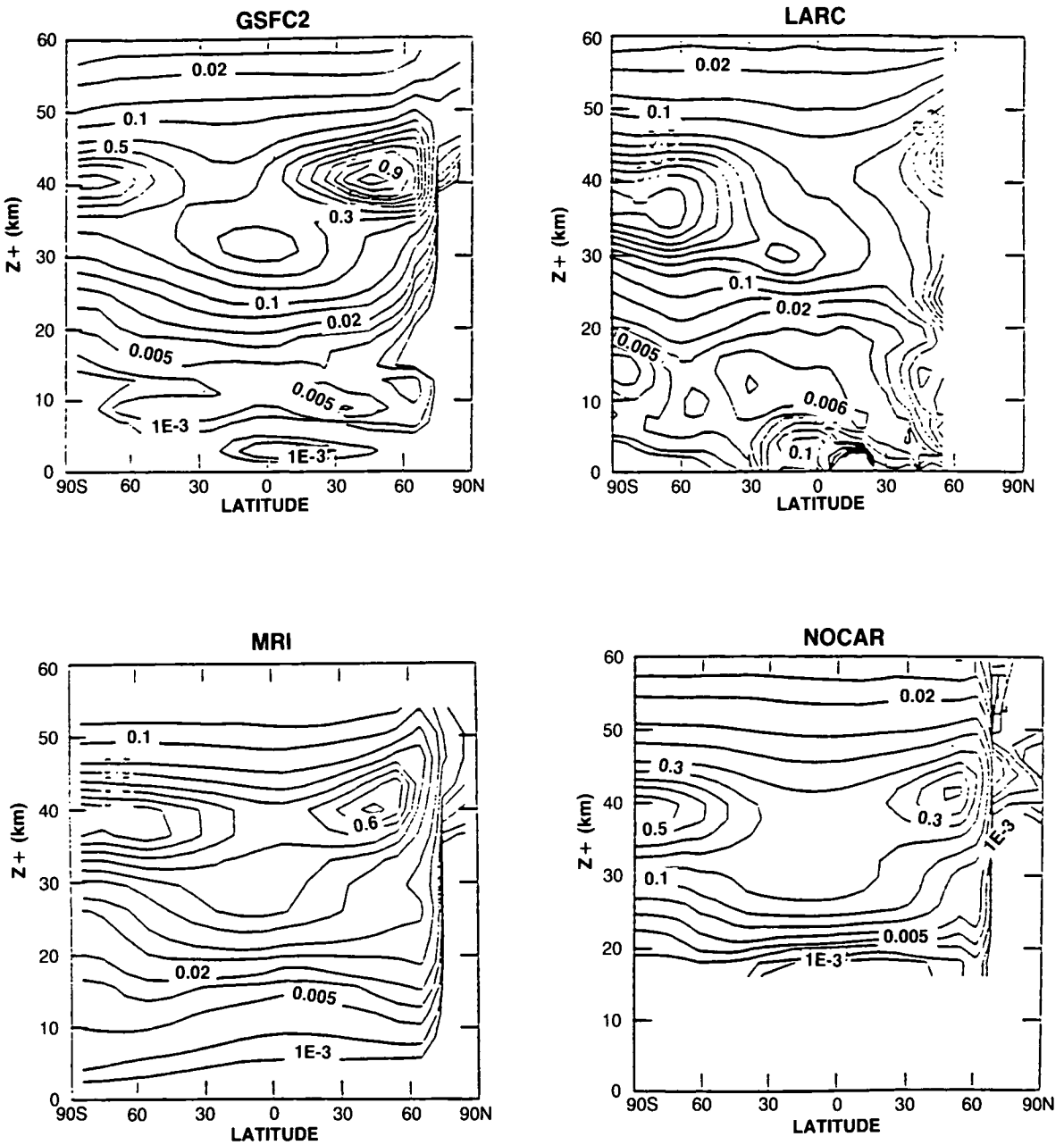

Figure 3.1-4., continued

3.1.3.7 Summary

The recent intercomparison (Jackman, et al., 1989b) overcame many technical obstacles in allowing a direct one-to-one comparison of results from many different models. The modeling community submitted their results in digital form to a central facility operated by Robert Seals at NASA/Langley where the calculations were re-gridded and plotted on a standard grid scale (e.g., Figures 3.1-3 and 3.1-4). The ability

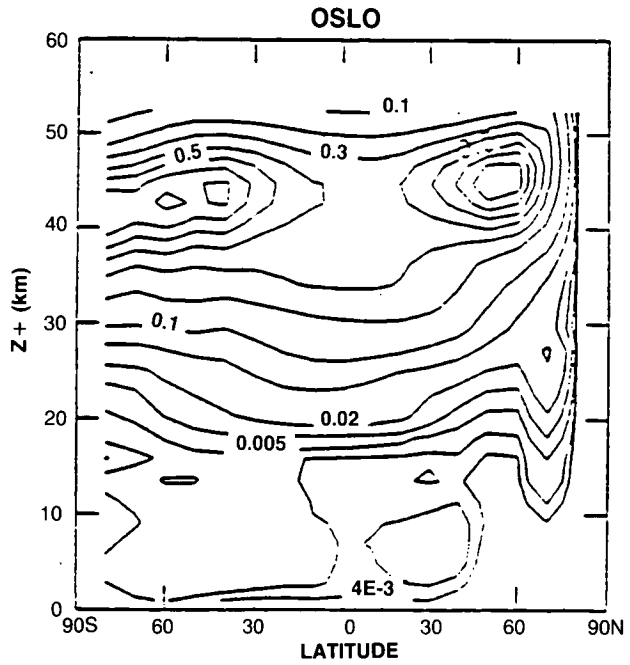

Figure 3.1-4., continued

Table 3.1-2. Comparison of ten rates and species at 3 mb, Equator, in March from five modeling groups

Group	P(tot) cm^{-3} day^{-1}	$L(O_x)$ cm^{-3} day^{-1}	$L(HO_x)$ cm^{-3} day^{-1}	$L(NO_x)$ cm^{-3} day^{-1}	$L(Cl_x)$ cm^{-3} day^{-1}	$J(O_3tot)$ sec^{-1}	O_3 ppmv	H_2O ppmv	NO_x ppbv	Cl_x ppbv
AER	4.49(11)[a]	8.12(10)	5.85(10)	2.30(11)	7.78(10)	1.00(-3)	5.82	4.50	17.8	2.23
GSFC1	4.72(11)	7.74(10)	6.32(10)	2.49(11)	8.73(10)	9.64(-4)	5.83	4.88	18.9	2.36
GSFC2	4.74(11)	9.14(10)	6.79(10)	2.38(11)	7.82(10)	9.57(-4)	6.04	5.03	18.2	2.01
LLNL	4.52(11)	8.10(10)	6.53(10)	2.20(11)	7.79(10)	1.12(-3)	4.85	4.95	23.0	2.26
MRI	4.61(11)	6.53(10)	7.03(10)	1.80(11)	1.26(11)	1.17(-3)	4.74	5.69	14.8	2.48

[a]4.49(11) means 4.49×10^{11}

to make such detailed comparisons helped to identify structural differences in model transport and photolysis rates. The meeting has spawned two subgroups with the objective of resolving the differences in the calculation of J-values and heating rates.

The next intercomparison will probably focus on model intercomparisons for the present atmosphere, with emphasis on matching models with observations. One task, for example, will likely be an examination of the transport of long-lived tracers in the winter polar vortex as identified by the recent aircraft campaigns to the Antarctic and Arctic (see Chapter 1 on Polar Ozone).

3.1.4 Comparison Between Model Calculations and Observations

An important prerequisite for the models used in any ozone assessment is that they represent with sufficient accuracy the present distributions of the atmospheric trace gases. The purpose of this section is therefore to examine how well the models reproduce a limited number of observations and to highlight areas of agreements and disagreements between calculated and observed distributions.

Different types of comparisons between models and observed data can be achieved. For example, to validate at the same time the treatment of the transport and the formulation of chemistry in the model, the comparison with data has to be made on the global scale and involve species measured on a continuous basis by space-borne instruments.

In this brief section, we will focus on a comparison between the meridional distributions of trace gases calculated by some of the 2-D models involved in this assessment and the corresponding zonally averaged distributions of these constituents derived from satellite observations (SBUV, LIMS, SAMS). In addition, Dobson maps produced by the different models will be compared with ozone column abundances derived from TOMS data.

In Figure 3.1-5, the distribution of nitrous oxide observed by SAMS is compared to the corresponding distribution calculated by the GSFC2 model. This gas, emitted by the Earth's surface, is transported into the stratosphere, and destroyed by photolysis and reaction with $O(^1D)$. Therefore, the formulation of the chemical processes involved in the budget of this species makes the distribution of this gas relatively

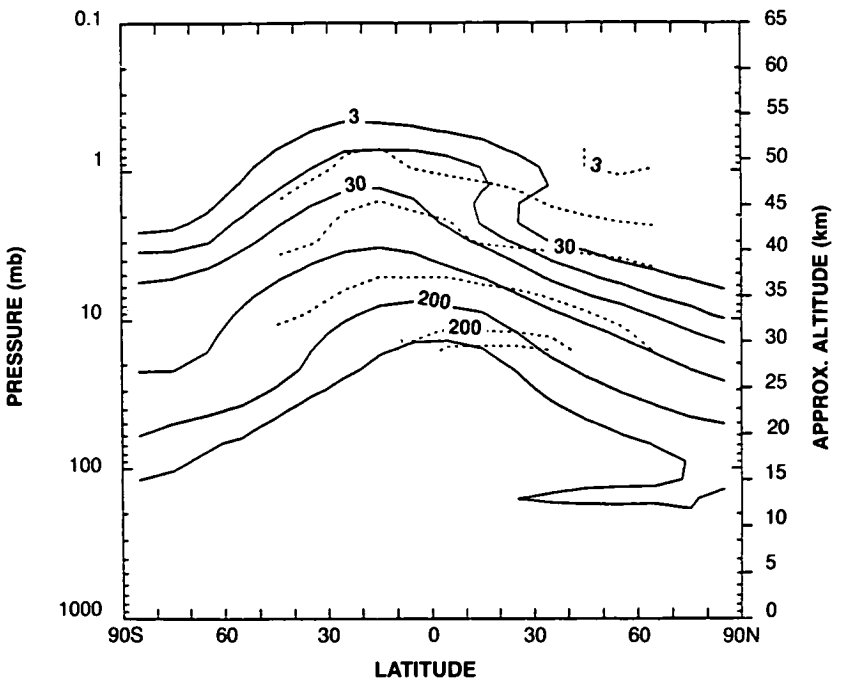

Figure 3.1-5. Zonally and monthly averaged distribution of nitrous oxide (ppbv) observed (dashed lines) in January 1979 by SAMS (on board the Nimbus-7 satellite) and calculated (solid lines) by the GSFC2 two-dimensional model.

independent of that of other chemical constituents. The SAMS data cover only a limited altitude range (28 to 50 km) over which the mixing ratio varies from about 50 to 3 ppbv. The mixing ratio determined by this model compares relatively well with the observations, at least in qualitative terms. All models involved in the present assessment predict, for a given height, the largest concentrations to be over the tropics. The appearance of a double peak in the mixing ratio isolines, observed for example in April and May, is usually not reproduced by the models. This feature is believed to result from momentum deposition in the tropics by Kelvin and mixed Rossby-gravity waves (Gray and Pyle, 1987).

The same type of conclusions can be drawn for methane. As to nitrous oxide, methane is released in the atmosphere at ground level but, in this case, the destruction of the molecule takes place already in the troposphere as well as in the stratosphere and is due to the action of hydroxyl radicals. The concentration of OH depends on a large number of factors and could therefore be different from model to model. The SAMS values cover an altitude range from about 32 and 57 km over which the mixing ratio varies from 1 to 0.2 ppmv. These observed data are again compared to the GSFC2 model (Figure 3.1-6). Again the agreement is good in January: the mean vertical distribution as well as the latitudinal gradient in the mixing ratio are well reproduced by the model. The problem of the double peak, already mentioned for nitrous oxide, also exists in the case of methane.

Figures 3.1-7(a, I, J, R) present the mixing ratio of nitrogen oxides (NO + NO_2) from the models developed at MRI and at the University of l'Aquila and at the Central Aerological Observatory and the Leningrad Institute for Meteorology and Hydrology (CAO/LIMH, USSR), as well as the mixing ratio of nighttime NO_2 observed by LIMS (which should be very similar to the 24-hour averaged mixing ratio of NO + NO_2 because of the rapid chemical conversion of NO into NO_2 after sunset). The observations suggest that the mixing ratio of NO_x reaches its maximum value (16–20 ppbv) over the tropics near 38 km

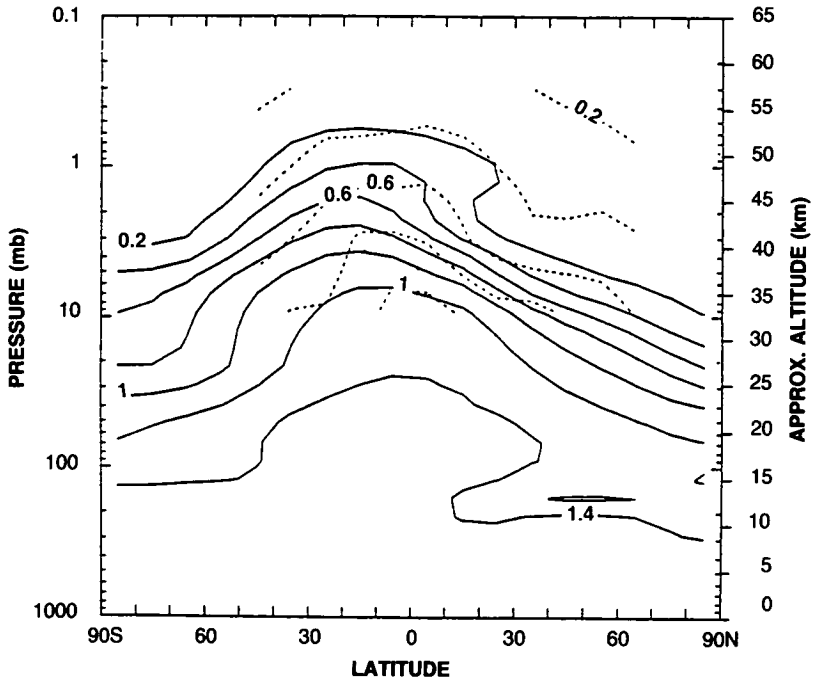

Figure 3.1-6. Same as in Figure 3.1-5 but for methane (ppmv).

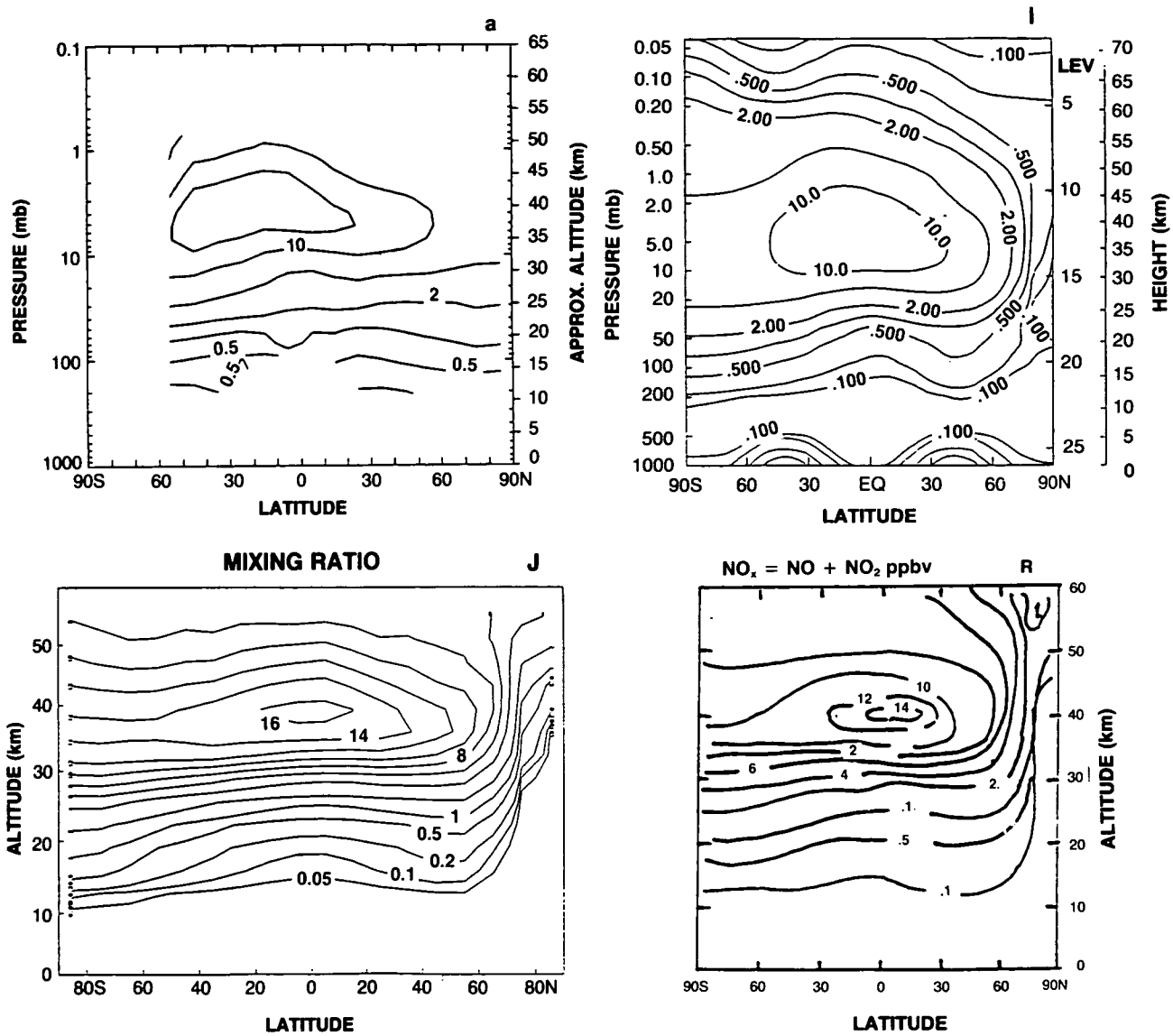

Figure 3.1-7. Zonally and monthly averaged distribution of nighttime NO_2 (ppbv) observed in January 1979 by LIMS (on board the Nimbus-7 satellite) and distributions of NO_x = NO ÷ NO_2 derived for January by different two-dimensional models. Note that nighttime densities of NO_2 should be very similar to 24-hour average NO_x densities. Codes for the different models are listed in Table 3.1.1.

altitude. From this height down to the tropopause level, the mixing ratio decreases by more than a factor of 50. The same type of behavior is found in the model. Significant differences however are observed in the lower stratosphere, where the distribution of odd nitrogen is largely determined by the strength of the poorly known sources of NO_x in the upper troposphere and the strength of vertical and meridional transport in the vicinity of the tropopause.

Shown in Figures 3.1-8(a, W) are the distributions of nitric acid observed by LIMS and derived by the WisCAR model. In both cases the maximum mixing ratio near 25 km altitude is of the order of 2 ppbv over the Equator and increases with latitude to values on the order of 5–8 ppbv over the summer pole and

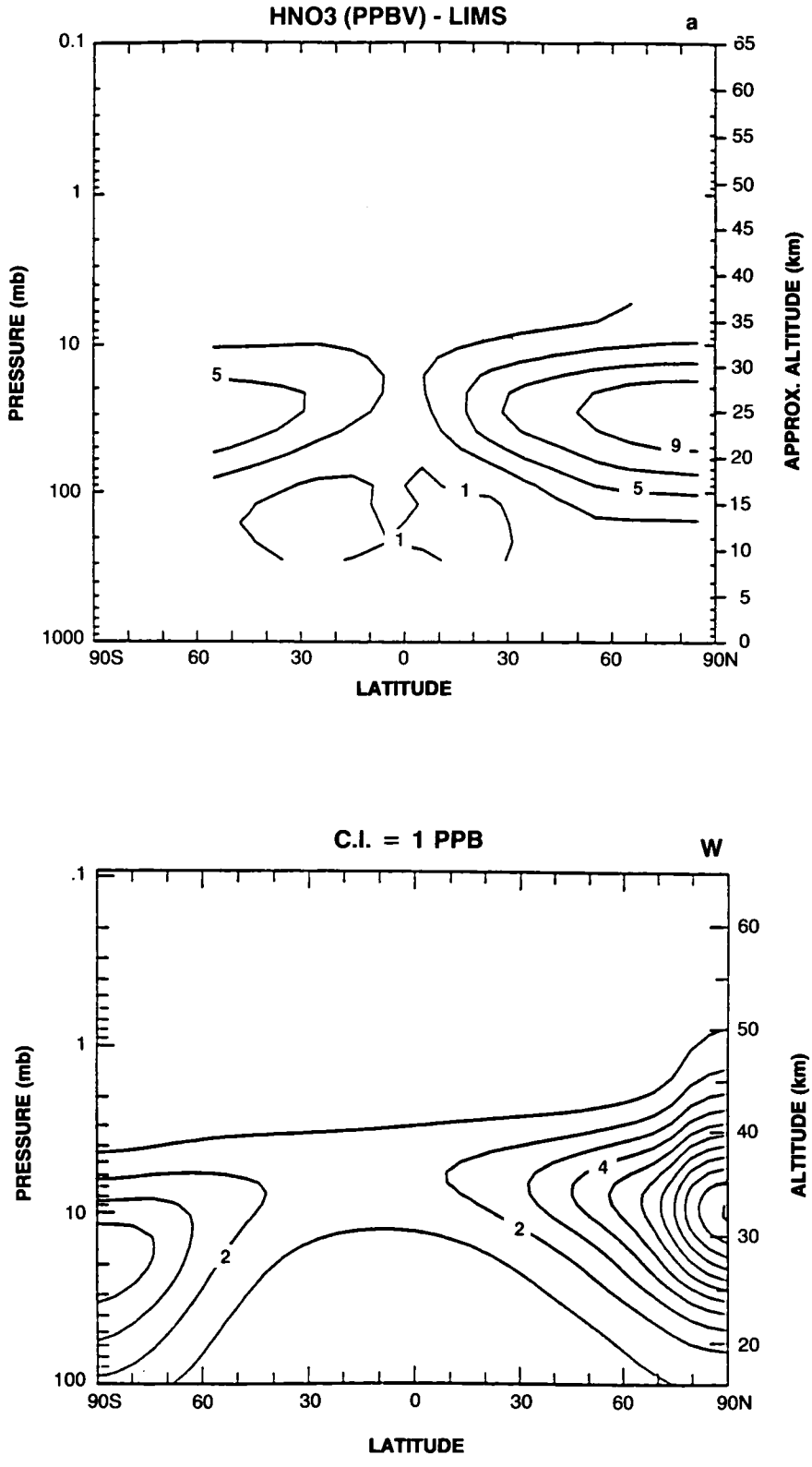

Figure 3.1-8. Same as in Figure 3.1-7 but for nitric acid (ppbv).

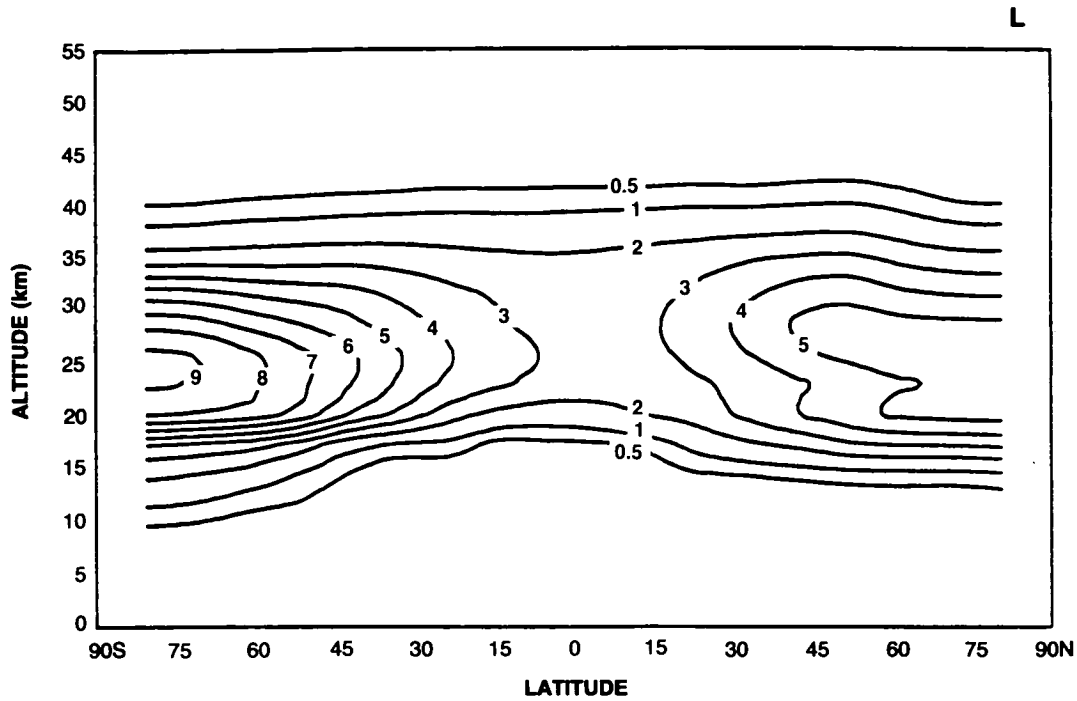

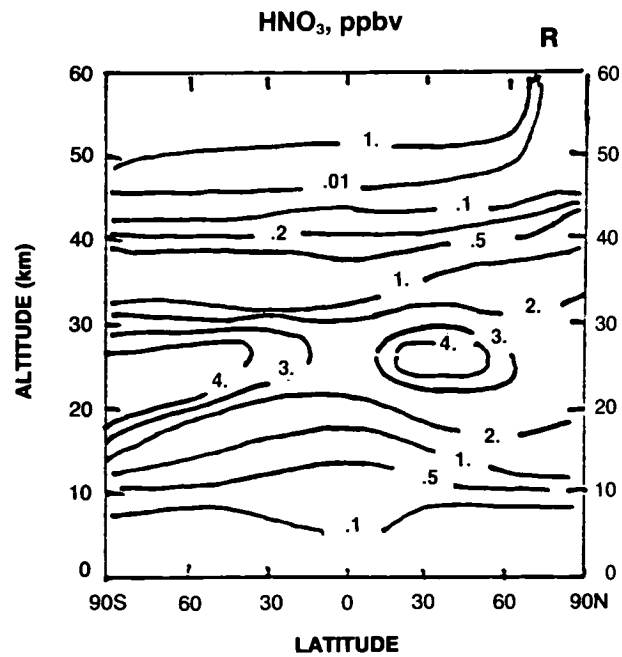

Figure 3.1-8., continued

10–12 ppbv over the winter polar region. This relatively good agreement is obtained because, in this particular model, a polar night conversion from N_2O_5 into HNO_3 with a time scale of 20 days has been added to the chemical scheme to account for heterogeneous processes occurring on the surface of water particles at high latitudes in winter. Other models such as the LLNL model or the CAO/LIMH model (Figure 3.1-8L and R) when they do not include such a conversion in their chemical scheme, produce the high-latitude maximum HNO_3 mixing ratio in summer rather than in winter.

The distributions of the ozone mixing ratio measured by SBUV and calculated by different models are shown in Figures 3.1-9(a, A, C, I, J, L, O, R, U, W). In general, the agreement between observed and theoretical distributions is fairly good: the maximum mixing ratio located over the Equator near 30–35 km altitude is well represented, the overall meridional distribution of the calculated ozone field is very similar to the observed one. However, most models underestimate the ozone density near 40 km altitude. This long-standing problem has not yet been solved and requires additional work. It should be noted at this point that none of the models discussed here includes the effects of heterogeneous chemistry, so that the "ozone hole" over Antarctica cannot be produced in any model simulation.

Finally, the ozone column displayed as a function of latitude for each month of the year and expressed in Dobson units is shown in Figures 3.1-10(a, A, C, G, I, J, L, O, U, W). The observed values are obtained from the TOMS data. The observations exhibit a minimum column abundance of less than 260 Dobson units in the tropics and the highest values in spring in both hemispheres. In the Northern Hemisphere, this maximum reaches 440 Dobson units and is located over the North Pole. In the Southern Hemisphere, the maximum, located at 60°S is of the order of 380 Dobson units. The models generally show the same type of distributions; differences are largely due to the strength of the meridional transport in the lower stratosphere during the different seasons.

There are hemispheric differences in the wintertime poleward transport. Although in some models there are ad hoc adjustments to transport parameters so that the model behavior will reflect measurements, there are efforts to calculate transport as a consistent representation of circulation and diffusion (see, e.g., Newman et al., 1988; Jackman et al., 1988, 1989; Hitchman and Brasseur, 1988; etc.).

To validate the details of the chemical kinetic scheme used in a given model, it is useful to compare (for a given altitude, latitude, and time of the day) the concentration ratio of species belonging to the same chemical family (e.g., NO_x, Cl_x). In this respect, simultaneous measurements of the concentrations of chemically active trace gases such as those performed by the ATMOS experiment (Raper et al., 1987; Russell et al., 1988) are extremely useful. Figures 3.1-11a and b show, for example, the ATMOS measurements at 30°N between April 30 and May 1, 1985 together with a simulation of the individual odd nitrogen and odd chlorine species made by the Harvard one-dimensional model (McElroy and Salawitch, 1989) for local sunset conditions. The model adopted ATMOS data for O_3, H_2O, CH_4 and the total amount of odd nitrogen and inorganic chlorine. This work thus provides a test of our understanding of the photochemical processes governing the partitioning between the individual nitrogen and chlorine species. The agreement is rather good for all species measured in the Northern Hemisphere, with the exception of $ClONO_2$, for which the model profile falls off much more slowly with height than the observed profile. A recent study by Natarajan and Callis (1989), using the LIMS and ATMOS data to constrain the levels of odd nitrogen and odd chlorine in their model, finds no major discrepancy between calculated and observed ozone (less than 20%) below 52 km.

In conclusion, the 2-D models involved in the present assessment generally reproduce the patterns observed in the ozone column, with a minimum in the tropics and maxima at high latitudes in the spring of

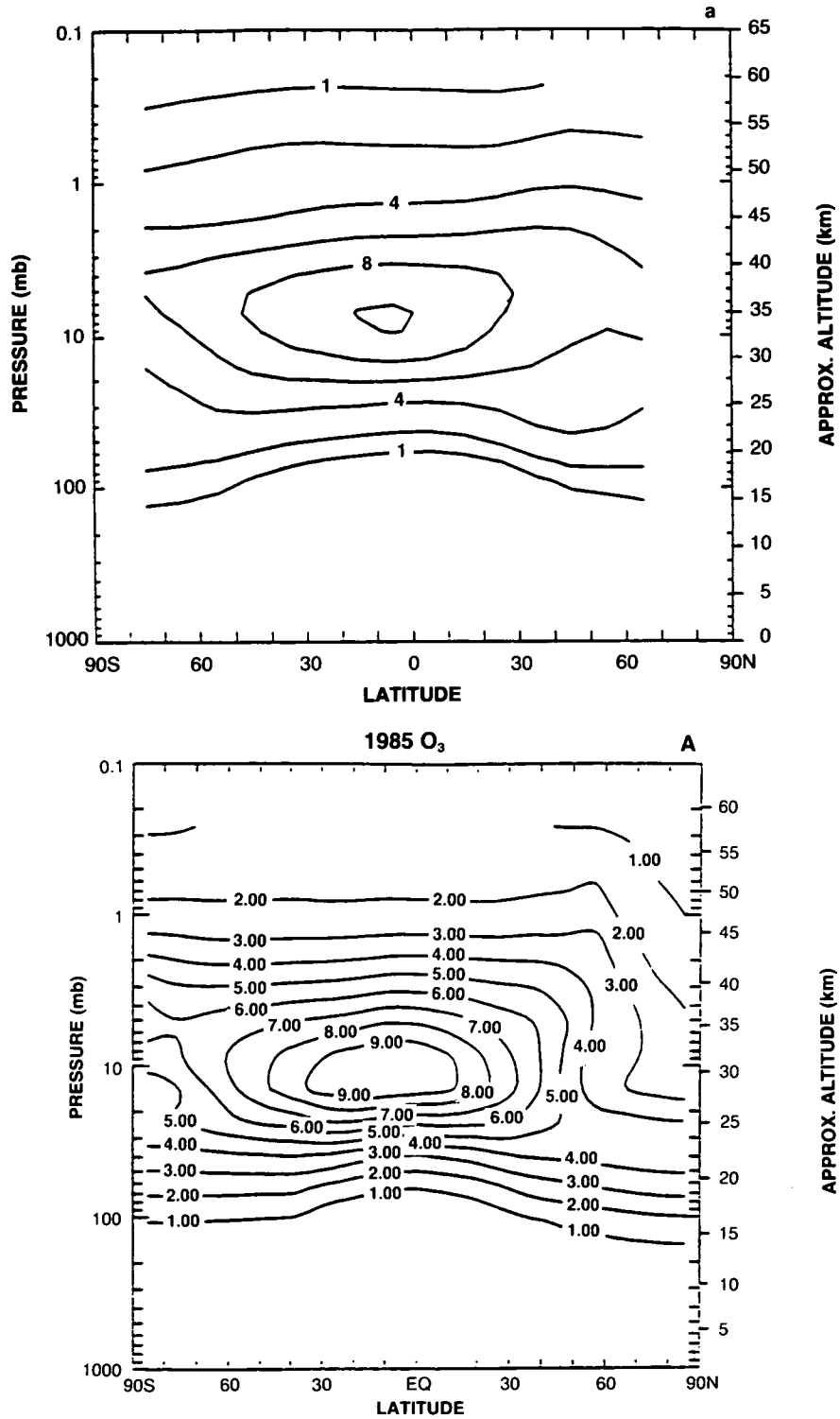

Figure 3.1-9. Zonally and monthly averaged distribution of ozone for January (based on data obtained by SBUV, on board Nimbus-7, in 1979, 1980, and 1981) and distributions of ozone derived for January (or December) by different two-dimensional models. Mixing ratios are expressed in ppmv. Codes of the different models are given in Table 3.1.1. In the case of the NSU model number densities expressed in cm^{-3} are displayed.

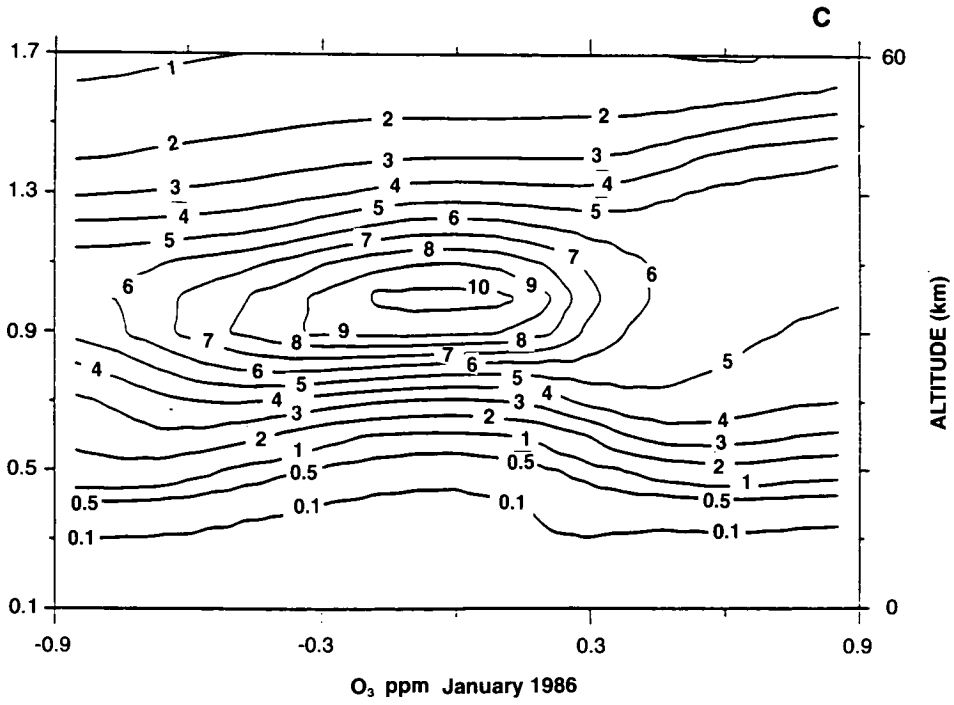

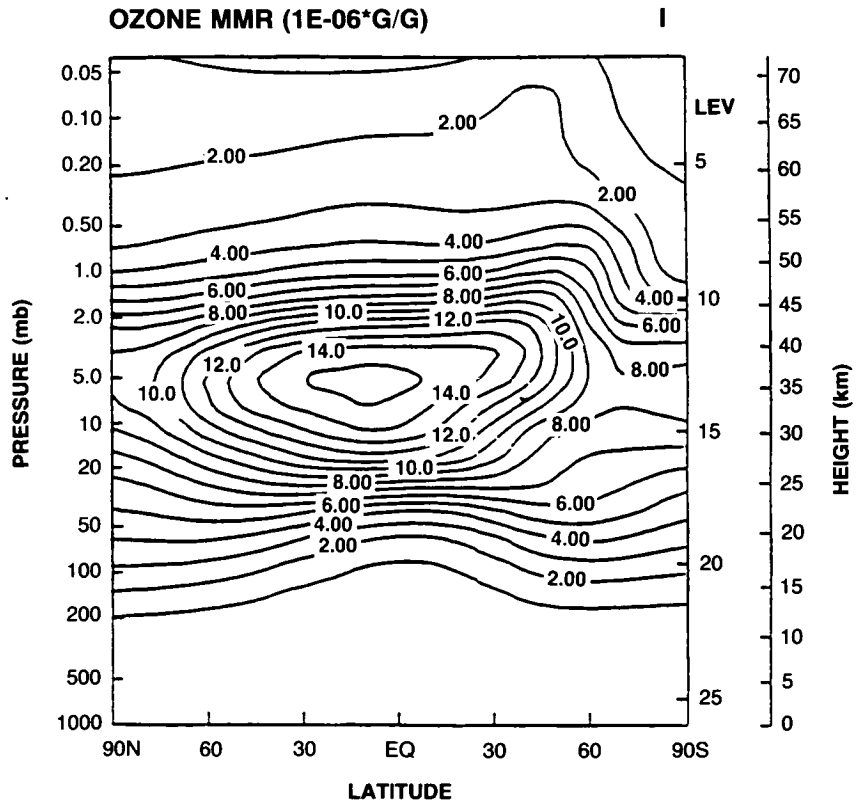

Figure 3.1-9., continued

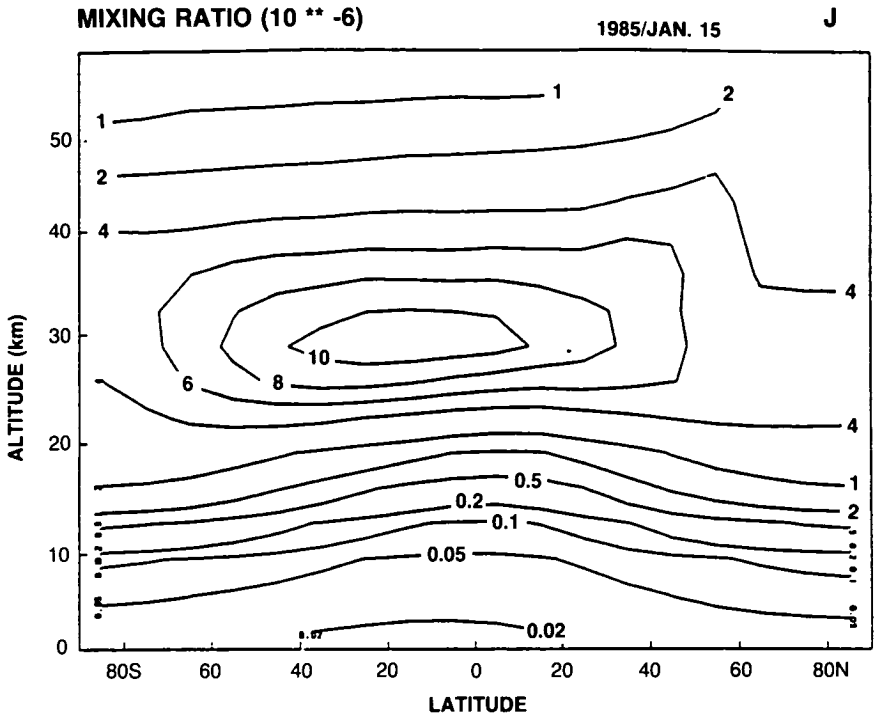

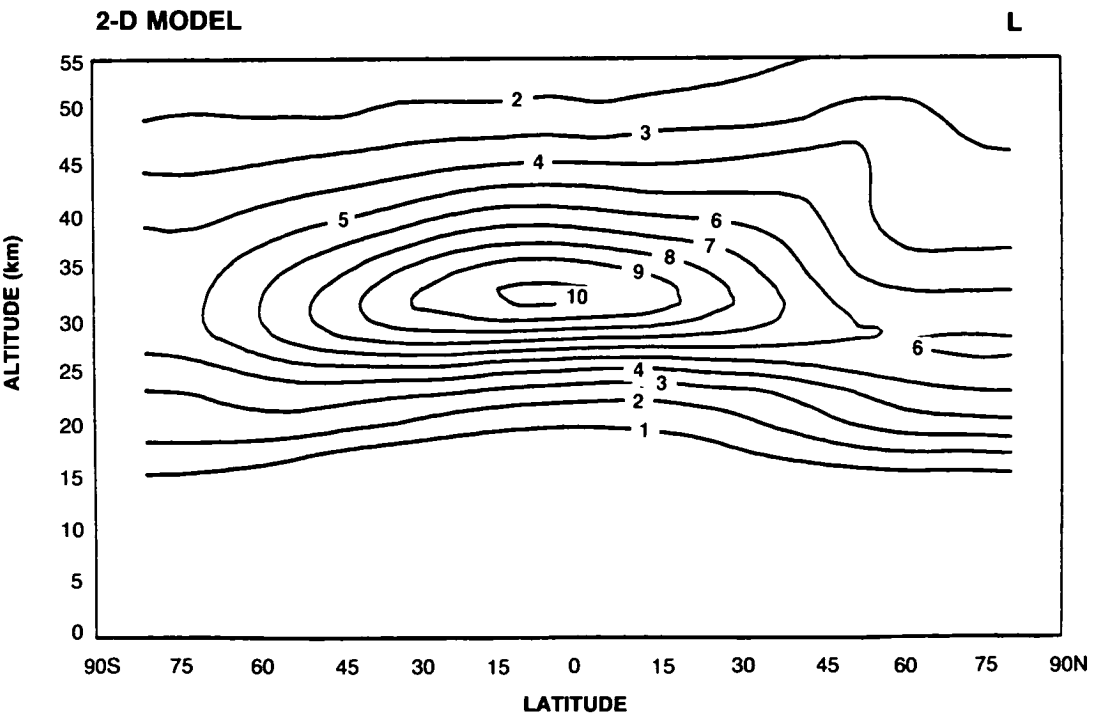

Figure 3.1-9., continued

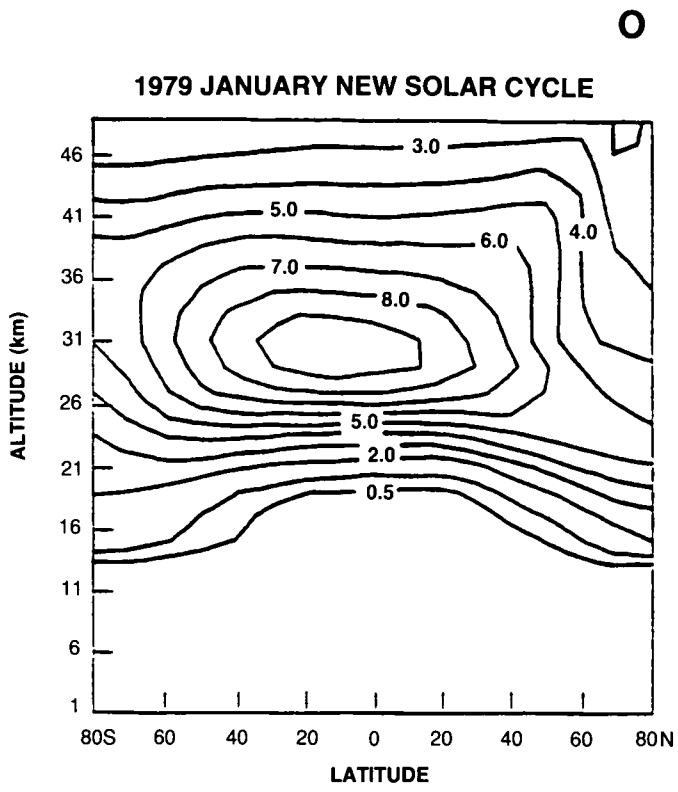

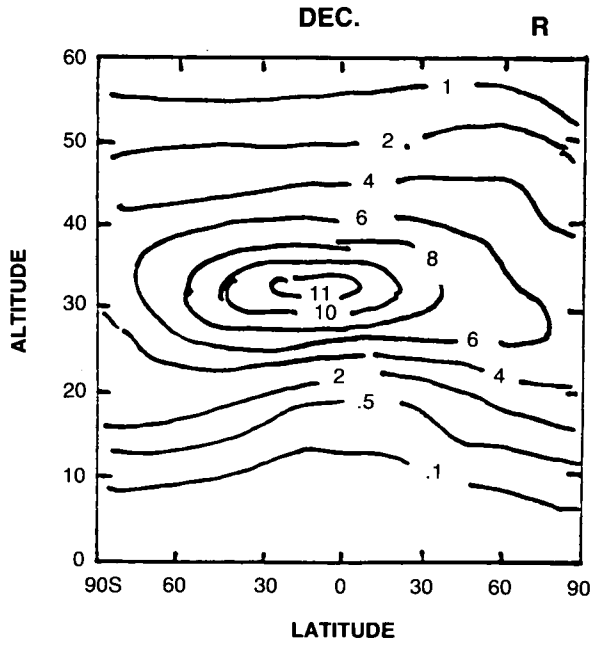

Figure 3.1-9., continued

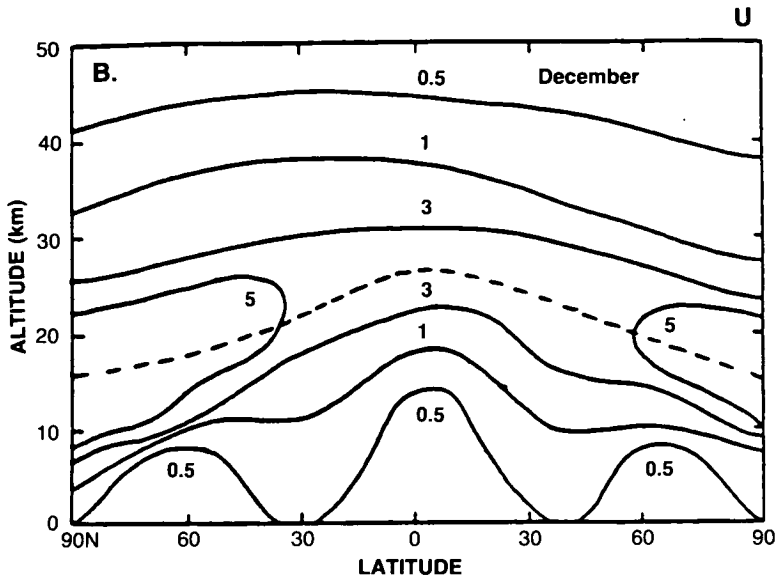

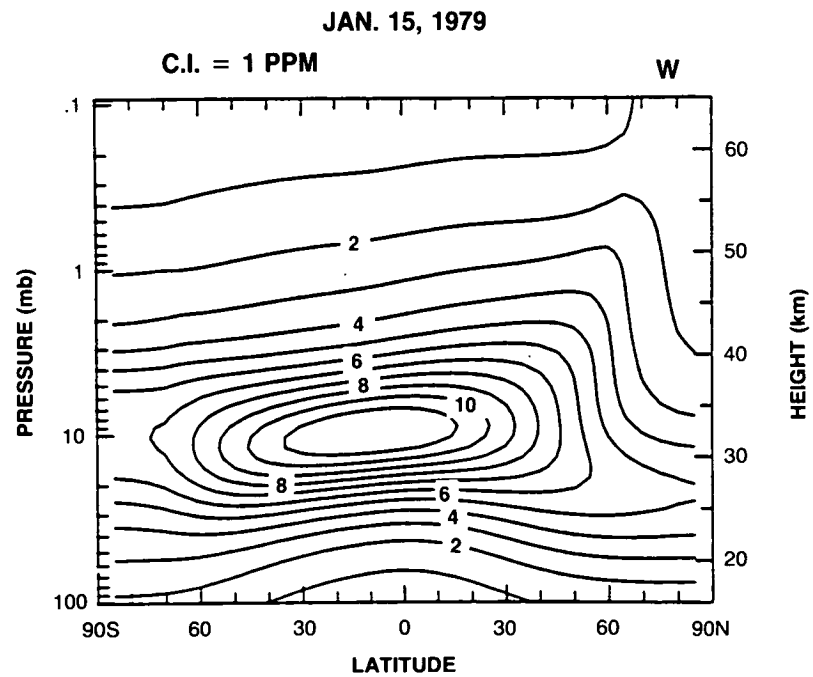

Figure 3.1-9., continued

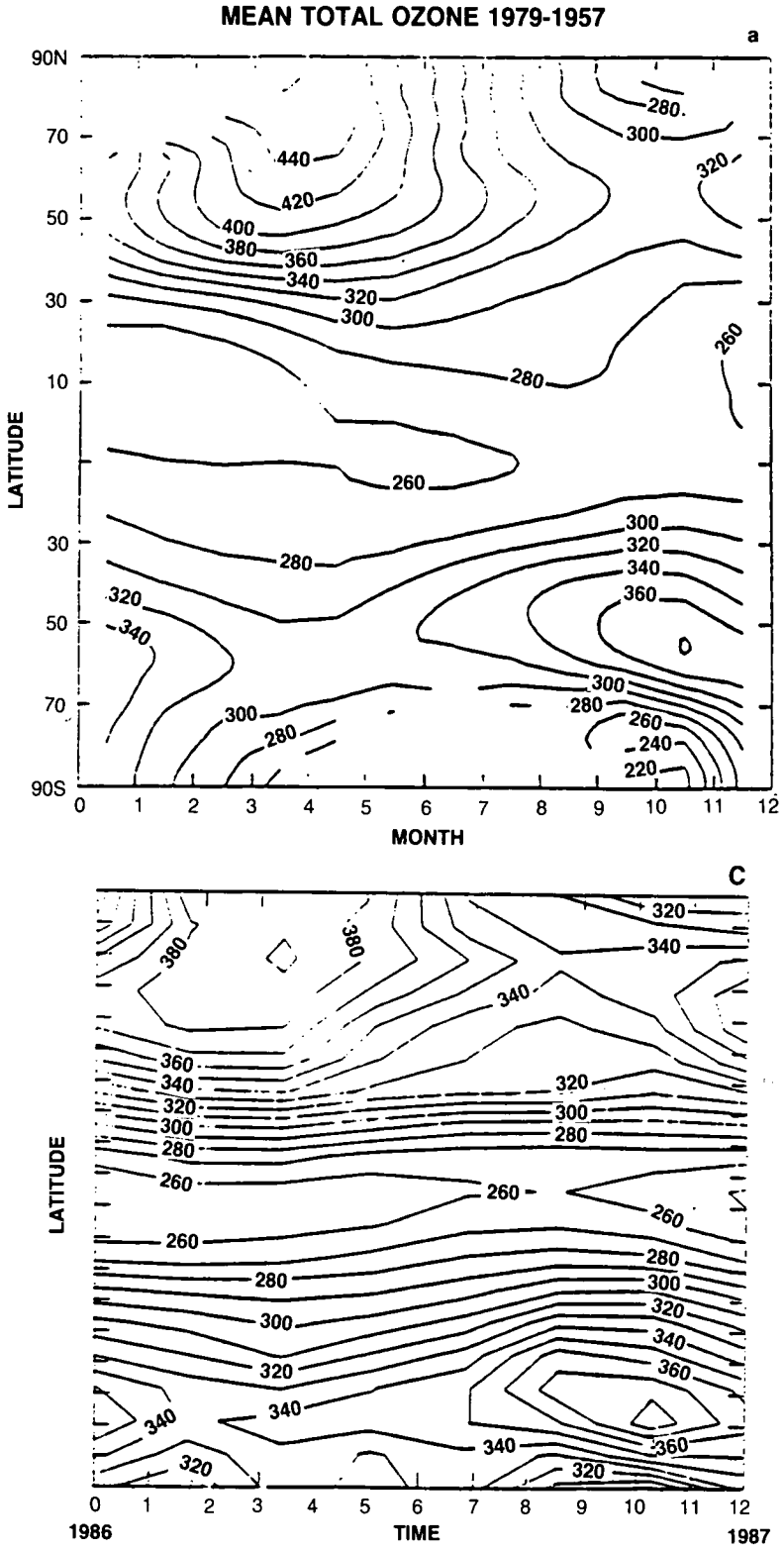

Figure 3.1-10. Latitudinal and seasonal variation of the ozone column abundance (Dobson) based on satellite observations (TOMS) and different model calculations.

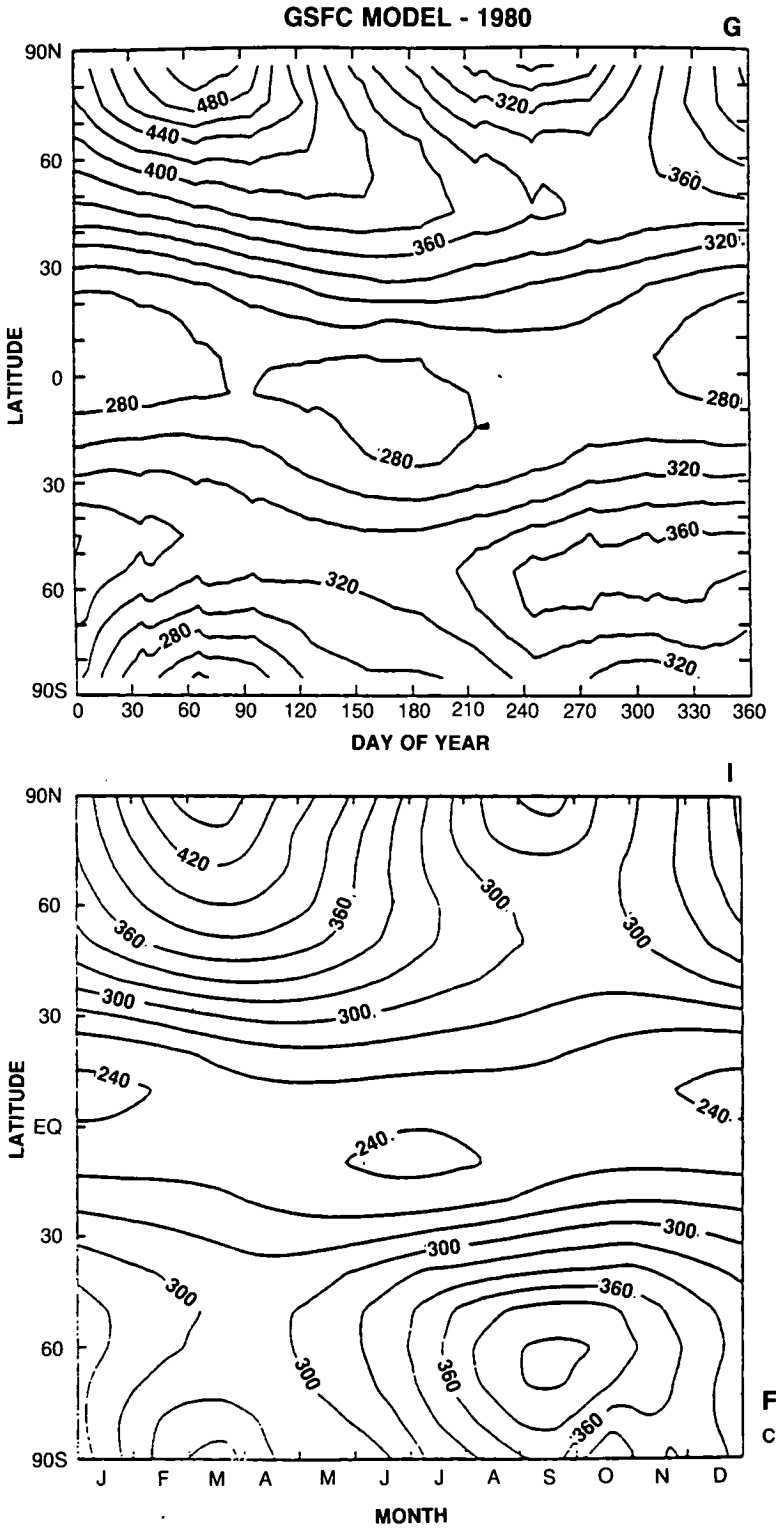

Figure 3.1-10., continued

both hemispheres. The meridional distribution of ozone is also in good agreement with satellite observations. Discrepancies however are noted; in particular, the models systematically underestimate ozone in the upper stratosphere. Calculated and observed distributions and seasonal variations of species such as nitrous oxide, methane, nitric acid and nitrogen oxides are in qualitative agreement, although substantial

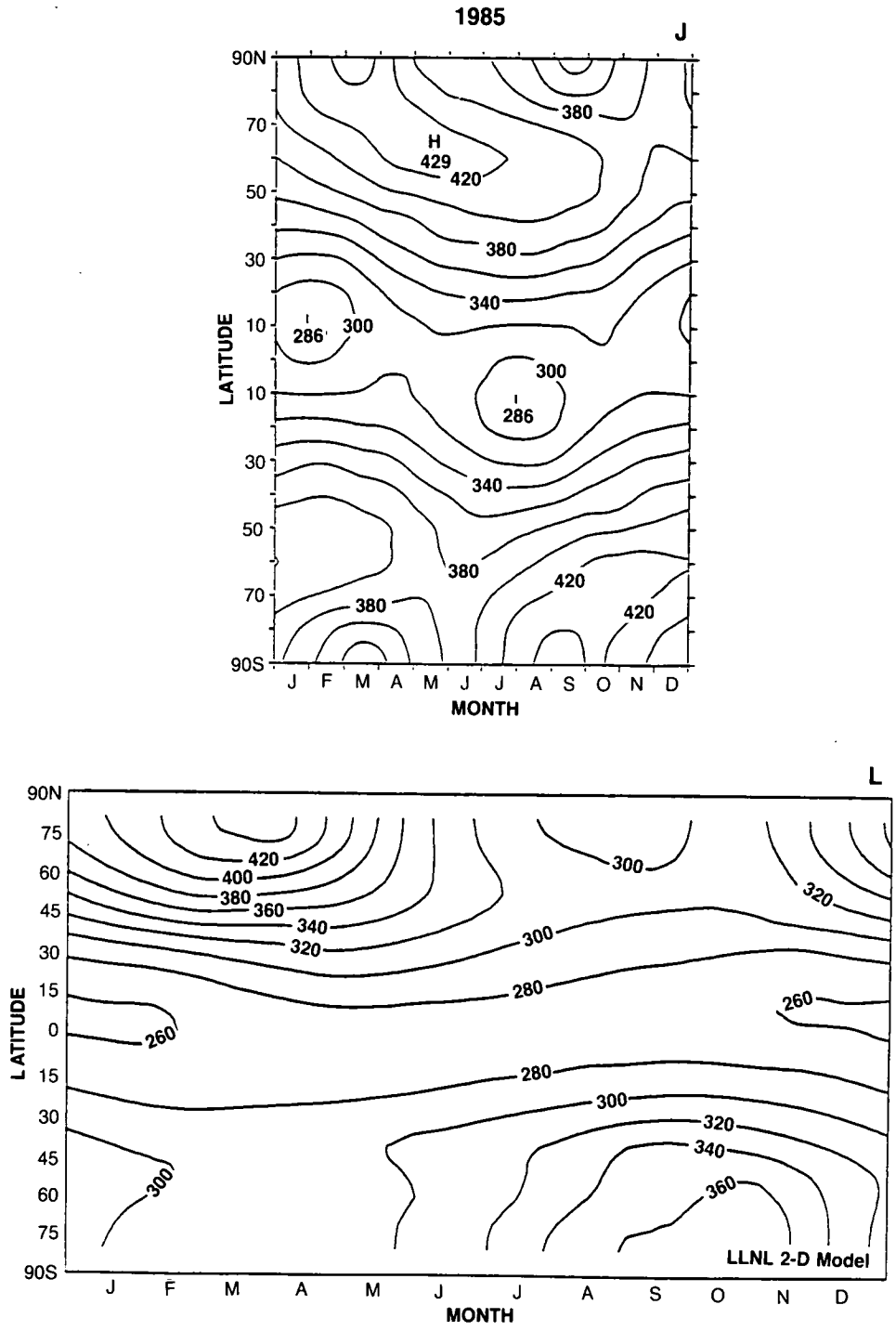

Figure 3.1-10., continued

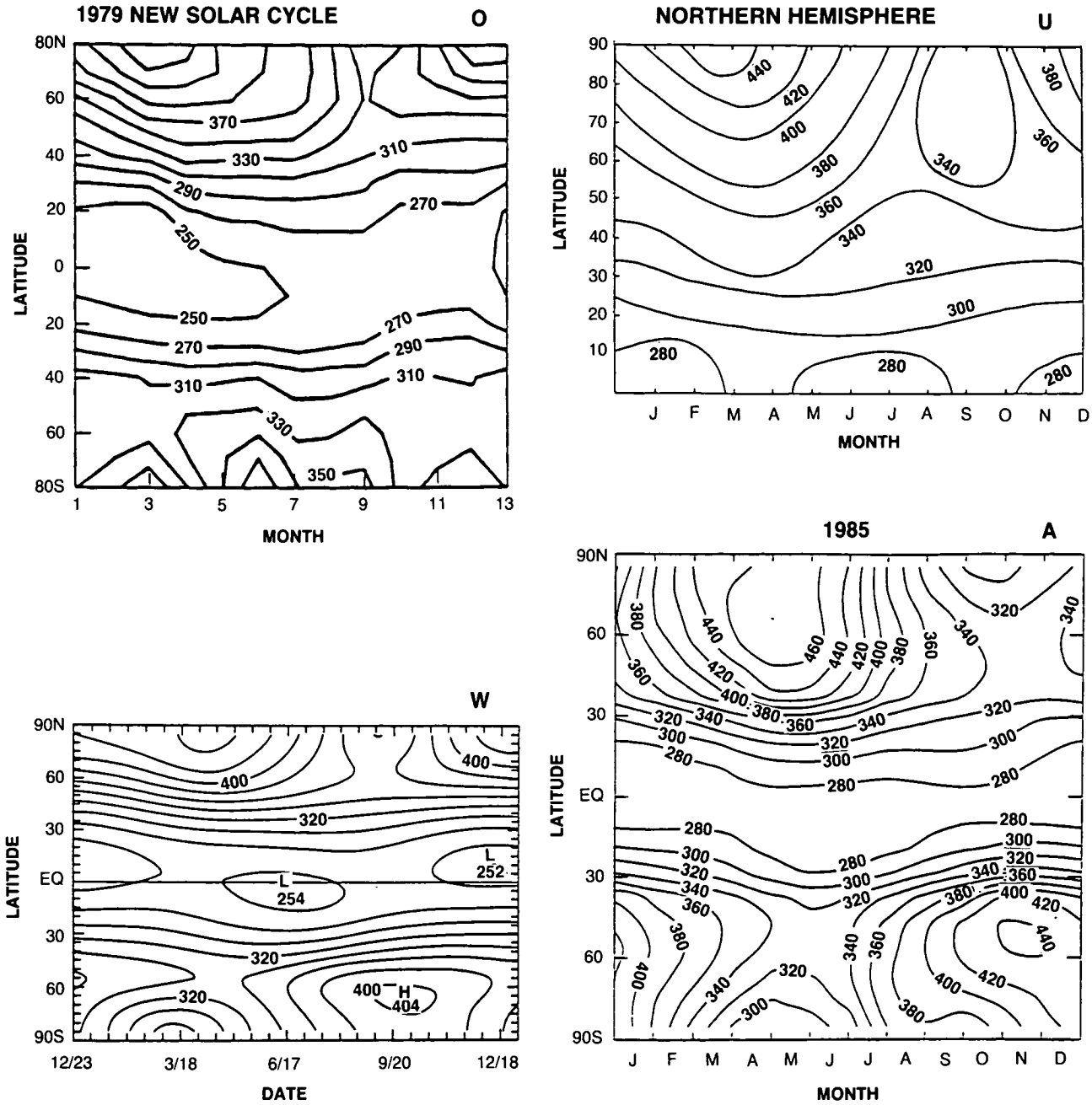

Figure 3.1-10., continued

quantitative differences are found in certain cases. The differences noted between models and observations should be attributed to deficiencies in the chemical scheme, in the radiative transfer codes, or in the transport formulation. Additional work will be performed in the future to improve these models and to validate them with measurements made from space observing systems.

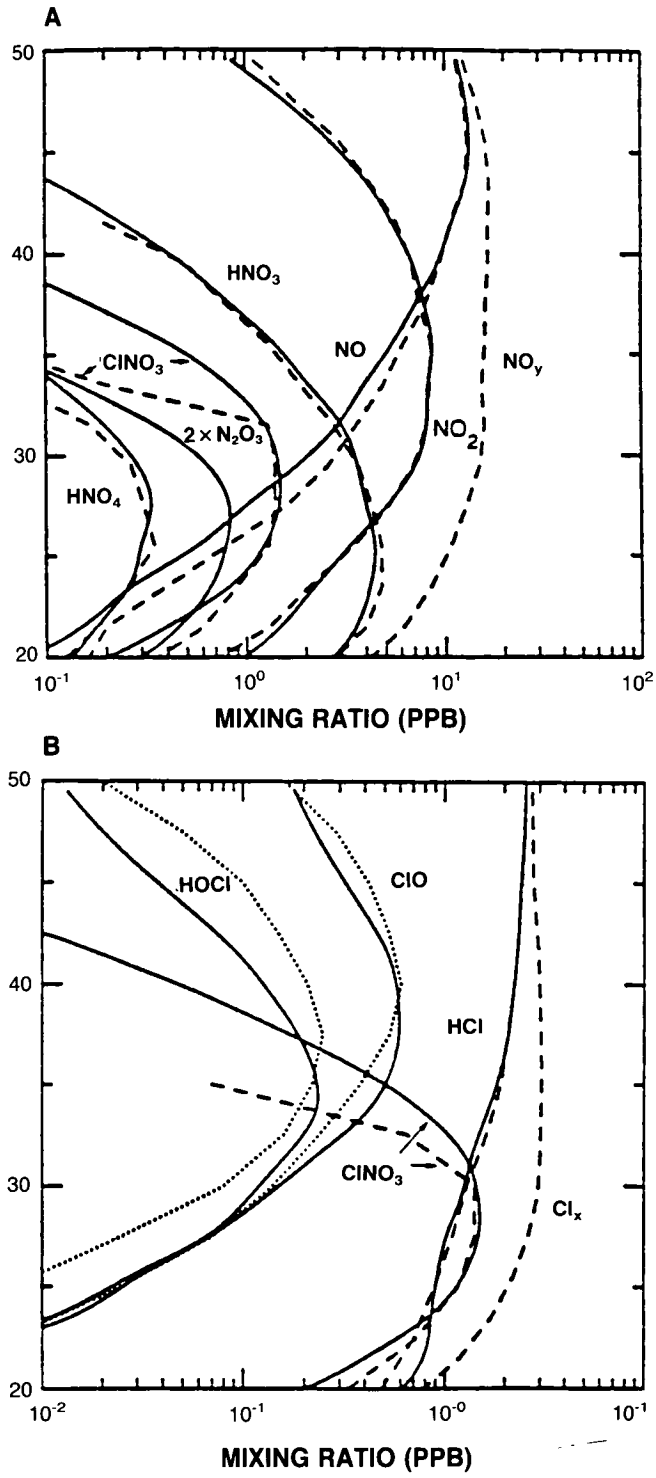

Figure 3.1-11. Comparison between one-dimensional mixing ratio profiles of chemically active trace gases measured by ATMOS at 30°N between April 30 and May 1, 1985, and a model of the odd nitrogen and odd chlorine species in the stratosphere (McElroy and Salawitch, 1989).

3.2 MODEL PREDICTIONS

3.2.1. Projected Scenarios for Halocarbons and Trace Gases

3.2.1.1 Introduction and Definitions

The future composition of the atmosphere will depend on the rate at which we continue to emit some halocarbons and other trace gases. Atmospheric composition will respond also to changes in the global biosphere (i.e., natural sources) and in atmospheric chemistry (i.e., chemical sinks). The calculations presented here examine the impact of global policies that would curtail the use of chlorofluorocarbons controlled under the Montreal Protocol.

We present here a set of projections, or scenarios, for the future atmosphere that focus on halocarbons. These scenarios are not intended to present a formal scientific assessment of future atmospheric composition, but have been chosen to give a spectrum of cases for studying the response of stratospheric ozone to a range of chlorine loading of the atmosphere. The Montreal products are distinguished from other halocarbons, and in these scenarios HCFC-22 acts as a surrogate for all CFC replacement products (except for the halons, which we assume have no brominated replacement). Tropospheric average mixing ratios are specified for all gases except the Montreal products and their replacement (HCFC-22); for these gases projected histories of atmospheric emissions are defined.

The scenarios are designated by letters A through D with a number 1–4 for alternate cases and are defined in Table 3.2-1. The most simply defined scenario, A1, has been designated the Reference Scenario since all other scenarios can be easily defined relative to it. Scenario A1 assumes that currently observed trends in CO_2, CH_4, N_2O, CCl_4, and CH_3CCl_3 will continue and that future emissions of the Montreal products (defined here as CFCs 11, 12, 113, 114, 115, and the halons 1211 and 1301) will remain fixed at the production levels estimated for 1985. We assume steady growth in industrial activity, and with it, a slow but sustained growth in emissions of HCFC-22, CCl_4, and CH_3CCl_3. Increases in CH_4 have been shown in previous assessments to counteract the effect of high chlorine levels on stratospheric ozone; and thus, we consider an alternate scenario A2 in which CH_4 concentrations do not increase after 1985. While this seems unlikely in the immediate future, we have not yet identified the cause of the current CH_4 increases, nor uniquely ascribed them to human activity.

A sequence of three basic scenarios—B, C, and D—examines the impact of a global reduction by the year 2000 in the production/emission of Montreal products by 50% (B1), 85% (C1), and 95% (D1). The history of trace gas mixing ratios for these scenarios is shown in Figure 3.2-1; and the total chlorine and bromine loading of the atmosphere in Figure 3.2-2 and Table 3.2-4. One can see that without draconian reductions in Montreal products (scenarios C and D), it would be difficult to keep chlorine levels from doubling by the middle of the next century. In order to study a scenario in which chlorine returns to 1990 levels, we must impose controls to keep CCl_4 and CH_3CCl_3 fixed (D2), and furthermore, not use a halocarbon like HCFC-22 as a substitute for the Montreal products (D3). Once again, we consider the possibility of CH_4 concentrations remaining fixed at 1985 levels (D4).

None of the standard scenarios (A-D) gives a total atmospheric chlorine content (summed over all halocarbons) that returns by the year 2060 to 1985 levels of about 3 ppbv. It is interesting to note which different combination of halocarbon reductions could possibly yield a chlorine loading of less than 3 ppbv by 2060, and also whether chlorine levels prior to the onset of the Antarctic ozone hole (at most 2 ppbv) could be achieved by 2060 or later in the century with any combination of freezes or cuts in halocarbon

Table 3.2-1. UNEP Scenarios: 1960 through 2060

For the period 1960 to 1985, all trace gas concentrations are given as mixing ratios based on historical records or approximations thereof. For the period 1985 to 2060 a combination of mixing ratios and fluxes are specified.

A1. Reference Scenario

For the Montreal products (see Table 3.2-2b) we assume constant atmospheric emissions after 1985, using 1986 production as the atmospheric flux. For other trace gases (see Table 3.2-2a) we assume a simple linear rate of change in tropospheric concentration or a compounded growth rate. HCFC-22 uses a regression formula to integrate fluxes into mixing ratios. HCFC-22 has an independent market, is assumed to grow linearly in emissions (see Table 3.2-2b), and in addition is used as a surrogate for all substitutes for the Montreal products.

A2. Reference Scenario with CH_4 fixed at 1600 ppb.

B1. Reference Scenario with 50% reduction in Montreal products

The emission of Montreal products (Table 3.2-2b) is reduced by 10% of their 1995 values for each year from 1996 through 2000 (a total of 50%). Half of the reduction in Montreal products (in kg) is added on top of the reference scenario for HCFC-22 (in kg). There is no halogenated substitute for the halons 1211 and 1301.

C1. Reference Scenario with 85% reduction in Montreal products: same as scenario B1 with 17% reduction per year (total 85%).

D1. Reference Scenario with 95% reduction in Montreal products: same as scenario B1 with 19% reduction per year (total 95%).

D2. Scenario D1 with CCl_4 and CH_3CCl_3 fixed at 1985 levels.

D3. Scenario D1 with CCl_4 and CH_3CCl_3 fixed at 1985 levels and NO replacement of Montreal products with HCFC-22.

D4. Scenario D1 with CH_4, CCl_4, and CH_3CCl_3 fixed at 1985 levels and NO replacement of Montreal products with HCFC-22.

emissions in the year 2000. Therefore, an additional scenario E (options 1–10, described in Table 3.2-7) is used to explore the range of chlorine loading under the assumption that we have the capability by the year 2000 of completely eliminating emissions of all halocarbons, except for CH_3Cl. Only a complete cut in emissions of CFCs, HCFC-22, CCl_4, and CH_3CCl_3 results in chlorine loading less than 2 ppbv by 2060, although a combination of cuts and reductions in emissions (including low levels of CFC emissions) can give values below 3 ppbv. If the time frame is extended to 2090, there is a slightly greater range of emission restrictions that will result in 2 ppbv of atmospheric chlorine and a much greater range that would return chlorine levels to 3 ppbv. Model assessments of these scenarios were not performed, since the ozone perturbations would be dominated by the increases in CH_4, N_2O, and CO_2 rather than the chlorine abundances.

The choice of production/emission levels for 1985 is somewhat uncertain. For example, the emissions of CFC-114 and CFC-115 are based on budgetary estimates using their measured growth in atmospheric

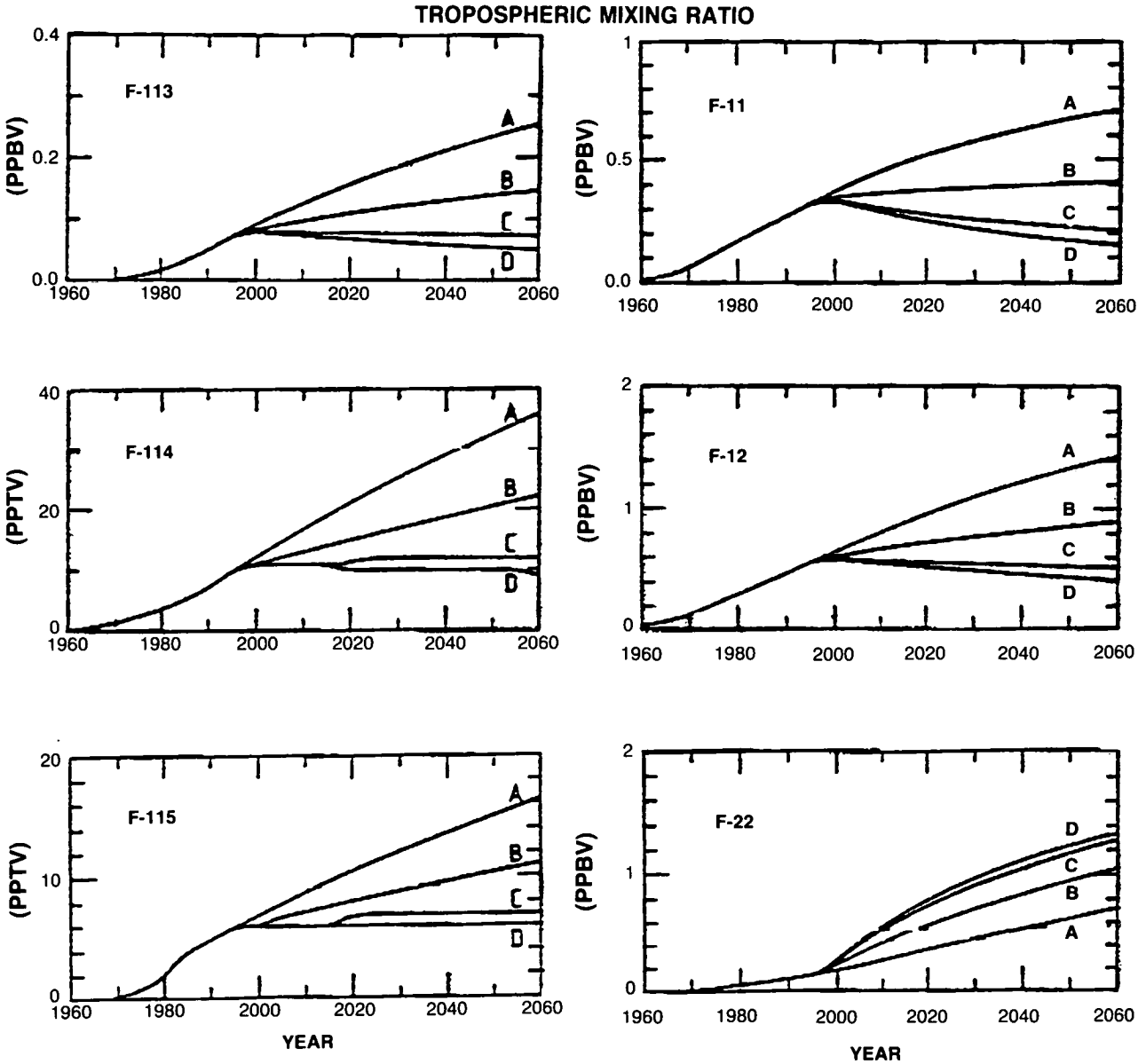

Figure 3.2-1. Time history, 1960-2060, of mean tropospheric concentrations of the trace gases asssumed for the different scenarios (see Tables 3.2.2 and 3.2.3).

abundance. There is some uncertainty regarding the absolute calibration of these measurements and, thus also, the corresponding values for emission in Tables 3.2-2a and b. The values for HCFC-11 and -12 do not reflect the *fait accompli* that HCFC production (by reporting companies alone!) has already grown by an average of 14% between 1985 and 1987 (Grant and Thornton: Production, sales and calculated release of CFC-11 and CFC-12, prepared for the Chemical Manufacturers Association, Washington, DC, 1988).

3.2.1.2 Fluxes or Mixing Ratios?

For the convenience of the model calculations we are also including a set of recommended tropospheric mixing ratios that correspond to a given emissions scenario. This conversion is necessary for HCFC-22,

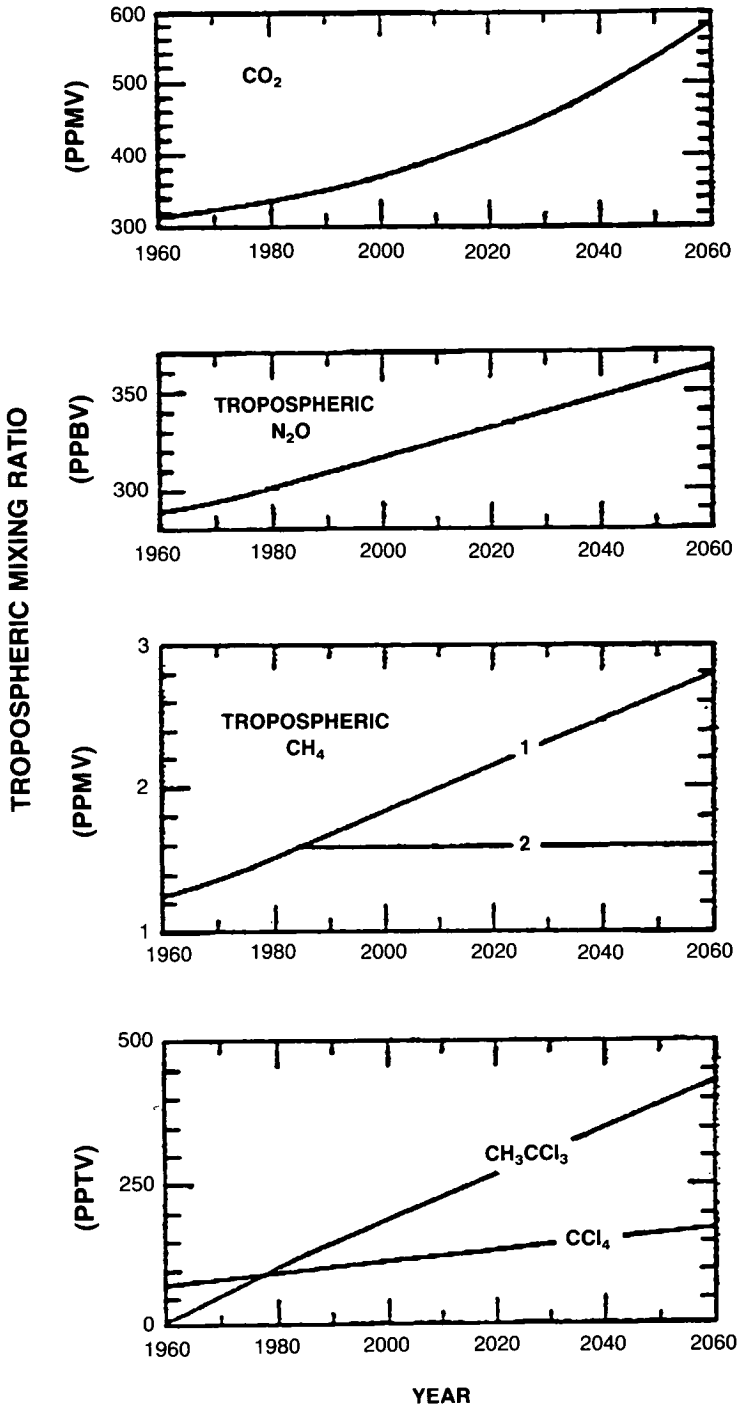

Figure 3.2-1., continued

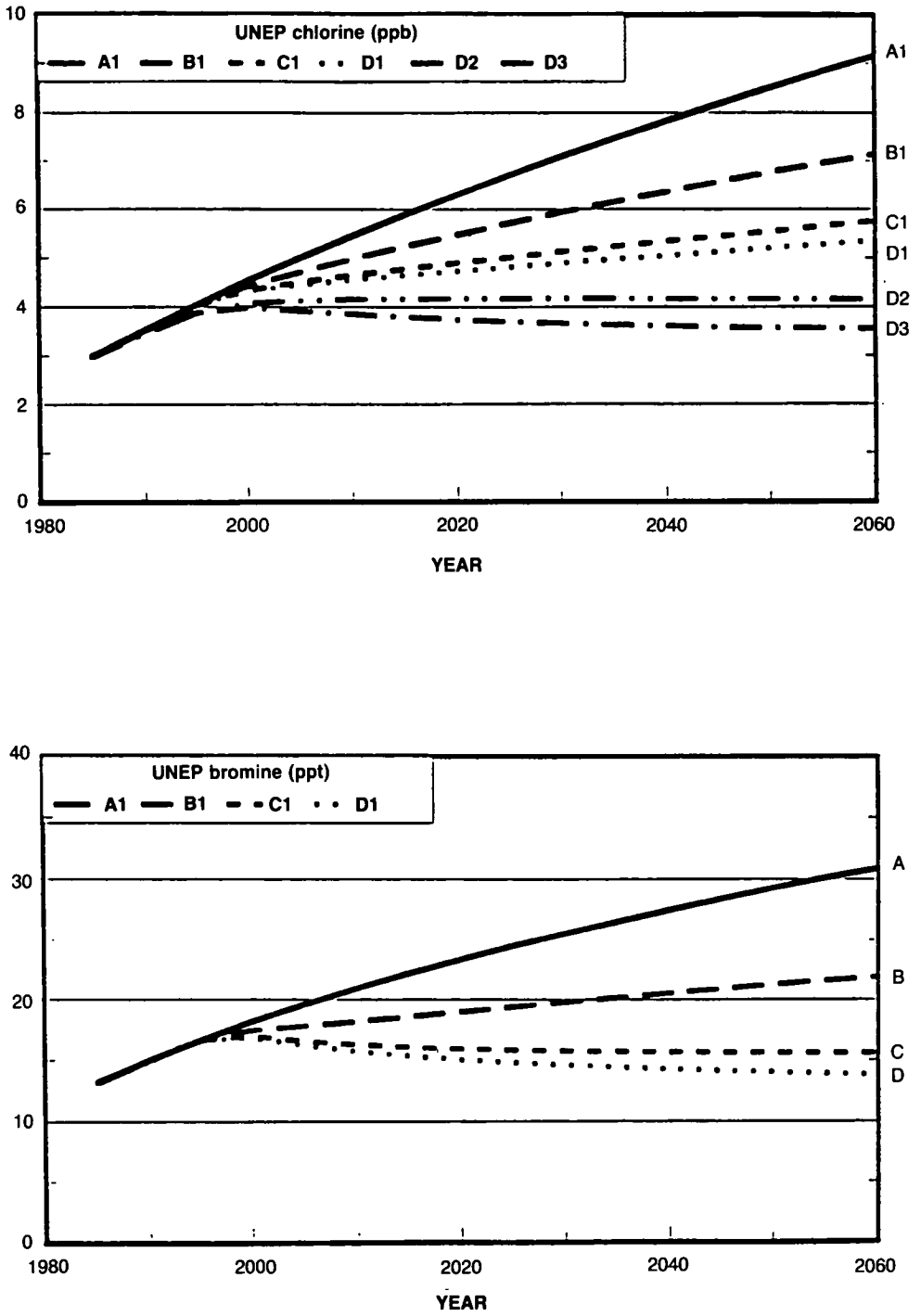

Figure 3.2-2. Time history, 1980–2060, of total atmospheric chlorine and total atmospheric bromine from the different scenarios (see Table 3.2.4).

Table 3.2-2a. Assumed history of trace gas concentrations: Halocarbons and other gases

Year	CO_2 ppmv	N_2O ppbv	CH_4 ppbv	CH_3Cl pptv	CH_3Br pptv	CCl_4 pptv	CH_3CCl_3 pptv
1960	316	289	1255	600	10	75	5
1965	321	292	1316	600	10	80	30
1970	327	295	1375	600	10	85	55
1975	333	298	1450	600	10	90	80
1980	339	302	1525	600	10	95	105
1985	345	306	1600	600	10	100	130
1986+	+0.4%	+0.25%	+15	fixed	fixed	+1	+4

Note: The assumed scenario for these gases from 1986 through 2060 involves exponential (i.e., compounded) growth denoted by an increase in %/yr, linear growth denoted by an annual increase in mixing ratio, or fixed concentrations.

Table 3.2-2b. Assumed history of trace gas concentrations: Montreal products and replacements (all pptv)

Year	CFC-11 $CFCl_3$	CFC-12 CF_2Cl_2	CFC-113 $C_2F_3Cl_3$	CFC-114 $C_2F_4Cl_2$	CFC-115 C_2F_5Cl	Halon 1211 CF_2BrCl	Halon 1301 CF_3Br	HCFC-22 CHF_2Cl
1960	11	33	0.2	0.2	—	—	—	1
1965	27	64	0.8	0.6	—	—	—	4
1970	60	121	2.3	1.4	0.2	0.1	0.1	10
1975	116	207	6.3	2.4	0.8	0.2	0.2	27
1980	173	297	15.3	3.8	2.1	0.5	0.6	54
1985	220	375	30.0	5.0	4.0	1.5	1.7	80
FX (Gg/yr)	350	450	150	15	5	5	8	140+7*
LT (yr)	60	120	90	200	400	15	110	20
CC (Gg/pptv)	23.2	20.4	31.6	28.9	26.1	27.9	25.1	14.6

Note: Fluxes (FX) denote emissions in 1985 (Gg = 1E9 g); HCFC-22 emissions* are assumed to grow linearly by an additional 7 Gg/yr for each year after 1985. The Reference Scenario (A) fixes all future emissions of Montreal products at the 1985 level; other scenarios (B, C, D) assume a cutback each year from 1996 to 2000 with part of this reduction (50% by mass) being added to the base scenario for HCFC-22. The conversion factor between emissions and concentration, CC, assumes that the halocarbons are mixed only throughout 95% of the atmosphere with a total dry weight of 5.148E21 g (1.777 10^{20} moles).

since the lifetime is determined by reactions with tropospheric OH and the current assessment models are not well tested or studied in terms of tropospheric chemistry. For the Montreal products, the predominant loss occurs in the stratosphere and the models should adequately calculate their global loss, but there is significant uncertainty (>25%) in the lifetimes for these gases as seen by the range of values reported by the assessment models in Table 3.2-6.

These calculations of atmospheric concentrations from emissions are simplistic and do not represent the best estimate of future composition (see discussion of uncertainties in lifetimes below). The atmospheric lifetime for each species (LT) is assumed to remain constant throughout the scenario and is given in Table 3.2-2b. The equation used to integrate the globally averaged tropospheric mixing ratios (TM) from the emissions (FX) is given by the following year-to-year regression formula :

$$TM(t+1) = TM(t) * DD + FX(t+1) * (1-DD) * LT/CC$$

where DD = exp(− 1/LT) represents the atmospheric decay of the species during one year, and CC is the conversion factor between tropospheric concentration (pptv, assumed to be well mixed) and mass (Gg), see Table 3.2-2b. Slightly greater abundances of these gases are anticipated in the Northern Hemisphere and over source regions, but the latitudinal gradients are not expected to have a significant impact on the stratospheric abundance. The resultant projections for HCFC-22 and the Montreal products are given in Tables 3.2-3(a-d) for scenarios A1–D1, respectively.

Table 3.2-3a. Projected surface mixing ratios for Scenario A: Montreal products and replacements (all pptv)

Year	CFC 11	CFC 12	CFC 113	CFC 114	CFC 115	Halon 1211	Halon 1301	HCFC 22
1985	220	375	30	5	4	1.5	1.7	80
1990	275	468	51	7	5	1.8	3.2	111
1995	325	557	72	10	6	2.1	4.6	146
2000	372	642	91	12	7	2.3	6.0	184
2005	414	724	109	14	8	2.4	7.2	224
2010	453	802	126	17	8	2.5	8.5	266
2015	490	878	143	19	9	2.5	9.7	309
2020	523	950	158	21	10	2.6	10.8	353
2025	553	1019	173	23	11	2.6	11.9	398
2030	582	1085	186	25	12	2.6	12.9	444
2035	607	1149	199	27	13	2.6	13.9	490
2040	631	1210	212	29	13	2.7	14.8	537
2045	653	1269	223	31	14	2.7	15.7	584
2050	673	1325	234	32	15	2.7	16.6	631
2055	692	1379	245	34	16	2.7	17.4	678
2060	709	1431	255	36	16	2.7	18.2	726

Table 3.2-3b. Projected surface mixing ratios for Scenario B: Montreal products and replacements (all pptv)

Year	CFC 11	CFC 12	CFC 113	CFC 114	CFC 115	Halon 1211	Halon 1301	HCFC 22
1985	220	375	30	5	4	1.5	1.7	80
1990	275	468	51	7	5	1.8	3.2	111
1995	325	557	72	10	6	2.1	4.6	146
2000	350	609	84	11	6	2.0	5.5	230
2005	358	639	91	12	7	1.8	6.0	333
2010	365	666	98	13	7	1.7	6.5	424
2015	372	693	104	14	8	1.6	7.0	506
2020	379	719	110	15	8	1.5	7.5	580
2025	385	744	115	16	8	1.5	7.9	649
2030	390	767	121	17	9	1.4	8.4	712
2035	395	790	126	18	9	1.4	8.8	773
2040	400	812	131	19	9	1.4	9.2	830
2045	404	833	135	20	10	1.4	9.5	886
2050	408	853	139	20	10	1.4	9.9	940
2055	411	872	143	21	10	1.4	10.2	992
2060	415	890	147	22	11	1.4	10.5	1044

Table 3.2-3c. Projected surface mixing ratios for Scenario C: Montreal products and replacements (all pptv)

Year	CFC 11	CFC 12	CFC 113	CFC 114	CFC 115	Halon 1211	Halon 1301	HCFC 22
1985	220	375	30	5	4	1.5	1.7	80
1990	275	468	51	7	5	1.8	3.2	111
1995	325	557	72	10	6	2.1	4.6	146
2000	334	587	79	11	6	1.8	5.2	262
2005	318	579	78	11	6	1.4	5.2	409
2010	304	571	78	11	6	1.1	5.2	535
2015	290	564	77	11	6	0.9	5.2	644
2020	278	557	76	11	6	0.8	5.2	739
2025	267	551	75	11	7	0.7	5.2	824
2030	256	545	75	11	7	0.6	5.2	900
2035	247	539	74	12	7	0.5	5.2	970
2040	238	533	74	12	7	0.5	5.2	1036
2045	230	527	73	12	7	0.5	5.2	1097
2050	222	522	73	12	7	0.5	5.2	1156
2055	215	517	72	12	7	0.4	5.2	1212
2060	209	512	72	12	7	0.4	5.2	1266

Table 3.2-3d. Projected surface mixing ratios for Scenario D:[a] Montreal products and replacements (all pptv)

Year	CFC 11	CFC 12	CFC 113	CFC 114	CFC 115	Halon 1211	Halon 1301	HCFC 22
1985	220	375	30	5	4	1.5	1.7	80
1990	275	468	51	7	5	1.8	3.2	111
1995	325	557	72	10	6	2.1	4.6	146
2000	330	580	78	11	6	1.8	5.1	271
2005	307	562	75	11	6	1.3	4.9	431
2010	286	544	72	10	6	1.0	4.8	567
2015	267	527	69	10	6	0.7	4.6	683
2020	249	511	66	10	6	0.6	4.5	784
2025	233	496	64	10	6	0.4	4.4	874
2030	218	481	62	10	6	0.4	4.3	954
2035	204	467	60	10	6	0.3	4.2	1027
2040	191	453	57	10	6	0.2	4.1	1094
2045	180	440	56	10	6	0.2	3.9	1158
2050	169	427	54	9	6	0.2	3.9	1217
2055	159	415	52	9	6	0.2	3.8	1275
2060	150	404	50	9	6	0.2	3.7	1330

[a]Given concentrations apply to all scenarios D1–D4 except for HCFC-22: use values here for scenarios D1 and D2 and from scenario A for D3 and D4.

3.2.1.3 Uncertainties

The historical record of trace gas concentrations back to 1960 is not well known, especially for some of the more exotic CFCs and for global coverage. However, this uncertainty does not introduce any

important source of error in these calculations, since the concentrations must have been small in 1960 and are constrained by the history of production and release over this period. Changes in CO_2 are documented since 1957, and the increases in CH_4 and N_2O are bounded by earlier spectroscopic data and ice core records.

Any scenario for future abundances of the trace gases has obvious uncertainties associated with:

1. the extrapolation of N_2O, CO_2, CH_4, and CCl_4 (current sources and sinks are not well quantified, nor predictable in the future);
2. the extrapolation of CH_3CCl_3 and HCFC-22 (even with knowledge of atmospheric emissions, these gases depend on predicting tropospheric OH levels and their changes in a future climate and chemistry);
3. the prediction of stratospheric losses of CFCs (lifetimes are still uncertain at the 20% level with corresponding uncertainty in the abundance of CFCs at steady state); and
4. the prediction of future emissions.

We ignore the uncertainties associated with item (4) by assuming that sources of Montreal products from the chemical industry are controlled, and with item (1) by assuming recent trends in other trace gases can be simply extrapolated. A more rigorous analysis and modeling of these processes is beyond the scope of the current study.

One caveat regarding item (4) concerns the assumption that emission equals production. This assumption holds for end uses in which the CFC is released rapidly into the atmosphere after production (e.g., open cell foams or aerosol propellants), but not for those applications in which the CFC is contained in a closed-cycle system such as refrigeration, certain foams, or fire retardants (i.e., banking). A study has been made for these scenarios (R. Hennig, Mainz) that considers the time lags associated with the current CFC markets. For scenario A, results are only a few percentage points different from those given here; but for scenario D, with large cuts in production, the banking of CFCs extends their emissions, increasing concentrations of CFC-11 and 12 by about 10% over the period 2020–2060.

Tropospheric chemistry (item 2) is expected to respond to changes in climate, stratospheric ozone, and other trace gases; it should be predictable with global models of tropospheric chemistry. The resulting perturbation to OH is likely to change the global mean lifetime of HCFC-22, CH_3CCl_3, and CH_4; and hence, their atmospheric abundances. For further analysis of the atmospheric oxidative capacity see Chapter 4. For CH_4 and CH_3CCl_3 we make no direct assumptions about OH, but for HCFC-22 we have assumed that the lifetime remains constant. If tropospheric OH changes as much as 20% by 2060, then the predicted HCFC-22 concentrations should also change correspondingly.

The lifetimes of the fully halogenated CFCs (item 3) are determined by stratospheric losses and should be calculated accurately with the models used in this assessment. There is, however, disagreement between models regarding the lifetimes of the CFCs: for example, the lifetime of CFC-11 in the current atmosphere is 47 years in the AER model and 60 years in the GSFC2 model (see Table 3.2-6). If the AER lifetime were used in Table 3.2-2, then CFC-11 concentrations in 2060 would be reduced by about a factor of 0.8. We recognize that the contribution of Montreal products to the chlorine and bromine loading of the stratosphere is uncertain at the 20% level.

A further complication is that by 2060 in scenario A1 the lifetimes of most CFCs will decrease by about 5–10% (see Table 3.2-6); the change is due to increased stratospheric losses because there is less

ozone in the upper stratosphere and more ultraviolet sunlight reaches the middle stratosphere. This effect was not included in the scenarios given in Table 3.2-3, which assumed a fixed lifetime. The model results given in Table 3.2-6 included only direct chemical effects and not any additional impact due to tropospheric climate change or alteration in the stratospheric circulation due to the ozone loss. Thus, predicting the future atmospheric chemical state and dynamical circulation should be an important component of subsequent assessments of CFCs.

Some models (Cambridge and Oslo) ran the assessment simulations with the flux boundary conditions that define the basic scenario (Table 3.2-1); their results will vary in comparison with the other models, in part because the halogen content of the atmosphere differs from the projected histories given in Table 3.2-3. This range in chlorine content, and in the resulting ozone perturbation, is an example of the uncertainty in making these predictions today, but it must not be considered a full estimate of the possible error in current model calculations.

3.2.2 Predicted Response of the Atmosphere for Sample Scenarios

3.2.2.1 Different Models and Different Chemistries

Predictions of stratospheric ozone and temperatures have been made for the standard UNEP scenarios described in Section 3.2.1 and defined by Tables 3.2-1 and 3.2-2. We examine here specific predictions from these scenarios for the recent past—from 1960 to 1980—in which chlorine levels have more than doubled, and for the future—from 1980 to 2020 and to 2060. We shall look at changes in the vertically integrated column of ozone, as well as changes in local ozone concentrations and temperatures throughout the stratosphere. One goal of this section will be to examine model predictions of stratospheric change using different scenarios for chlorine and bromine loading of the atmosphere.

The models used in these calculations are predominantly the standard 2-D stratospheric chemistry models, including also some 1-D climate/chemistry models and 2-D models incorporating heterogeneous chemistry. All models have adopted the same homogeneous gas-phase chemistry from the recent kinetics assessment (DeMore et al., 1987). One-dimensional models are useful for some diagnostic studies, but two-dimensional models are required to simulate ozone over latitudes and seasons, and to compare with observations. The basic predictions presented here were made with the standard 2-D assessment models: we have had the most experience with these models, and a major intercomparison was just completed (see Section 3.1.3).

The appearance of the Antarctic ozone hole revealed significant limitations in our stratospheric modeling and predictive capabilities. The mobilization of the scientific community—including field campaigns, laboratory measurements, and theoretical modeling— has led recently to an understanding of the processes controlling ozone destruction over Antarctica (see Chapter 1, Polar Ozone). The ozone hole has been shown to be related to heterogeneous chemistry occurring on particles in polar stratospheric clouds (PSCs, see Chapter 1). The processing by PSCs occurs irregularly on small spatial scales in the polar stratosphere during winter and is critically dependent on the occurrence of very low temperatures, even if only for brief episodes. Furthermore, during winter the polar regions appear to be chemically isolated from the rest of the lower stratosphere by the circumpolar vortex of high winds. Within the polar stratospheric vortex, extremely low concentrations of source gases (N_2O, CFCs) are observed at 19 km, and can be explained only by descent of photochemically aged air from the middle stratosphere (25–35 km). These chemical and dynamical processes associated with the Antarctic ozone hole are difficult to simulate with the current global models.

The assessment models used here to predict global ozone change include only gas-phase chemistry. Furthermore, they do not acceptably reproduce the dynamical circulation of the polar vortex that leads to low concentrations of trace gases within the vortex. Accordingly, they do not simulate the Antarctic ozone hole nor make predictions of ozone loss in the lower polar stratosphere for the late spring. The models should, however, provide accurate assessment of large-scale ozone perturbations driven by chlorine-catalyzed chemistry in the middle to upper stratosphere.

Some of the 2-D assessment models have versions that now include a parameterized form of PSC chemistry. These models are now able to predict some form of Antarctic ozone hole, and also to a lesser extent ozone loss that is due to chlorine and bromine catalytic cycles in the Arctic stratosphere. The scientific community has not yet had the opportunity to examine and validate these new forms of chemistry in the 2-D models. Therefore, we do not include their results here as part of the basic predictions, but have put results from the models with heterogeneous chemistry in a special section; with improved treatment of the polar dynamics these models should become part of the standard predictions in subsequent assessments.

We have received calculations for the UNEP scenarios (Tables 3.2-1 and 3.2-2) from several modeling groups and shall examine these in some detail. Only the GSFC2 model was used for all eight scenarios. Other modeling groups have contributed calculations using scenarios that are similar, but not equivalent to any of the UNEP scenarios. We include a brief discussion of these results where applicable.

3.2.2.2 Standard Scenario: 1960–1980

All scenarios are identical through 1985 since they are based on the assumed history of atmospheric composition. We look here at the predicted change over the period 1960 to 1980, a time interval similar to that examined by the International Ozone Trends Panel (OTP, see Watson et al., 1988 for executive summary of Chapter 7). The OTP Report spent significant effort in modeling the solar cycle and atmospheric nuclear tests in addition to the trace gases. Here we consider only the changes caused by increases in the

Table 3.2-4. Chlorine and bromine loading of the atmosphere for the UNEP scenarios

	Total Chlorine (ppbv)						Total Bromine (pptv)			
Year	A1–2	B1	C1	D1	D2	D3–4	A1–2	B1	C1	D1–4
1985	2.98	2.98	2.98	2.98	2.98	2.98	13.2	13.2	13.2	13.2
1990	3.52	3.52	3.52	3.52	3.44	3.44	15.0	15.0	15.0	15.0
1995	4.03	4.03	4.03	4.03	3.87	3.87	16.7	16.7	16.7	16.7
2000	4.52	4.41	4.33	4.31	4.07	3.98	18.2	17.5	17.0	16.9
2005	4.99	4.70	4.50	4.44	4.12	3.91	19.6	17.8	16.6	16.2
2010	5.44	4.97	4.64	4.55	4.15	3.85	21.0	18.2	16.3	15.8
2015	5.88	5.23	4.77	4.64	4.16	3.79	22.2	18.6	16.1	15.4
2020	6.30	5.47	4.90	4.73	4.17	3.74	23.4	19.0	16.0	15.1
2025	6.70	5.71	5.01	4.81	4.17	3.70	24.5	19.4	15.9	14.8
2030	7.09	5.93	5.12	4.89	4.17	3.66	25.5	19.8	15.8	14.6
2035	7.47	6.15	5.23	4.97	4.17	3.63	26.5	20.2	15.7	14.5
2040	7.83	6.36	5.34	5.04	4.16	3.61	27.5	20.6	15.7	14.3
2045	8.18	6.57	5.44	5.12	4.16	3.58	28.4	20.9	15.7	14.2
2050	8.51	6.77	5.54	5.20	4.16	3.57	29.3	21.3	15.7	14.1
2055	8.84	6.96	5.65	5.27	4.15	3.56	30.1	21.6	15.6	13.9
2060	9.16	7.15	5.75	5.35	4.15	3.55	30.9	21.9	15.6	13.8

trace gases. We specifically did not include the variation in ultraviolet sunlight over the solar cycle: the magnitude of solar change is uncertain and varies from cycle to cycle as noted in the OTP Report; and the 11-year modulation would have made it difficult to compare trends over periods that were not in the same phase of the solar cycle (e.g., 1960–1980 and 1980–2060).

The calculated change in column ozone (%) from 1960 to 1980 in the different 2-D models is plotted in the form of a Dobson map (abscissa = month, ordinate = latitude) in Figures 3.2-3(A,G,J,L,M,O,W). The letter on each figure in this section denotes the model (see Table 3.2-5 for mnemonic codes). The AER, JMRI, GSFC2, and Oslo models predict a latitudinal/seasonal pattern of perturbations to the ozone column that will be seen in many of the calculations shown here: small changes in the tropics (about -0.5 to -1.5%), becoming larger at higher latitudes, peaking at the end of winter (about -2.5 to -3.5%). Among these four models, the patterns are almost identical and the depletions differ globally by up to 1%. The WisCAR model calculates small but varied changes in the tropics extending to mid-latitudes (-1 to $+1\%$) and larger, more typical losses at the poles in late winter (-2 to -3%). The LLNL and Mainz models predict a quite different pattern, with ozone depletion only in the high latitude winter, and increases as large as 1% elsewhere. The Mainz model did not follow the prescribed scenarios (by including tropospheric NO_x increases), and we cannot ascertain whether this factor is the cause of these differences. One major cause of the different predictions for ozone column lies with the large variation in calculating the magnitude of the ozone increases predicted for the lower stratosphere and upper troposphere as discussed next.

The calculated change on local ozone concentrations (%) from 1960 to 1980 is shown in Figures 3.2-4 (A,G,J,L,M,N,O[March],W) for the month of January. Maximum ozone loss occurs in two regions: the winter mid-latitudes between 35 and 45 km and the same altitude range over the summer pole. The AER, JMRI, GSFC2, NOCAR, and Oslo models have a peak change of about -16% at 70°N, and have zero change lines ranging from 26 km to 20 km and below (JMRI). The LLNL and Mainz models have peak ozone loss of only 7 to 12% and, along with the Oslo model, show general increases in tropospheric ozone that are much larger than the other models. (Prediction of increases in tropospheric ozone with these stratospheric models is regarded with much uncertainty by the modeling community, since tropospheric aspects of these models have not been extensively tested and studied; see also discussion of tropospheric ozone chemistry in Chapter 4). The cause of the substantially smaller ozone decreases over the 1960–1980 period by these latter two models needs to be investigated further. It is likely that the changes in temperature (calculated by the LLNL, NOCAR, and Oslo models, but not by the AER, JMRI, GSFC2, and Mainz models) are part of the difference.

In the NOCAR model the largest decreases in temperature over the 1960–1980 period occur near the stratopause (40–58 km) and are typically 2 K, increasing to 4 K over the summer pole (Figure 3.2-4NT). The predicted temperature changes over the past decades from most of the models including temperature feedbacks were not available for this study, should be examined in greater detail, and need to be verified by the research groups through comparison with observations.

In comparing these results with the OTP Report, we note that the scenarios are slightly different and the models have been further developed since those calculations (generally performed in 1987). The OTP results as shown are not directly comparable to these figures; however, from Figure 7–10 of the OTP Report one can see the latitudinal pattern similar to that shown here: annual average decreases in column ozone becoming larger (up to -3%) from 30°N to 60°N in the AER, LLNL, and Oslo models. In the OTP Report, the Cambridge model shows little latitudinal dependence, a result that is also seen here (Figure 3.2-7C) for the longer period 1980–2060 of scenario A1 and that may be due to summer increases in column ozone.

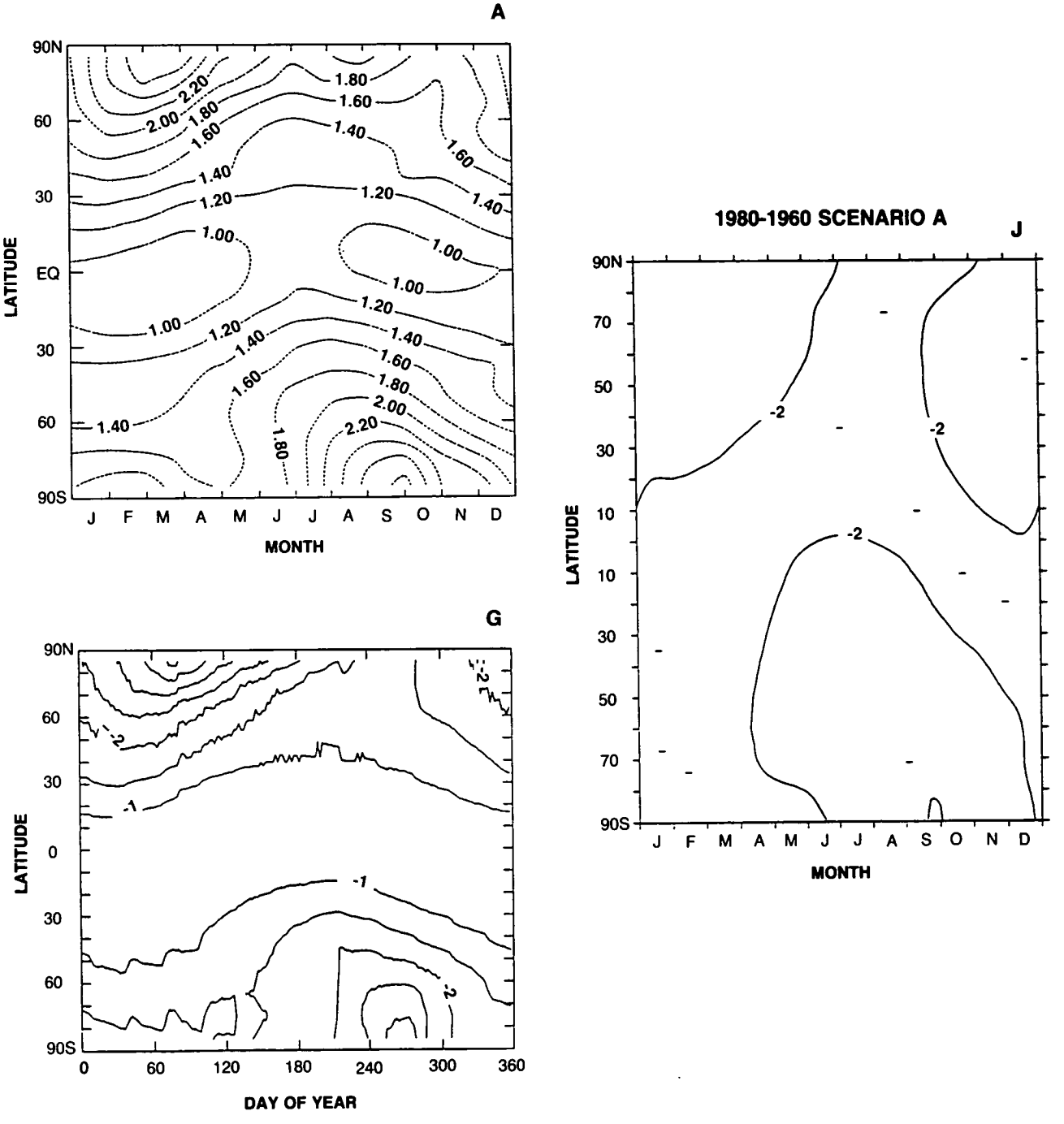

Figure 3.2-3. Dobson map (latitude by month) of percent change in column ozone from 1960 to 1980 using the specified trace-gas scenario. The panels are coded with the model mnemonics (see Table 3.2.5).

The overall changes predicted in ozone from 1960 to 1980 (not including the Antarctic ozone hole and related decreases) are significant and should be detectable, especially if one extends the comparison with observations until 1990. By this time we should be able to test the predictions of the temperature feedback (and correspondingly different ozone perturbations) as well as those of large summertime ozone increases

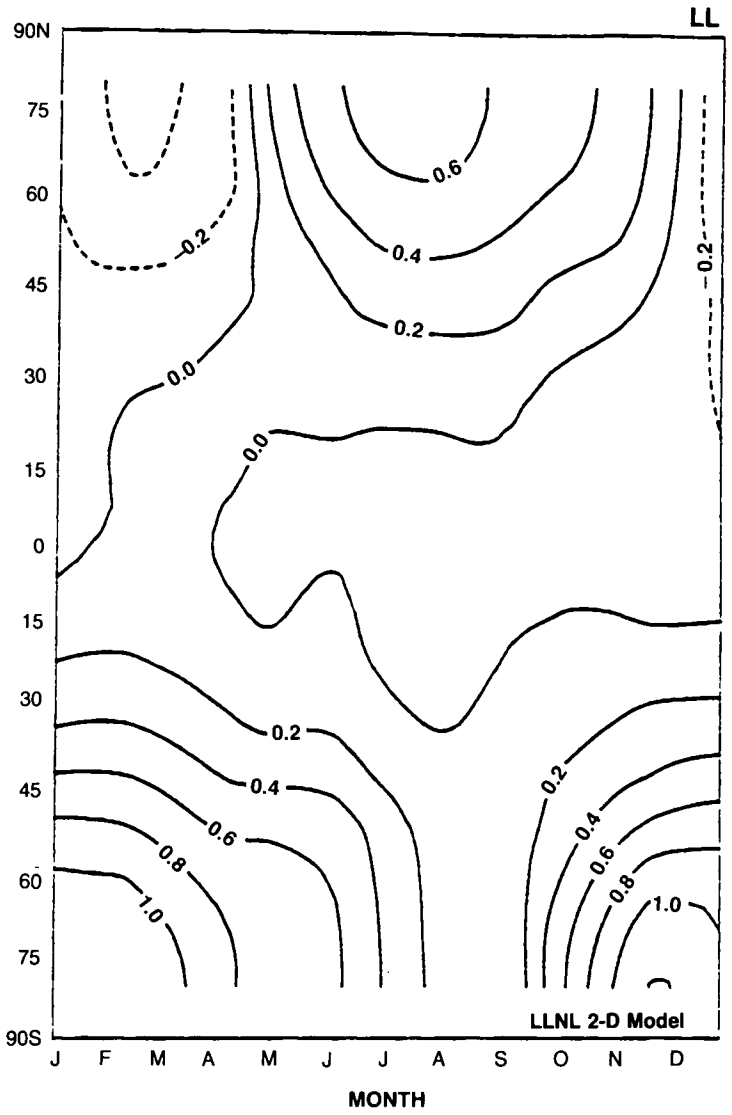

Figure 3.2-3., continued

in the troposphere and lower stratosphere at mid-latitudes. These tests are essential because the different characteristics of the models shown in this 1960–1980 comparison are carried through to the long-term predictions discussed below.

3.2.2.3 Scenario A: 1980–2060

The scenarios A1 and A2 exhibit the most rapid growth in atmospheric chlorine and bromine, and thus produce the largest perturbations among all the scenarios. The impact of large stratospheric abundances of halogens by 2060 (9 ppb of chlorine and 31 ppt of bromine) is offset in part by the rise in methane and carbon dioxide. Methane plays a major role in partitioning of chlorine species (the ratio of HCl to Cl_x) and in ozone production by "smog" chemistry (reactions of CH_3OO and HO_2 with NO). Carbon dioxide is the

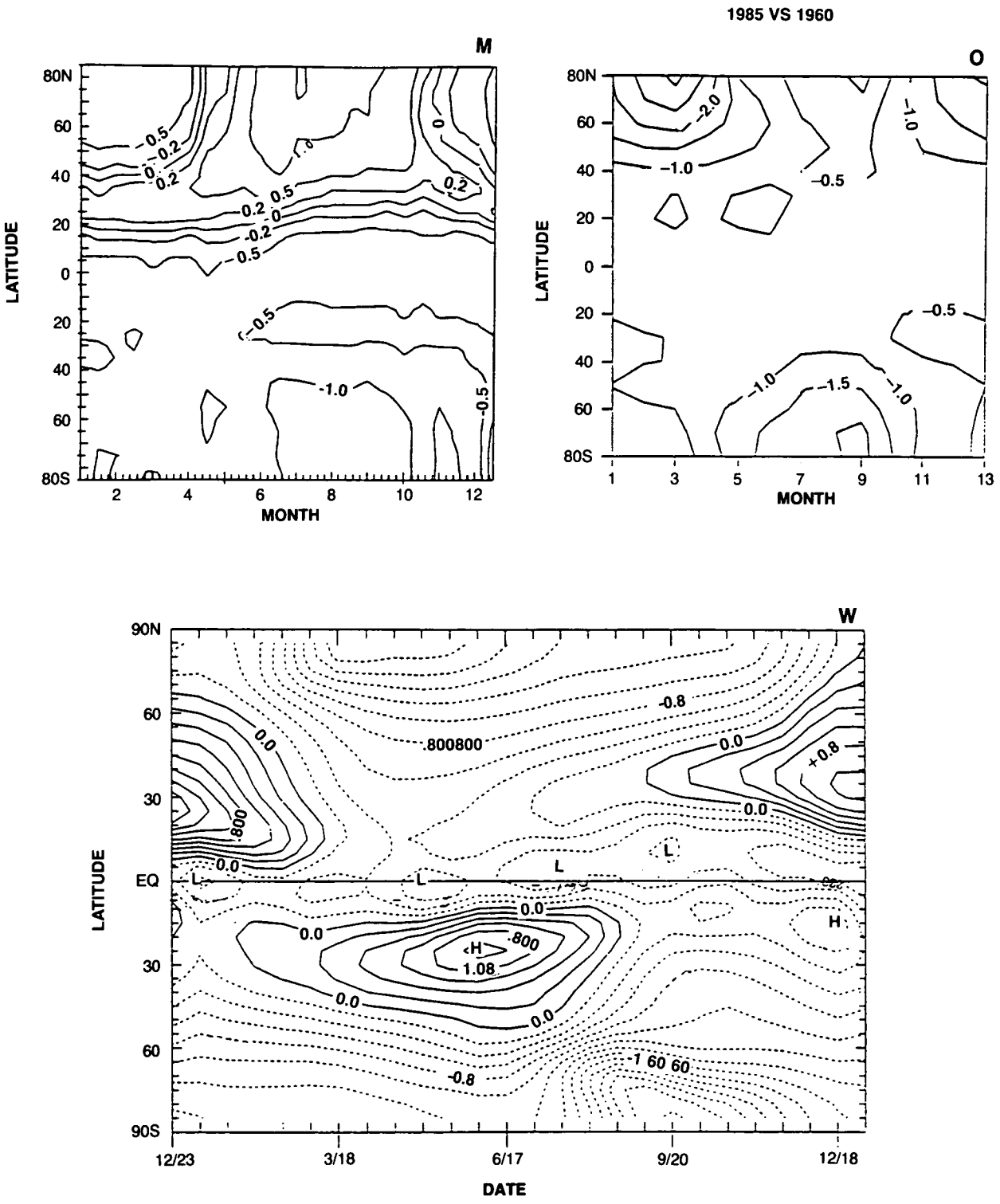

Figure 3.2-3., continued

Table 3.2-5. Participating assessment models

Name	Code	Scenarios	Institution	Scientists
AER	A	A1, B1, b1*	AER, Inc., MA	Ko, Sze
Camb	C	A1*	U. Camb. & RAL, UK	Pyle
GSFC2	G	A–D all	NASA/Goddard, MD	Jackman, Douglass
Aquila	I	A1	U. Aquila, Italy	Visconti
JMRI	J	A1, B1, D1	Met. Res. Inst., Japan	Sasaki
LLNL	L	A1, A1*, D1	L. Livermore, CA	Wuebbles, Connell
Mainz	M	A1	Max Planck, Mainz	Brühl, Crutzen
NOCAR	N	a1*, d1*	NOAA & NCAR, CO	Solomon, Garcia
Oslo	O	A1*, A2*, D4*	U. Oslo, Norway	Isaksen, Stordal
NSU	U	A1*, D1*	U. Novosibirsk, USSR	Dyominov, Zadorozhny
WisCAR	W	a1*, a2*, d1*	U. Wisc. & NCAR, CO	Hitchman, Brasseur
IASB	(1D)	all	Inst. Sp. Aer., Belgium	De Rudder
MPI	(1D)	all	Max Planck, Mainz	Hennig, Brühl, Crutzen

Note: All models are 2-D unless noted. The lowercase letter means that calculations were performed for a steady-state atmosphere using 1980 and 2060 concentrations. An asterisk (*) denotes a model contribution that also includes feedbacks (CO_2 and O_3 changes) on temperatures. The model codes are used in all figures.

Table 3.2-6. Global mean lifetimes (yr) of the trace gases

Model	CFC 11	CFC 12	CFC 113	CFC 114	CFC 115	Halon 1211	Halon 1301	N_2O	CCl_4
AER									
(1980)[a]	47	99	87	261	399	11	75	113	40
(2060)	43	89	74	230	340	11	62	106	38
GSFC2									
(1980)	60	132	120			13	74	168	52
(2060)	57	124	113			13	70	156	49
JMRI	52	132						151	42
LLNL	60	121	109	240	480			130	52
Oslo	52	102	98	247	522		127	51	
WisCAR									
(1980)	51	130	105					140	36
(2060)	46	123	97					130	32
IASB(1D)	85	166	127					166	67
AER(1D)	60	110	96	~275	~500	11	81	145	53
MPI(1D)	67	135	108	230	455	12	82		58

[a]All results are for contemporary atmosphere (1980) unless otherwise noted; the DuPont model did not do the scenario calculations but is used later in this report.

major infrared-active gas responsible for cooling the stratosphere, and a colder stratosphere generally results in greater ozone abundances. The magnitude of these positive ozone changes (as CH_4 and CO_2 increase) can vary significantly from model to model, and for scenario A1, appear to be the major source of the different results shown here. Scenario A2 (CH_4 fixed) removes some of this sensitivity, and results (from a more limited set of models) show larger and more consistent ozone depletions.

Most of the participating models calculated scenario A1, and results are presented in Figures 3.2-5 through 3.2-8 (same notation for different models as described above). A continuous time-line of the percent

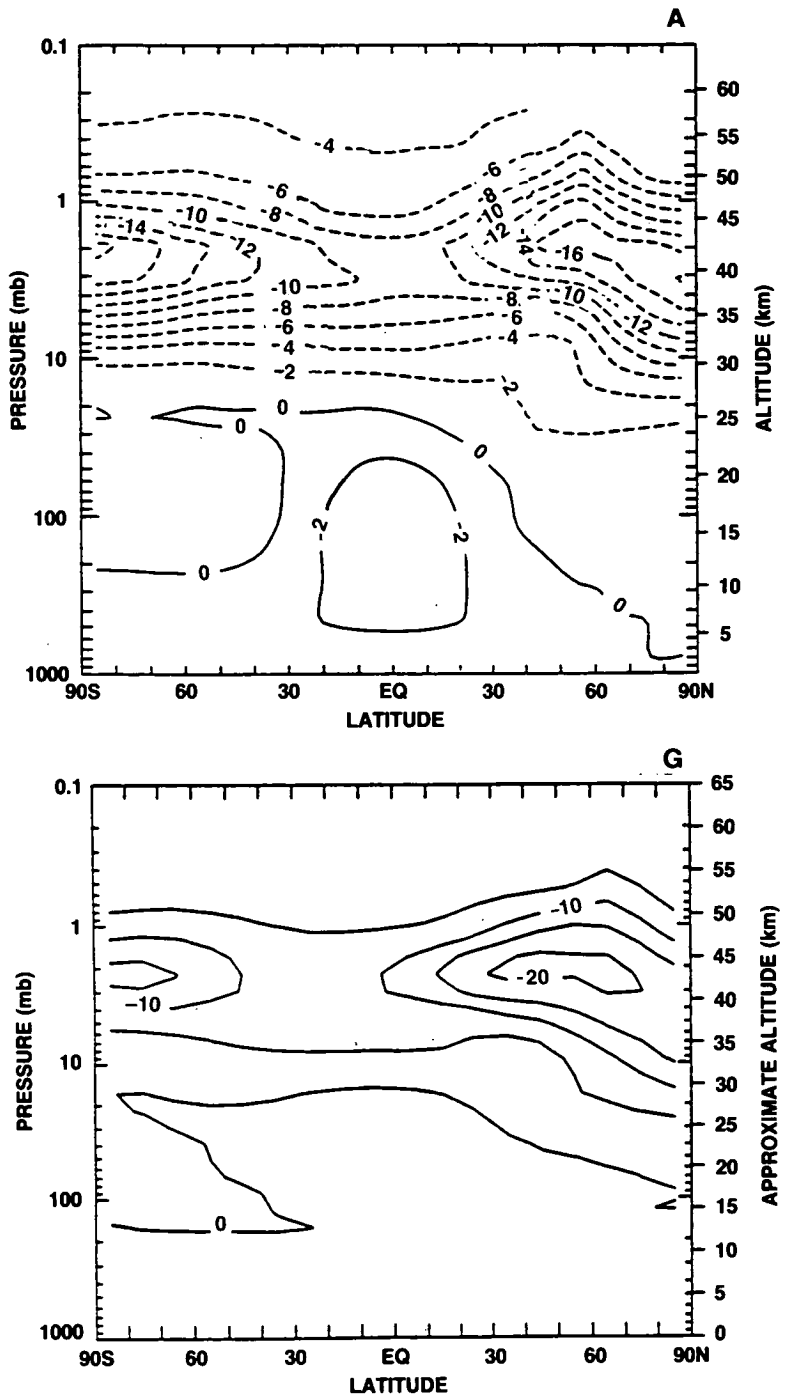

Figure 3.2-4. Latitude-by-altitude (log pressure or height [km]) contour map of the percent change in local ozone concentration from 1960 to 1980 for the specified trace-gas scenario. The panels are coded with the model mnemonics as above. Also included (code NT) is the temperature change (degrees K) from the NOCAR model.

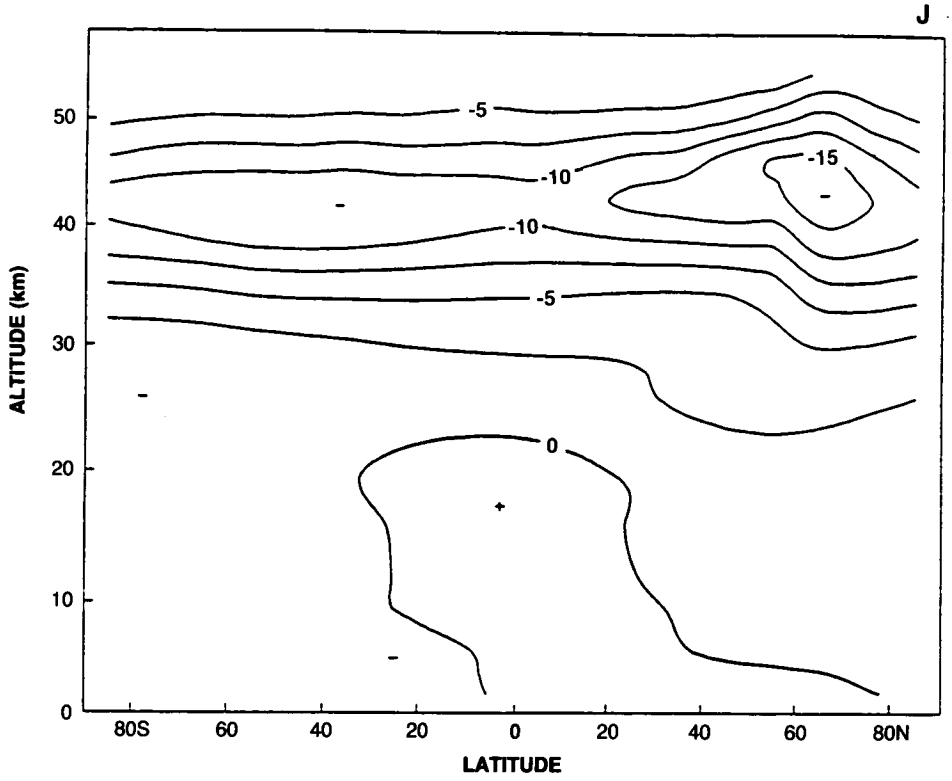

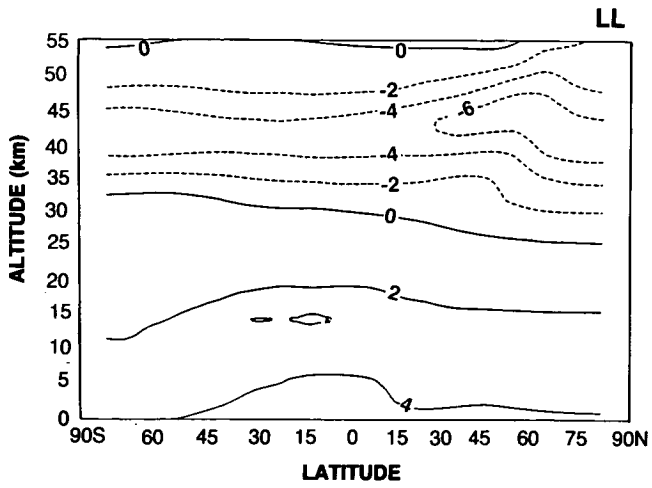

3.2.4 cont,.

Figure 3.2-4., continued

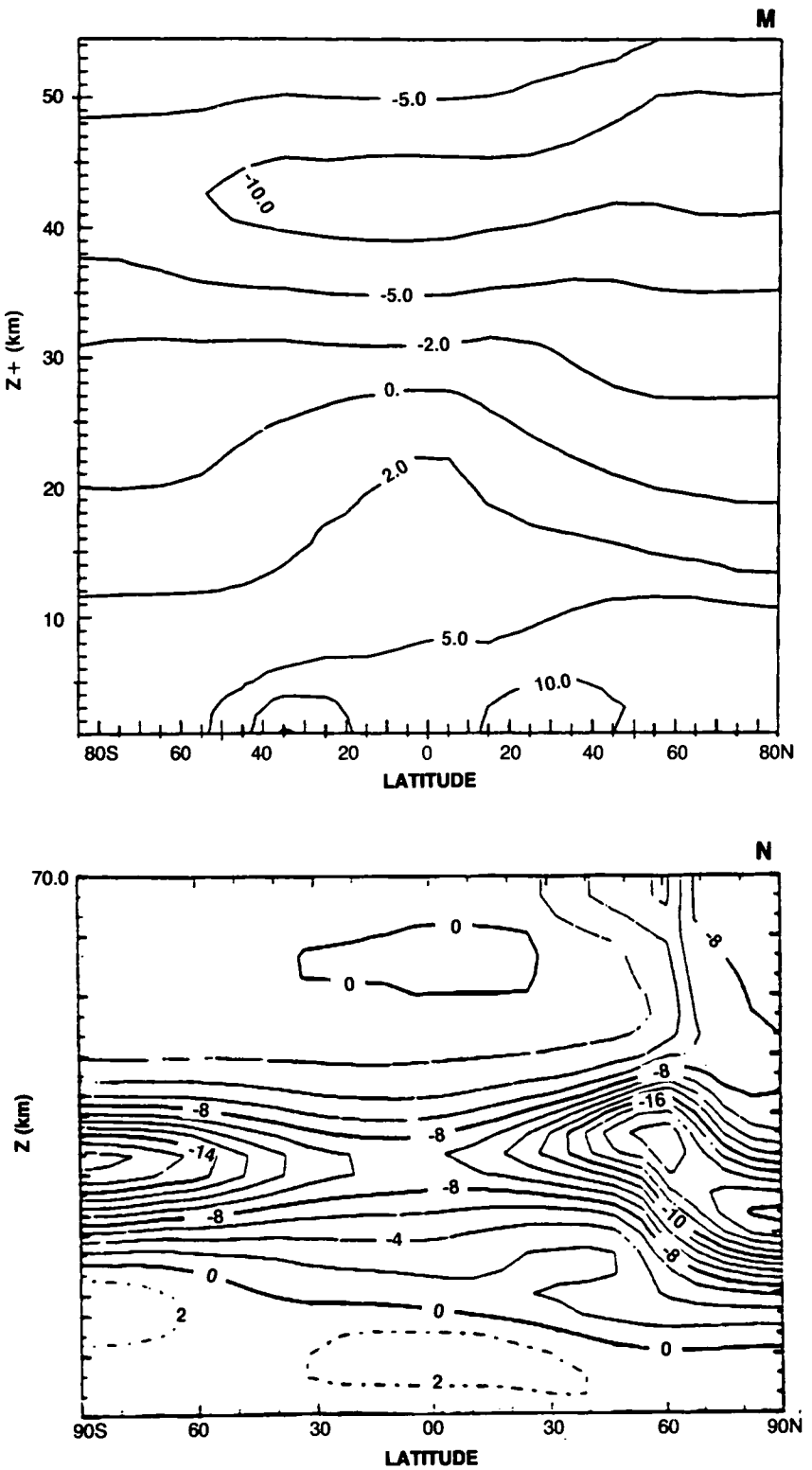

Figure 3.2-4., continued

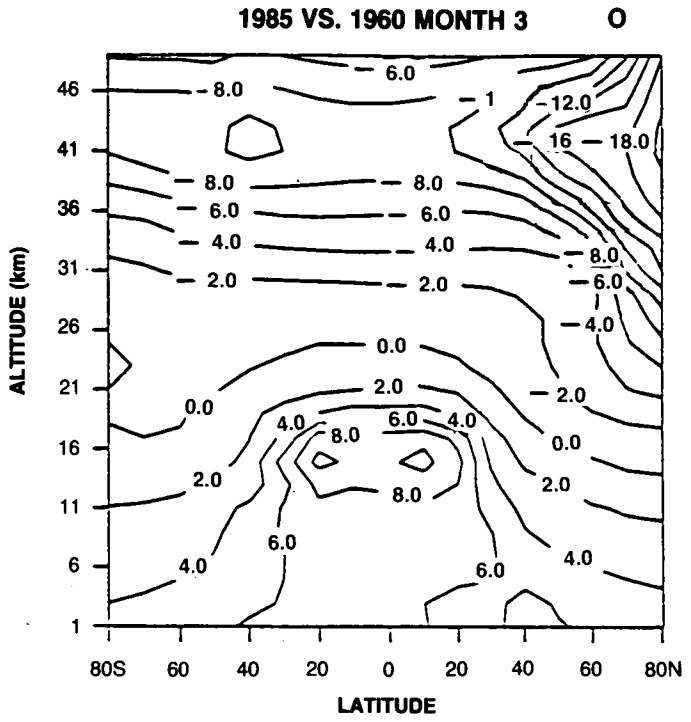

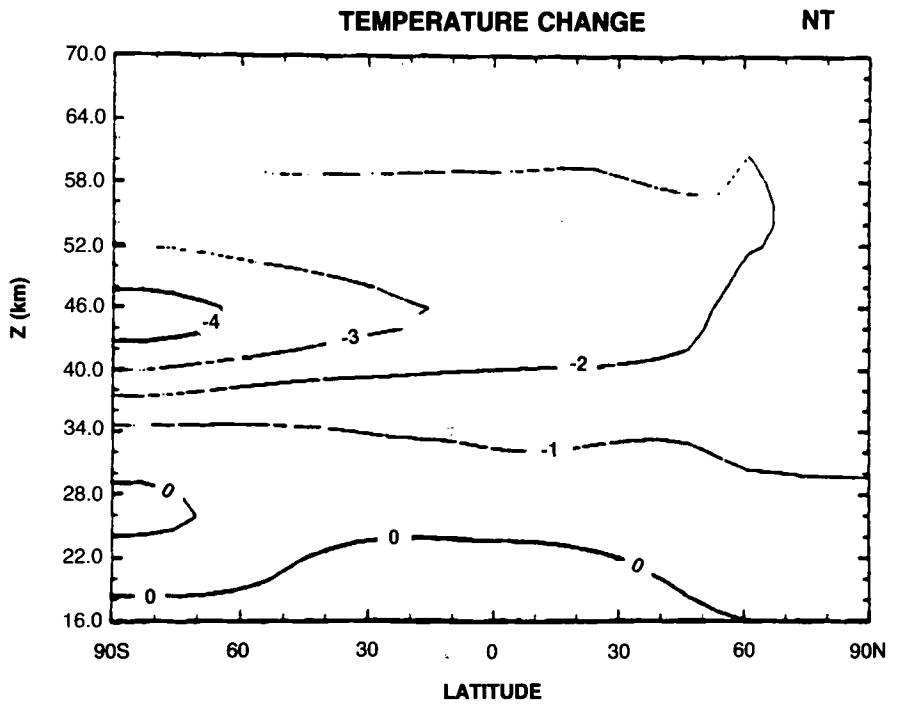

Figure 3.2-4., continued

change in column ozone relative to March 1980 is shown in Figures 3.2-5(A,G,J,L,M) as a function of latitude for all the months of March from 1980 through 2060. All models show the same pattern: ozone depletions are larger at high latitudes, about 7–10% at 50°N and about 3–8% at 50°S by 2060; tropical losses are always much less, 2–5% by 2060, and lag behind the high latitude regions by at least 40 years. The maximum depletion for all models is asymmetric in these figures because March was chosen as the month for comparison; a reverse pattern would occur if September were selected (see Dobson maps in Figures 3.2-6 and 7).

The Dobson maps of the percent change in ozone column from 1980 to 2020 and from 1980 to 2060 are shown in Figures 3.2-6(A,G,J,L,M) and 3.2-7(A,C,G,I,J,L,LL,M,O,U,W), respectively. By 2020 ozone depletions are typically 1 to 3% in the tropics with maximum losses, usually 6 to 8%, at high latitudes in late winter and early spring. The same latitudinal and seasonal pattern persists at 2060. The largest late winter depletions at high latitudes (poleward of 50 degrees latitude) are greater than 10% in the AER,

Table 3.2-7. Extended scenarios for halocarbon abundances

Code	CFC Cut (1996–2000)	Replace as HCFC-22	HCFC-22 Flux	CCl_4 Growth	CH_3CCl_3 Growth
		Scenario Definitions			
A1	0%	—	+7 Gg/yr/yr	+1 ppt/yr	+4 ppt/yr
B1	50%	50%	+7 Gg/yr/yr	+1 ppt/yr	+4 ppt/yr
C1	85%	50%	+7 Gg/yr/yr	+1 ppt/yr	+4 ppt/yr
D1	95%	50%	+7 Gg/yr/yr	+1 ppt/yr	+4 ppt/yr
D2	95%	50%	+7 Gg/yr/yr	fix (1985)	fix (1985)
D3	95%	0%	+7 Gg/yr/yr	fix (1985)	fix (1985)
E1	100%	50%	+7 Gg/yr/yr	+1 ppt/yr	+4 ppt/yr
E2	100%	50%	+7 Gg/yr/yr	fix (2000)	fix (2000)
E3	100%	50%	+7 Gg/yr/yr	cut (2000)	fix (2000)
E4	100%	50%	+7 Gg/yr/yr	cut (2000)	cut (2000)
E5	100%	0%	+7 Gg/yr/yr	cut (2000)	cut (2000)
E6	100%	0%	fix (2000)	cut (2000)	cut (2000)
E7	100%	0%	cut (2000)	cut (2000)	cut (2000)
E8	95%	0%	cut (2000)	cut (2000)	cut (2000)
E9	85%	0%	cut (2000)	cut (2000)	cut (2000)
E10	100%	50% cut (2030)	cut (2030)	cut (2000)	cut (2000)

Total Chlorine Abundance (all halocarbons, ppbv)

Year	A1	B1	C1	D1	D2	D3
1985	2.98	2.98	2.98	2.98	2.98	2.98
2000	4.52	4.41	4.33	4.31	4.07	3.98
2030	7.09	5.93	5.12	4.89	4.17	3.66
2060	9.16	7.15	5.75	5.35	4.15	3.55
2090	10.72	8.09	6.25	5.73	4.05	3.42

Year	E1	E2	E3	E4	E5	E6	E7	E8	E9	E10
1985	2.98	2.98	2.98	2.98	2.98	2.98	2.98	2.98	2.98	2.98
2000	4.30	4.30	4.30	4.30	4.21	4.21	4.21	4.22	4.26	4.30
2030	4.77	4.29	4.09	3.52	2.98	2.84	2.58	2.72	3.01	3.38
2060	5.15	4.19	3.87	3.30	2.67	2.27	1.95	2.18	2.64	2.13
2090	5.47	4.03	3.64	3.07	2.41	1.88	1.55	1.84	2.43	1.59

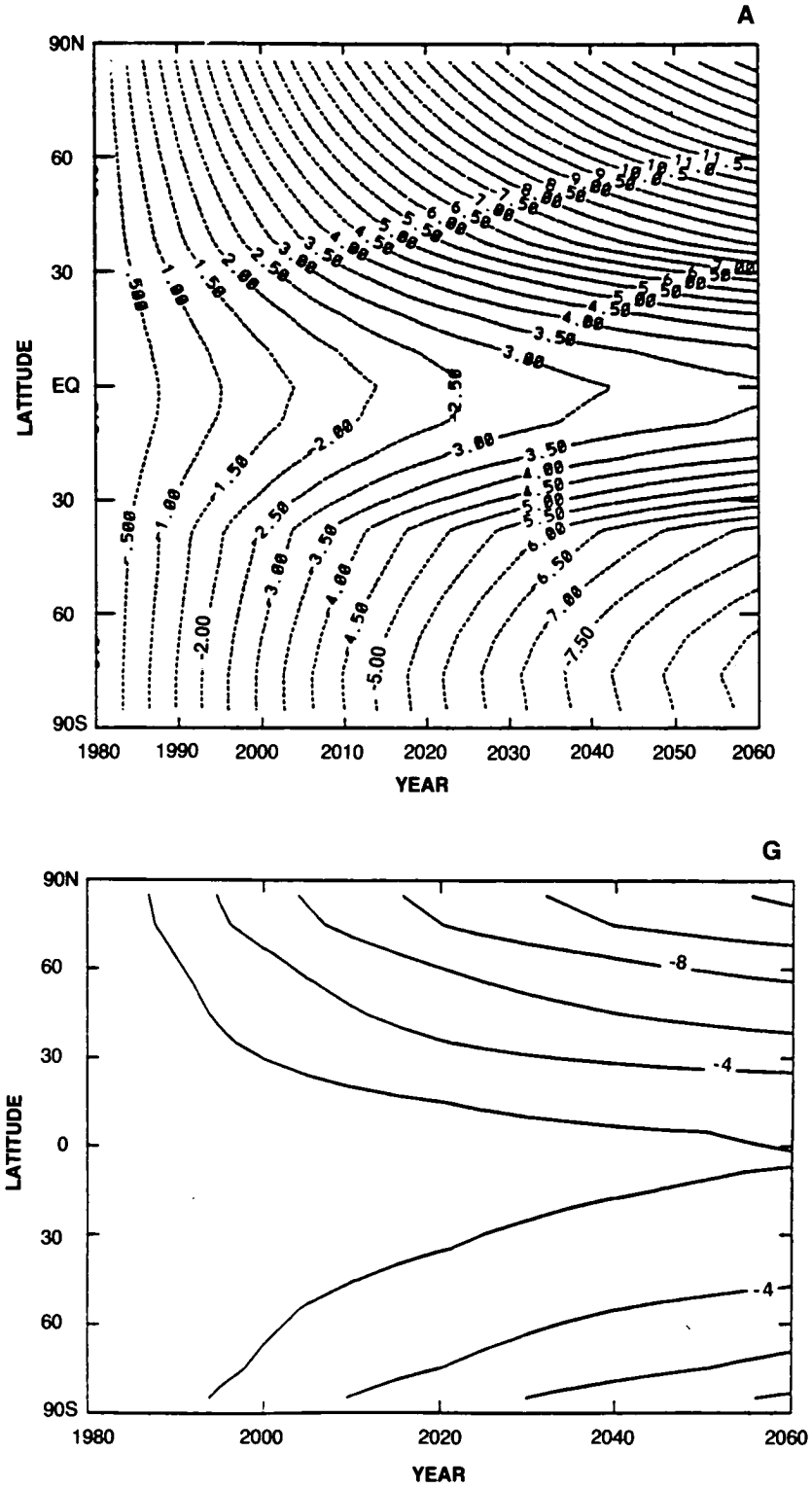

Figure 3.2-5. Time-line of the percent change in column ozone as a function of latitude for the month of March from 1980 through 2060 for scenario A1. (Note the exceptions: the reference year for the JMRI and Mainz plots is 1960 rather than 1980.)

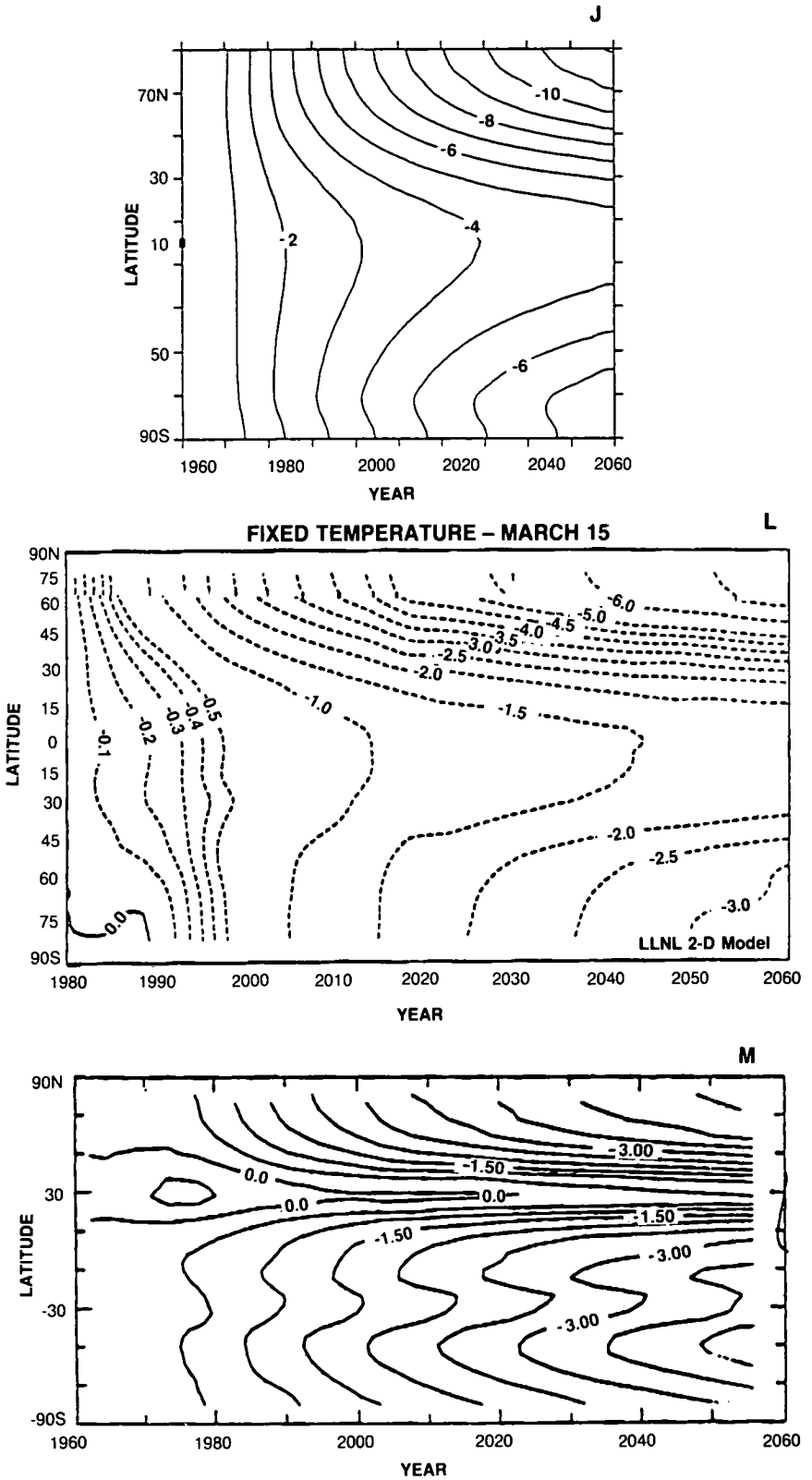

Figure 3.2-5. continued

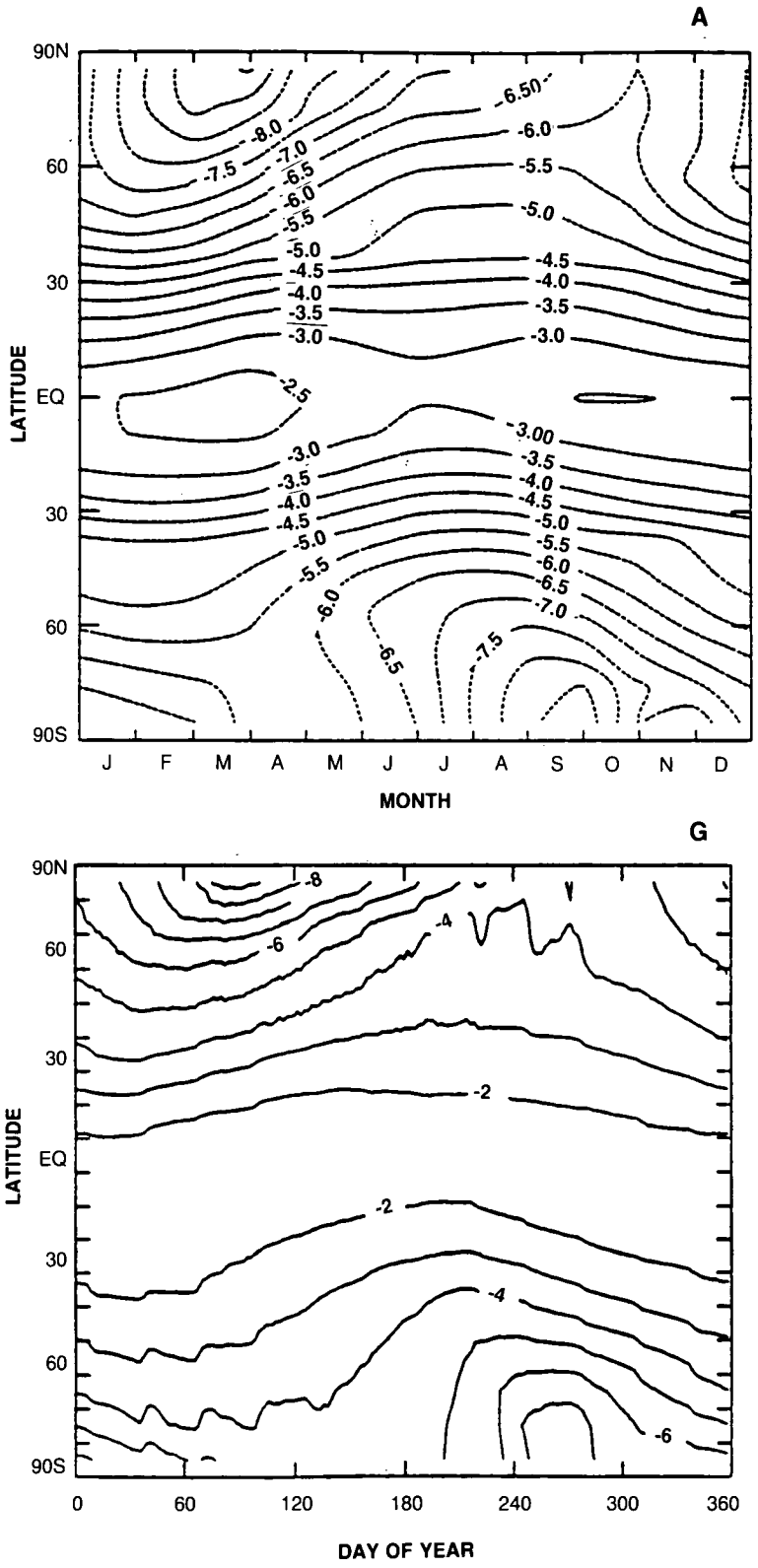

Figure 3.2-6. Dobson map (latitude by month) of percent change in column ozone from 1980 to 2060 using scenario A1.

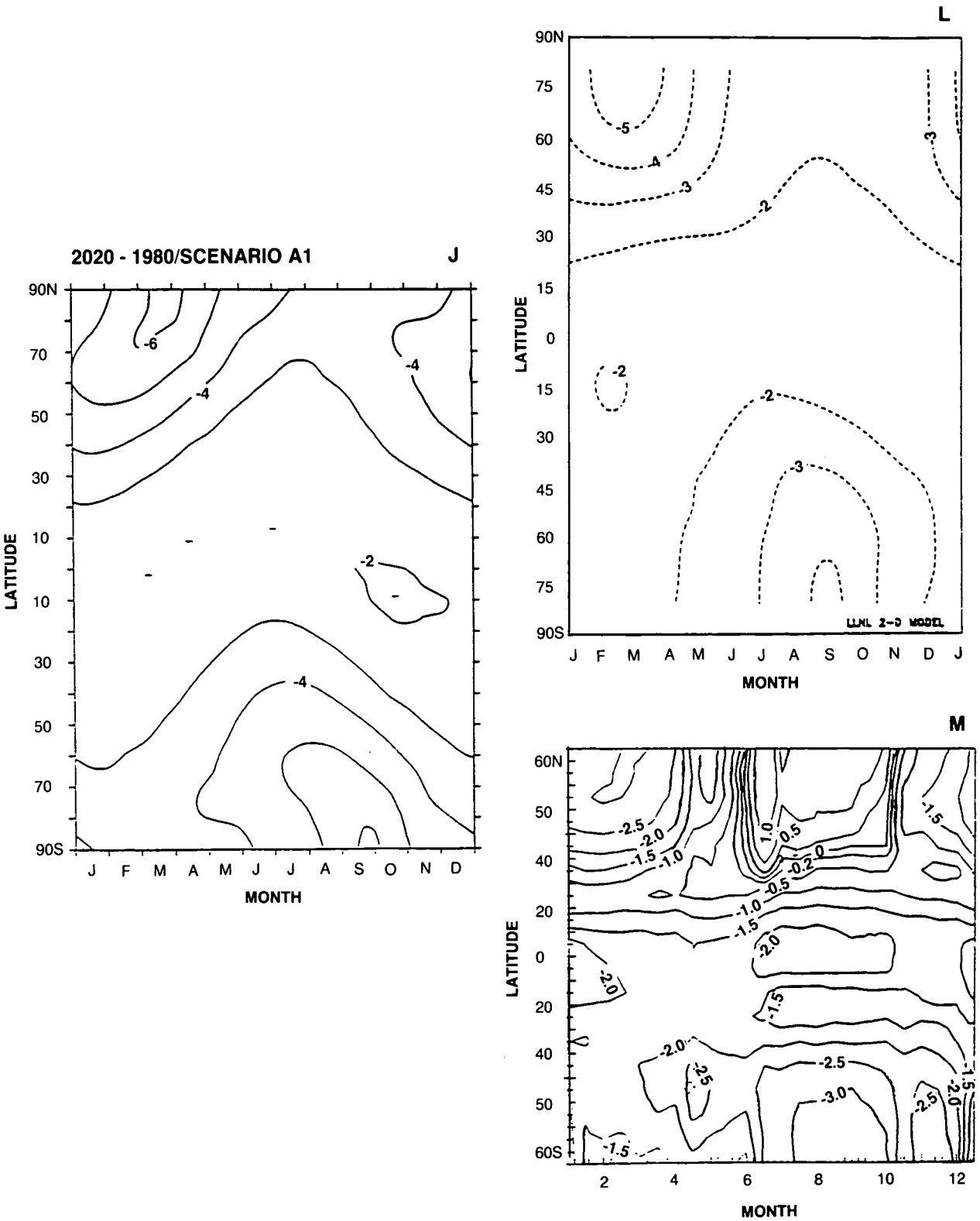

Figure 3.2-6., continued

C-5

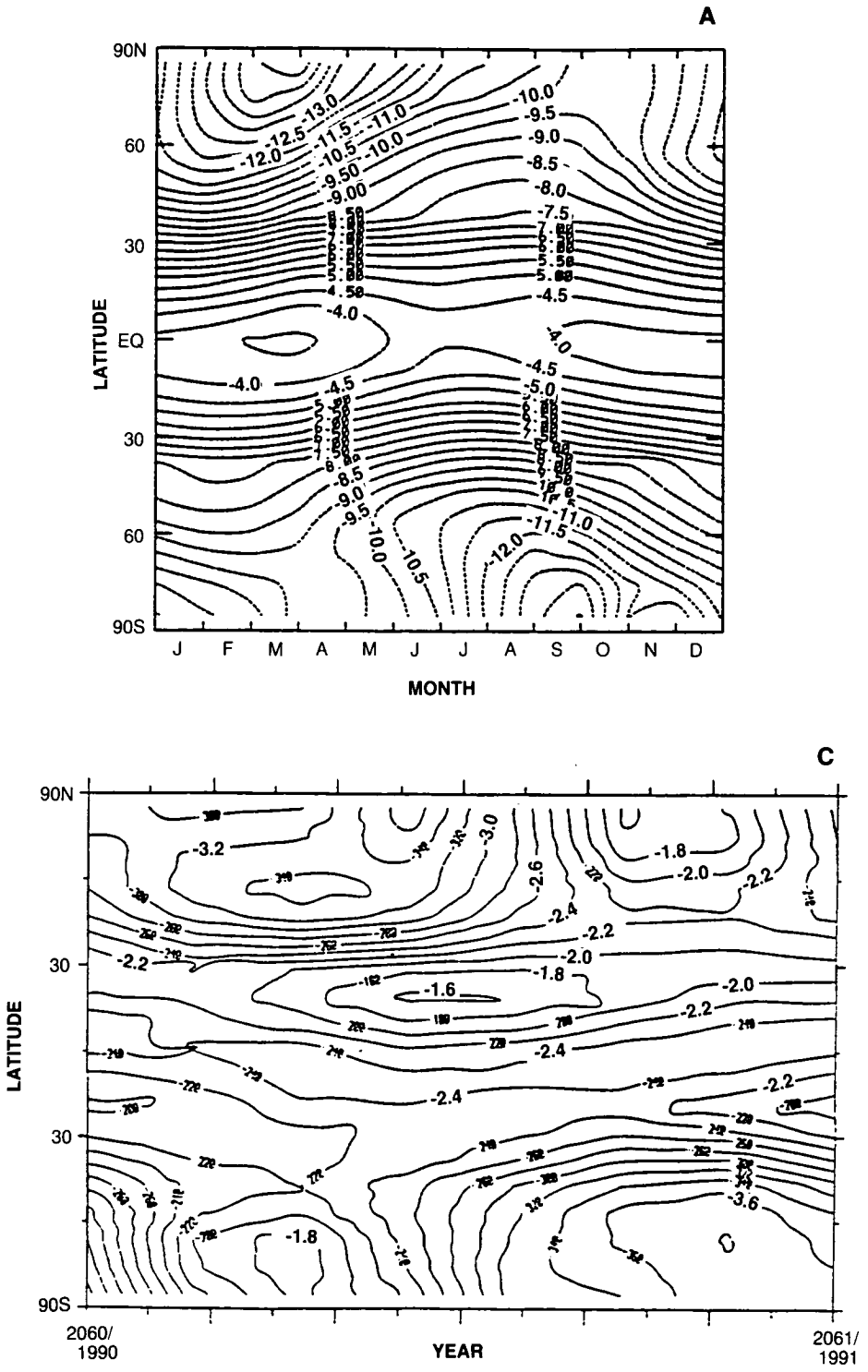

Figure 3.2-7. Dobson map of percent change in column ozone from 1980 to 2060 using scenario A1. (Note the exceptions: Cambridge plots 2060 vs. 1990 beginning with October; the LL plot refers to the LLNL model including temperature feedback; the Oslo model plots 2050 vs. 1985.)

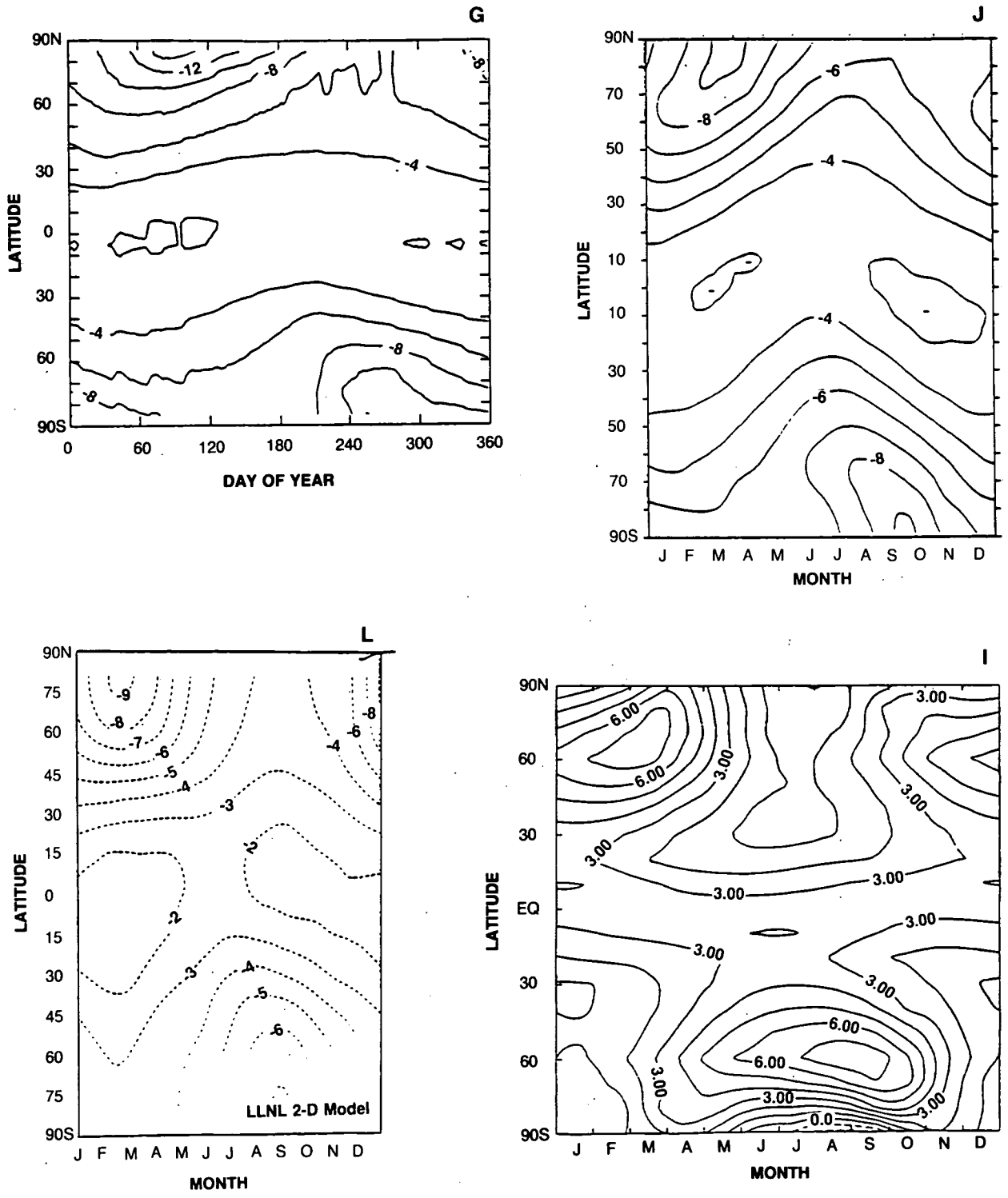

Figure 3.2-7., continued

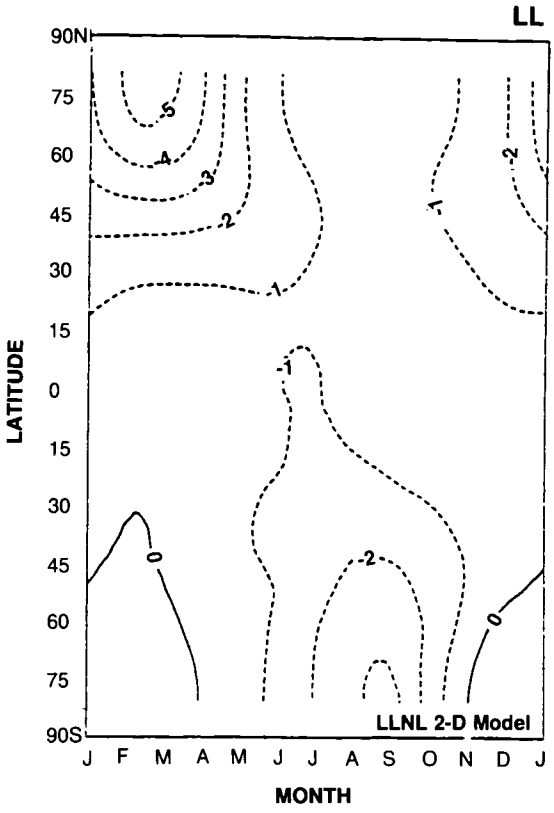

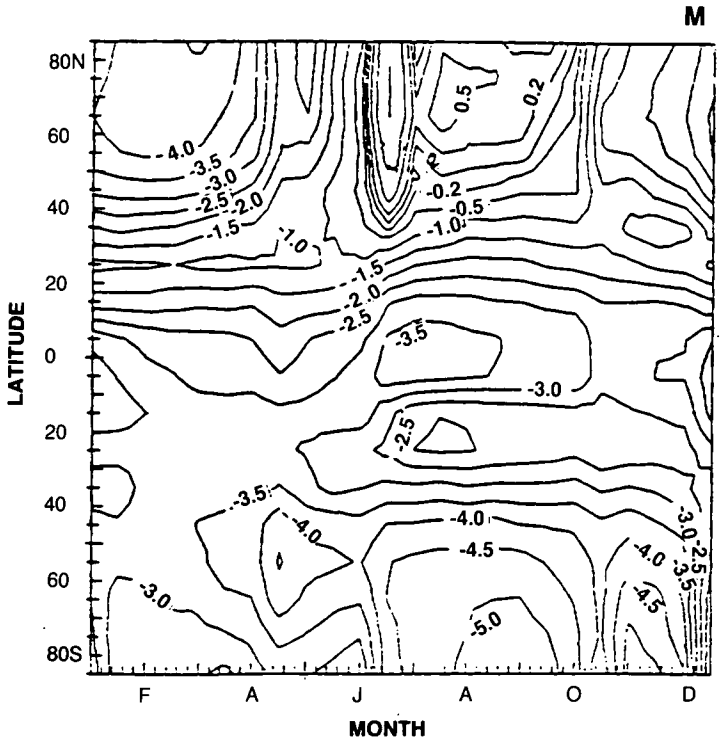

Figure 3.2-7., continued

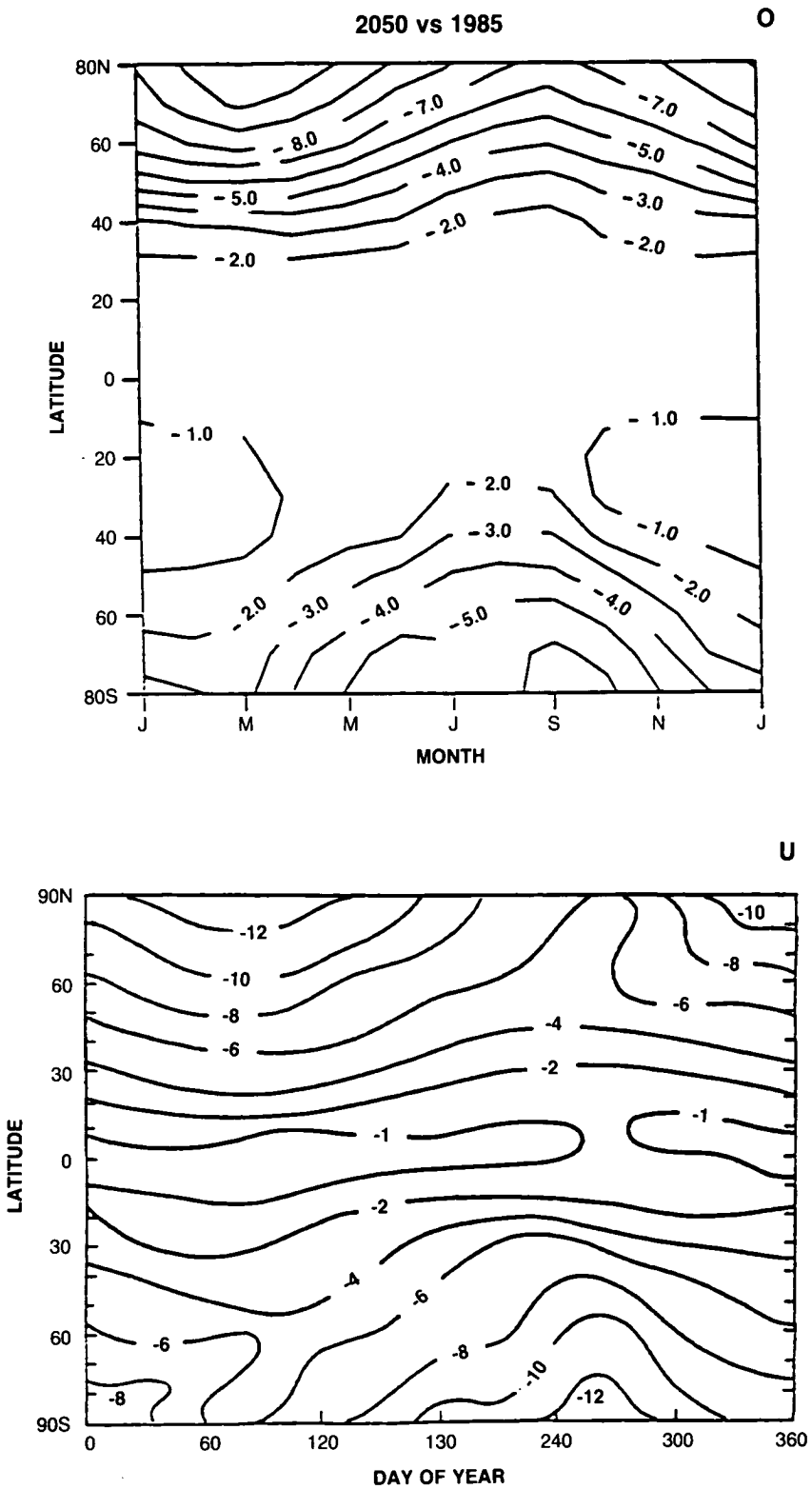

Figure 3.2-7., continued

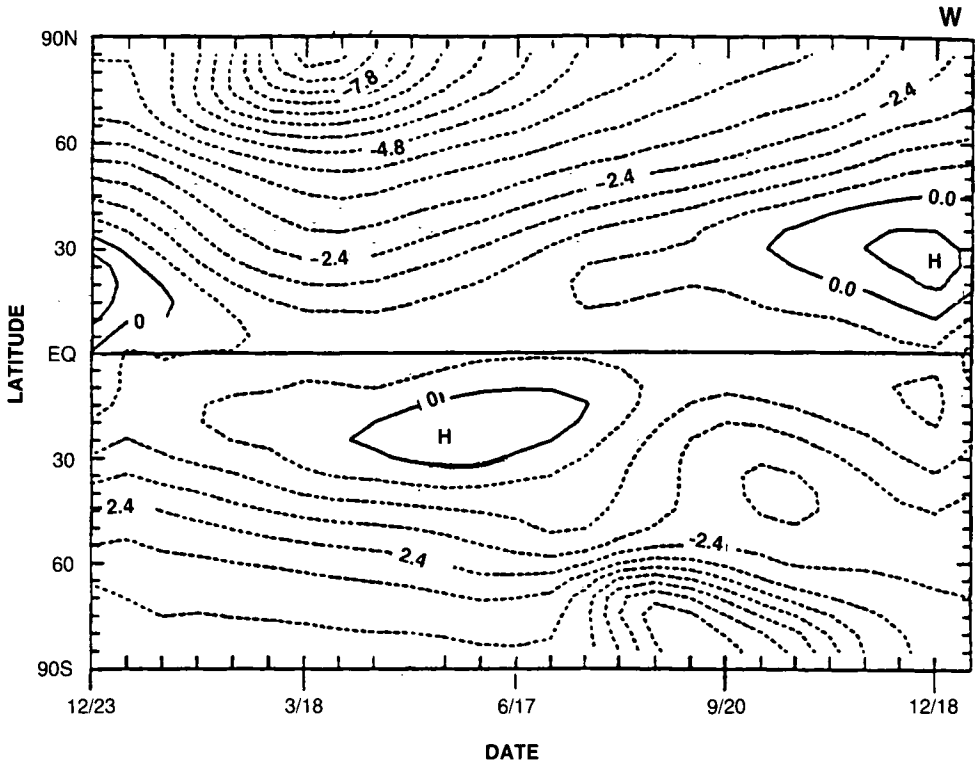

Figure 3.2-7., continued

GSFC2, and NSU models; greater than 7% in the Aquila, JMRI, LLNL, Oslo, and WisCAR models; but only 3–4% in the Cambridge and Mainz models. The LLNL model contributed an additional calculation in which temperature feedbacks were allowed (denoted LL) that resulted in significantly less ozone depletion by 2060, only 4–5% maximum in the northern winter and 2–3% in the southern winter.

One likely cause of this discrepancy among the models is the calculated temperature "feedback" (i.e., decrease in response to O_3 and CO_2 changes) and the photochemical response to it. The temperature of the stratosphere is expected to be lower in the future mainly due to increases in the CO_2 long-wave cooling. The models exhibiting the largest depletions (AER and GSFC2) assume fixed temperatures and circulations; and those with the smallest include temperature feedbacks (generally decreases). This simple explanation does not fit the Oslo and WisCAR models which include temperature feedbacks. The Mainz model is anomalous in predicting significant increases in ozone at mid-latitudes throughout the summer, apparently due to increased production of ozone by methane-related smog chemistry and the inclusion of unprescribed NO_x increases.

The latitude-by-height contours of percent change in the local ozone concentration from January 1980 to January 2060 are shown in Figures 3.2-8 (A,C,G,J,L,LL,M,O,W). The maximum loss in ozone occurs at about 42 km, is greater near the poles, and ranges from 40 to 60%. (The Mainz model is again anomalous, predicting maximum loss in the tropics in addition to high latitude winter). Two models, Cambridge and the LLNL version with temperature feedback (LL), predict similar patterns in ozone depletion with smaller values near the stratopause, 25–40% for Cambridge and 30–35% for LLNL.

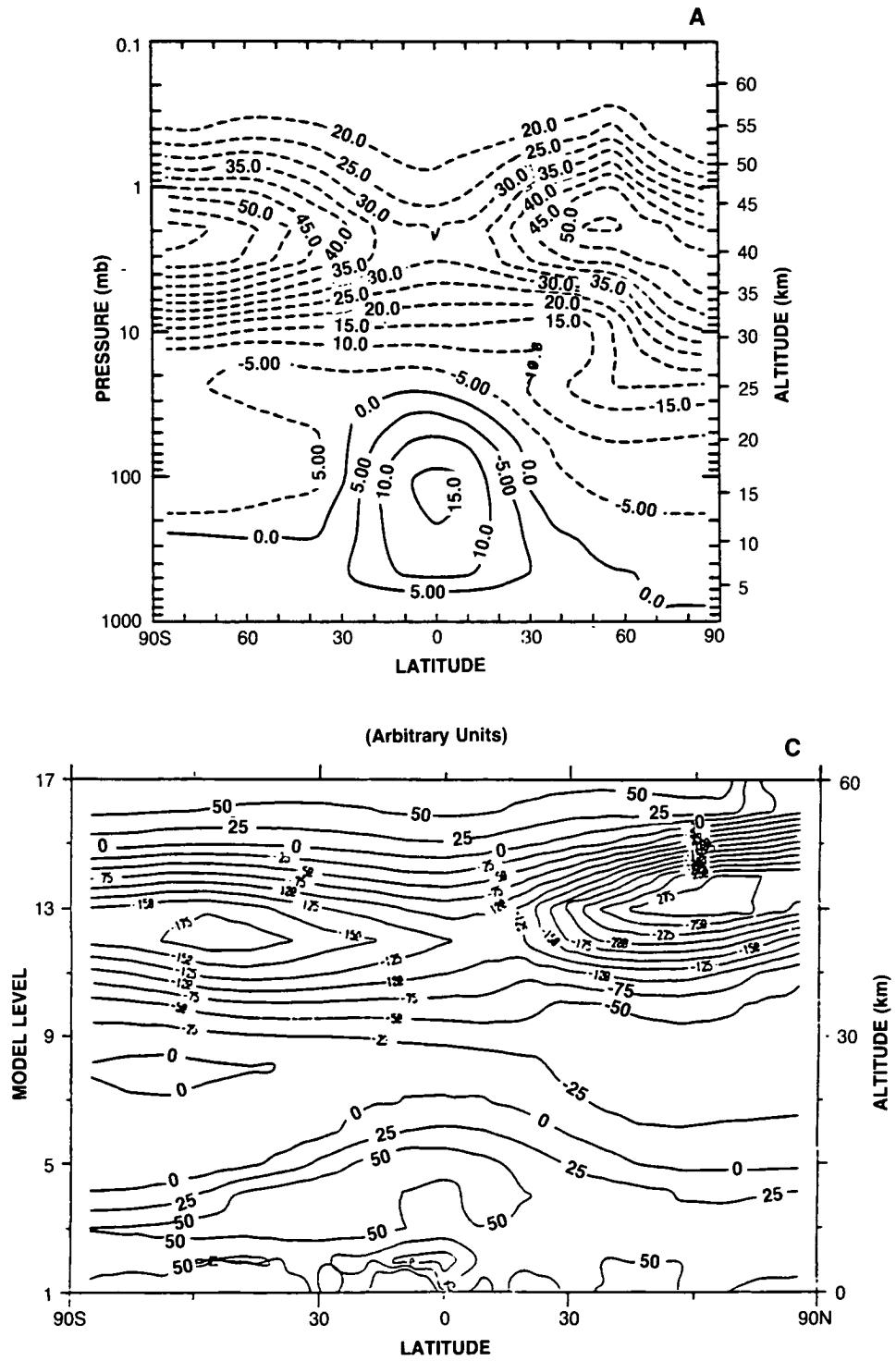

Figure 3.2-8 Latitude-by-altitude (log pressure of height [km]) contour map of the percent change in local ozone concentration from 1980 to 2060 for scenario A1. (The exceptions are noted in 3.2.7.)

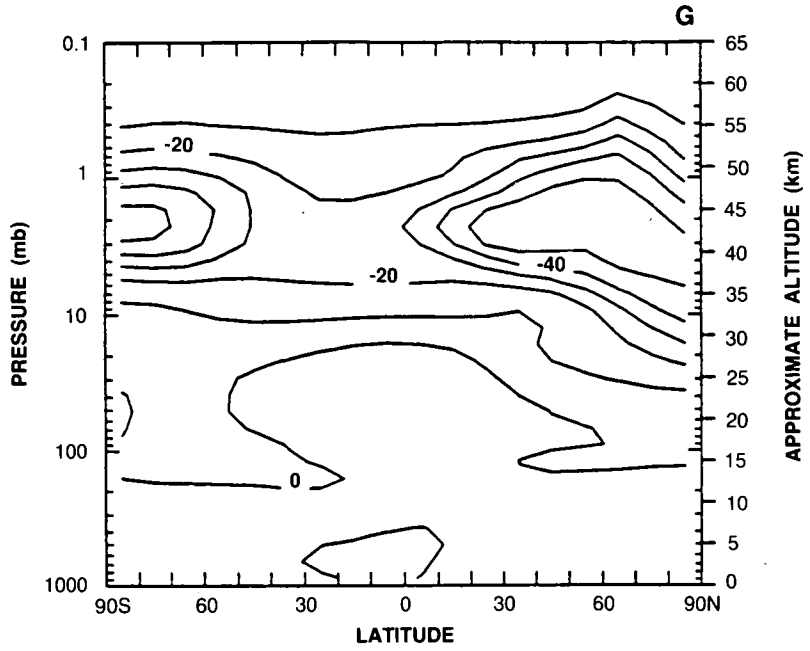

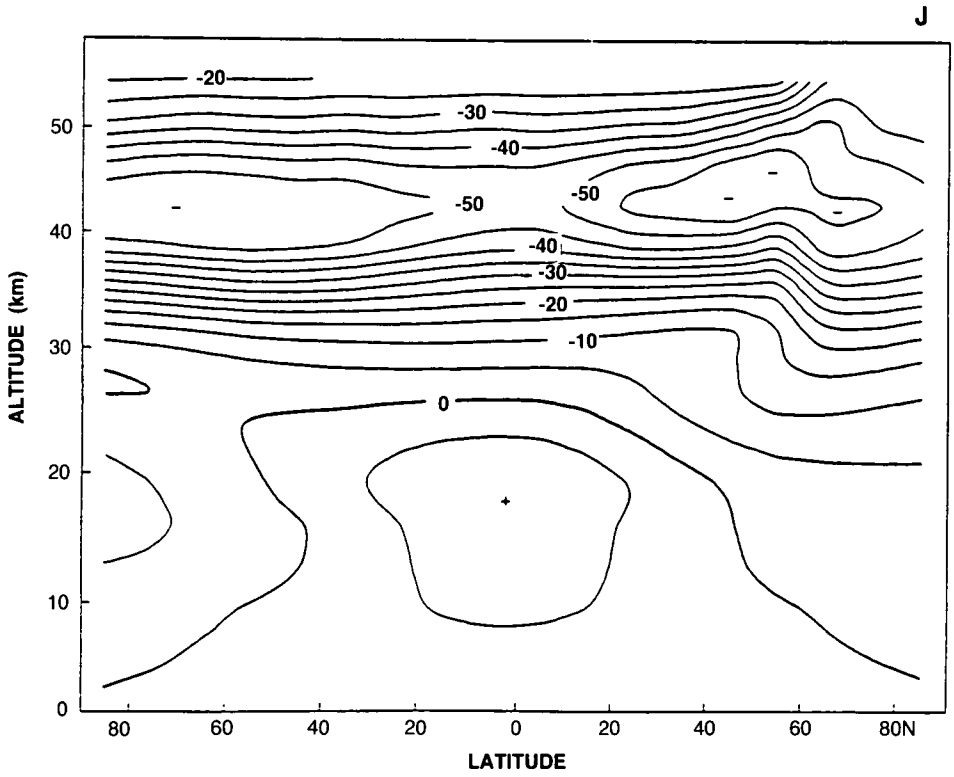

Figure 3.2-8., continued

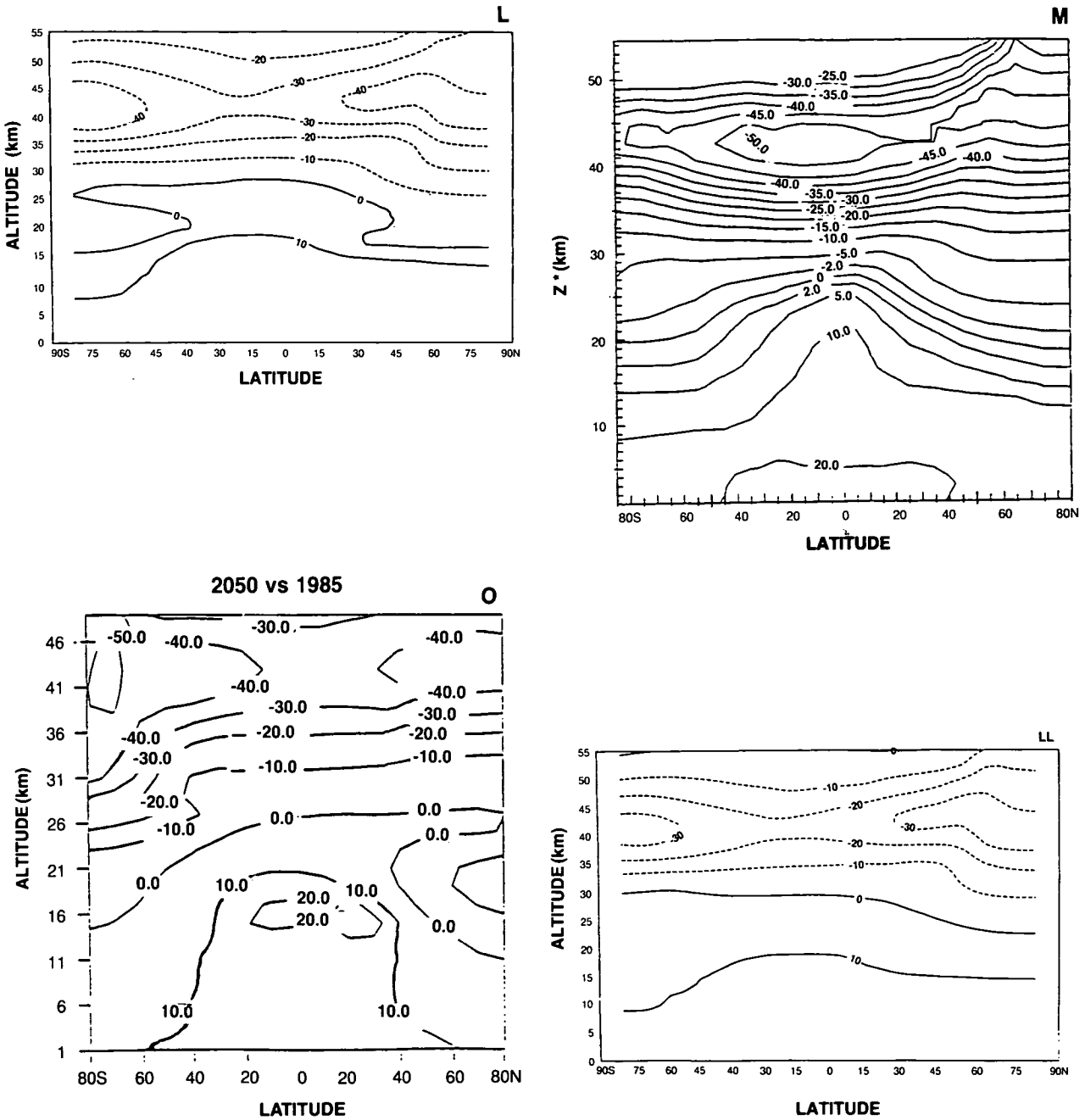

Figure 3.2-8., continued

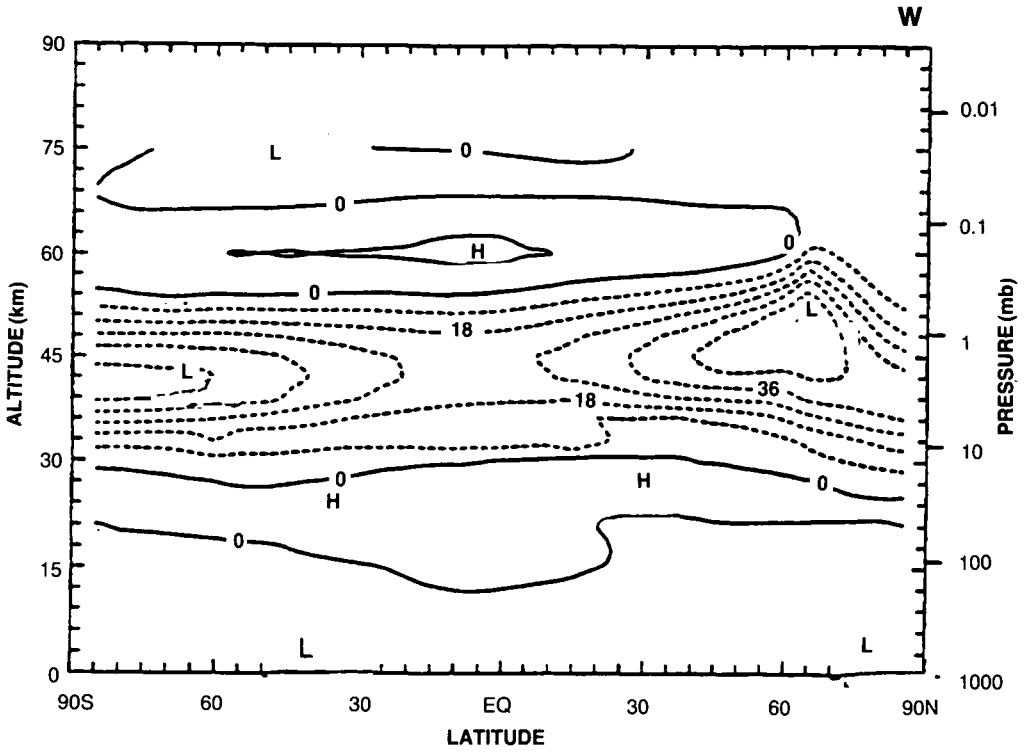

Figure 3.2-8., continued

Overall, the agreement among the models is irregular. All predict some levels of ozone increase in the troposphere and lower stratosphere. The critical difference here is the predicted zero-change contour, which varies considerably from model to model. Much of the calculated change in total column (Figures 3.2-6 and 7) is driven by the small changes in the lower stratosphere. In the upper stratosphere (35–50 km), the predicted ozone depletion is robust among the models if we allow for corrections to values reported from models that do not account for the expected temperature reductions due to decreases in O_3 and increases in CO_2 . In the lower stratosphere (15–25 km) results are more diverse and reflect, among other uncertainties, the difficulty in modeling the temperature change. Note that predictions of perturbations to tropospheric ozone in these calculations are not a robust feature of the models and must be interpreted as having large uncertainty.

Corresponding results for A2 (fixed CH_4) are shown in Figures 3.2-9 through 3.2-11. The continuous time-line of ozone depletion in March (Figure 3.2-9G) shows that when CH_4 does not increase, predicted ozone loss is uniformly greater by about 3% from equator to pole. The Dobson maps of change in column ozone (Figures 3.2-10 [G,O,W]) from the GSFC2, Oslo and WisCAR models show similar results: the seasonal pattern is almost unchanged from A1, but depletions are larger by 3–4% percent for all seasons and latitudes. The change in local ozone concentration (Figures 3.2-11 [G,O,W]) is greater in the region of maximum loss near 42 km by as much as 10%. More importantly, the region of ozone increase occurs at lower altitudes, and much of the lower stratosphere and even troposphere is predicted to experience ozone loss by 2060. Clearly most of the local increases in ozone predicted in A1 are associated with the enhanced methane chemistry in the lower stratosphere and upper troposphere.

The capability to represent the feedback among perturbations in radiatively active trace gases, temperature, and transport is essential if we hope to model the real atmosphere. Ozone reductions should lead to reduced solar heating and consequent changes in the temperature distribution and zonal winds,

hence wave propagation and absorption, and tracer transport. Similarly, "greenhouse" temperature changes may be expected to alter the ozone distribution through photochemical and transport effects. Recently, a few modeling groups have begun to develop the capability to account for these feedbacks. Results for scenario A1 in the AER and WisCAR models are shown in Figures 3.2-12–3.2-15. In both models, increased cooling to space by CO_2 and reduced ultraviolet absorption by O_3 combine to weaken the stratopause markedly (Figure 3.2-12). Due to the temperature dependence of Planck emission to space, cooling is strongest near the summer stratopause. Through the thermal wind relation, this results in weakened summer easterlies near the stratopause (Figure 3.2-13). Similarly, the cold polar winter stratosphere does not cool as much as the tropical stratosphere and leads to slightly reduced westerlies in the polar stratosphere.

The net radiative heating for the 1980 reference atmosphere in December for these two models is shown in Figure 3.2-14. This illustrates how the wave-driven circulation causes departures from radiative equilibrium. The two models agree regarding the dynamically driven descent in the winter hemisphere, which leads to higher temperatures and increased cooling to space, and ascent in the summer hemisphere, which leads to slightly cooler temperatures and net heating. With reduced temperature gradients, weaker zonal winds result in weaker wave driving (Rayleigh drag in the AER model; gravity wave driving in the WisCAR model). This in turn results in a weakened summer to winter interhemispheric flow and reduced summer upwelling and winter downwelling in the upper stratosphere and lower mesosphere, which is reflected in the difference plots for heating rates (Figure 3.2-15). The situation in the lower stratosphere is less clear. Initial results for the WisCAR model, however, suggest that with strengthened westerlies over the south polar lower stratosphere (Figure 3.2-13), Rossby waves would more readily propagate into the region, leading to enhanced upward motion in the summer polar stratosphere, hence stronger net radiative heating, as seen in Figure 3.2-15. Since changes in tropospheric temperature and wave forcing are not included in current 2-D models, these results must be interpreted with caution.

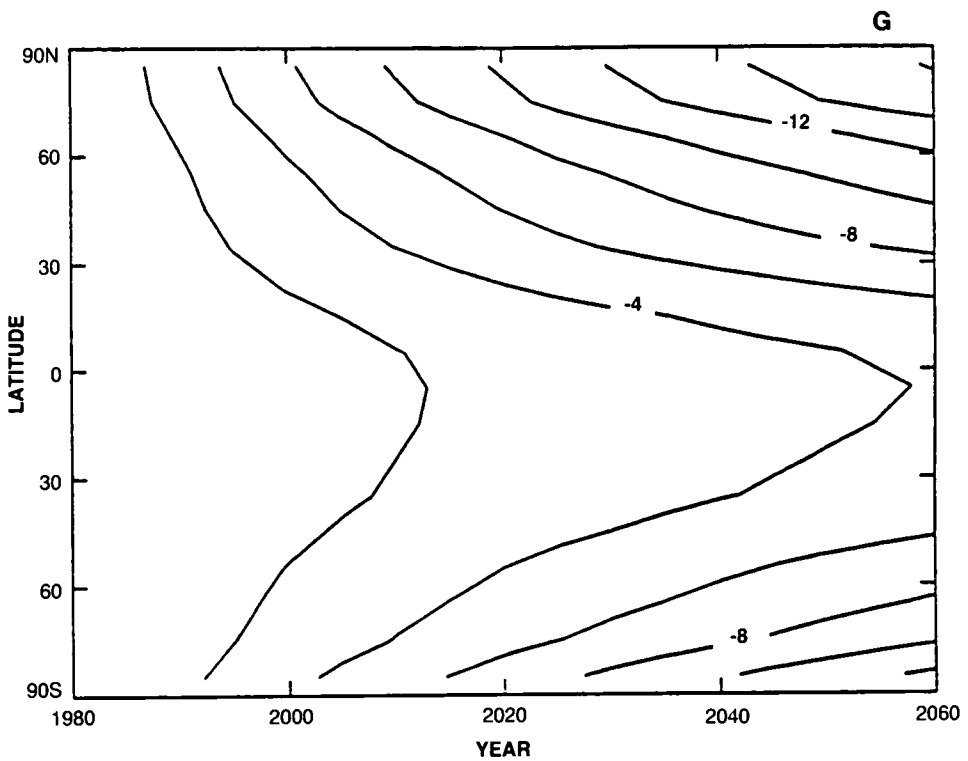

Figure 3.2-9. Time-line vs. latitude of the percent change in column ozone during March from 1980 to 2060 for scenario A2.

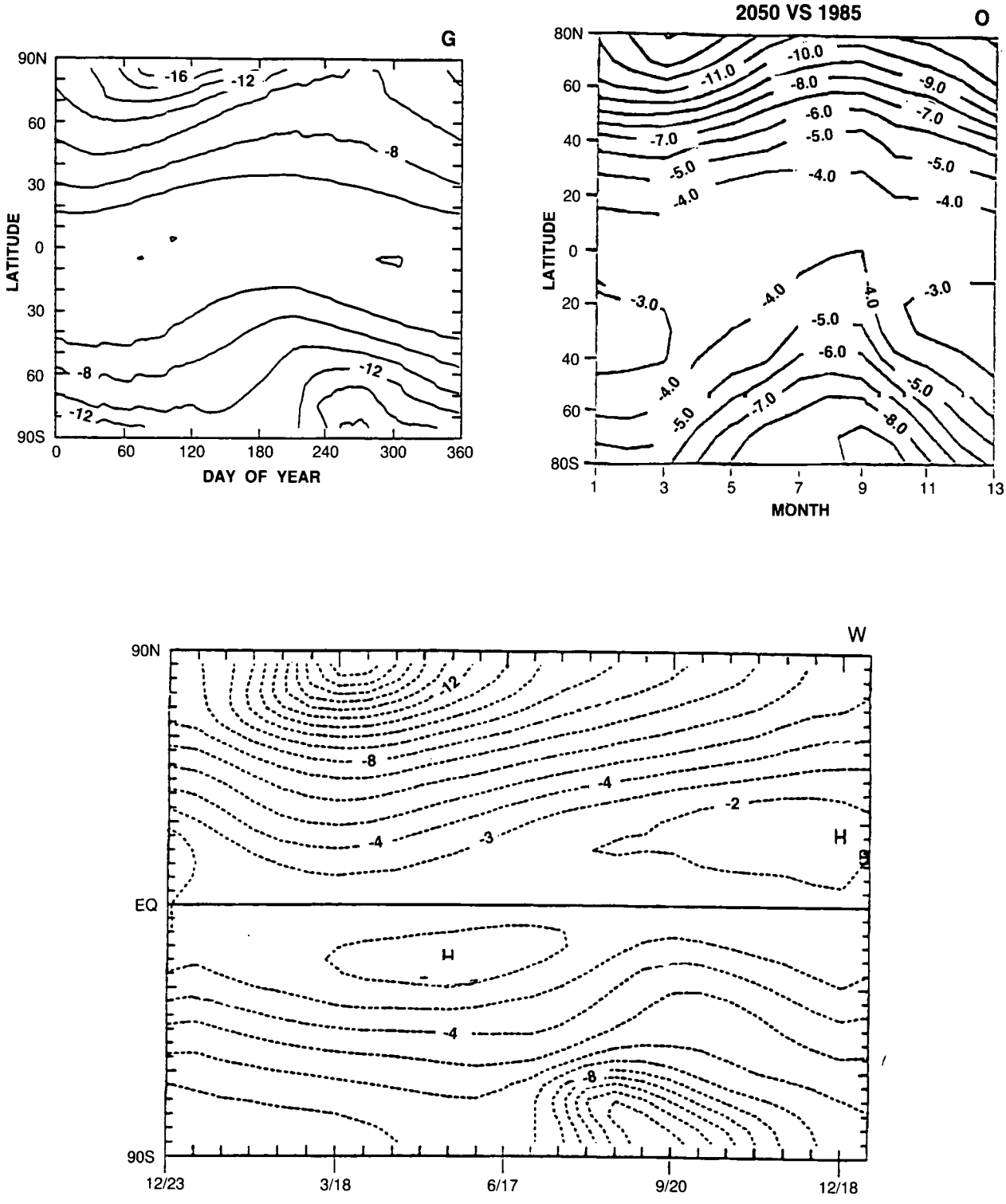

Figure 3.2-10. Dobson map of percent change in column ozone from 1980 to 2060 using scenario A2.

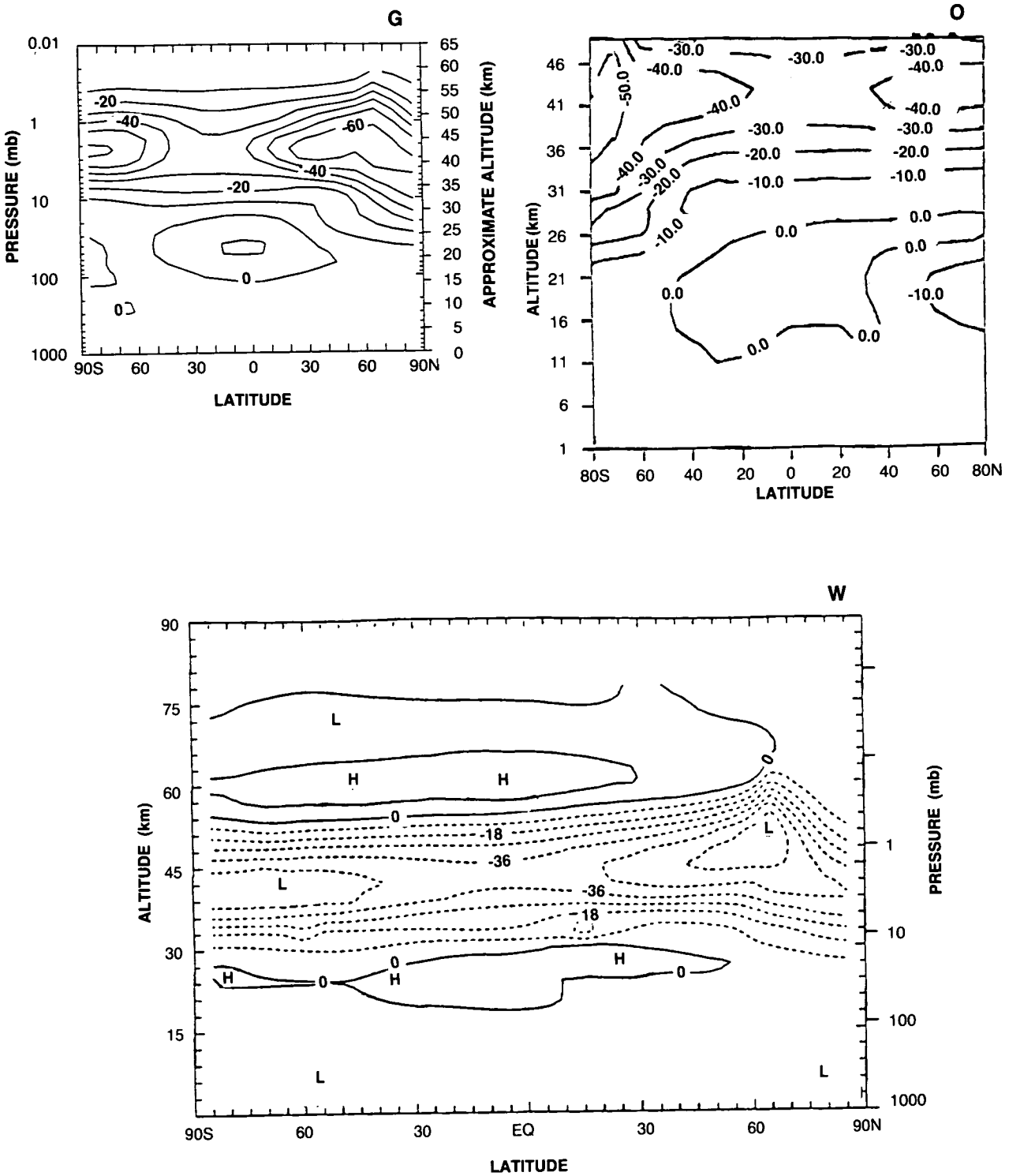

Figure 3.2-11. Latitude-by-altitude map of the percent change in local ozone concentration from 1980 to 2060 for scenario A2.

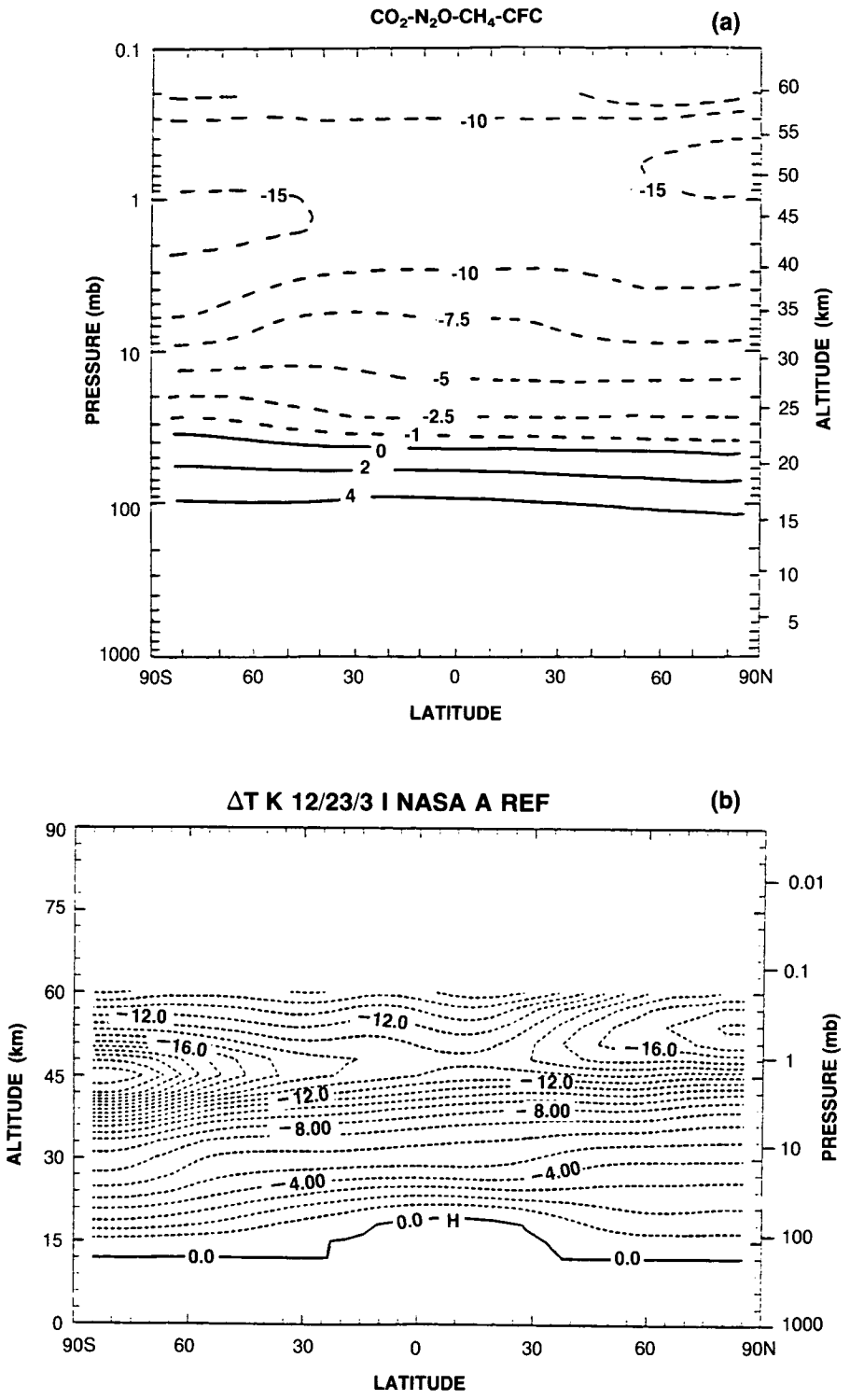

Figure 3.2-12. Temperature change (K) for December (scenario A1: 1980-2060) from the (a) AER and (b) WisCAR models.

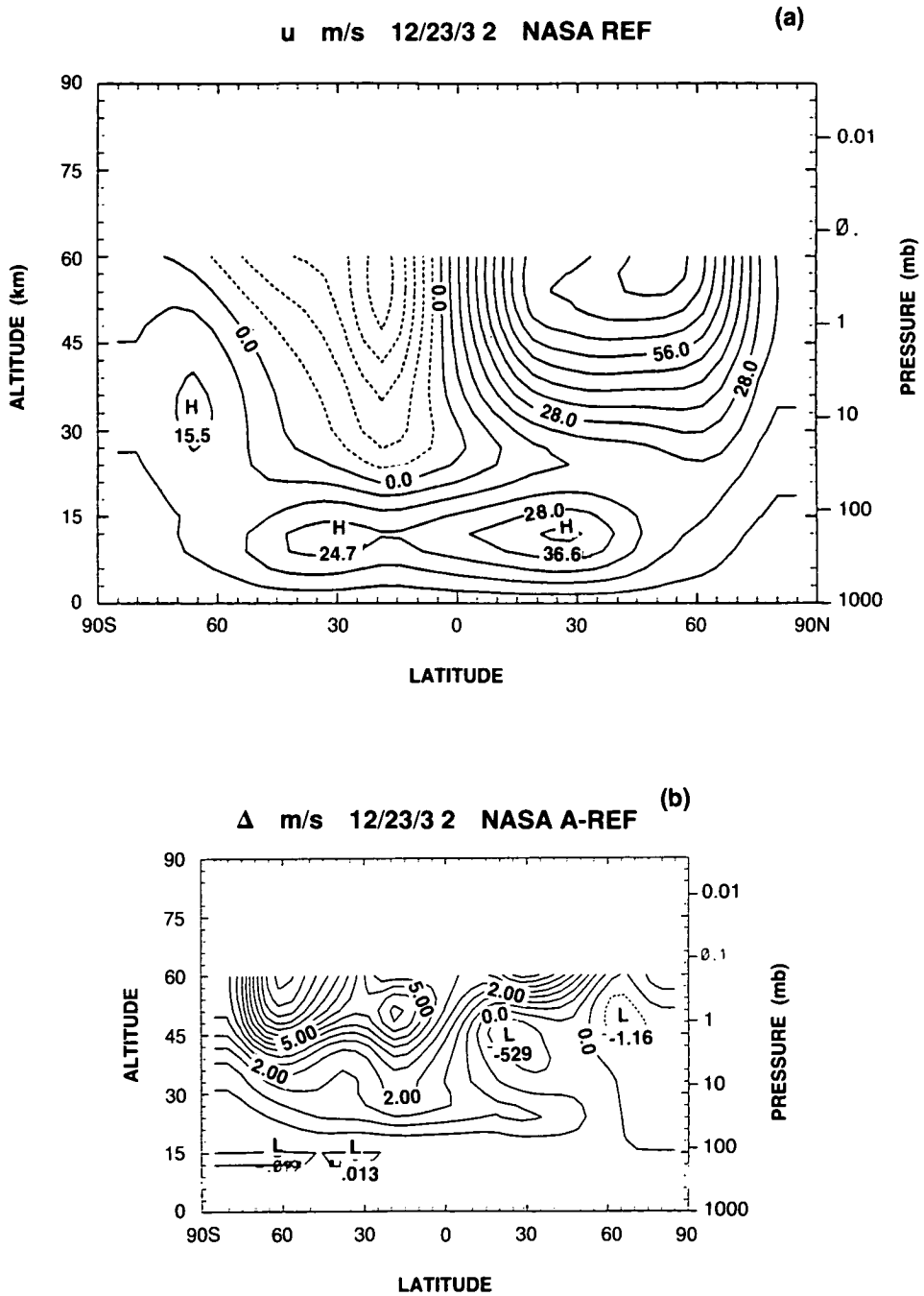

Figure 3.2-13 Zonal wind (a) and zonal wind change from December 1980 to December 2060 (b) for the WisCAR model (scenario A1). Contour intervals are 7 and 0.7 m/s, respectively.

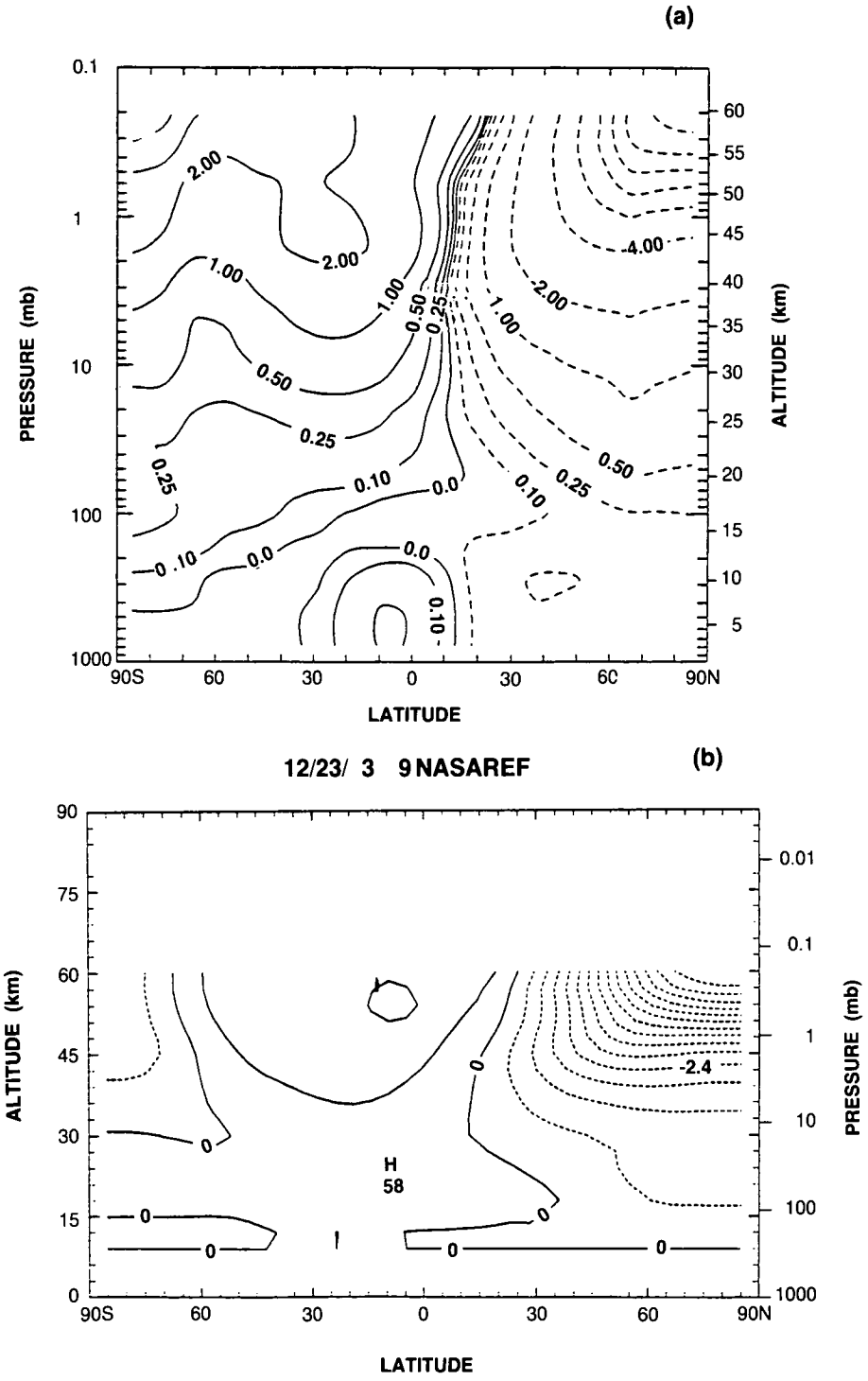

Figure 3.2-14. Net radiative heating (K/day) for December 1980 in the (a) AER and (b) WisCAR models.

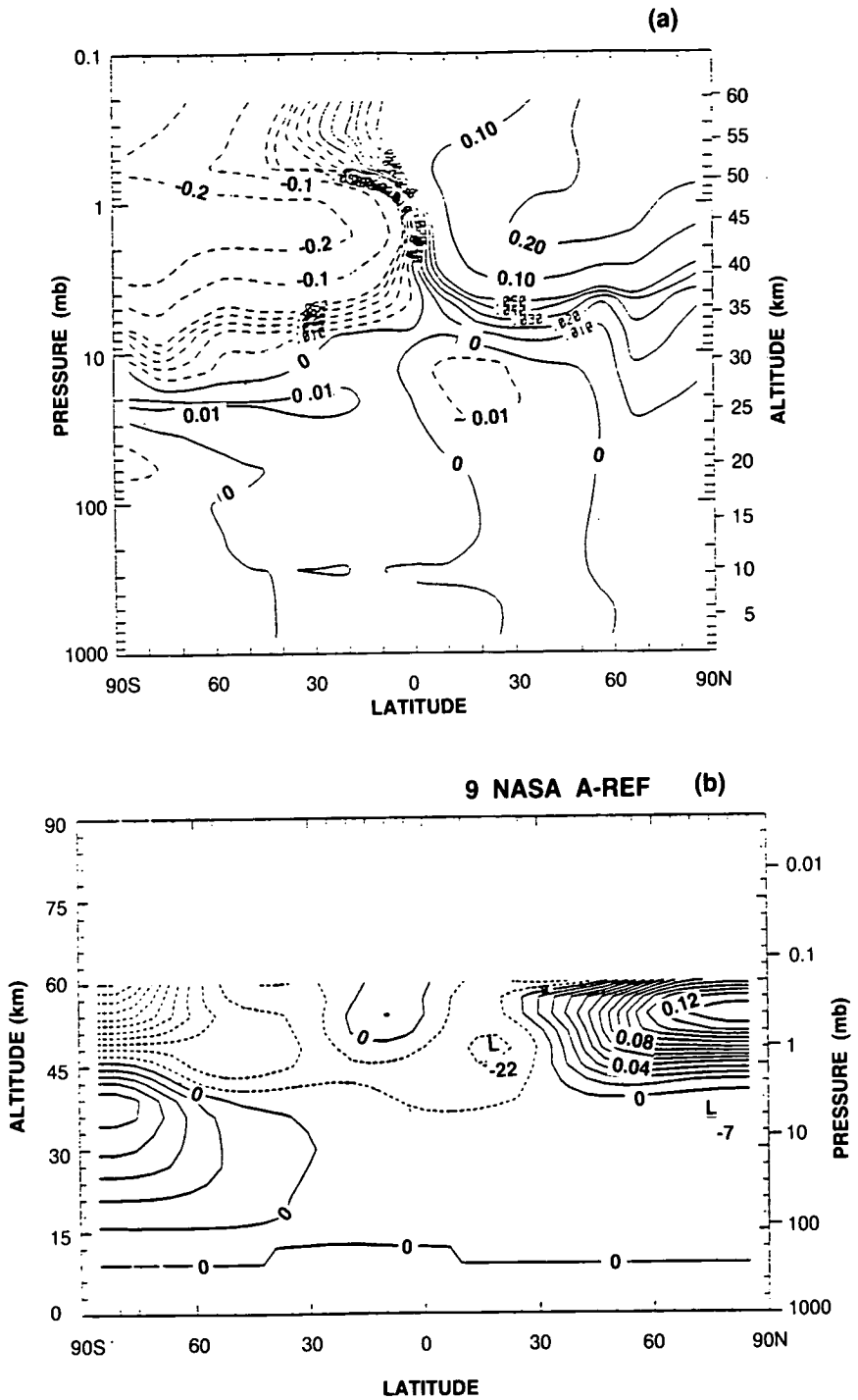

Figure 3.2-15. Change in net radiative heating (K/day) from December 1980 to December 2060 (scenario A1) in the (a) AER and (b) WisCAR models.

In summary, the chlorine loading of the atmosphere in the reference scenario (A1) increases from 3.0 ppbv in 1985 to 4.5 ppbv in the year 2000, to 7.1 in the year 2030, and to 9.2 in the year 2060. The bromine loading increases from 13 pptv in 1985 (10 pptv CH_3Br constant) to 31 pptv in the year 2060. For models that did not contain the carbon dioxide effect and other temperature feedbacks, reductions in column ozone from 1980 to 2060 ranged from 1% to 4% in the tropics and from 8% to 12% at high latitudes in late winter. For models that included the carbon dioxide effect, the corresponding ozone reductions were less: 0% to 1.5% in the tropics and 4% to 8% in high latitudes in late winter. Ozone reductions at 40 km were about 35–50% in models with no temperature feedback, and about 25–40% in models with temperature feedback, resulting in temperature decreases of 10–20 K. No heterogeneous chemistry was included in these models. When methane increases are suspended in 1985, ozone column reductions are larger in all latitudes and seasons by about 3%. Methane increases reduce the efficiency of the chlorine catalytic cycle and further contribute to the direct production of ozone by "smog chemistry" in the lower stratosphere and troposphere. Many of the differences in the model results occur in the lower stratosphere where it is more difficult to predict the impacts of radiative and chemical forcing.

3.2.2.4 Scenario B: 1980–2060

The scenario B1 corresponds to an idealized simulation of the Montreal Protocol in which production/emissions are cut by 50%. Growth of atmospheric halogens is reduced relative to scenarios A1 and A2: 7 ppb of chlorine and 22 ppt of bromine by 2060. The time-line of column ozone depletion from March 1980 through March 2060 is shown in Figures 3.2-16(A,G,J). Predictions from the AER, GSFC2, and JMRI models are similar, but note that these three models are usually in agreement and that all use fixed temperatures and circulations. The impact of cutting CFC production by 50% is to reduce the ozone depletion by March 2060 at mid-latitudes, relative to scenario A1, by about 2% from approximately 8% to 6%. The Dobson maps of column ozone change from 1980 to 2060, Figures 3.2-17(A,G,J), show similar results: 1–3% in the tropics and 5–8% at high latitudes in late winter. The changes in local ozone concentration over this period (Figures 3.2-18 [A,G,J,N]) are similar to those from A1, with reduced ozone loss in the upper stratosphere (25–40% depletion at 40 km) and a similar enhancement in the lower stratosphere and troposphere that is associated with the increase in methane. The changes in local temperature from the NOCAR model, shown in Figure 3.2-18NT, are largest in the 40–50 km region where ozone loss is greatest and reach a maximum of −13 K over the summer pole.

3.2.2.5 Scenario C: 1980–2060

The scenario C1 (85% cut in CFC production/emissions) further reduces halogen concentrations in 2060 (5.8 ppb of chlorine and 16 ppt of bromine). Results are available only from the GSFC2 model and include the time-line of column ozone depletion from March 1980 through March 2060 (Figure 3.2-19G), the Dobson maps of change in column ozone from 1980 to 2060 (Figure 3.2-20G), and the changes in local January ozone concentrations over this period (Figure 3.2-21G). The impact of further cuts in CFC emissions is seen clearly in the upper stratosphere, and reductions in column ozone are approximately 50% of those calculated in the reference scenario with column ozone losses still as large as 6% at high latitudes in spring.

3.2.2.6 Scenario D: 1980–2060

The scenarios D1, D2, and D3 explore a sequence of reduced chlorine loading to the stratosphere (see Figure 3.2-2). In D2 and D3 the chlorine levels peak and begin to fall by 2030 and 2000, respectively. Scenario D4 reexamines the minimum halogen scenario D3 without the ameliorating effects of methane increases.

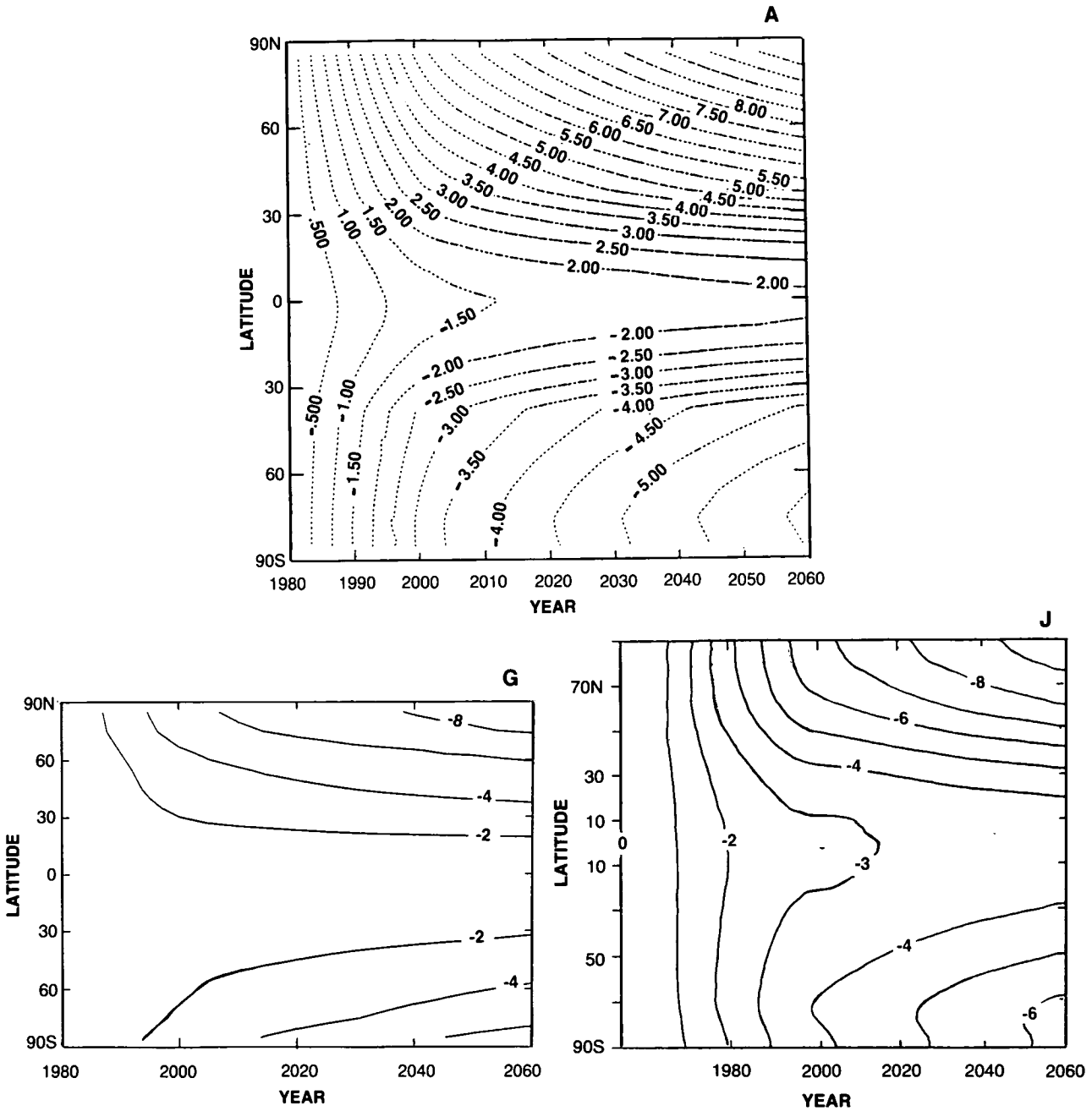

Figure 3.2-16. Time-line vs. latitude of the percent change in column ozone during March from 1980 to 2060 for scenario B1.

The time-line of depletion of column ozone for D1 shown in Figures 3.2-22(G,J,L) displays the familiar latitudinal pattern of greatest losses at high northern latitudes in March. The major difference between this and previous scenarios is that the ozone depletion now reverses at northern mid-latitudes and tends to decline after the year 2000 (although depletion at high southern latitudes continues to rise). The Dobson maps, shown in Figures 3.2-23(G,J,L,U,W), predict the same pattern of ozone depletion as in A1, but

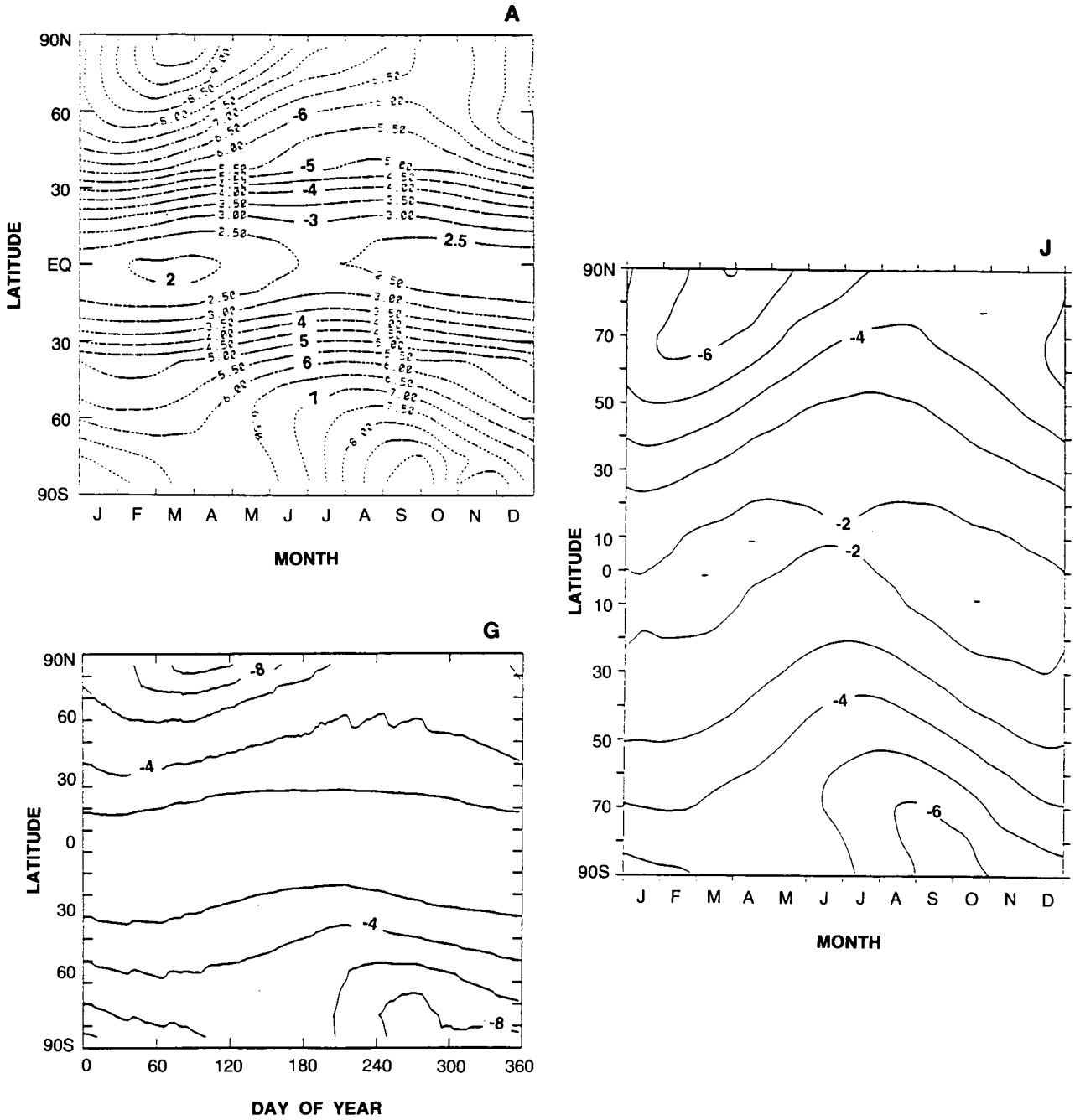

Figure 3.2-17. Dobson map of percent change in column ozone from 1980 to 2060 using scenario B1.

about a factor of 2 smaller at all latitudes. The notable exception being the WisCAR model, which predicts ozone increases of 1–3% everywhere. Local ozone changes (Figures 3.2-24 [G,J,L,W]) in the GSFC2, JMRI, and LLNL models are similar to those predicted for A1, again about a factor of 2 smaller in the upper stratosphere. The WisCAR model predicts ozone loss only in very restricted regions poleward of 30 degrees between 1 and 10 mb. These differences in model predictions for D1 are substantial, associated most likely with model-predicted changes in temperature and circulation, and should be resolved.

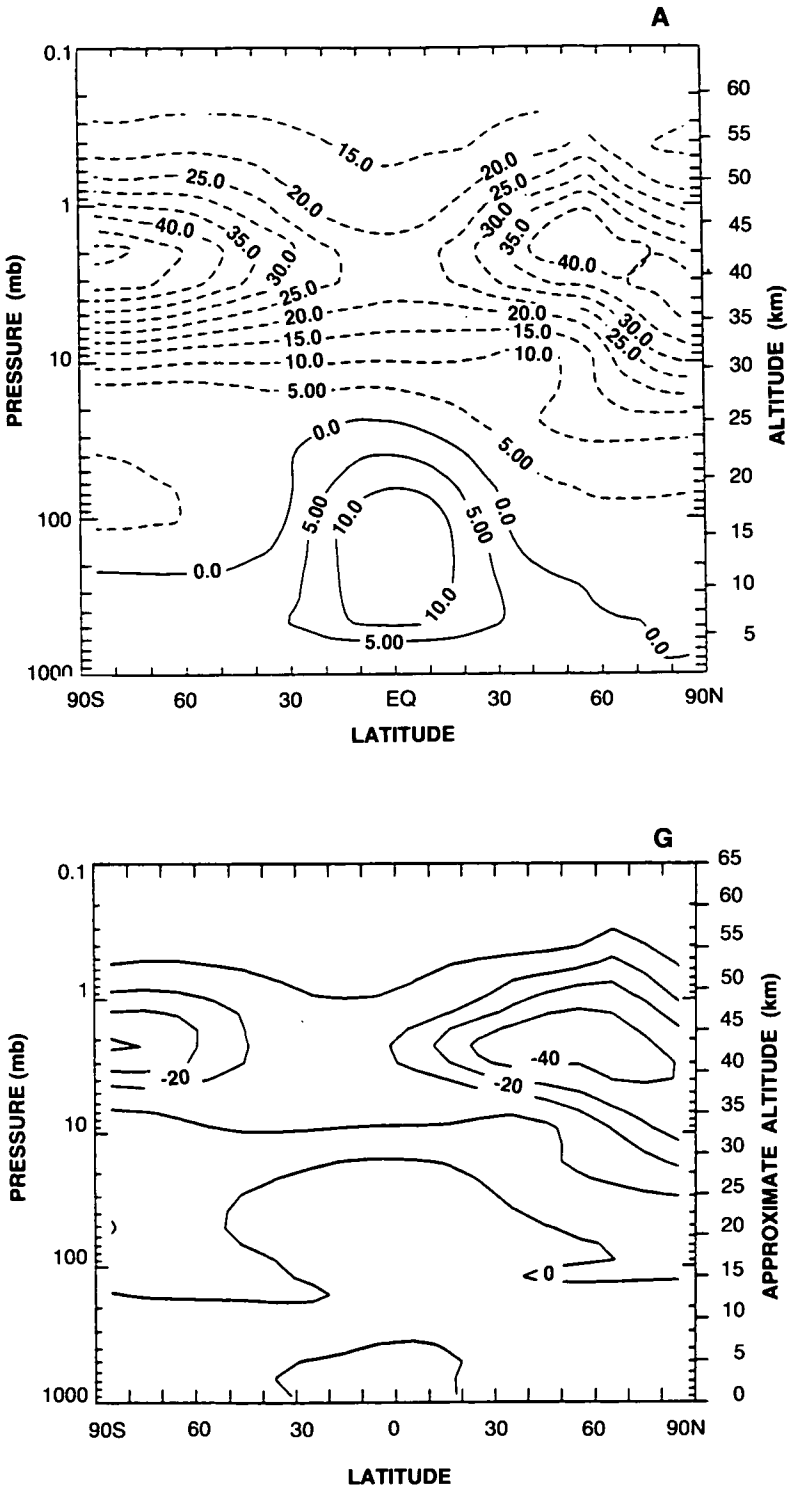

Figure 3.2-18. Latitude-by-altitude map of the percent change in local ozone concentration from 1980 to 2060 for scenario B1.

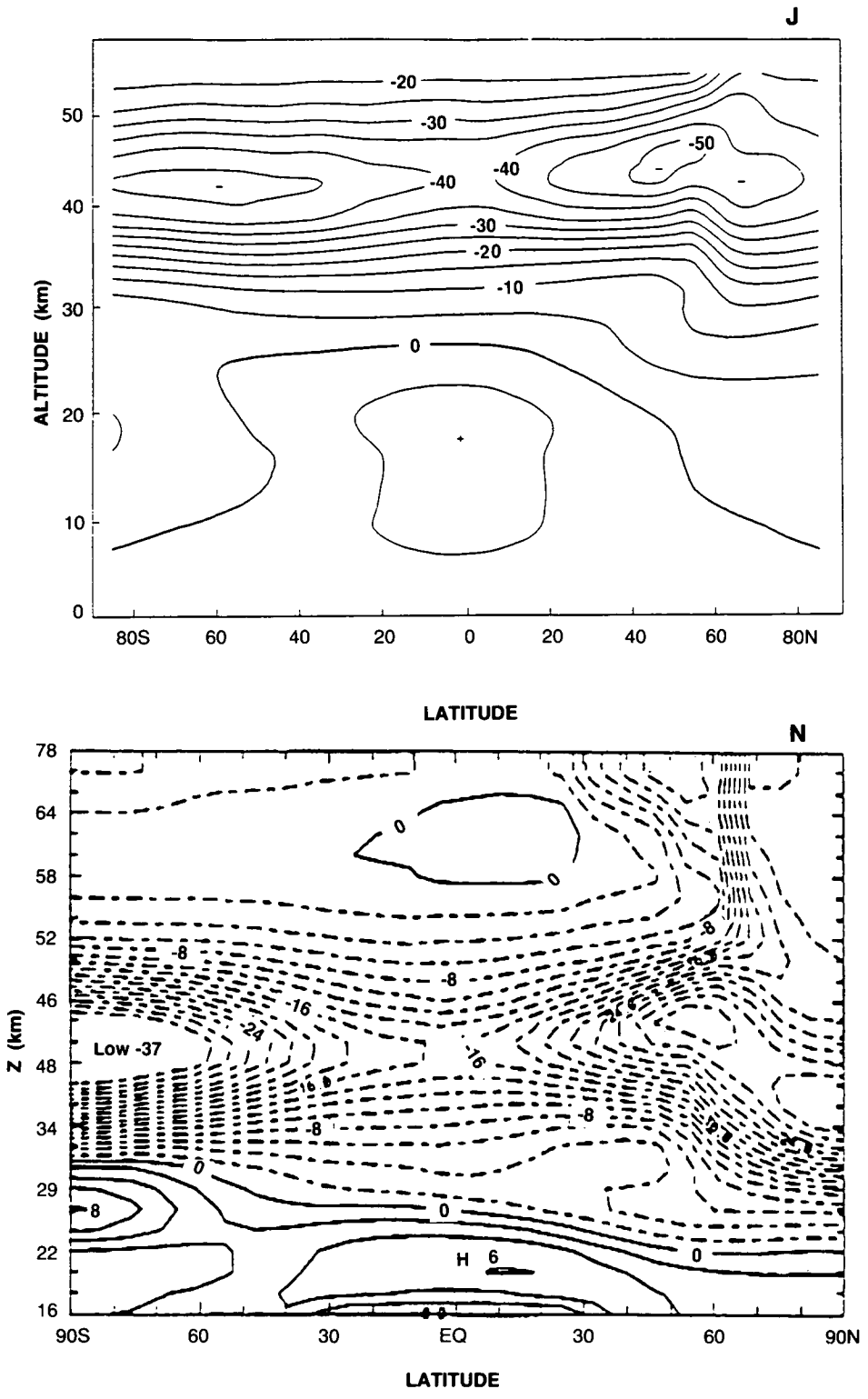

Figure 3.2-18., continued

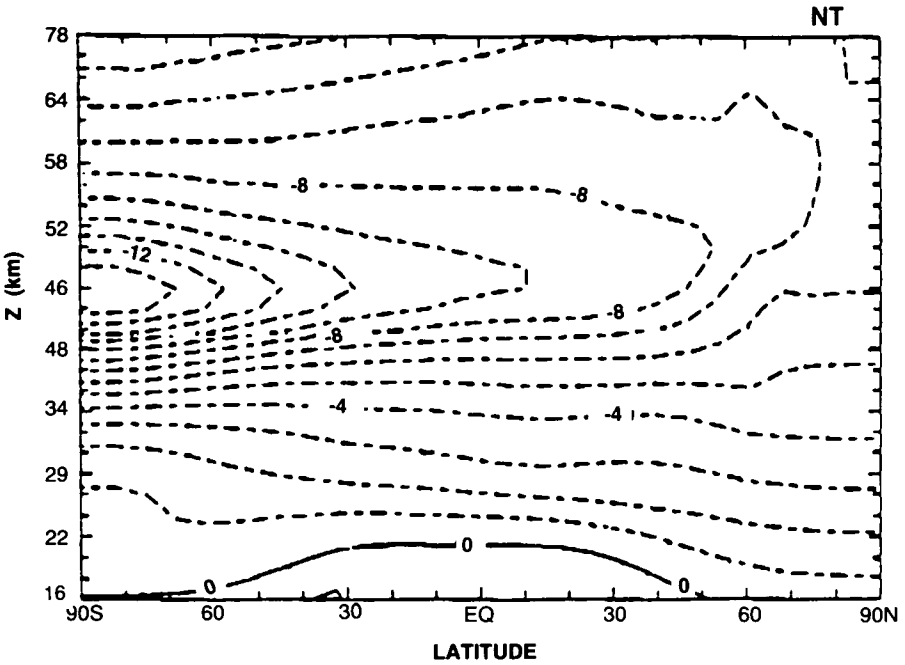

Figure 3.2-18., continued

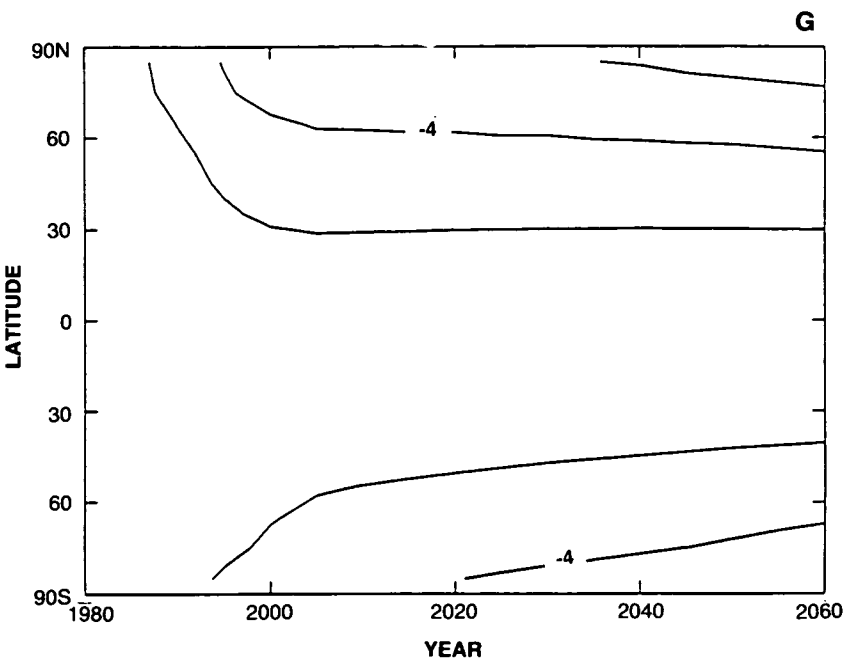

Figure 3.2-19. Time-line vs. latitude of percent change in column ozone during March from 1980 to 2060 for scenario C1.

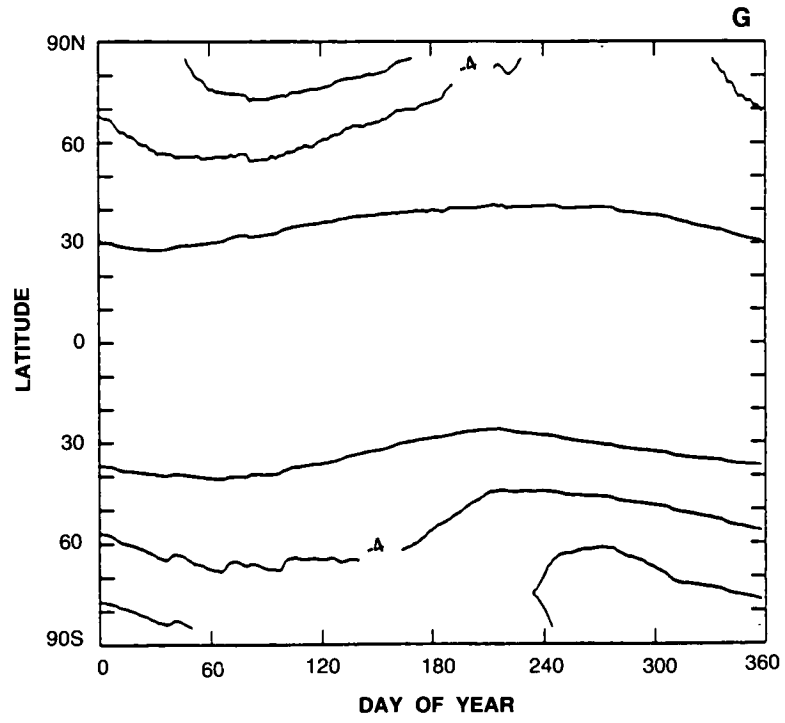

Figure 3.2-20. Dobson map of percent change in column ozone from 1980 to 2060 using scenario C1.

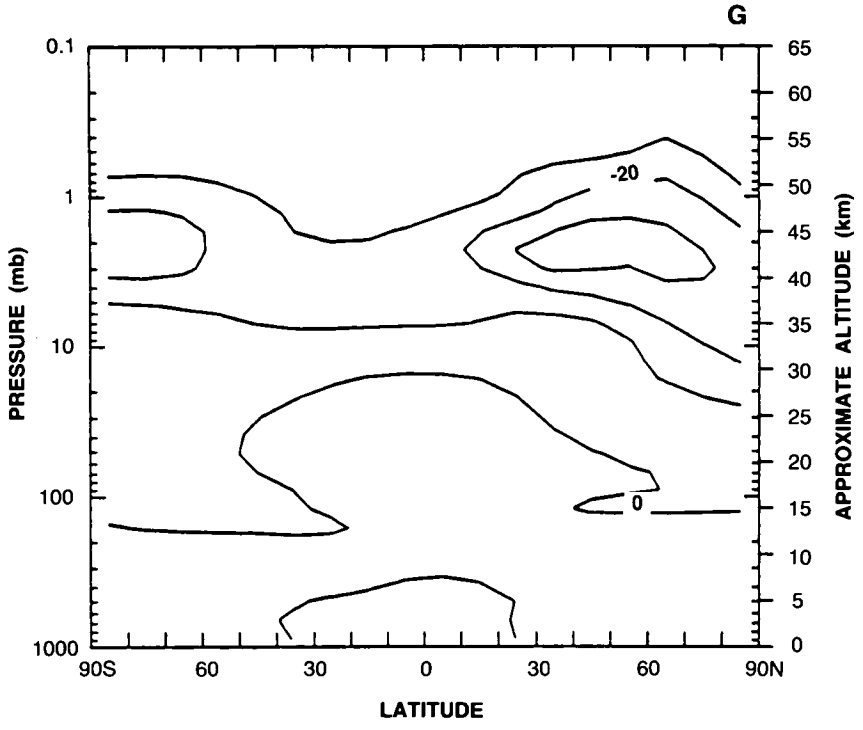

Figure 3.2-21. Latitude-by-altitude map of the percent change in local concentration from 1980 to 2060 for scenario C1.

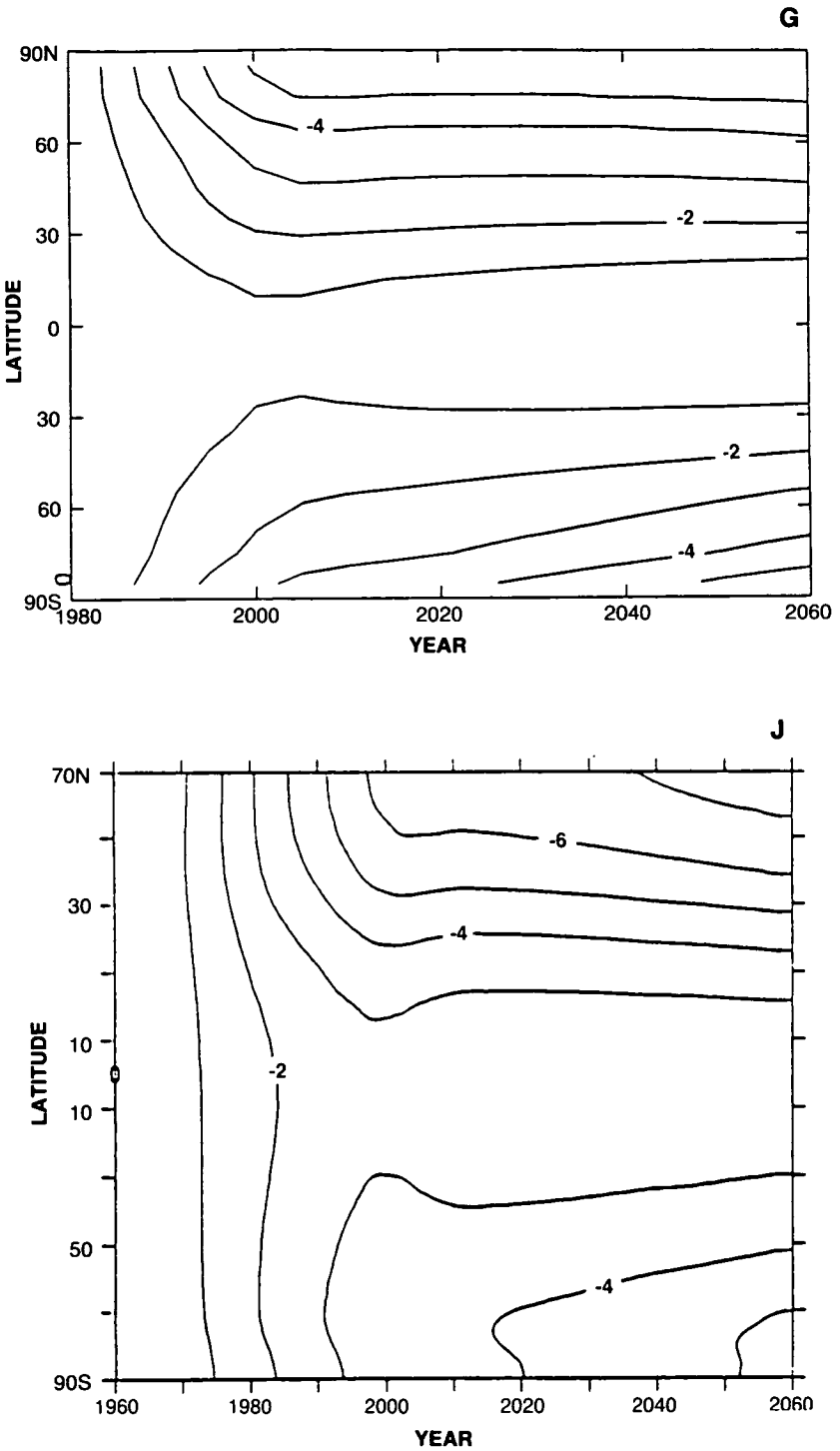

Figure 3.2-22. Time-line vs. latitude of the percent change in column ozone during March from 1980 to 2060 for scenario D1.

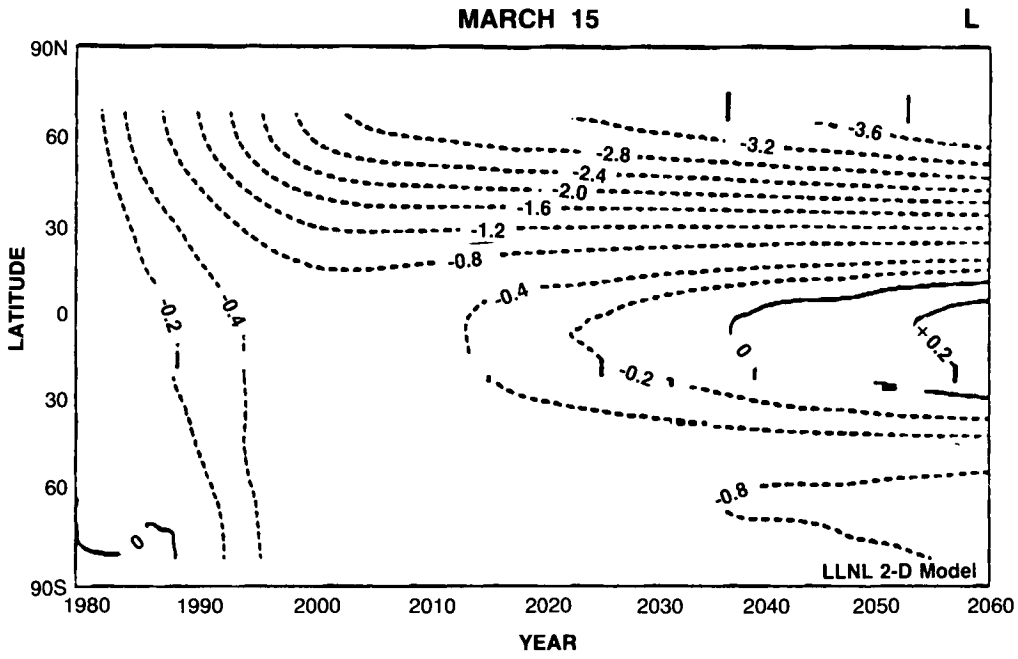

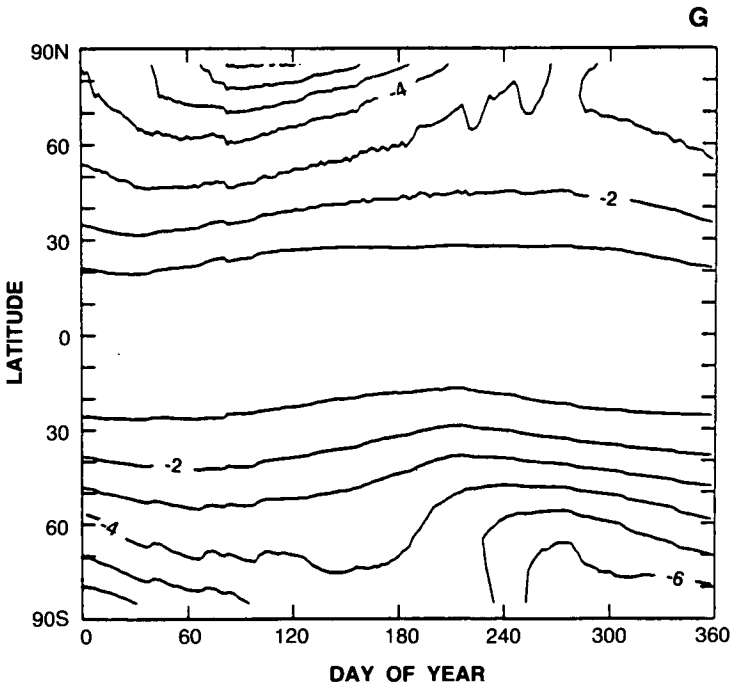

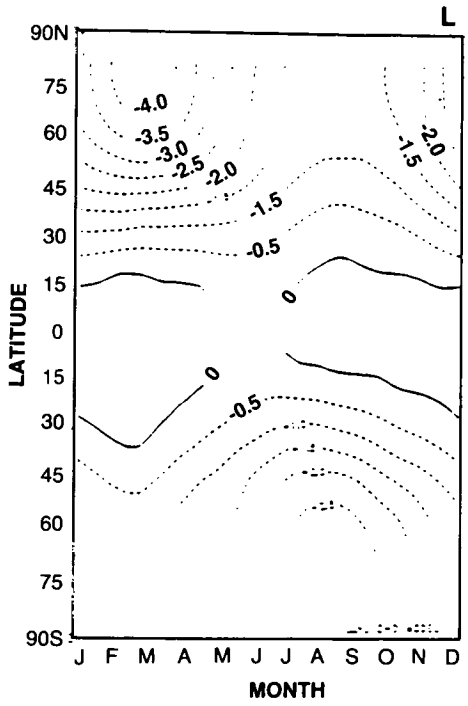

Figure 3.2-23 Dobson map of percent change in column ozone from 1980 to 2060 using scenario D1.

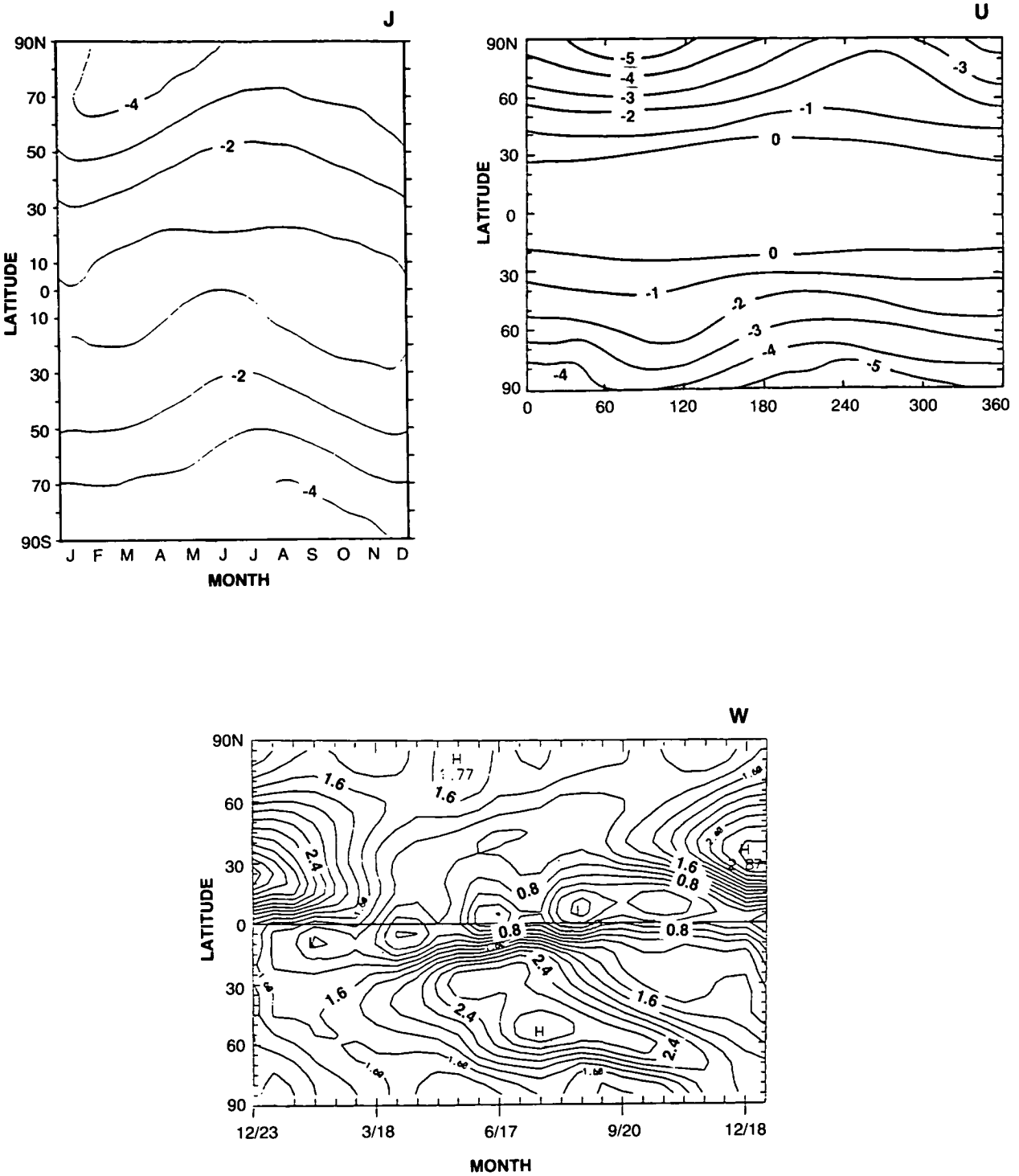

Figure 3.2-23., continued

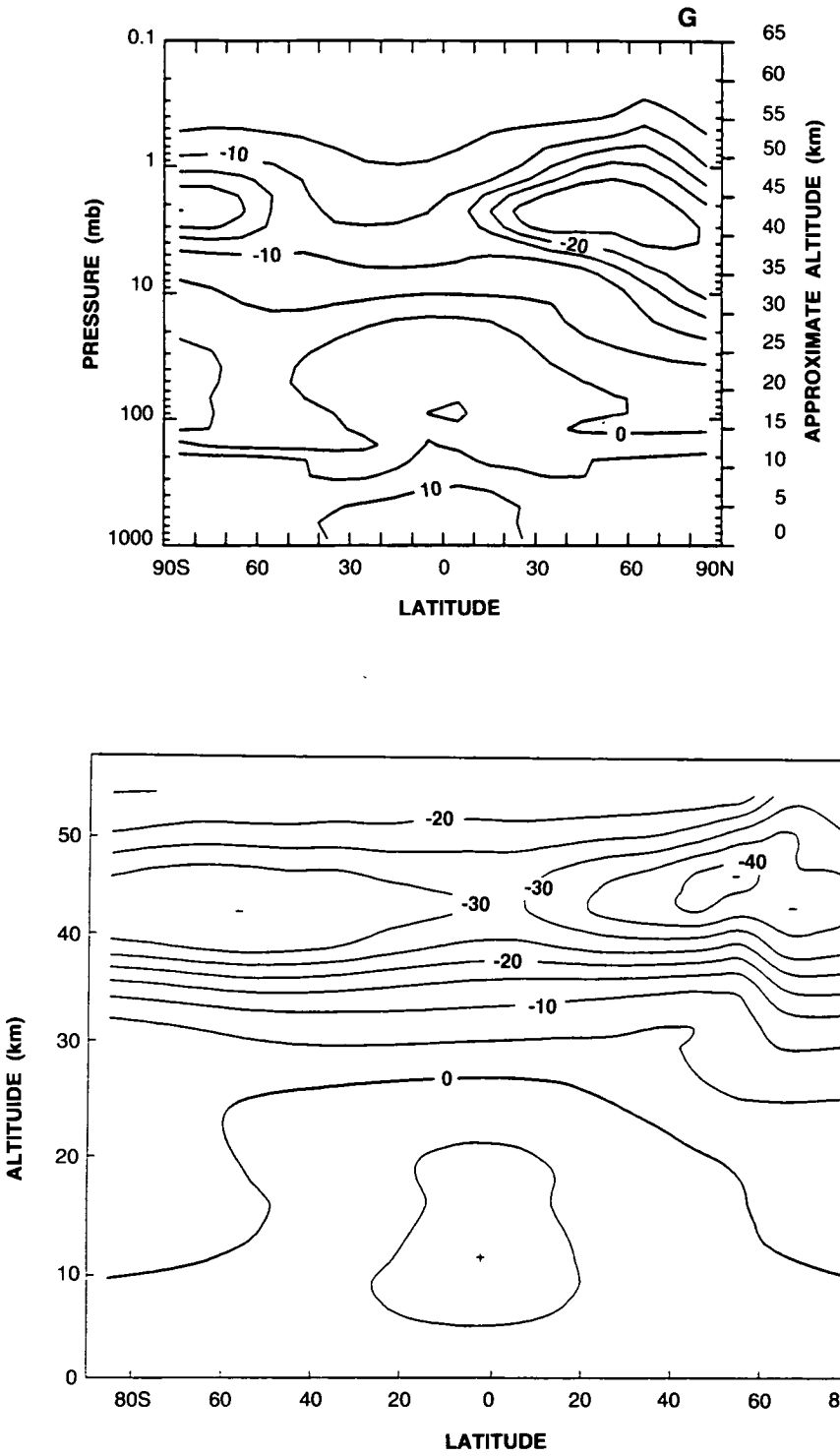

Figure 3.2-24. Latitude-by-altitude map of the percent change in local ozone concentration from 1980 to 2060 for scenario D1.

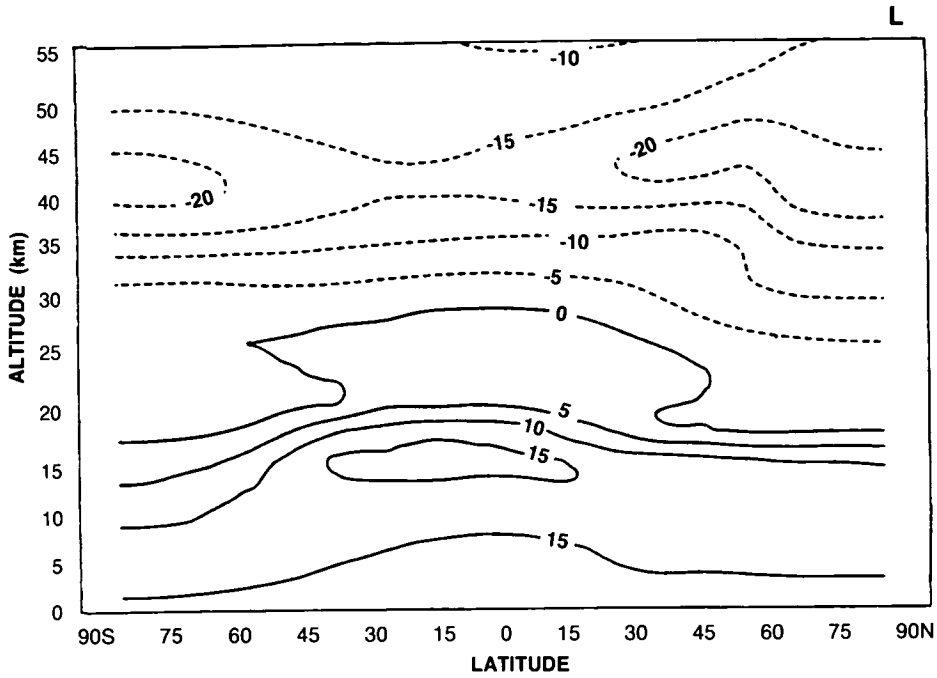

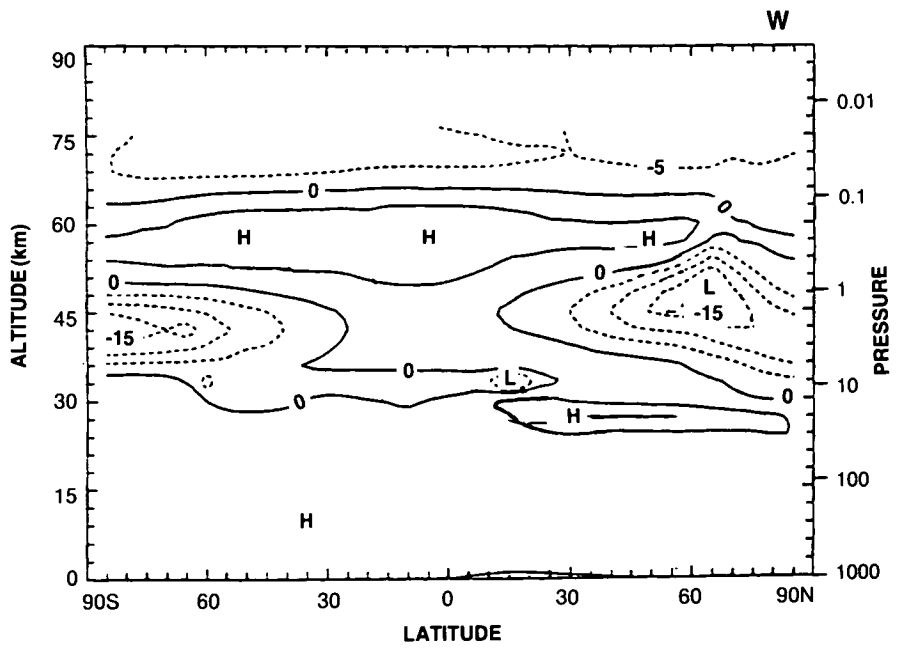

Figure 3.2-24., continued

Results from scenarios D2 and D3 are shown for the GSFC2 model in Figures 3.2-25 through 3.2-30. The successively lower chlorine loading reduces the ozone depletion and results in more rapid recovery. By 2060 in scenario D3, column ozone depletions are less than 2% everywhere except at high southern latitudes and the north polar spring. If, however, we were to extrapolate the predictions of the WisCAR model (using results from A1 and D1), large ozone increases would be expected.

Scenario D4, without methane increases, shows substantially greater ozone depletion in northern mid-latitudes by 2060: 3% versus 1% in D3 (see Figure 3.2-31G). Furthermore, the recovery of stratospheric ozone seen in D3 is less apparent in D4. The Dobson maps of column ozone change in Figures 3.2-32(G,O) are consistent in overall magnitude; but the GSFC2 model predicts much larger depletions in the Southern Hemisphere, and the Oslo model calculates equally asymmetric depletions in favor of the Northern Hemisphere. Both models predict modest depletions in local ozone concentrations (see Figures 3.2-33 [G,O]), with maximum losses of 10–15% in the high latitude upper stratosphere.

Within the assessment calculations presented here there is apparently larger uncertainty associated with predicting the impact of increasing CH_4 and CO_2 than there is in assessing the impact of additional chlorine and bromine. However, these models do not include the heterogeneous processes assumed to be responsible for the Antarctic ozone hole and possibly some current Arctic ozone loss. The uncertainties associated with predicting the halogen-catalyzed loss of ozone in the lower stratosphere are much greater than indicated by the results presented for scenarios A1 through D4 above. We next consider examples from models that now include some form of heterogeneous chemical processing.

In summary, when the CFC emissions are reduced by 95% (D1), the chlorine and bromine loadings in 2060 are 5.4 ppbv and 14 pptv, respectively. The reductions in column ozone at mid- to high latitudes are less than half of those calculated in the reference scenario: very little change in the tropics and 2–4% at mid-latitudes for models without temperature feedback. Ozone reductions at 40 km are 20–30%. In the one model that included the CO_2 effect, small increases in ozone column, 0–2%, are found at most latitudes. Further reductions in chlorine loading were considered by additionally freezing concentrations of methyl chloroform and carbon tetrachloride (D2), and the chlorine loading at 2060 was reduced to 4.2 ppbv. The reductions in column ozone were about 30% of those in the reference scenario. If the 95% cut in CFC emissions is not compensated for by increased emission of HCFC-22 (D3), the chlorine loading at 2060 is reduced further to 3.6 ppbv, but the calculated ozone columns are not significantly different: little change in the tropics and a decrease of up to 4% at high latitudes. This change in chlorine loading, from 4.2 to 3.6 ppbv, has little effect on column ozone because it is associated with changes in HCFC-22 abundance. In these current assessment models, HCFC-22 does not release a large fraction of its chlorine in the middle stratosphere where chlorine-catalyzed loss of ozone is most important. No heterogeneous chemistry was included in these models.

3.2.2.7 Special Contributions: Heterogeneous Chemistry

The effects of heterogenous chemistry on ozone have been studied in specialized photochemical models (e.g., non-global, restricted dimensions), but have only recently been incorporated into the global stratospheric models necessary for this assessment. We report here on some preliminary results of this latter research, with the caveat that these models need to be studied, intercompared and further evaluated by the scientific community before we can rely on their predictions. We first present modeling studies of the perturbations to global ozone by heterogeneous reactions on polar stratospheric clouds (PSCs). We then consider the impact of similar heterogeneous mechanisms that may occur on the global sulfate aerosols in the lower stratosphere.

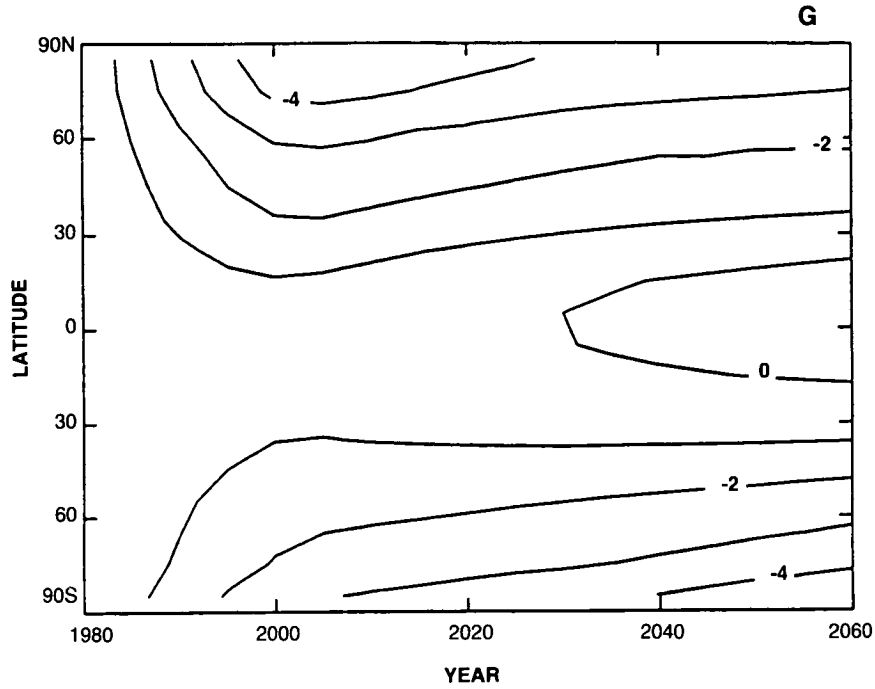

Figure 3.2-25. Time-line vs. latitude of the percent change in column ozone during March from 1980 to 2060 for scenario D2.

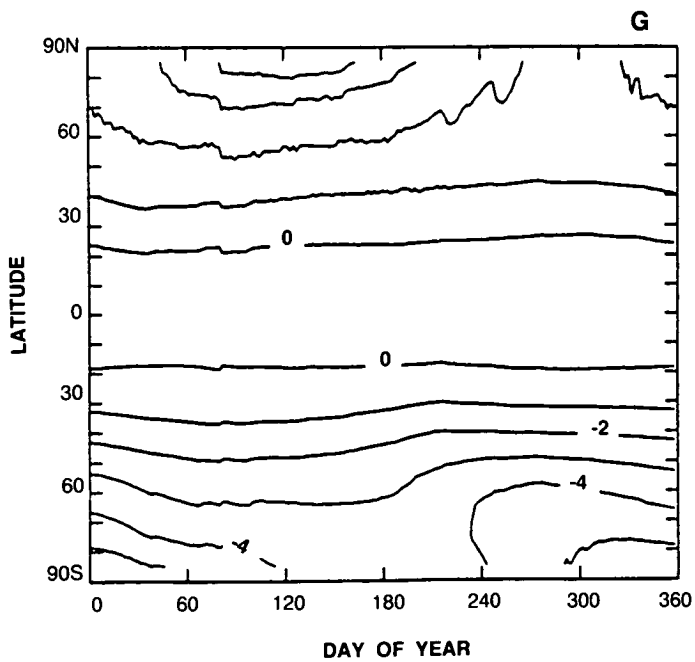

Figure 3.2-26 Dobson map of percent change in column ozone from 1980 to 2060 using scenario D2.

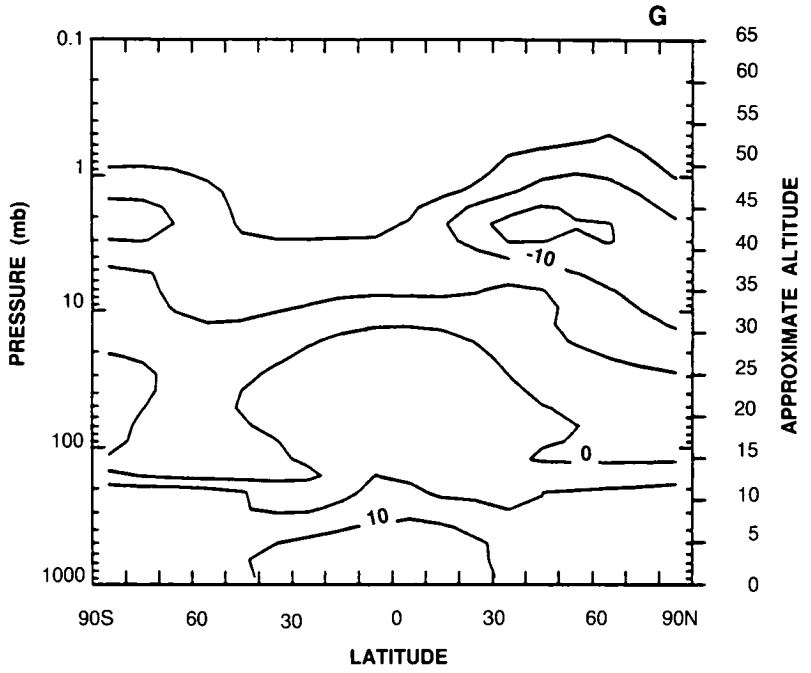

Figure 3.2-27. Latitude-by-altitude map of the percent change in local ozone concentration from 1980 to 2060 for scenario D2.

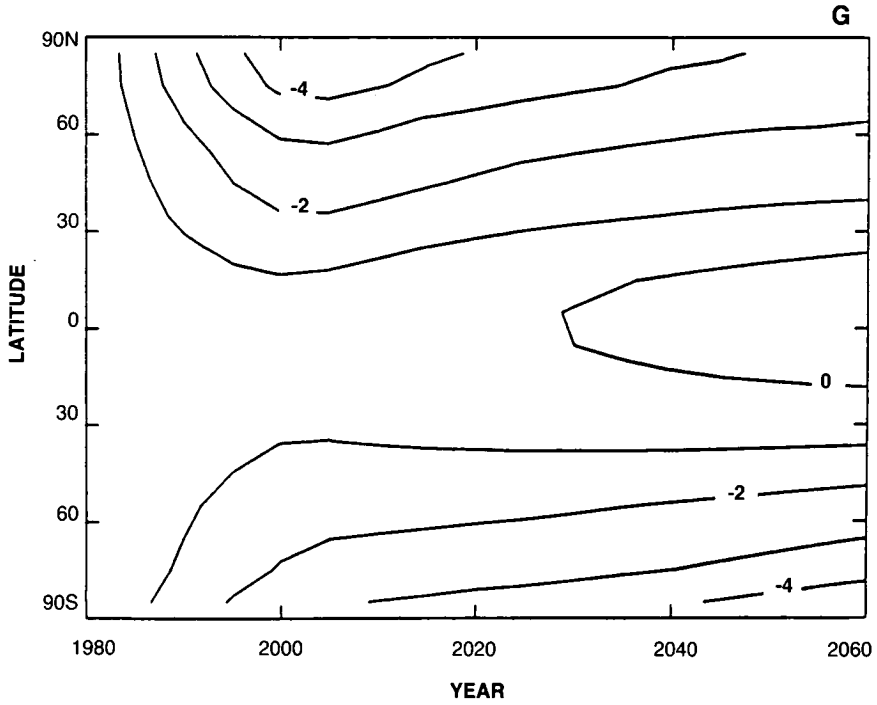

Figure 3.2-28. Time-line vs. latitude of the percent change in column ozone during March from 1980 to 2060 for scenario D3.

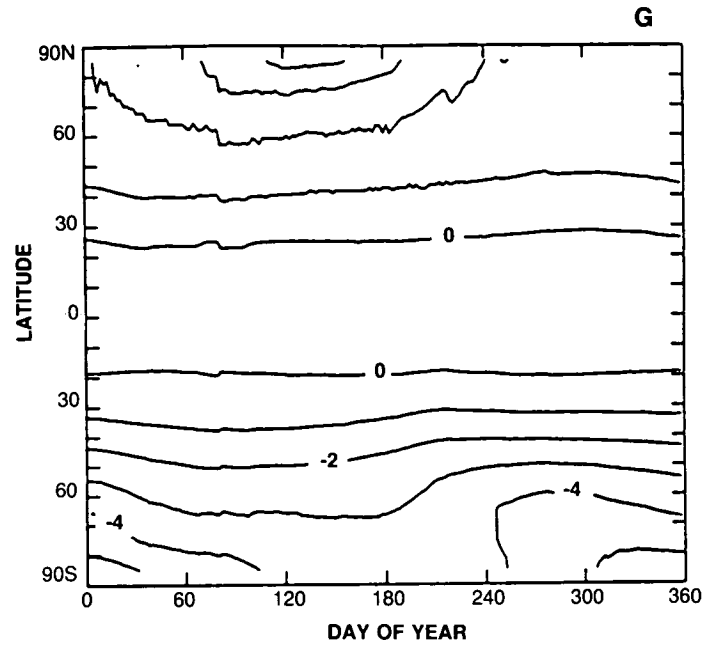

Figure 3.2-29. Dobson map of percent change in column ozone fom 1980 to 2060 using scenario D3.

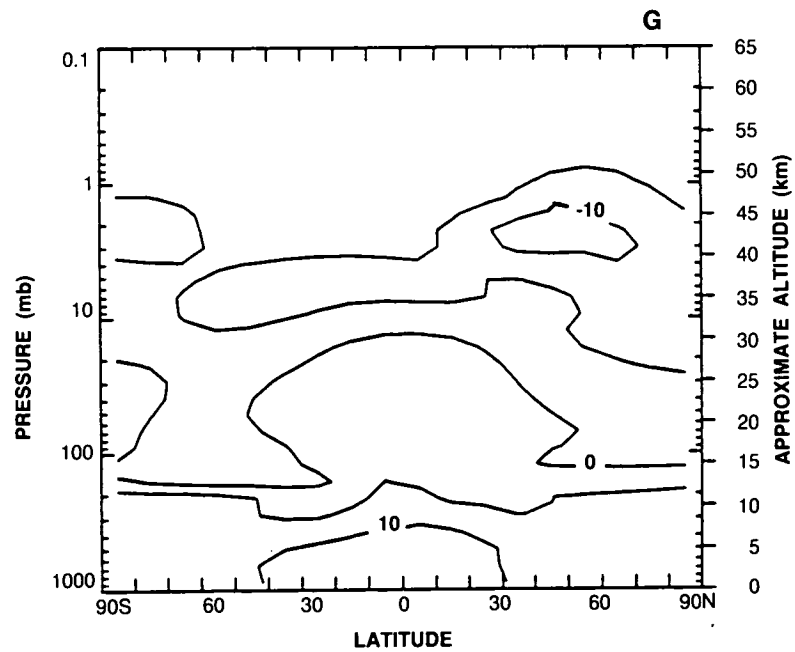

Figure 3.2-30. Latitude-by-altitude map of the percent change in local ozone concentration from 1980 to 2060 for scenario D3.

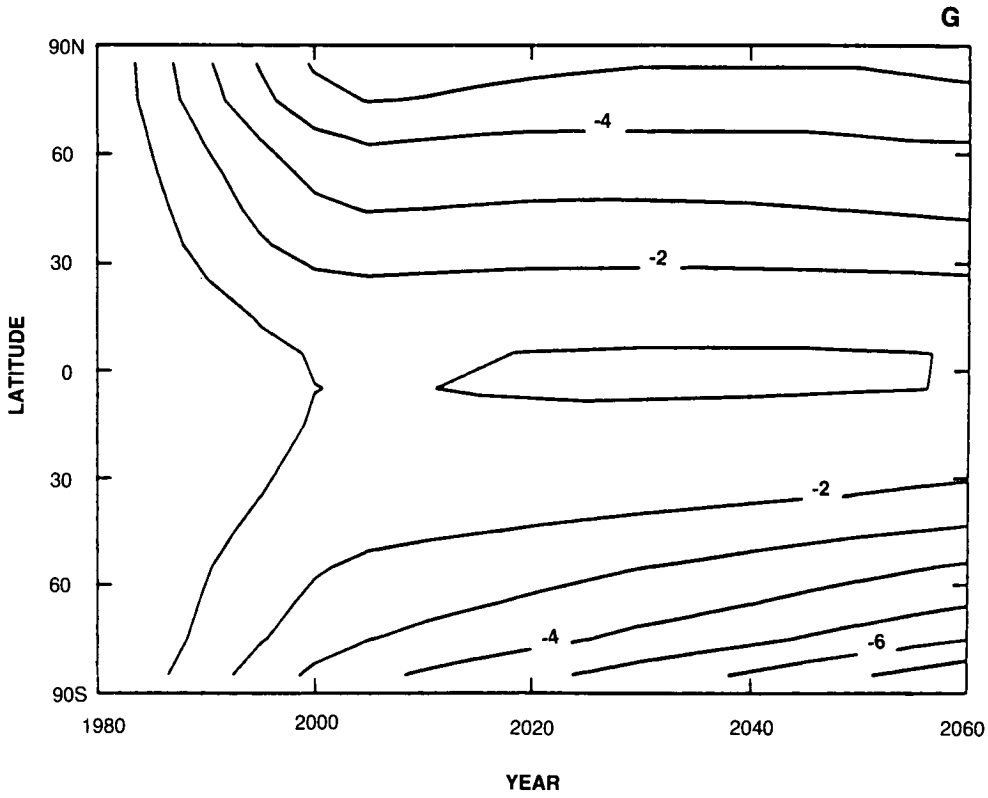

Figure 3.2-31. Time-line vs. latitude of the percent change in column ozone during March from 1980 to 2060 for scenario D4.

Reactions occurring on the surfaces of particles in the stratosphere are now believed to play an important role in the generation of the Antarctic ozone hole every year (See Chapter 1, Polar Ozone). These reactions are believed to take place on PSCs, which occur in at least two forms: nitric acid trihydrate and water ice. The heterogeneous reactions lead to major changes in the partitioning of chlorine species, resulting in enhanced concentrations of ClO; they also reduce concentrations of nitrogen oxides. These net effects, but not the reactions themselves, have been observed in both polar regions. Laboratory measurements of the following heterogeneous reactions have been obtained (Molina et al., 1987; Tolbert et al., 1987, 1988a, 1988b; Leu, 1988a, 1988b; Mozurkewich and Calvert, 1988) :

$$ClONO_2(g) + H_2O(s) \rightarrow HNO_3(s) + HOCl(g)$$
$$ClONO_2(g) + HCl(s) \rightarrow HNO_3(s) + Cl_2(g)$$
$$N_2O_5(g) + H_2O(s) \rightarrow 2HNO_3(s)$$
$$N_2O_5(g) + HCl(s) \rightarrow HNO_3(s) + ClNO_2(g)$$

It should be noted that the treatment of heterogeneous chemistry in these models is highly uncertain due to both the parameterization of PSCs and the uncertainty in the reaction rates.

The Cambridge model studied the potential impact of PSCs on ozone in the Northern Hemisphere by prescribing their presence and properties poleward of 67°N in the lower stratosphere from mid-December

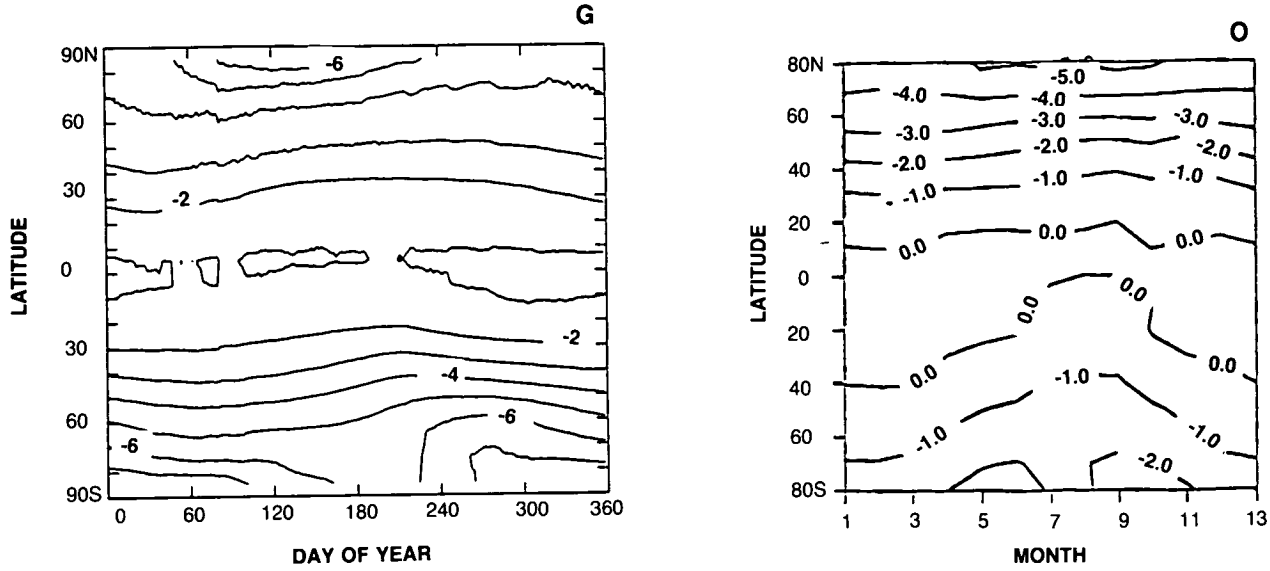

Figure 3.2-32. Dobson map of percent change in column ozone from 1980 to 2060 using scenario D4.

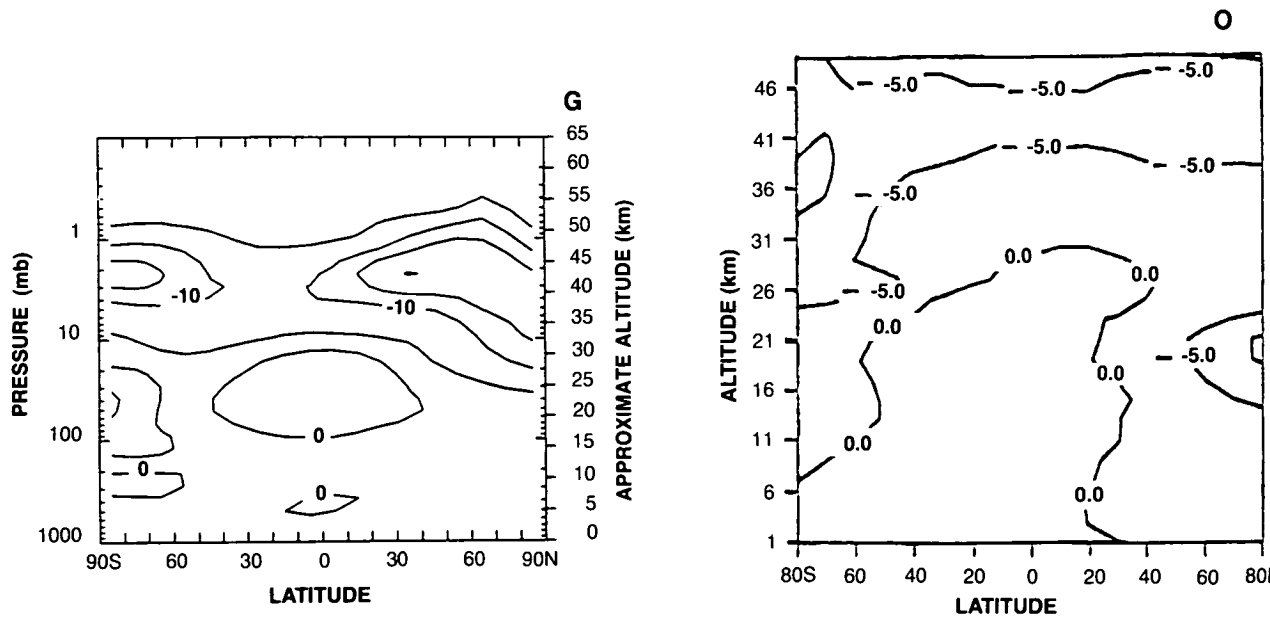

Figure 3.2-33. Latitude-by-altitude map of the percent change in local ozone concentration from 1980 to 2060 for scenario D4.

through mid-March. They used the reactions listed above and examined the ozone depletions at stratospheric chlorine levels (Cl_x) equal to 3 ppbv. Figure 3.2-34 shows the Dobson map of a 2-year sequence of the simulation with PSCs relative to that without. Including the PSCs leads to substantially larger ozone loss (an additional 5–9%) north of 60°N in the early spring. This parameterization should apply also to the Antarctic ozone hole but was not included in this calculation.

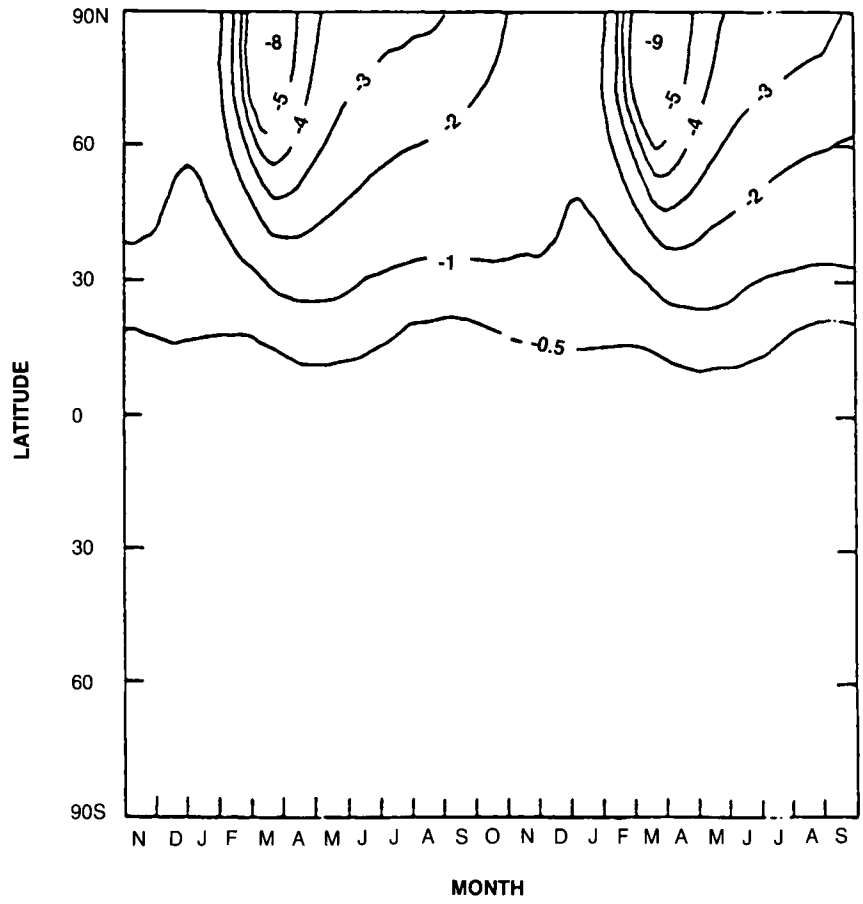

Figure 3.2-34. Two-year sequence of percent change in column ozone from the Cambridge model with PSC chemistry in the Northern Hemisphere. Results are relative to the standard model without PSC chemistry, and models use 3 ppb of free chlorine.

The WisCAR model examined the effects of heterogeneous chemistry by invoking PSC formation when the temperature fell below 195 K. PSCs were assumed to denitrify, dehydrate, and to react $ClONO_2$ with HCl. Results from calculations of scenario A1, both with and without this polar chemistry, are shown in Figure 3.2-35. The global ozone depletion with this polar chemistry is 6% greater than without; by 2060 depletions in the high latitude springtime exceed 16% in the north and 60% in the south.

The AER model examined the possible impacts of PSC chemistry using a parameterization (second-order rates) of the heterogeneous reactions of $ClONO_2$ and N_2O_5 with HCl. The calculation was hemispheric, focusing on the Arctic; and reactions are invoked north of 62°N in the wintertime, denitrified lower stratosphere. When compared with the standard AER model for the period 1960–1980 (compare Figure 3.2-36a with 3.2-3A), the ozone depletion doubles at high latitudes (>45°N) for all seasons and increases in the tropics by at most 1%. For the period 1985 to 2060 using scenario B1 (Figure 3.2-36b), depletions of ozone column are substantially larger at high latitudes between February and May than of those from the standard (homogeneous chemistry) calculation for B1 (Figure 3.2-13A), and are generally 1% larger over the rest of the hemisphere.

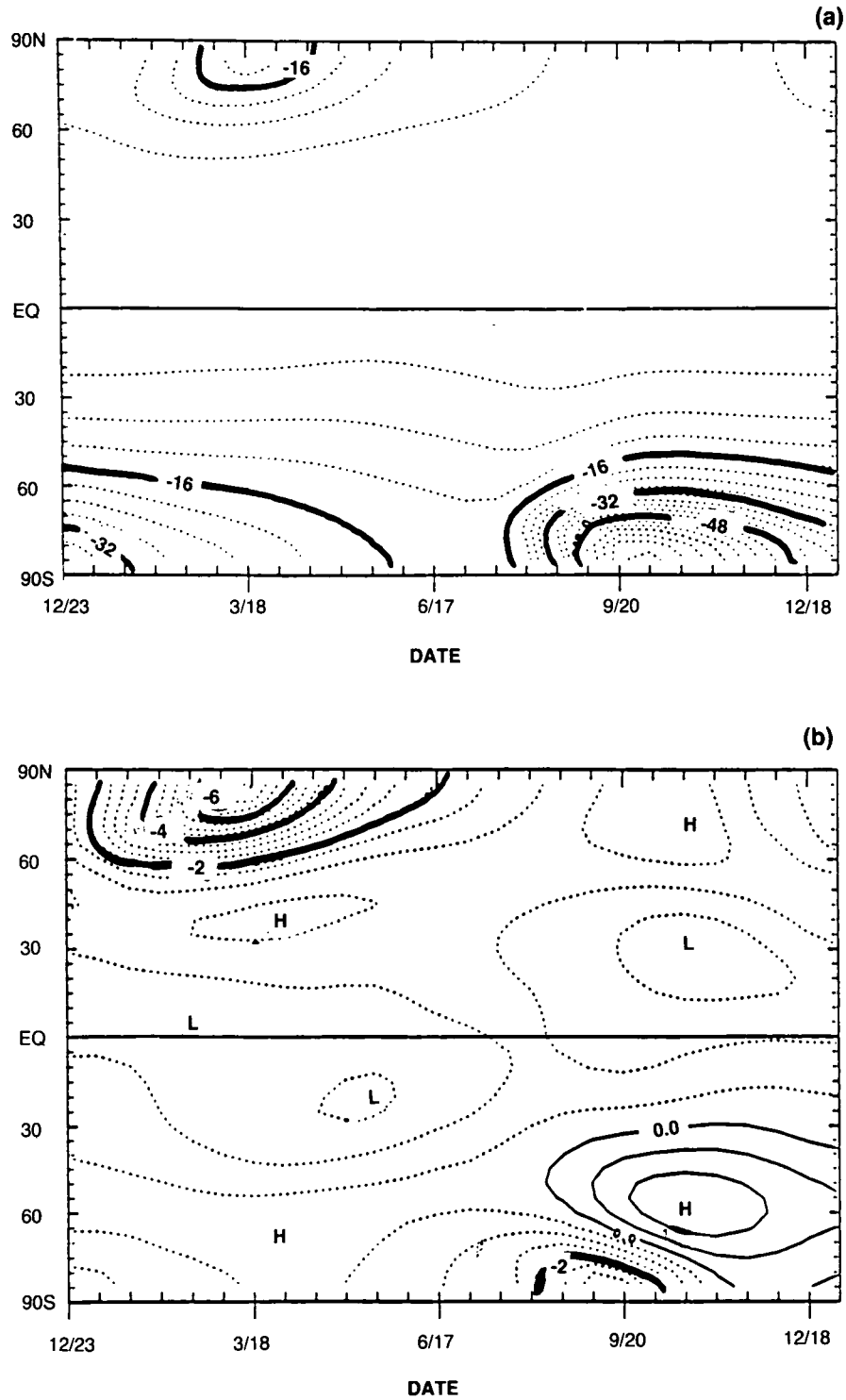

Figure 3.2-35. Dobson maps of percent change in column ozone between 1960 and 2060 from the WisCAR model with (a) and without (b) heterogeneous chemistry on PSCs for scenario A1.

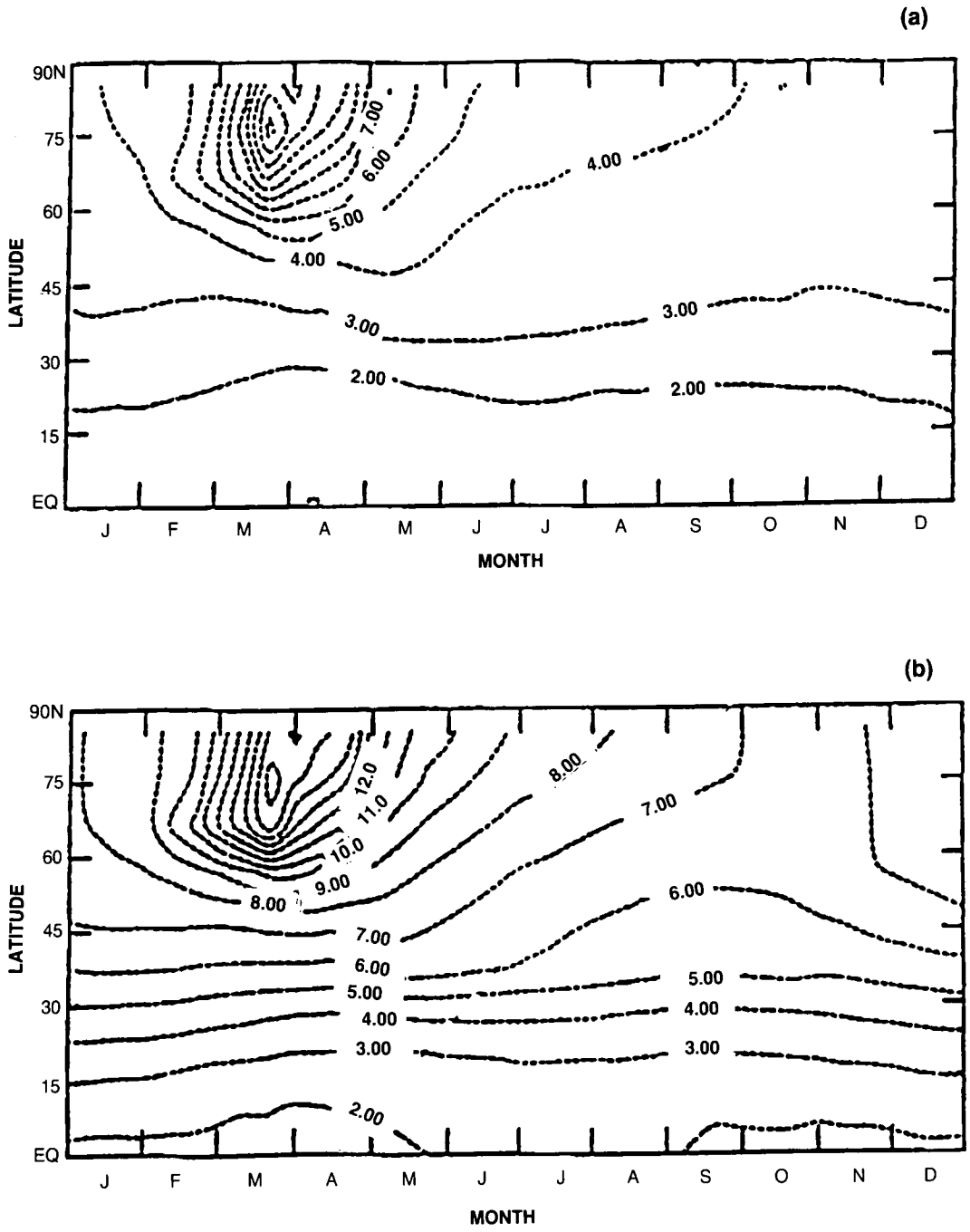

Figure 3.2-36. Dobson maps of percent change in column ozone from 1960 to 1985 (a) and from 1985 to 2060 (b) from the AER model using scenario B1. The model assumed PSC heterogeneous chemistry and denitrification at high northern latitudes in winter.

3.2.2.8 Junge-Layer Chemistry

Recent laboratory studies (Tolbert et al., 1988b) have indicated that reactions similar to those discussed above for PSCs may also occur on water-sulfuric acid solutions, typical of the measured composition of the Junge-layer aerosols. Some uncertainties in modeling the stratospheric chemistry of these reactions include: measurements have been made only for sticking coefficients, not net reaction efficiencies; the sticking coefficients are extremely sensitive to the H_2O content of the solution; in the stratosphere, the sulfuric-acid aerosols absorb water with decreasing temperature and may only be sufficiently reactive at temperatures less than 210 K. Some reactions noted above require sufficient amount of HCl to be dissolved in or adsorbed on the aerosols; however, no data are available on the solubility of HCl in H_2SO_4 /H_2O solutions for stratospheric conditions.

Earlier studies of the effects of Junge-layer chemistry (models by Rodriguez et al., 1988; observations by Brune et al., 1987) pointed out that heterogeneous reactions on the sulfate aerosols, particularly those involving HCl, could have a dramatic impact on the calculated ozone reductions for future years. However, model results showed significant enhancements of ClO below 20 km and thus provided an important observational constraint on the adopted heterogeneous rates. Hofmann and Solomon (1989) also included heterogeneous chemistry to study the impact of enhanced sulfate aerosol concentrations after the El Chichon eruption. Their results showed significant reductions in NO_2 and ozone, the latter being driven by enhanced chlorine chemistry. Because of the uncertainty in the heterogeneous reactions rates, it is clearly important that model simulations of Junge-layer chemistry must be validated by comparison with atmospheric observations, in particular the vertical and latitudinal profiles of ClO and NO_2 in the lower stratosphere.

The Oslo model investigated the impact of heterogeneous Junge-layer chemistry using the chemical model of the sulfate layer from Hofmann and Solomon (1989), except for the reaction of N_2O_5 and HCl. A scenario similar to A1 is calculated and the resultant Dobson maps of percent change in column ozone from 1985 to 2050 are shown for the model with and without the particulate chemistry in Figure 3.2-37. In this model the impact of heterogeneous chemistry enhances the ozone depletion, primarily towards high latitudes. Additional studies with the WisCAR model are similar to those described for the Oslo model and confirm the potential importance of heterogeneous chemistry on the Junge-layer particles, especially at high abundances of chlorine and bromine.

The AER model also examined the global impact of the heterogeneous reaction of HCl with $ClONO_2$ occurring on the natural sulfate layer. An equivalent second-order rate of 2×10^{-16} cm^{-3} s^{-1} was adopted at 20 km (corresponding to a reaction efficiency of 3×10^{-3} between $ClONO_2$ and the aerosols), and scaled with the altitude distribution of aerosol surface concentration. The results from scenario B1 with this model are compared with those from the same AER homogeneous chemistry model (Figures 3.2.13A). Ozone depletion is dramatically enhanced by a factor of 3 on average at high latitudes in winter, and a factor of 2 in summer and throughout the tropics (Figure 3.2-38). For the current atmosphere, this model predicts ClO abundances that are higher by factors of 3–4 than the limited set of mid-latitude observations below 20 km; and it may thus overestimate the future ozone depletions. Interestingly, the ozone depletions calculated for the period 1960–1985 (not shown) are similar in magnitude and distribution to those for the PSC simulation from the AER model described above.

A mechanically forced three-dimensional model with heterogeneous chemistry prescribed similarly to the WisCAR model has been developed by Granier and Brasseur (NCAR) (unpublished data). This model is able to generate substantial chemical loss of ozone over Antarctica. Similarly, experiments with

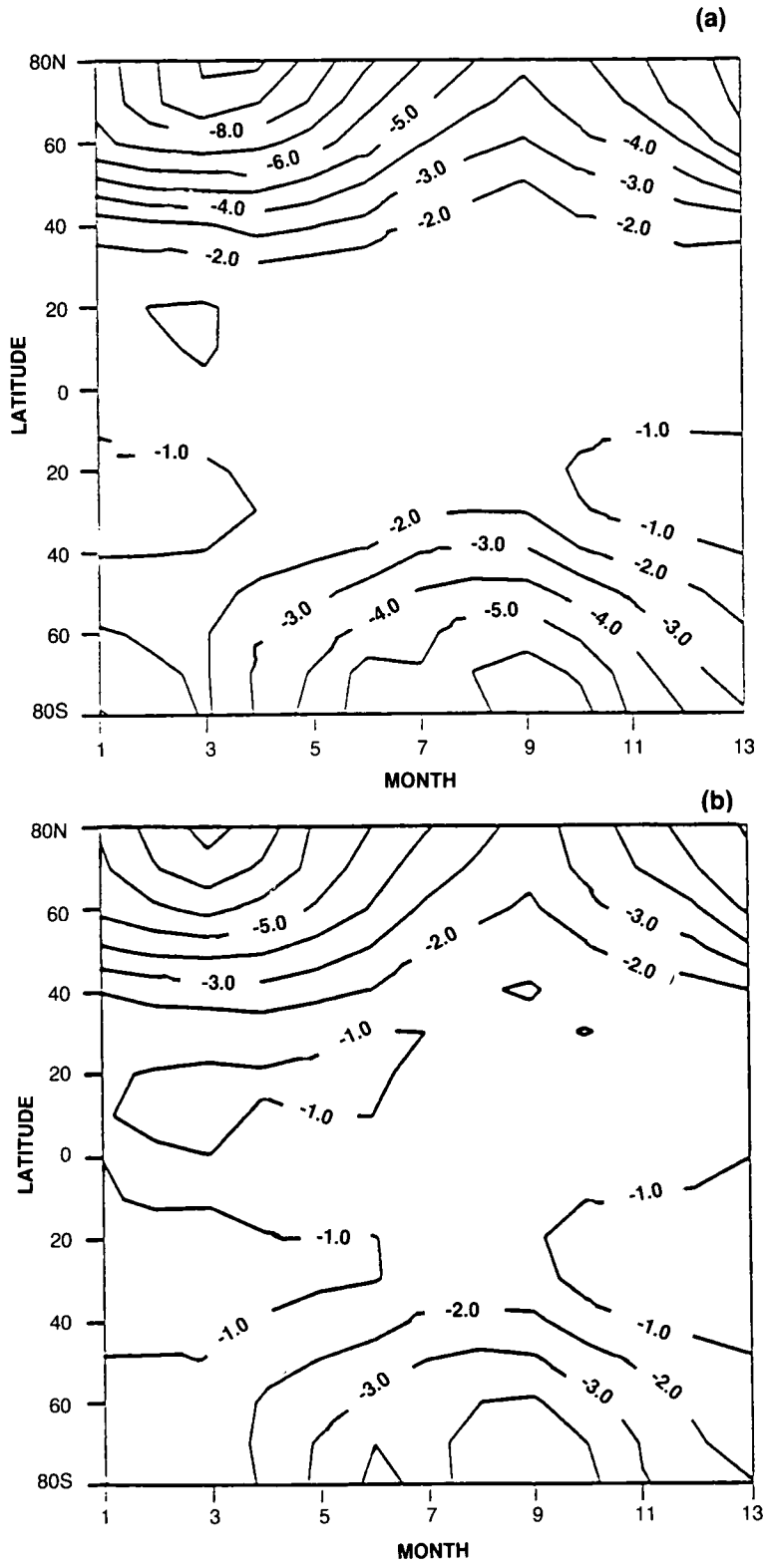

Figure 3.2-37. Dobson maps of percent change in column ozone between 1985 and 2050 from the Oslo model with (a) and without (b) heterogeneous chemistry on the natural sulfate layer. The scenario is similar to A1.

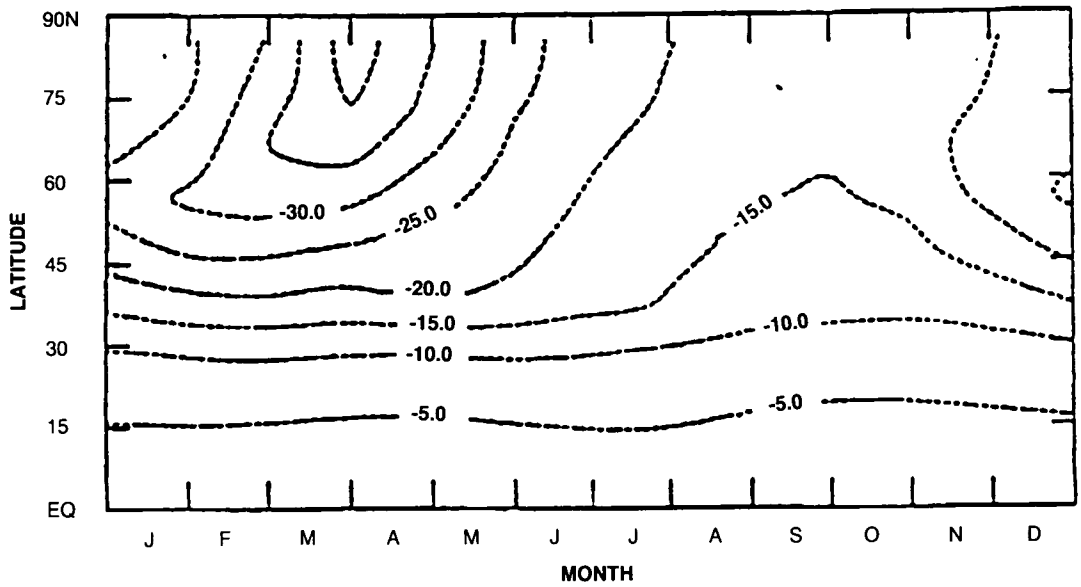

Figure 3.2-38. Dobson maps of percent change in column ozone from 1985 to 2060 from the AER model using scenario B1. The model assumed a Junge-layer heterogeneous chemistry.

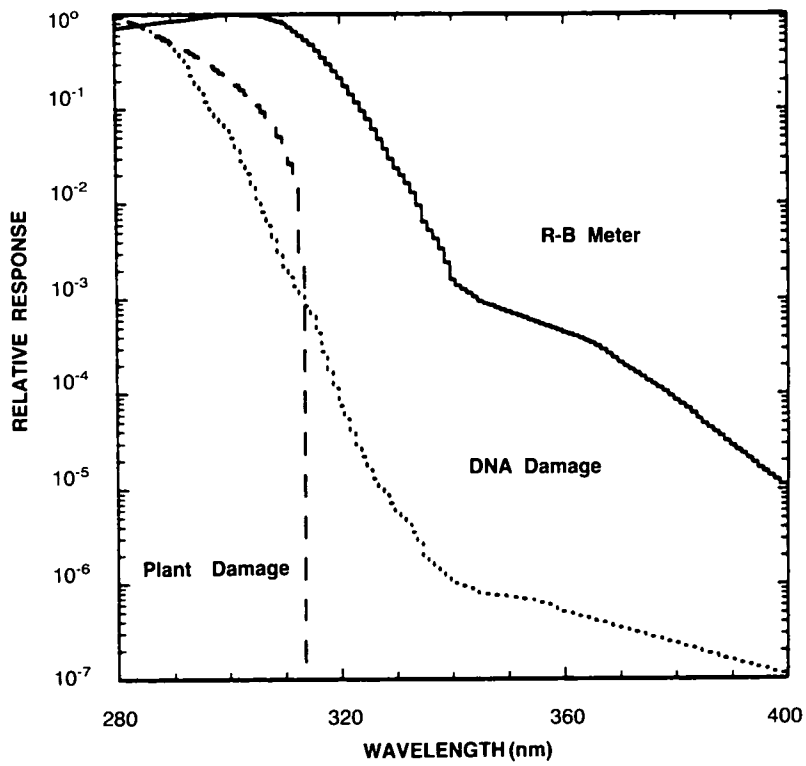

Figure 3.2-39. Action spectra used as weighting functions to calculate biologically effective radiation. All curves are normalized to unity. Values given are relative efficiencies per unit energy.

a 3-D model developed by Pitari, Verdecchia and Visconti (Aquila) (unpublished data) have been able to induce large ozone depletions over Antarctica using prescribed heterogeneous chemistry. All of these experiments, especially those with 3-D models, are in the early stages of research and must await further development and validation of the models.

3.2.2.9 One-dimensional Models

The application of one-dimensional stratospheric models in recent assessments has been to facilitate the study of many scenarios that would otherwise be too costly to perform with 2-D assessment models. This restriction no longer applies to all of the 2-D models (notably GSFC2 and Oslo), but the 1-D models might still be accurate in assessing changes in the upper stratosphere. Furthermore, they provide a useful forum by enlarging the modeling community that is involved in these assessments. The different approaches and uncertainties in modeling atmospheric photochemistry make it desirable to intercompare as many models as possible.

The perturbations to ozone and temperature at 40 km altitude, mid-latitudes, and during equinox (March or September) in the 2-D models should be comparable to the 40-km changes in the 1-D models (no latitudes or seasons resolved). We choose to compare these changes, 2060 relative to 1980, for some scenarios in Table 3.2-8. The comparison is not extensive, however, and the ozone depletions calculated with the 1-D models are broadly consistent with the 2-D results.

3.2.2.10 Conclusions

Results presented here are based on the standard 2-D stratospheric models that include only the effects of gas-phase chemistry. We have also included some examples of predictions from those same models in which the effects of enhanced chlorine-catalyzed loss of ozone, associated with heterogeneous chemistry on stratospheric aerosols, have been parameterized. Given the new and innovative nature of the modeling of heterogeneous chemistry and the large uncertainties associated with the kinetic data, we cannot yet rely quantitatively on these latter predictions. Nevertheless, in comparing these results it is clear that

Table 3.2-8. Stratopause changes from 1980 to 2060 (40 km or 3 mb, 40°N, March)

Model		Scenario									
		A1	A2	B1	C1	D1	A1	A2	B1	C1	D1
		Ozone Change (%)					Temperature Change (K)				
AER	(2-D)	−42		−31							
Camb	(2-D[a])	−25					−13				
GSFC2	(2-D)	−43	−54	−32	−23	−20					
LLNL	(2-D)	−40				−20					
	(2-D[a])	−30					−8				
Mainz	(2-D)	−56									
NSU	(2-D[a])	−49				−13	−5				
Oslo	(2-D[a])	−43	−45			−7					
WisCAR	(2-D[a])	−36					−7				
IASB	(1-D)	−52	−58	−41	−31	−28	−13	−14	−12	−10	−1
MPI	(1-D)	−39	−45				−10	−10			

[a]Models with CO_2 and T feedbacks.

predictions of ozone depletion associated with increasing halocarbons (chlorine and bromine) are less in models using gas-phase chemistry than similar predictions in which heterogeneous chemistry has been included in the models.

One clear conclusion from these assessments is that significant depletion of ozone is likely to continue if chlorine and bromine levels are allowed to double (scenarios A and B). Loss of ozone at 40 km is a robust prediction of the models; whereas, depletions of column ozone vary considerably and depend on changes in climate and other trace gases. For the range of scenarios considered here, ozone perturbations are nearly linear in response to additional chlorine. The present combination of models and scenarios does not allow us to separate the impacts of increasing bromine (i.e., halons) relative to the overall increases in chlorinated CFCs.

The increasing atmospheric abundances of CH_4 and CO_2 are a key factor in the predictions of future column ozone. Methane is involved in three major stratospheric cycles: water vapor budget, enhanced ozone production through smog chemistry, and partitioning of the chlorine family between ClO and HCl. Carbon dioxide enhances the radiative cooling of the stratosphere while heating the troposphere and thus possibly changing the overall circulation patterns. In the current scenarios, their individual and combined impacts lead to increased ozone, but there are large differences among the models as to the magnitude of these feedbacks. The effects are not obviously linear and become increasingly more important at low levels of chlorine. For example, the differences between scenarios D1 through D4 cannot be predicted robustly with the current set of assessment models. A major uncertainty with CH_4 and CO_2 is our estimate of future concentrations, since a substantial fraction of their emissions is natural and not under the control of human activities or regulation.

The incomplete treatment of tropospheric chemistry in the current 2-D stratospheric models adds additional uncertainty to the predicted trends in tropospheric ozone, both recent and long-term. This uncertainty affects not only the ozone columns but also tropospheric OH (see Chapter 4) and, hence, the lifetimes and abundances of HCFC-22 and CH_3CCl_3.

Two major questions that have not yet been answered by these predictions for global ozone in the future are: (1) What is the future of the Antarctic ozone hole, will it get deeper or more spatially extensive? and (2) What are the global impacts of polar chemistry, will there be a corresponding Arctic ozone hole? A third major uncertainty in modeling the future atmosphere involves predicting the impact of real climate change to the entire atmosphere, not just the CO_2 cooling in the stratosphere. These difficult questions have been recognized in the most recent assessments (e.g., Watson et al., 1988; SORG, 1988) and unfortunately are not yet answered. Through continued research and model intercomparison, especially testing against the observed changes over the past several decades, we expect to develop atmospheric models that will be able to provide some answers to these questions for the next assessment.

3.2.3 Predicted Changes in Surface UV Radiation

This section discusses the changes in biologically damaging ultraviolet (UV-B) radiation at the Earth's surface that are expected to result from changes in atmospheric ozone concentrations. The calculation is complicated by the fact that the amount of UV radiation reaching the surface is not related to the amount of ozone by a simple inverse proportion. For example, a 1% reduction in the ozone column may not necessarily yield a 1% increase in biologically damaging radiation. Depending on the particular biological system and environment under consideration, the damage may be much larger or much smaller. This complex behavior is a result of several factors, including the strong wavelength dependence of the absorp-

tion of light by ozone and of the biological response functions, the contribution of diffuse (sky) radiation, and the effect of environmental factors such as the sun angle, the amount of cloud cover and haze, the reflectivity of the ground, and the elevation of the ground above sea level. Detailed models of the propagation of radiation through the atmosphere have been developed previously (Chandrasekhar, 1960; Stamnes, 1986; and references therein), and have been applied with varying degrees of approximation to the problem of estimating biological dose rates related to ozone depletion (Cutchis, 1974; Pyle and Derwent, 1980; Gerstl et al., 1981; Stordal et al., 1982; Frederick and Lubin, 1988a, b; Brühl and Crutzen, 1989). The model used here (and described below) combines a reasonably accurate radiative transfer method with high spectral resolution and good computational efficiency.

3.2.3.1 Model for the Propagation of UV Radiation Through the Atmosphere

The model used in the present work was developed at NCAR for the purpose of photochemical calculations (Madronich, 1987) and was modified somewhat for the calculation of biologically damaging radiation. It includes absorption of light by atmospheric ozone and aerosol particles, and multiple scattering by air molecules (Rayleigh scattering) and by aerosol particles and cloud droplets (Mie scattering). The radiative transfer scheme is based on the delta-Eddington approximation of Shettle and Weinman (1970) and Joseph et al. (1976). The accuracy of this scheme has been discussed by Meadow and Weaver (1980) and King and Harshvardhan (1986), and is sufficient for the present purposes.

The model covers the biologically significant UV wavelength range 280-400 nm. The wavelength grid used in the present calculations is that given by WMO (1986), except that each WMO wavelength interval has been subdivided into five subintervals of equal width to represent more accurately the steep wavelength variation of ozone absorption and biological response spectra. High resolution extraterrestrial irradiance data are from Mentall et al. (1981) (over 280–330 nm) and from Neckel and Labs (1984) (over 330–400 nm). To conform with current recommendations, the irradiance values are scaled to the WMO (1986) values by comparing the integral over each set of five subintervals with the corresponding WMO interval value. Ozone absorption cross sections are from Molina and Molina (1986). These cross sections are somewhat temperature dependent in the UV-B region, so they are re-evaluated for each atmospheric layer of the model using the local temperature. Rayleigh-scattering cross sections are evaluated at the center of each wavelength interval using the expression given by Fröhlich and Shaw (1980). The solar zenith angle and the total ozone column (in Dobson units) must be specified.

To estimate the biological effects of the UV radiation, it is necessary to consider how effective photons of different wavelengths are in inducing biological damage. This is expressed by the action (or response) spectrum. The present calculations consider three different action spectra: a generalized DNA damage spectrum (Setlow, 1974), a generalized plant damage spectrum (Caldwell et al., 1986), and the response spectrum of a UV meter that was designed to approximate the erythemal (sunburn) response of Caucasian skin (Robertson-Berger or R-B meter; Robertson, 1975). The R-B meter response is actually somewhat different than the erythema spectrum, but is of interest because of the wide utilization of this instrument in monitoring surface UV radiation (see for example Scotto et al., 1988). Figure 3.2-39 shows the action spectra used in the present work. Note that the spectra were arbitrarily normalized to unity at their maximum, since their absolute magnitudes are not meaningful—only the relative changes with wavelength are of interest here. The biologically effective dose rate is defined as the convolution of the spectral irradiance, $E(\lambda)$, and the action spectrum, $A(\lambda)$,

$$R = \int E(\lambda)\, A(\lambda)\, d\lambda = \text{dose rate, } Joules\ m^{-2}\ s^{-1}$$

and may be integrated over time to obtain the biologically effective dose, e.g., on a daily, monthly, or annual basis.

A "base" model of the atmosphere was used to perform most of the calculations given below. The base model applies to clear sky (no clouds or aerosols), ground at 0 km above sea level with an albedo of 5%, and a flat horizontal receiver. The altitude profiles of temperature, ozone, and air density are taken from the standard profiles of Nicolet et al. (1982). A detailed comparison of the base model predictions was carried out against the model recently developed by Frederick and Lubin (1988a). Table 3.2.9 shows the results for the R-B meter dose rate, for noon on two different days of the year and a range of latitudes. The two models disagree by no more than 8% over a factor of 40 variation in the irradiance. This 40-fold variation is much larger than the UV changes expected from changes in atmospheric ozone concentrations, so that the models may be considered to be in excellent agreement for the purpose of the present calculations.

3.2.3.2 Surface UV Changes for Different Ozone Change Scenarios

Daily dose rates computed with the NCAR base model are shown in the upper panel of Figure 3.2-40 for the ozone distribution of 1979/1980 (2-year average of TOMS data, R. Stolarski, private communication). The absolute dose values (given in J m^{-2} day^{-1}) for the DNA damage, plant damage, and the R-B meter cannot be compared directly since the action spectra are relative. However, trends with latitude, time of the year, and local ozone columns are meaningful. The lower panels of Figure 3.2-40 show the radiation

Table 3.2-9. Surface UV irradiance:[a] Comparison of model predictions

Latitude	Dobson	Zenith Angle	UC[b]	NCAR[c]
		January 16		
60	368.5	81.01	0.0166	0.0179
40	335.6	61.01	0.1798	0.1870
20	247.1	41.01	0.5901	0.5980
0	244.2	21.01	0.9134	0.9160
−20	262.2	1.01	1.0000[d]	1.0000[d]
−40	291.2	18.99	0.8377	0.8414
−60	324.8	38.99	0.5180	0.5254
−80	304.2	58.99	0.2238	0.2318
		July 16		
80	319.4	58.73	0.2185	0.2265
60	338.8	38.73	0.5115	0.5132
40	307.9	18.73	0.8098	0.8137
20	281.8	1.27	0.9567	0.9566
0	258.1	21.27	0.8794	0.8826
−20	262.1	41.27	0.5622	0.5703
−40	319.1	61.27	0.1844	0.1918
−60	309.0	81.27	0.0191	0.0205

[a]Weighted for Robertson-Berger meter response.
[b]University of Chicago model (Frederick and Lubin, 1988).
[c]National Center for Atmospheric Research model (Madronich, 1987)—used in this study.
[d]Normalization point.

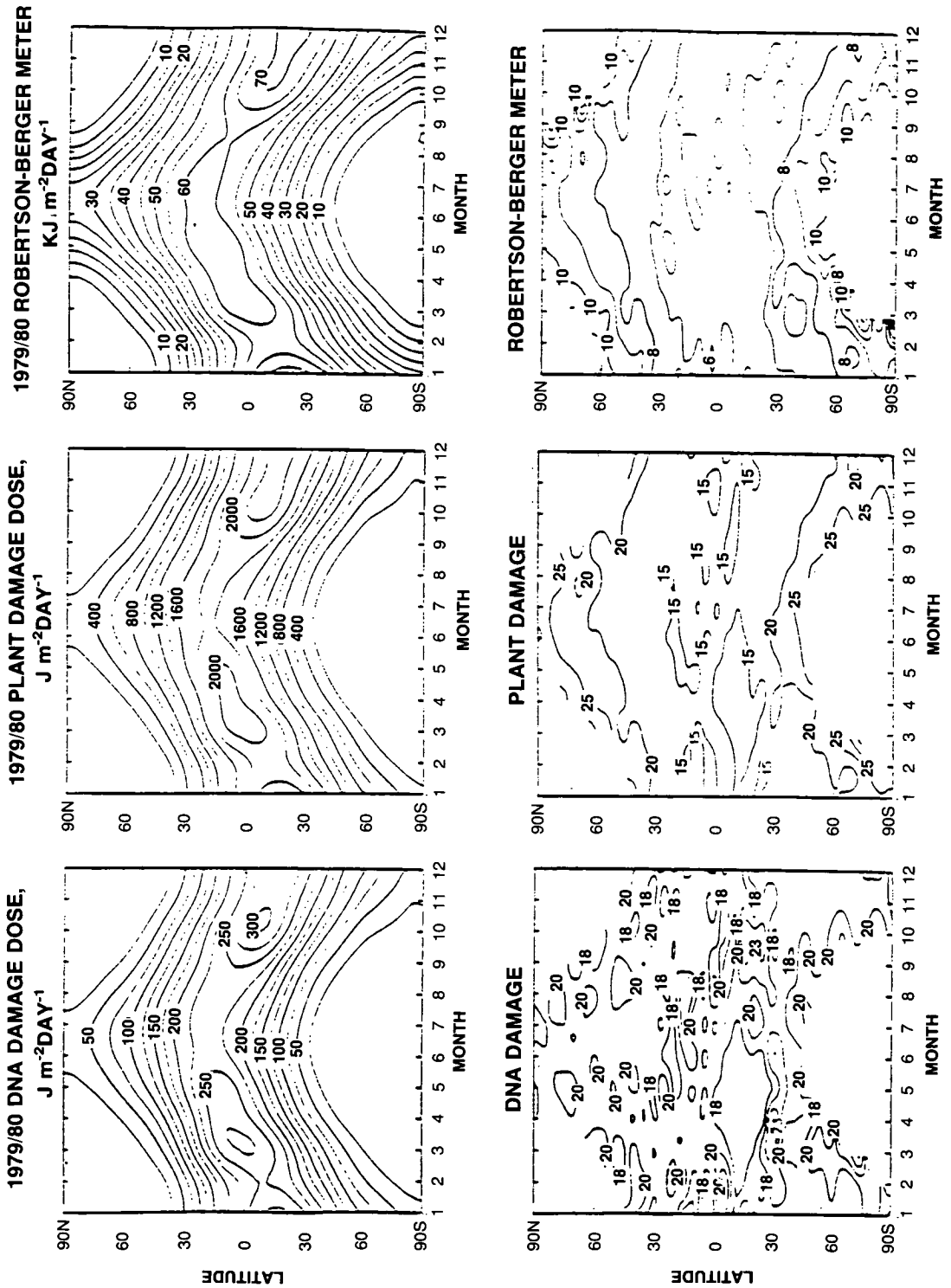

Figure 3.2-40. Daily doses for 1979/80 based on ozone column from TOMS measurements normalized to Dobson. Upper panels show absolute doses for DNA damage, plant damage, and R-B-meter response. Lower panels show radiation amplification factors (RAF) defined as the percent increase in daily dose for a 1% decrease of the local ozone column. RAF values were multiplied by 10.

amplification factors (RAF), defined as the percentage change in dose for a 1% change in the ozone column. These values show the sensitivity of different latitudes and months to changes in the ozone column, and serve to illustrate the non-linear response of UV dose. However, it is important to note that these values are meaningful only for small changes (1%) in the ozone column, since, as was shown by Stordal et al. (1982), RAF values associated with larger changes in ozone may be significantly different.

Changes in surface UV dose may have occurred in the past, as a result of changes in the ozone column abundance. Figure 3.2-41 shows the dose increases computed from measured changes in ozone column over the 8-year period 1979/80–1987/88. The ozone column data used in these plots were estimated from TOMS data normalized with Dobson measurements (R. Stolarski, personal communication). In the Southern Hemisphere, dose increases of 10–50% or more are seen during October and November poleward of 60°S, with smaller increases (2–10%) between 30°S and 60°S. In the Northern Hemisphere, biological dose increases range from 2% to 5%. These changes, attained over an 8-year period, should be compared to the changes predicted over a much longer period by the 2-D models.

Figures 3.2-42–44 show the changes in biologically effective radiation corresponding to the ozone columns calculated with the Goddard Space Flight Center Model2 (GSFC2). Figure 3.2-42 gives the changes in daily doses from 1960 to 1980. For DNA and plant damage, dose increases are calculated to be less than 4% for all locations and times except near the terminator where the absolute amounts of radiation are small. The percent changes for the R-B meter are consistently smaller (about half) than those for plant and DNA damage.

Results for scenario A1 (see Section 3.2.1), which assumes that emissions of the Montreal products will remain constant at 1986 levels, are shown in Figure 3.2-42 (ozone columns calculated with the GSFC2 model). The largest increases in daily doses are predicted to occur in the springtime at mid-latitudes. However, expressed as percent, the largest changes are predicted to occur at high latitudes, with increases in DNA and plant damage near 20–40%. Although these relatively large changes would occur in DNA and plant damage, R-B meters would indicate lesser changes.

Scenario D1 differs from the A1 scenario by assuming that the emissions of Montreal products are reduced by 95%, with the reductions becoming effective over the years 1996–2000. The effects on daily biological doses are shown in Figure 3.2-43 (ozone columns calculated with the GSFC2 model). Compared with the A1 scenario, scenario D1 leads to about half the increases in the doses. The geographical and seasonal distributions of these changes are similar to those predicted for the A1 scenario.

The predicted changes in biologically effective UV are sensitive to the assumptions and parameterizations used in different models and more specifically to the calculated changes in the ozone column by these models. For example, for scenario A1, the WisCAR (University of Wisconsin and NCAR) model predicts only about half of the dose increase predicted by the GSFC2 model.

3.2.3.3 Uncertainties in the Prediction of Surface UV Radiation Changes

The theoretical prediction of surface UV radiation is complicated enormously by the natural variability of the optical characteristics of the atmosphere. For example, it is literally impossible to model all of the natural geometric configurations of partly cloudy skies. Fortunately, and this is an important point, we are mostly interested in the relative changes in surface UV which would result from systematic changes in the concentrations of atmospheric ozone. This assumes implicitly that other environmental factors, such as cloud cover and surface albedo, will on the average remain constant over the period 1960–2060.

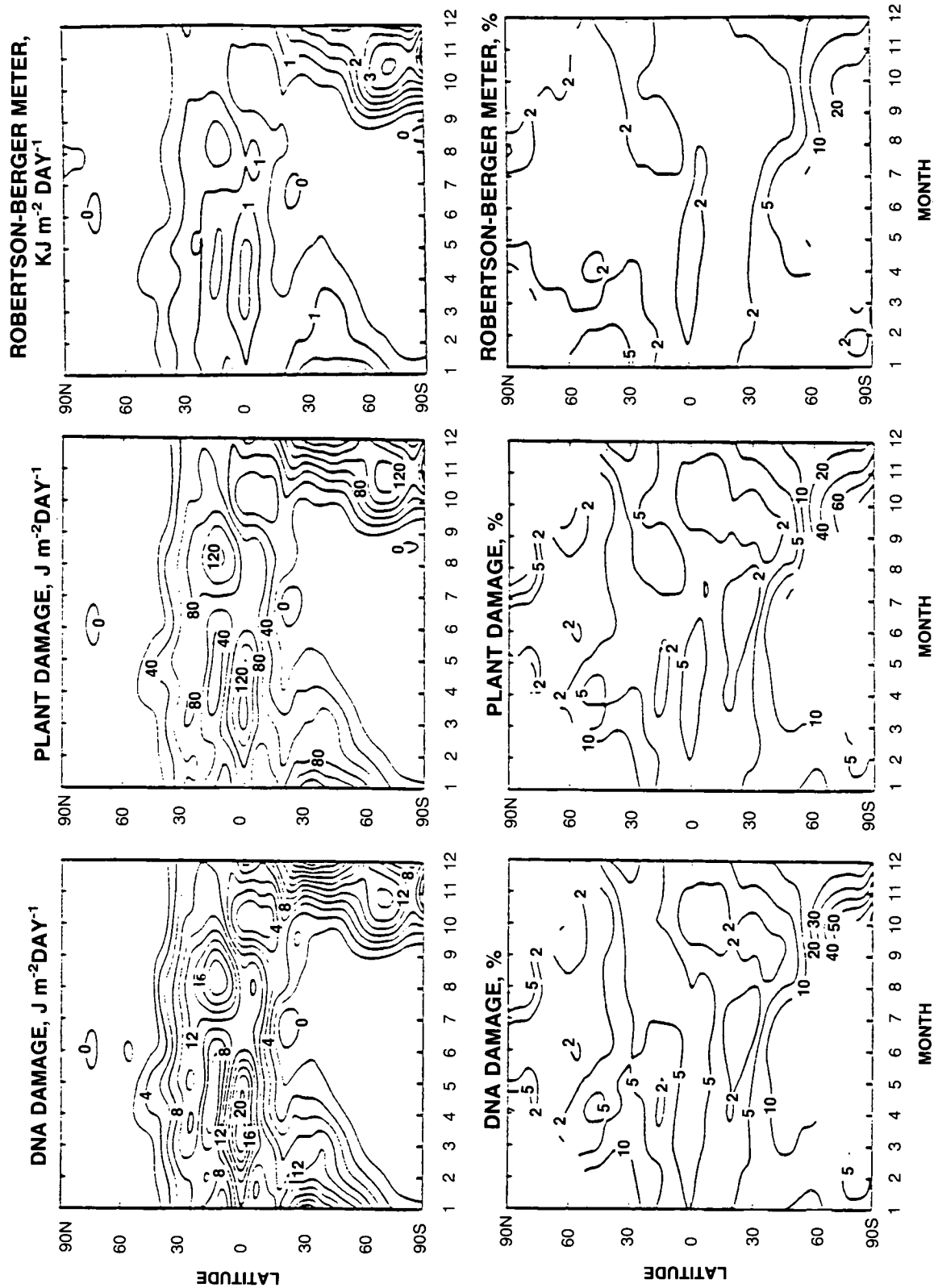

Figure 3.2-41. Daily dose changes from 1960 to 1980, GSFC2 model. Upper panels give absolute dose changes, lower panels give percent changes.

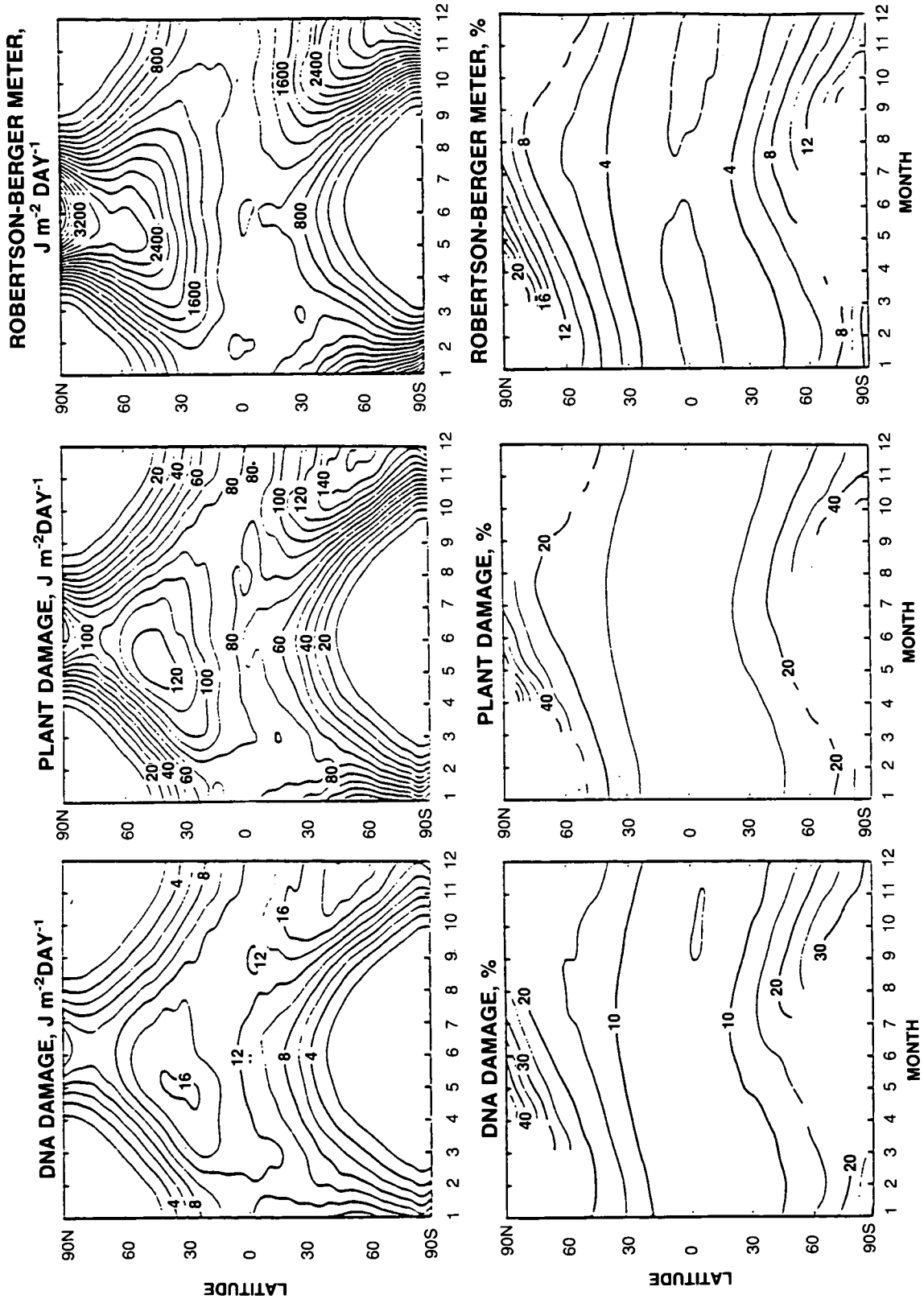

Figure 3.2-42. Daily dose changes from 1960 to 2060, GSFC2 model, scenario A1. Upper panels give absolute dose changes, lower panels give percent changes.

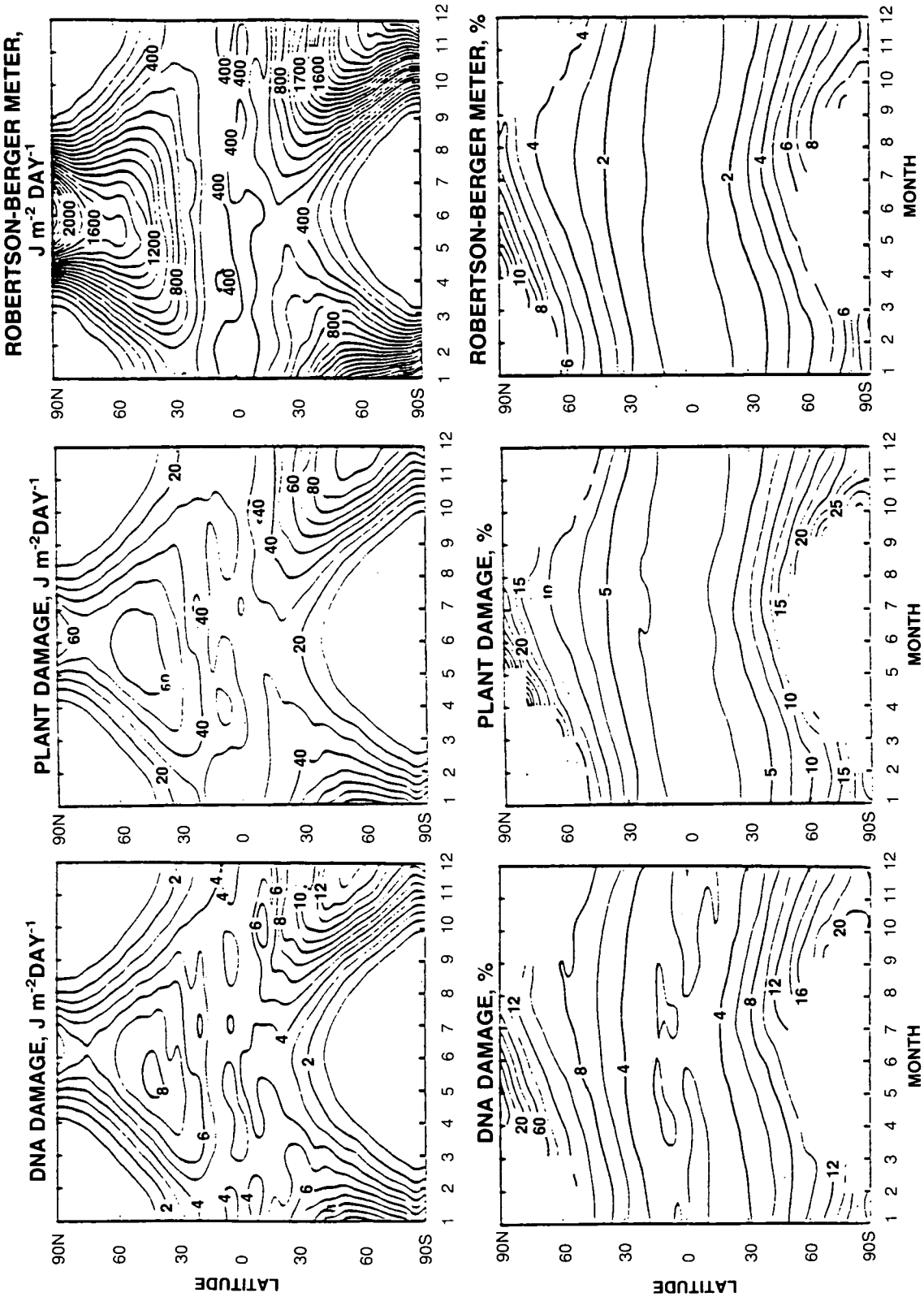

Figure 3.2-43. Daily dose changes from 1960 to 2060, GSFC2 model, scenario D1. Upper panels give absolute dose changes, lower panels give percent changes.

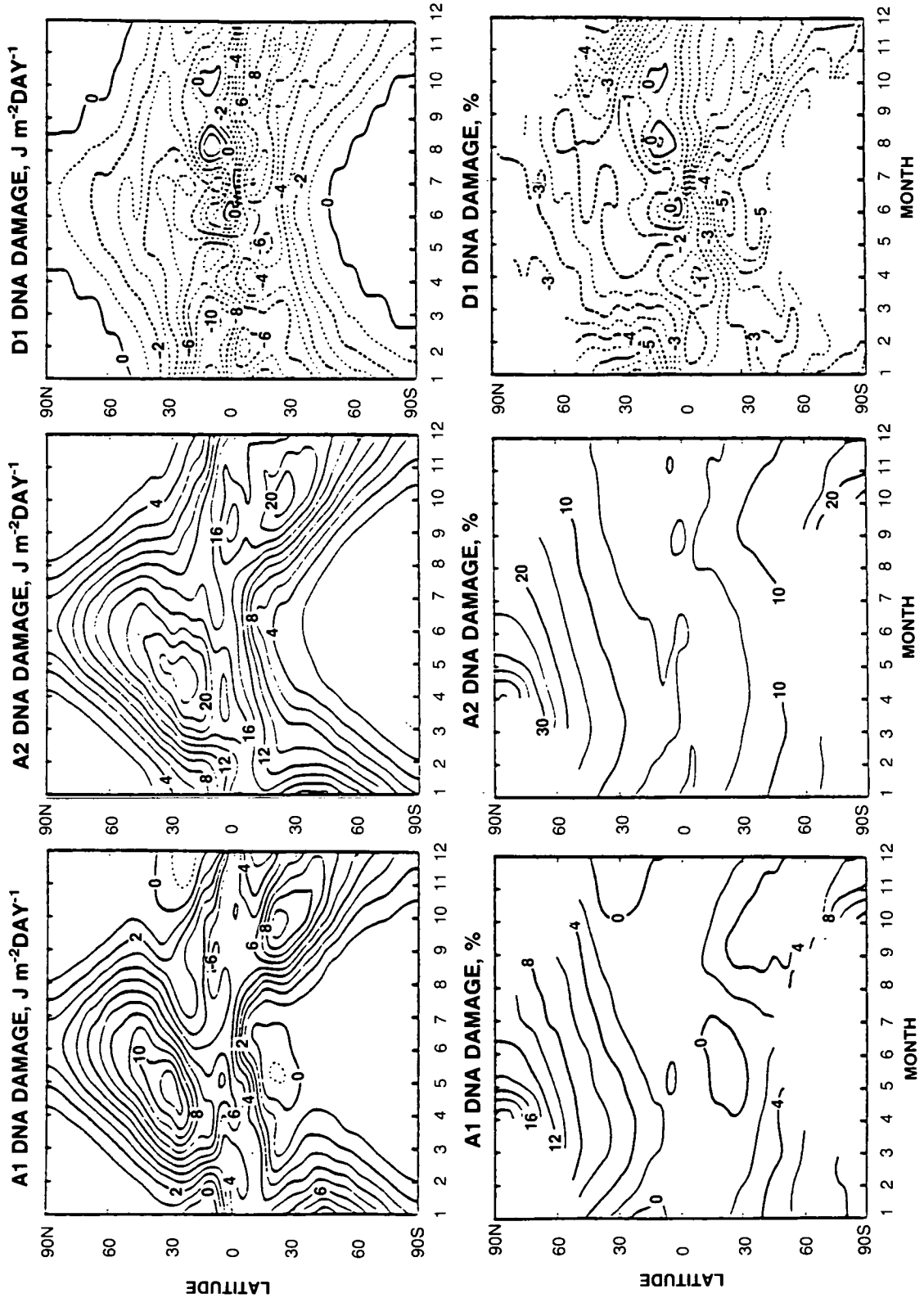

Figure 3.2-44. Daily DNA damage dose changes from 1980 to 2060, WisCAR model scenarios A1, A2, and D1. Upper panels give absolute dose changes, lower panels give percent changes.

If the assumption of constant environmental factors is valid, the calculation of relative changes in doses is insensitive to the choice of specific environmental factors. This is illustrated in Table 3.2.10, which compares the radiation amplification factor for the DNA damage dose rate calculated with the "base" model to that calculated under different environmental conditions. Clouds, surface albedo, surface elevation, and aerosol haze affect the absolute value of the DNA dose rate, but have a relatively small effect on the RAF and therefore on the sensitivity of the dose rate to future ozone changes. Similarly, the shape and orientation of the receiving surface relative to the incident light is not important in determining the relative dose rate change.

Large errors in the surface UV predictions will result if cloud cover patterns change systematically in the future due to changes in weather patterns associated with the so-called greenhouse effect. Relatively small changes in the average cloud cover may produce large changes in the average surface UV radiation (Frederick and Lubin, 1988b). Changes in the average ground albedo may also be important. At present, these changes are not very predictable.

Another significant uncertainty is the future of tropospheric ozone, which is expected to increase due to human activities. This effectively was included in some of the modeling scenarios discussed in the previous sections. To the extent that the tropospheric ozone contributes to the total ozone column, it was included in the calculations of the surface UV radiation, and tends to cancel the UV enhancements which result from the depletion of the stratospheric ozone. However, this effective shift of ozone from the stratosphere to the troposphere may induce some errors in the calculation of the surface UV. This is because in the stratosphere most of the UV radiation is present in the direct solar beam, while in the troposphere a greater fraction is diffused by Rayleigh and Mie scattering. The effective photon pathlengths through absorbing ozone layers are therefore different for the stratosphere than the troposphere (Brühl and Crutzen, 1989). While this effect is not expected to be large, it contributes to the uncertainty in the prediction of surface UV. More work is needed in the quantification of this effect and especially in reducing the large uncertainties in the prediction of future tropospheric ozone trends.

3.2.4 The Effects of Ozone Changes on Circulation

The dominant processes forcing the circulation of the middle atmosphere are radiative heating by ozone absorption of insolation, radiative cooling by CO_2 longwave emission, and momentum deposition by the dissipation of vertically propagating disturbances (waves) generated in the troposphere. Photochemically driven perturbations in ozone will change the radiative heating of the stratosphere and, consequently,

Table 3.2-10. Environmental effects on DNA radiation amplification factor (RAF)

Model	Solar Zenith Angle 0°	60°	75°	85°
Base model[a]	1.88	1.97	2.00	1.99
Surface albedo = 0.50	1.90	1.98	2.02	2.00
Aerosols (Elterman, 1968)	1.89	1.99	2.02	2.01
Cloud, thin	1.90	2.00	2.03	2.01
Cloud, thick	1.93	2.02	2.05	2.03
Hemispherical receiver	1.92	1.98	2.00	2.00
Surface at 3 km above sea level	1.88	1.98	2.01	2.00

[a]Base model: surface albedo 0.05, no aerosols, no clouds, horizontal receiver, sea level. RAF computed for ozone column change from 300 to 303 Dobson units.

the balance among the three dominant forcing processes. Since both the longwave emission and the wave momentum deposition are likely to change in response to substantial radiative heating changes, significant changes in the stratospheric circulation are possible. Stratospheric circulation changes are important because they would affect the transport of ozone and other trace constituents. For example, relatively small changes in the vertical motion within the winter polar vortex would produce substantial changes in the column-integrated ozone abundance at high latitudes.

In addition to photochemically driven perturbations to ozone and stratospheric circulation, we should also consider changes in the concentrations of CO_2 and other greenhouse gases. Increasing greenhouse gas concentrations will act to increase the longwave emission in the upper stratosphere and thus to cool the temperatures. Since reduced radiative heating due to ozone depletion has a similar effect, the two processes will reinforce each other, with the potential for larger changes to the stratospheric circulation. Greenhouse gases also have significant effect on the tropospheric circulation and may change the wave forcing of the stratosphere. The wave momentum deposition is a sensitive function of the wave generation in the troposphere and of the background stratospheric flow, which determines wave propagation and dissipation characteristics.

Unfortunately, very few of the presently available models adequately represent the physical processes important in determining possible circulation changes. This problem is most easily addressed in a 3-D modeling framework where wave generation, propagation, and dissipation processes are explicitly represented, at least for the large-scale waves. Some of the most recent 2-D models include the radiative effects of greenhouse gas increases, and at least one model includes the wave forcing effect through parameterized planetary wave propagation and dissipation (see discussion following scenario A in Section 3.2.2). However, the wave sources must be specified near the tropopause. Two-dimensional models cannot adequately predict changes in tropospheric temperatures and wave forcing of the stratospheric circulation.

Much more work has been done on the transport of trace constituents in 3-D models than on circulation changes resulting from altered ozone and greenhouse gas concentrations. At this time no fully coupled simulations have been performed in 3-D models with the radiative heating determined by a predicted ozone distribution including transport and photochemical effects within the model. There have been a small number of studies that have examined the effects of specified ozone or CO_2 changes. Fels et al. (1980) and Kiehl and Boville (1988) considered the effects of spatially uniform ozone reductions for annual mean conditions and for Northern Hemisphere winter conditions, respectively. For large ozone reductions (>50%), Kiehl and Boville found major differences in the stratospheric circulation with a much weaker polar vortex accompanied by reduced vertical motion (Figure 3.3-45).

The ozone depletions predicted by 2-D models are highly nonuniform, much larger depletions are predicted at high latitudes than at low latitudes and in the upper rather than lower stratosphere. Using a typical ozone depletion scenario, Kiehl and Boville found an increase in the strength of the polar vortex. The changes in the dynamical forcing of the stratosphere were quite modest so that a 2-D model including radiative feedbacks would have predicted similar changes outside of high latitudes in winter. The small vertical velocity changes in high latitudes (Figure 3.3-46) would not be simulated by most 2-D models but could significantly alter the column ozone abundance.

One recent model simulation of doubled CO_2 with a stratospheric GCM predicts noticeable increases in the mean diabatic circulation of the lower stratosphere (Rind et al., 1989). The combination of tropospheric warming and stratospheric cooling leads to an increase in the temperature lapse rate near the tropopause, and also to increased "wave forcing" of the mean diabatic circulation in the lower tropical

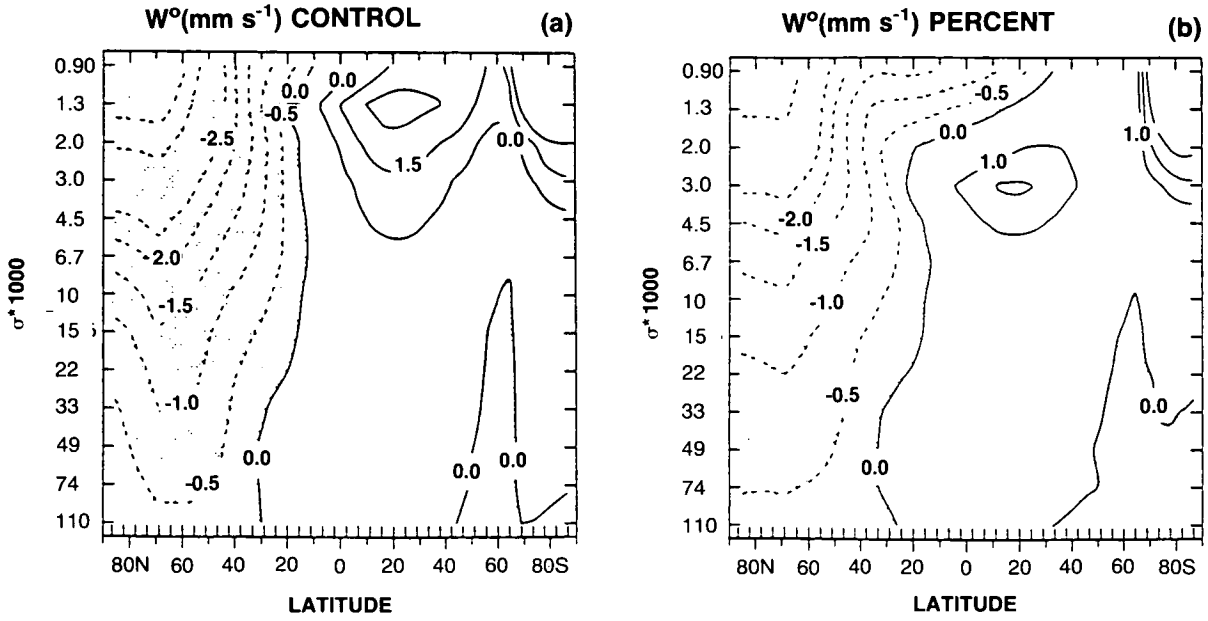

Figure 3.2-45. Transformed Eulerian mean vertical velocity for a 240-day average simulation performed with the NCAR Community Climate Model (Kiehl and Boville, 1988); (a) control case, (b) 75% uniform reduction in the ozone density.

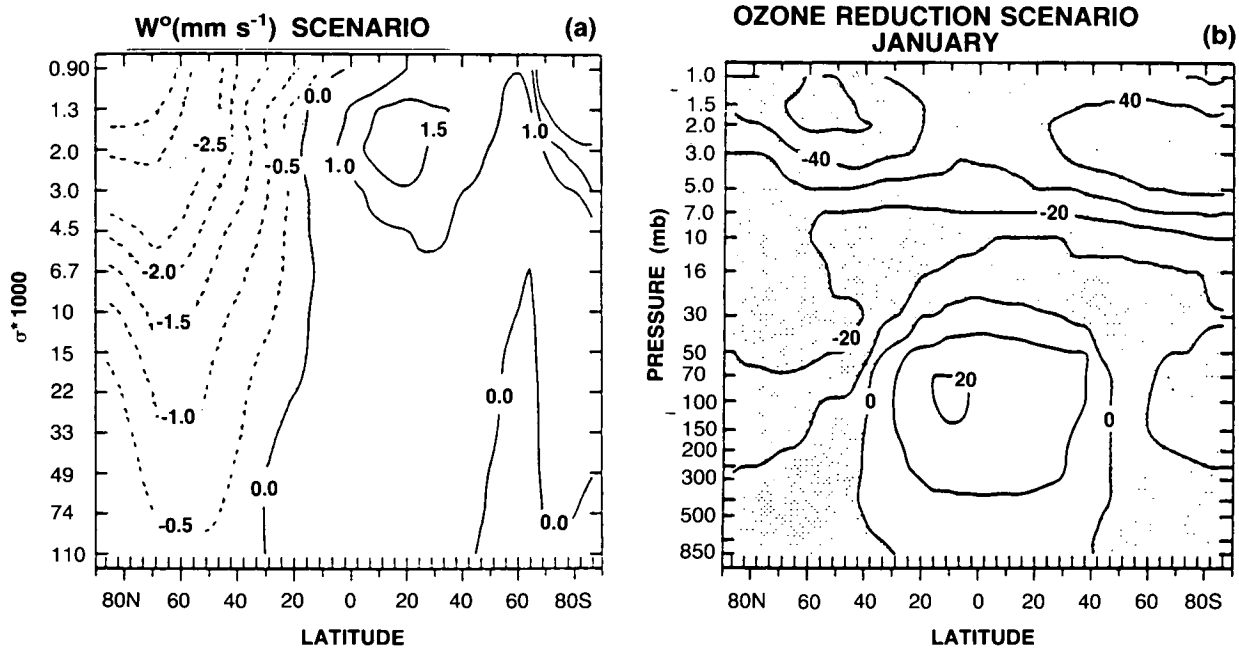

Figure 3.2-46. (a) As in Figure 3.2.40 but for the ozone reduction scenario shown in Figure 3.2.41b; (b) percent change in ozone from the two-dimensional model of Ko et al., 1985.

stratosphere. Another interesting issue for the doubled-CO_2 climate is the altitude at which the temperature change goes from positive (implying consequent ozone reductions) to negative (ozone increases). Results from the GISS model show that this level is sensitive to the tropospheric response, which has been shown in many climate models to vary with latitude and to take several decades to approach a steady state.

So little work has been done on the possible changes in stratospheric circulation that our current understanding of the issues involved and of the possible consequences is minimal. In the next few years we hope that 3-D climate models will examine this problem, diagnosing greenhouse gas-driven changes in the tropospheric climate and resulting stratospheric wave forcing. The response of stratospheric ozone and changes in the lifetimes of CFCs and N_2O should also be predicted within the same 3-D models.

REFERENCES

Anderson, G. P., and L. A. Hall, Stratospheric determination of O_2 cross sections and photodissociation rate coefficients:191–215 nm, *J. Geophys. Res., 91,* 14509–14515, 1986.

Andrews, D. G., and M. E. McIntyre, Planetary waves in horizontal and vertical shear: The generalized Eliassen-Palm relation and mean zonal acceleration, *J. Atmos. Sci., 33,* 2031–2048, 1976.

Boyd, J., The noninteraction of waves with the zonally-averaged flow on a spherical earth and the ionterrelationships of eddy fluxes of energy, heat and momentum, *J. Atmos. Sci., 33,* 2285–2291, 1976.

Brasseur, G., and M. H. Hitchman, The effect of breaking gravity waves on the distribution of trace species in the middle atmosphere, in *Transport Processes in the Middle Atmosphere,* pp. 215–227, Reidel, Dordrecht, Holland, 1987.

Brühl, C., and P. J. Crutzen, On the disproportionate role of tropospheric ozone as a filter against solar UV-B radiation, submitted to *Geophys. Res. Lett.*, 1989.

Caldwell, M. M., Plant response to solar ultraviolet radiation, in *Encyclopedia of Plant Physiology, Vol. 12A, Physiological Plant Ecology. I. Responses to the Physical Environment,* edited by O. L. Lange, P. S. Nobel, C. B. Osmond, and H. Ziegler, Springer-Verlag, Berlin, 1981.

Caldwell, M. M., L. B. Camp, C. W. Warner, and S. D. Flint, Action spectra and their key role in assessing biological consequences of solar UV-B radiation change, in *Stratospheric Ozone Reduction, Solar Ultraviolet Radiation and Plant Life,* edited by R. C. Worrest and M. M. Caldwell, pp. 87–111, Springer-Verlag, Berlin, 1986.

Chandrasekhar, S., *Radiative Transfer,* Dover, New York, 1960.

Cutchis, P., Stratospheric ozone depletion and solar ultraviolet radiation on Earth, *Science, 184,* 13, 1974.

DeMore, W. B., M. J. Molina, S. P. Sander, D. M. Golden, R. F. Hampson, M. J. Kurylo, C. J. Howard, and A. R. Ravishankara, Chemical kinetics and photochemical data for use in stratospheric modeling, evaluation number 8, JPL Publ. 87-41, 1987.

Dunkerton, T. J., On the role of the Kelvin wave in the westerly phase of the semiannual zonal wind oscillation, *J. Atmos. Sci., 36,* 32–41, 1979.

Dutsch, H. U., Photochemistry of atmospheric ozone, *Adv. Geophys., 15,* 219–232, 1971.

Edmon, H. J., B. J. Hoskins, and M. E. McIntyre, Eliassen-Palm cross sections for the troposphere, *J. Atmos. Sci., 37,* 2600–2616, 1980.

Elterman L., UV, visible, and IR attenuation for altitudes to 50 km, 1968, *AFCRL-68-0153, No. 285,* Air Force Cambridge Research Laboratories, Bedford, MA., 1968.

Fels, S. B., J. D. Mahlman, M. D. Schwarzkopf, and R. W. Sinclair, Stratospheric sensitivity to perturbations in ozone and carbon dioxide: Radiative and dynamical response, *J. Atmos. Sci., 37,* 2265–2297, 1980.

Frederick J. E., and D. Lubin, Possible long-term changes in the biologically active ultra-violet radiation reaching the ground, *Photochem. Photobio.*, *47*, 571–578, 1988a.

Frederick J. E., and D. Lubin, The budget of biologically active ultraviolet radiation in the Earth-atmosphere system, *J. Geophys. Res*, *93*, 3825–3832, 1988b.

Fröhlich C., and G. E. Shaw, New determination of Rayleigh scattering in the terrestrial atmosphere, *Appl. Opt.*, *19*, 1773–1775, 1980.

Garcia, R. R., On the mean meridional circulation of the middle atmosphere, *J. Atmos. Sci.*, *44*, 3599–3609, 1987.

Garcia, R. R., and S. Solomon, The effect of breaking gravity waves on the dynamics and chemical composition of the mesosphere and lower thermosphere, *J. Geophys. Res.*, *90*, D2, 3850–3868, 1985.

Gerstl, S. A. W., A. Zardecki, and H. L. Wiser, Biologically damaging radiation amplified by ozone depletions, *Nature, 294*, 352–354, 1981.

Granier, C., and G. Brasseur, Ozone and other trace gases in the Arctic and Antarctic regions: A three-dimensional model, in preparation, 1990.

Gray, L. J., and J. A. Pyle, Two-dimensional model studies of equatorial dynamics and tracer distributions, *Q. J. Roy. Meteorol. Soc.*, *113*, 635–651, 1987.

Gray, L. J., and J. A. Pyle, A two-dimensional model of the quasi-biennial oscillation of ozone, *J. Atmos. Sci.*, *46*, 203–220, 1989.

Grose, W. L., J. E. Nealy, R. E. Turner, and W. T. Blackshear, Modeling the transport of chemically active constituents in the stratosphere, in *Transport Processes in the Middle Atmosphere*, Reidel, Dordecht, Holland,1987.

Herman, J. R., and J. E. Mentall, O_2 absorption cross sections (187–225 nm) from stratospheric solar flux measurements, *J. Geophys. Res.*, *87*, 8967–8975, 1982.

Hitchman, M. H., and G. Brasseur, Rossby wave activity in a two-dimensional model: Closure for wave driving and meridional eddy diffusivity, *J. Geophys. Res.*, *93*, D8, 9405–9417, 1988.

Hofmann, D. J., and S. Solomon, Ozone destruction through heterogeneous chemistry following the eruption of El Chichon, *J. Geophys. Res, 94*, 5029, 1989.

Holton, J. R., Wave propagation and transport in the middle atmosphere. *Phil. Trans Roy. Soc.* London, A296, 73–85, 1980.

Holton, J. R., The role of gravity wave induced drag and diffusion in the momentum budget of the mesosphere, *J. Atmos. Sci.*, *39*, 791–799, 1982.

Jackman, C. H., P. A. Newman, P. D. Guthrie, and M. R. Schoeberl, Effect of self-consistent horizontal diffusion coefficients on two-dimensional N_2O model distributions, *J. Geophys. Res.*, *93*, 5213–5219, 1988.

Jackman, C. H., A. R. Douglass, P. D. Guthrie, and R. S. Stolarski, The sensitivity of total ozone and ozone perturbation scenarios in a two-dimensional model due to dynamical inputs, *J. Geophys. Res.*, in press, 1989a.

Jackman, C. H., R. K. Seals, and M. J. Prather (eds.), *Two-Dimensional Intercomparison of Stratospheric Models,* Proceedings of the NASA Workshop held in Virginia Beach, Virginia, September 11–16, 1988, NASA Conference Publication 3042, NASA, 1989b.

Joseph, J. H., W. J. Wiscombe, and J. A. Weinman, The delta-Eddington approximation for radiative flux transfer, *J. Atmos. Sci.*, *33*, 2452–2459, 1976.

Juckes, M. N., and M. E. McIntyre, A high-resolution one-layer model of breaking planetary waves in the stratosphere, *Nature, 328*, 590–596, 1987.

Kaye, J. A., and R. B. Rood, Chemistry and transport in a three-dimensional stratospheric model: Chlorine species during a simulated stratospheric warming, *J. Geophys. Res.*, *94*, 1057–1083, 1989.

Kida, H., General circulation of air parcels and transport characteristics derived from a hemispheric GCM. Part 1. A determination of advective mass flow in the lower stratosphere, *J. Meteor. Soc. Japan, 61*, 171–186, 1983.

Kiehl, J. T., and B. A. Boville, The radiative-dynamical response of a stratospheric-tropospheric general circulation model to changes in ozone, *J. Atmos. Sci., 45*, 1798–1817, 1988.

King, M. D., and Harshvardhan, Comparative accuracy of selected multiple scattering approximations, *J. Atmos. Sci., 43*, 784–801, 1986.

Ko, M. K. W., K. K. Tung, D. K. Weinstein, and N. D. Sze, A zonal-mean model of stratospheric tracer transport in isentropic coordinates: Numerical simulations for nitrous oxide and nitric acid, *J. Geophys. Res., 90*, 2313-2329, 1985.

Ko, M. K. W., N. D. Sze, and D. Weisenstein, The roles of dynamical and chemical processes in determining the stratospheric concentration of ozone in one-dimensional and two-dimensional models, *J. Geophys. Res.*, in press, 1989.

Leu, M. T., Laboratory studies of sticking coefficients and heterogeneous reactions important in the Antarctic stratosphere, *Geophys. Res. Lett., 15*, 17–20, 1988a.

Leu, M. T., Heterogeneous reactions of N_2O_5 with H_2O and HCl on ice surfaces: Implications for Antarctic ozone depletion, *Geophys. Res. Lett., 15*, 855–858, 1988b.

Lindzen, R. S., Turbulence and stress due to gravity wave and tidal breakdown, *J. Geophys. Res., 86*, 9707–9714, 1981.

Lyjak, L. V., Diffusion coefficients calculated from satellite data, in *Transport Processes in the Middle Atmosphere*, pp. 343–352, Dordecht, Holland, 1987.

Madronich S., Photodissociation in the atmosphere: 1. Actinic flux and the effects of ground albedo and clouds, *J. Geophys. Res., 92*, 9740–9752, 1987.

Mahlman, J. D., and L. J. Umscheid, Dynamics of the middle atmosphere: Successes and problems of the GFDL "SKYHI" general circulation model, in *Dynamics of the Middle Atmosphere*, edited by J. R. Holton and T. Matsuno, pp. 501–525, Terrapub, Tokyo, 1984.

McElroy, M. B., and R. J. Salawitch, Changing composition of the global stratosphere, *Science, 243*, 763–770, 1989.

Meadow W. E., and W. R. Weaver, Two–stream approximations to radiative transfer in planetary atmospheres: A unified description of existing methods and a new improvement, *J. Atmos. Sci., 37*, 630–643, 1980.

Mentall J. E., J. E. Frederick, and J. R. Herman, The solar irradiance from 200 to 330 nm, *J. Geophys. Res., 86*, 9881–9884, 1981.

Molina L. T., and M. J. Molina, Absolute absorption cross sections of ozone in the 185- to 350-wavelength range, *J. Geophys. Res., 91*, 14501–14508, 1986.

Molina, M. J., T. L. Tso, L. T. Molina, and F. C. Y. Wang, Antarctic stratospheric chemistry of chlorine nitrate, hydrogen chloride, and ice: Release of active chlorine, *Science, 238*, 1253–1257, 1987.

Mozurkewich, M., and J. G. Calvert, Reaction probability on N_2O_5 on aqueous aerosols, *J. Geophys. Res., 93*, 15889, 1988.

Natarajan, M., and L. B. Callis, Examination of stratospheric ozone photochemistry in light of recent data, *Geophys. Res. Lett., 16*, 473–476, 1989.

Neckel H., and D. Labs, The solar radiation between 3300 and 12500 A, *Solar Physics, 90*, 205–258, 1984.

Newman, P. A., M. R. Schoeberl, and R. A. Plumb, Horizontal mixing coefficients for two-dimensional chemical models calculated from National Meteorological Center data, *J. Geophys. Res., 91*, D7, 7919–7924, 1986.

Newman, P. A., M. R. Schoeberl, R. A. Plumb, and J. E. Rosenfield, Mixing rates calculated from potential vorticity, *J. Geophys. Res., 93*, 5210–5240, 1988.

Nicolet M., R. R. Meier, and D. E. Anderson, Jr., Radiation field in the troposphere and stratosphere-II. Numerical analysis, *Planet. Space Sci., 30*, 935–983, 1982.

Pitari G., M. Verdecchia, and G. Visconti, Ozone hole simulation using a prescribed dynamical field, in preparation, 1990.

Plumb, R. A., The interaction of two internal waves with the mean flow: Implications for the theory of the quasi-biennial oscillation, *J. Atmos. Sci., 34*, 1847–1858, 1977.

Plumb, R. A., and J. D. Mahlman, The zonally averaged transport characteristics of the GFDL general circulation/transport model, *J. Atmos. Sci., 44*, 298–327, 1987.

Pyle, J. A., and R. G. Derwent, Possible ozone reductions and UV changes at the Earth's surface, *Nature, 286*, 373–375, 1980.

Raper, O. F., C. B. Farmer, R. Zander, and J. H. Park, Infrared spectroscopic measurements of halogenated sink and reservoir gases in the stratosphere with the ATMOS instrument, *J. Geophys. Res., 92*, 9851–9858, 1987.

Reed, R. J., and K. E. German, A contribution to the problem of stratospheric diffusion by large-scale mixing, *Mon. Wea. Rev., 93*, 313–321, 1965.

Rind, D., R. Suozzo, and N. K. Balachandran, The GISS global climate-middle atmosphere model. Part II: Model variability due to interactions between planetary waves, the mean circulation and gravity wave drag, *J. Atmos. Sci., 45*, 371–386, 1989.

Robertson, D. F., The sunburn unit for comparison of variation of erythemal effectiveness, in *Impacts of Climactic Change on the Biosphere, Part I, Ultraviolet Radiation Effects*, edited by D. S. Nachtwey, M. M. Caldwell, and R. H. Biggs, Monograph 5. Climactic Impact Assessment Program, U.S. Dept. Transportation Report No. DOT-TST-75-55, NTIS, Springfield, Virginia, 1975.

Rodriguez, J. M., M. K. W. Ko, and N. D. Sze, Antarctic chlorine chemistry: Possible global implications, *Geophys. Res. Lett., 15*, 257–260, 1988.

Rood, R. B., and J. A. Kaye, Stratospheric ozone models and supercomputers, to appear in *Proceedings of the Fourth International Conference on Supercomputing*, International Supercomputing Institute, St. Petersburg, Florida, in press, 1989.

Rood R. B., D. J. Allen, W. E. Baker, D. J. Lamich, and J. A. Kaye, The use of assimilated stratospheric data in constituent transport experiments, *J. Atmos. Sci., 46*, 687–701, 1989.

Rose, K., and G. Brasseur, Ozone during a sudden stratospheric warming: A three dimensional simulation, in *Atmospheric Ozone, Proceedings of the Quadrennial Ozone Symposium*, Halkidiki, Greece, edited by C. S. Zerefos and A. Ghazi, D. Reidel, Hingham, Mass., 1985.

Rose, K., and G. Brasseur, A three-dimensional model of chemically active trace species in the middle atmosphere during disturbed winter conditions, *J. Geophys. Res., 94*, 16387–16403, 1989.

Russell III, J. M., C. B. Farmer, C. P. Rinsland, R. Zander, L. Frordevaux, G. C. Toon, B. Gao, J. Shaw, and M. Gunson, Measurements of odd nitrogen compounds in the stratosphere by the ATMOS experiment on Spacelab 3, *J. Geophys. Res., 93*, 1718–1736, 1988.

Schneider, H. R., M. E. W. Ko, N. D. Sze, G.-Y. Shi, and W.-C. Wang, The effects of eddy diffusion, drag, and nonlinear terms on the meridional circulation and ozone distributions in an interactive 2-D model, *J. Atmos. Sci.*, in press, 1989.

Scotto J., G. Cotton, F. Urbach, D. Berger, and T. Ferris, Biologically effective ultraviolet radiation: Surface measurements in the United States, 1974 to 1985, *Science, 238*, 762–764, 1988.

Setlow, R. B., The wavelengths in sunlight effective in producing skin cancer: A theoretical analysis, *Proc. Natl. Acad. Sci. USA, 71*, 3363–3366, 1974.

Shettle E. P., and J. A. Weinman, The transfer of solar irradiance through inhomogeneous turbid atmospheres evaluated by Eddington's approximation, *J. Atmos. Sci., 27*, 1048–1055, 1970.

Smith, A. K., L. V. Lyjak, and J. C. Gille, The eddy transport of nonconserved trace species derived from satellite data, *J. Geophys. Res., 93*, D9, 11103–11122, 1988.

Snieder, R. K., and S. B. Fels, The flywheel effect in the middle atmosphere, *J. Atmos. Sci.*, *45*, 3996–4004, 1988.

SORG, U. K. Stratospheric Ozone Review Group Report, September 1988, H. M. Stationary, London, ISBN 0 11 752 1485, 1988.

Stamnes, K., The theory of multiple scattering of radiation in plane parallel atmospheres, *Rev. Geophys.*, *24*, 299–310, 1986.

Stordal, F., O. Hov, and I. S. A. Isaksen, The effect of perturbation of the total ozone column due to CFC on the spectral distribution of UV fluxes and the damaging UV doses at the ocean surface: A model study, in *The Role of Solar Ultraviolet Radiation in Marine Ecosystems*, edited by J. Calkins, Plenum, New York, 1982.

Tung, K. K., Nongeostrophic theory of zonally averaged circulation. Part I: Formulation, *J. Atmos. Sci.*, 43, 2600–2618, 1986.

Tung, K. K., A coupled model of zonally averaged dynamics, radiation, and chemistry, in *Transport Processes in the Middle Atmosphere*, pp. 183–198, Reidel, Dordecht, Holland, 1987.

Watson, R. T., and Ozone Trends Panel; M. J. Prather and Ad Hoc Theory Panel; and M. J. Kurylo and NASA Panel for Data Evaluation, *Present State of Knowledge of the Upper Atmosphere 1988: An Assessment Report*, NASA Reference Publication 12081, U.S. Govt. Print. Off., Washington, D.C., 1988.

WMO, Atmospheric Ozone 1985. Assessment of Our Understanding of the Processes Controlling Its Present Distribution and Change, *WMO Report No. 16*, Sponsored by WMO, NASA, NOAA, FAA, UNEP, CEC, and BMFT, Washington, D.C., 1986.